Life Science Journal

Life Science Journal

2010   Volume 7,   Number 1   ISSN:1097-8135

Marsland Press

PO Box 180432, Richmond Hill, New York 11418, USA

Website:
http://www.sciencepub.net

Emails:
editor@sciencepub.net
sciencepub@gmail.com

Phone: (347) 321-7172

9 771097 813002

MARSLAND PRESS
Multidisciplinary Academic Journal Publisher

Websites:
http://www.lifesciencesite.com
http://www.sciencepub.net

Emails:
lifesciencej@gmail.com
editor@sciencepub.net

Life Science Journal

Life Science Journal, the Acta Zhengzhou University Oversea Version, is an international journal with the purpose to enhance our natural and scientific knowledge dissemination in the world under the free publication principle. The journal is calling for papers from all who are associated with Zhengzhou University-home and abroad. Any valuable papers or reports that are related to life science - in their broadest sense - are welcome. Other academic articles that are less relevant but are of high quality will also be considered and published. Papers submitted could be reviews, objective descriptions, research reports, opinions/debates, news, letters, and other types of writings. Let's work together to disseminate our research results and our opinions.

Introductions to Authors
1. General Information
(1) **Goals**: As an international journal published both in print and on internet, **Life Science Journal** is dedicated to the dissemination of fundamental knowledge in all areas of nature and science. The main purpose of **Life Science Journal** is to enhance our knowledge spreading in the world under the free publication principle. It publishes full-length papers (original contributions), reviews, rapid communications, and any debates and opinions in all the fields of nature and science.

(2) **What to Do**: The **Life Science Journal** provides a place for discussion of scientific news, research, theory, philosophy, profession and technology - that will drive scientific progress. Research reports and regular manuscripts that contain new and significant information of general interest are welcome.

(3) **Who**: All people are welcome to submit manuscripts in life science fields. Papers of other fields are also considered.

(4) **Copyright and Responsibility of Authors to their Articles:** When the manuscript(s) is submitted to the journal, the authors agree the following: All the authors have participated sufficiently in this work; The article is not published elsewhere; Authors are responsibility on the contents of the article; The journal and author(s) have same right for the copyright of the article and either of the journal or author(s) can use it by anyway without noting the other party.

(5) **Publication Costs**: US$500 per article to defray costs of the publication will be paid by the authors when it is received. Extra expense for color reproduction of figures will be paid by authors (estimate of cost will be provided by the publisher for the author's approval).

(6) **Advertisements**: The price will be calculated as US$400/page, i.e. US$200/a half page, US$100/a quarter page, etc. Any size of the advertisement is welcome.

2. Manuscript Preparation
Each manuscript is suggested to include the following components but authors can do their own ways:

(1) **Title**: including the complete article title; each author's full name; institution(s) with which each author is affiliated, with city, state/province, zip code, and country; and the name, complete mailing address, telephone number, facsimile number (if available), and at least one email address for author(s). (2) **Abstract**: including Background, Materials and Methods, Results, and Discussions. (3) **Key Words**. (4) **Introduction**. (5) **Materials and Methods**. (6) **Results**. (7) **Discussions**. (8) **Acknowledgments**. (9) **References**.

3. Manuscripts Submission
(1) **Submission Methods**: Submission through email (editor@sciencepub.net) is encouraged.

(2) **Software**: The Microsoft Word file will be preferred.

(3) **Font**: Normal, Times New Roman, 10 pt, single space.

(4) **Indent**: Type 2 space in the beginning of each new paragraph.

(5) **Manuscript**: Don't use "Footnote" or "Header and Footer".

(6) **Email:** At least one author's email must be put under title.

(7) **Title:** Use Title Case in the title and subtitles, e.g. "**Debt and Agency Costs**".

(8) **Figures and Tables:** Use full word of figure and table, e.g. "**Figure 1.** Annul Income of Different Groups**, Table 1. Annual Increase of Investment".**

(9) **References**: Cite references by "last name, year", e.g. "(Smith, 2003)". References should include all the authors' last names and initials, title, journal, year, volume, issue, and pages etc.
  Reference Examples:
  Journal Article: Hacker J, Hentschel U, Dobrindt U. Prokaryotic chromosomes and disease. Science 2003;301(34):790-3. **Book**: Berkowitz BA, Katzung BG. Basic and clinical evaluation of new drugs. In: Katzung BG, ed. Basic and clinical pharmacology. Appleton & Lance Publisher. Norwalk, Connecticut, USA. 1995:60-9.

(10) **Submission Address:** editor@sciencepub.net, Marsland Press, PO Box 180432, Richmond Hill, New York 11418, USA, 347-321-7172.

CONTENTS

I

Enhanced immunogenicity in the mice immunized with lyophilized recombinant adenoviral HIV vaccine prime/MVA boost vaccine regimen

Yizhe Zhang[1], Wei Kong[2]

1. *Department of Bioengineering   Zhengzhou University, Zhengzhou, Henan*, China; 2. *College of life Science, Jilin University, Changchun, Jilin*, China. yizhezhang@126.com

Abstract

Background HIV-1 pandemic posed an unprecedent challenge to the global health and it is believed that an effective vaccine will be the final solution against HIV-1. **Objective.** To compare the immunogenicity of lyophilized recombinant replication-defective adenovirus 5-based vaccine expressing HIV gagpol gene (rAd5-gagpol vaccine) and of a vaccine combining rAd5-gagpol and lyophilized recombinant modified vaccinia virus Ankara (MVA)-based vaccine expressing HIV gagpol gene (MVA-gagpol). **Methods** Lyophilized rAd5-gagpol vaccine was priming injected intramuscular followed by MVA boosting into BALB/ c mice , then the Western blot analysis and IFN- Elispot assay were used to detect the immunogenicity of lyophilized vaccine in mice. **Results** The mice immunized with lyophilized rAd5-gagpol vaccine elicited HIV-1 specific antibody and cell mediated immune response .The lyophilized rAd5 /MVA combination was able to enhance IFN- secretion by Ag-specific $CD8^+$ T cells. **Conclusion** Lyophilized rAd5-gagpol vaccine was found to induce a strong $CD8^+$ T cell response after intramuscular immunisation. Boosting of lyophilized rAd5-gagpol vaccine-primed immune response with the lyophilized MVA-gagpol vaccine led to enhanced immunogenicity. [Life Science Journal. 2010; 7(1): 1 – 4] (ISSN: 1097 – 8135).

Key words: HIV-1; lyophilized vaccine; immunogenicity; Prime-Boost

1 Introduction

Recently it has been shown that prime-boost vaccination strategies not only increase frequencies of responding $CD8^+$ T cells but also may have consequences on $CD8^+$ T cell quality, which in turn may impact the efficacy of T cell-inducing vaccines [1-3]. HIV-specific cellular and humoral responses play a critical role in controlling viral replication and disease progression[4,5].

Replication-defective adenovirus type 5 (Ad5) is developed as vaccine vehicles to immunize against a number of pathogens[6]. Ad5-based vaccines are known to induce strong immunity against immunodeficiency viruses. A regimen that primes with DNA and then boosts with rAd5 is known to protect macaques against SHIV challenge by inducing high levels of viral-specific immunities[7,8].

Several clinical trials to evaluate recombinant modified vaccinia virus Ankara (MVA) as a vaccine for HIV prevention and treatment have been initiated [9,10]. Nevertheless, MVA vectors may need to be further optimized and additional routes of immunization explored to achieve effective protection in human trials. In particular, natural transmission of HIV is through a mucosal surface, and targeting immune responses to the gastrointestinal entry site before viral dissemination could protect and more effectively clear virus from the major site of HIV replication in the intestinal mucosa [11,12].

Due to the limited replication capacity of MVA, it is necessary to develop procedures that can enhance the specific cellular immune responses to the recombinant antigen delivered by the MVA vector [13].

Furthermore, recombinant adenovirus type 5 and MVA-based vaccine are sensitive to repeat freeze-thaw cycle and easy to lose activity. The rapid loss of vector infectivity during storage and shipment has been reported [14]. Owing to their poor thermostability, the safe continuum handling practices, including materials, equipment and procedures, which maintain vaccines below -20 from the time they are being manufactured to the time they are administered to patients, must be insured. If the "cold chain" is broken, a significant loss of infectivity may occur at any time.

In earlier studies, we have already identified optimal protector excipient and buffer system of lyophilized recombinant adenovirus 5-based vaccine (Ad5-gagpol vaccine) and lyophilized recombinant MVA-based vaccine expressing HIV gagpol gene[15,16]. The two lyophilized recombinant live virus- based vaccines showed good stability and immunogenicity [15,17].In addition, they can be shipped and stored at the room temperature, supporting their further evaluation and application in clinical studies. In this study we have tested the capacity of lyophilized rAd5-gagpol vaccine to induce $CD8^+$ T cell responses in mice either alone or in combination with MVA-gagpol vaccine.

2 Materials and Methods

2.1 Preparation of lyophilized rAd5-gagpol vaccine and MVA-gagpol vaccine

Lyophilized recombinant adenovirus 5-based vaccine (rAd5-gagpol vaccine) and lyophilized recombinant MVA-based vaccine expressing HIV gagpol gene (MVA-gagpol vaccine) have been described in detail previously (Zhang et al, 2006; Zhang et al, 2007a).

2.2 Mice and Immunization schedule

Female 6- to 8-week-old BALB/c mice were purchased from Jilin University (China). Mice were divided into the rAd5-gagpol vaccine group the rAd5/MVA combined vaccine group and the control group. Each group contained five mice. The rAd5-gagpol vaccine group mice were administered a single

intramuscular injection containing 5×10^8 pfu of lyophilized rAd5-gagpol vaccine per mouse. For prime-boost experiments, mice were primed intramuscular injection with rAd5-gagpol vaccine at a dose of 5×10^8 pfu per mouse. After 7 days, mice were boosted with recombinant MVA viruses at a dose of 10^7 pfu delivered by intraperitoneal injection. Control group mice were inoculated by PBS. Blood samples were collected on days 7, 14 from the on-start of immunization and assayed by Western blot. Thirteen days after inoculation, the mice were sacrificed and their spleens were processed for ELISPOT assay.

2.3 Antibody detection

Collect Molt III B cell(stably expresses the HIV-protein cell line) supernatant , then centrifuge at 26000 rpm / min. Resuspend the precipitation and run SDS-PAGE, transfer to cellulose membrane as antigen detecting mouse blood serum. The blocked membranes were placed in a multiscreen apparatus (Bio-Rad, USA), and approximately 100μl of diluted serum was pipetted into individual lanes. Serum samples were diluted 1:50 with 3% milk-PBS. Following a 2 h incubation at RT, the blots were removed from the apparatus and washed three times in T-PBS. The membranes were then incubated 1 h at RT with antimouse IgG antibodies conjugated with AP and washed three times with T-PBS. The blots were visualized with NBT and BCIP in AP buffer (Sigma, USA), as recommended by the manufacturer. The blots were developed by using the ECL Plus Western blotting detection system (Amersham Pharmacia Biotech).

2.4 IFN- ELISPOT assay

An ELISPOT assay kits (USA)was used to determine vaccine elicited IFN- responses in BALB/c mice. Spleen lymphocytes from the immunized mice were cultured in a plate with medium. 96-well plates were coated with purified anti-mouse IFN- monoclonal antibodies, and incubated at 4 overnight. Mice splenocytes were isolated and red blood cells were lysed by RBC lysis buffer. Cells were washed two times and re-suspended in complete culture medium. After counting, splenocytes were then adjusted to the concentration of 4×10^6 cells/ml and plated into pre-coated 96-well Elispot plate at 100μl/ well with addition of 100μl peptide P7G AMQMLKETI, 1μg/ml .The Elispot plates were incubated and developed according to the kit instruction. Finally, plates were air-dried and the resulting spots were counted with Immunospot Reader (USA). Peptide specific IFN- Elispot responses were considered as positive only when the responses were 4-fold above negative control with no peptide stimulation.

2.5 Statistical analysis

Comparisons of test results among groups of mice were performed using the Kruskal–Wallis H-test followed by Student–Newman–Keuls correction.

3 Results
3.1 Humoral immune responses

The mouse blood serum according to 1:50 dilution, anti-P_{24} antibody was used to detect humoral immune response in blood serum with Western blot law. A specific 24kDa band corresponding to gagpol was observed detected by an anti-mouse IgG mAb. The lane 2 corresponding to rAd5 prime / MVA boost vaccinated mice was much stronger than the lane 3 corresponding to rAd5-gagpol alone (Figure.1). Figure.1 demonstrates that rAd5 prime / MVA boost combined vaccine group produce antibody level noticeable higher than rAd5-gagpol vaccine alone group.
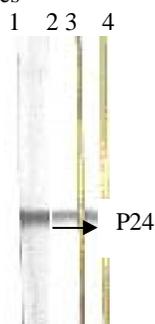
Figure 1. Western blot analysis the antibody level of lyophilized and liquid Ad-gagpol vaccine immunized mice

1: PBS negative control	2: rAd5 prime / MVA boost
3: rAd5-gagpol alone	4: mice P_{24} Ab positive control

3.2 The role of CD8 T cells bias in prime-boost immunization

To investigate whether rAd5-gagpol vaccine prime and MVA-gagpol vaccine boost immunizations induce Ag-specific CD8 T cells with enhanced IFN- production, Ag -specific CD8 T cells were analyzed by IFN- ELISPOT. The evaluated results for IFN-production are expressed as the mean numbers of IFN-secreting cells (spots) per 10^5 splenocytes. As determined by the ELISPOT assay, the rAd5 prime / MVA boost combined vaccine elicited a significantly higher number of IFN- -secreting lymphocytes than rAd5-gagpol vaccine alone (795 versus 287, $P < 0.01$) (Figure 2). These results illustrate that a rAd5 prime and MVA boost immunization strategy, increased the IFN- secretion of individual Ag-specific CD8 T cells.
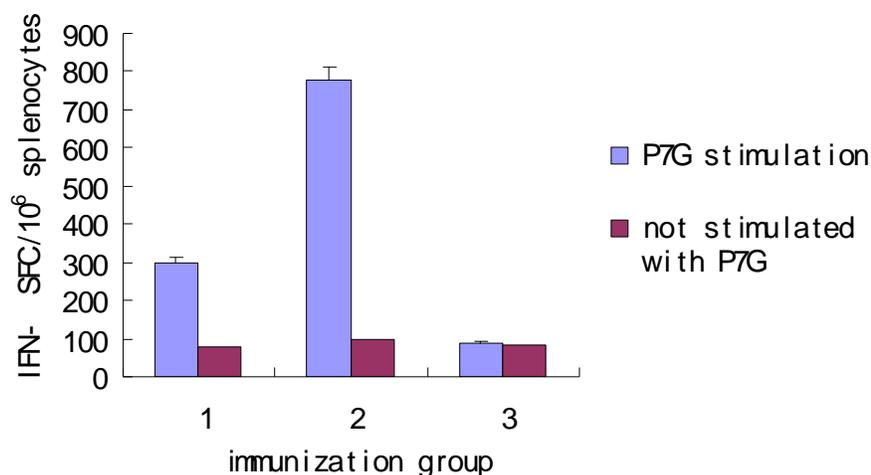
Figure 2.   Cell-mediated immune response by ELISPOT
1   rAd5-gagpol alone   2   rAd5 prime / MVA boost   3   PBS negative control

4 Discussion

Most successful vaccines to date rely on the induction of neutralizing antibodies. Unfortunately, induction of protective levels of antibodies has not yet been achieved with HIV-1 vaccines. Thus, the focus for HIV-1 vaccines has shifted to induction of cellular immune responses, namely memory CD8^{+} T cells. Generation of specific CD8^{+} CTL responses by vaccines may facilitate efficient control of HIV replication [7].

Recombinant Ad5-based and MVA-based vectors as new vaccine delivery systems are capable of inducing cell mediated immune responses against encoded antigens, in many cases these have been of limited protective efficacy. In contrast, the recent development of prime-boost vaccination strategies has proven to be highly effective in generating cell mediated immune responses that are protective against diverse pathogenic challenge [18].

Much of the immunological data generated so far have focused on CD8^{+} T cell responses resulting from a single immunization, while clinical trials with HIV-1 vaccines are generally based on prime boost regimens. Different combinations of prime-boost vaccines are currently being tested in multiple experiments and clinical trials for AIDS [19,20]. The prime-boost strategy is capable of inducing broad and high levels of T-cell immunity and ameliorating SIV infection in macaques [21,22]. It is therefore crucial to elucidate the effects of multiple immunizations on the quality of CD8^{+} T cells.

In the present study, we found that the lyophilized virus-based vaccine induced strong humoral and cell-mediated HIV-specific immune responses in mice. This study indicates that the main advantage of the lyophilized rAd5-gagpol prime and MVA-gagpol boost vaccination strategy is enhanced immunogenicity.

Both rAd5 vaccines and MVA vectors efficiently introduce encoded proteins into MHC class I and II antigen-processing pathways, leading to the efficient induction of specific CD4 and CD8 T cells. The generation of high-avidity T cell populations by rAd5 vaccination which are greatly and efficiently expanded following boosting by MVA vectors expressing higher levels of the same antigen may account, at least in part, for the efficacy of this immunizing strategy.

rAd5 and MVA are both viruses with an excellent safety record in human immunisations. The generation of recombinant viruses can be accomplished simply, and they can be manufactured reproducibly in large quantities. Administration of rAd5 followed by recombinant MVA therefore could be suitable for prophylactic vaccination of humans against HIV and possibly other diseases which can be controlled by a CD8^{+} T cell response.

The current study may facilitate the design of improved prime boost vaccine strategies. This raises the possibility of manufacturing individually prepared doses of the vaccine that do not need cold storage. This would be a great advantage for a vaccine that is needed in rural areas .

References

1.   Jabbari A, Harty JT . Secondary memory CD8^{+} T cells are more protective but slower to acquire a central-memory phenotype. J Exp Med 2006;203 (4):919–32.

2.   Masopust D, Ha SJ, Vezys V, et al. Stimulation history dictates memory CD8^{+} T cell phenotype: implications for prime-boost vaccination. J Immunol, 2006; 177 (2): 831–9.

3.   Tatsis N, Lin SW, Harris-McCoy K, *et al.* Multiple immunizations with adenovirus and MVA vectors improve CD8^{+} T cell functionality and mucosal homing. Virology, 2007; 367(1):156-67.

4.   Mascola JR, Sambor A, Beaudry K, *et al.* Neutralizing antibodies elicited by immunization of monkeys with DNA plasmids and recombinant

adenoviral vectors expressing human immunodeficiency virus type 1 proteins. J Virol, 2005; 79: 771–9.

5. Someya K, Xin KQ, Ami Y, *et al.* Chimeric adenovirus type 5/35 vector encoding SIV gag and HIV env genes affords protective immunity against the simian/human immunodeficiency virus in monkeys. Virology, 2007;367(2): 390-7.

6. Kobinger GP, Feldmann H, Zhi Y, *et al.* Chimpanzee adenovirus vaccine protects against Zaire Ebola virus. Virology, 2006; 346 :394–401.

7. Shiver JW, Fu TM, Chen L, *et al.* Replication-incompetent adenoviral vaccine vector elicits effective anti-immunodeficiency-virus immunity. Nature, 2002; 415: 331–5.

8. Belyakov IM, Ahlers JD, Nabel GJ, *et al.* Generation of functionally active HIV-1 specific CD8$^+$ CTL in intestinal mucosa following mucosal, systemic or mixed prime-boost immunization. Virology, 2008; 381(1):106-15.

9. Cebere I, Dorrell L, McShane H, *et al.* Phase I clinical trial safety of DNA- and modified virus Ankara-vectored human immunodeficiency virus type 1 (HIV-1) vaccines administered alone and in a prime-boost regime to healthy HIV-1-uninfected volunteers. Vaccine, 2006;24:417–25.

10. Harrer E, Bauerle M, Ferstl B, *et al.* Therapeutic vaccination of HIV-1-infected patients on HAART with a recombinant HIV-1 nef-expressing MVA: safety, immunogenicity and influence on viral load during treatment interruption. Antivir Ther, 2005; 10: 285–300.

11. Belyakov IM, Hel Z, Kelsall B, *et al.* Mucosal AIDS vaccine reduces disease and viral load in gut reservoir and blood after mucosal infection of macaques. Nat Med, 2001; 7:1320–6.

12. Wyatt LS, Belyakov IM, Earl PL, *et al.* Enhanced cell surface expression, immunogenicity and genetic stability resulting from a spontaneous truncation of HIV Env expressed by a recombinant MVA. Virology, 2008;372(2):260-72.

13. Abaitua F, Rodríguez JR, Garzón A, *et al.* Improving recombinant MVA immune responses: Potentiation of the immune responses to HIV-1 with MVA and DNA vectors expressing Env and the cytokines IL-12 and IFN-gamma. Virus Res, 2006 ;116(1-2):11-20.

14. Obenauer-Kutner LJ Ihnat PM Yang TY , *et al*. The use of field emission scanning electron microscopy to assess recombinant adenovirus stability. Hum. Gene Ther, 2002;13 :1687-96.

15. Zhang YZ , Jiang CL ,Wang ZC, *et al*. Preparation of stabilizer of freeze-dried recombinant MVA virus vector vaccine. Chem Res Chinese U, 2006;19(2):174-6.

16. Zhang YZ, Teng HG, LV SR, *et al*. Preparation of stabilizer of freeze-dried adenovirus-based live HIV vaccine. Chin J Biologicals, 2007a;20(2):104-6.

17. Zhang YZ, Jiang CL, Yu XH, *et al*. Immunogenicity of lyophilized MVA vaccine for HIV-1 in mice model. Chem Res Chinese U, 2007b;23:329-32.

18. Ramshaw IA, Ramsay AJ. The prime-boost strategy:exciting prospects for improved vaccination. Immunol Today, 2000; 21:163.

19. Berzofsky JA, Terabe M, Oh S, *et al*. Progress on new vaccine strategies for the immunotherapy and prevention of cancer. J Clin Invest, 2004;113 (11): 1515–25.

20. Dale CJ, Thomson S. Prime-boost strategies in DNA vaccines. Methods Mol Med, 2006; 127:171–97.

21. Belyakov IM, Kuznetsov VA, Kelsall B, *et al*. Impact of vaccine-induced mucosal high avidity CD8$^+$ CTLs in delay of AIDS-viral dissemination from mucosa. Blood, 2006; 107 (8): 3258–64.

22. Neeson P, Boyer J, Kumar S, *et al*. A DNA prime-oral Listeria boost vaccine in rhesus macaques induces a SIVspecific CD8$^+$ T cell mucosal response characterized by high levels of alpha4beta7 integrin and an effector memory phenotype. Virology, 2006; 354 (2): 299–315.

Expression changes of DSCAM in induction of MSCs to differentiate into neurons

Tao Peng, Yanjie Jia , Junfang Teng, Boai Zhang, Guiyuan Fang

Department of Neurology, First Affiliated Hospital of Zhengzhou University, Zhengzhou, Henan 450052, China
jiayanjie1971@yahoo.com.cn

Abstract

Objective To explore the role of Down syndrome cellular adhesion molecule (DSCAM) in the course of the rat marrow mesenchymal stem cells (MSCs) differentiated to neurons in vitro. **Methods** MSCs from Sprague-Dawley rats were induced into neurons by baicalin. Immunocytochemistry, Western blot and other methods were performed to detect DSCAM in neurons. At the same time, RNA interfere technique was performed to observe the induction and differentiation after DSCAM-siRNA was transfected into MSCs. **Results** Before induction, the expression of DSCAM was not detectable in MSCs. After 24h pre-induction, DSCAM was slightly expressed in MSCs(1.71 ±0.67).After 6h induction by baicalin ,the expression of DSCAM increased (15.79 ±4.24) and reached the peak (53.16 ±5.94) after 3d induction. After 6d induction, DSCAM expression obviously decreased (28.99 ±6.72). After DSCAM-siRNA was transfected into MSCs, DSCAM expression obviously decreased. However, MSCs did not express neuron-specific -III-tubulin, expression of -III-tubulin was (1.40 ±0.79)after 6h induction, 41.59%±3.17% after 3d induction and (59.11 ±4.76)after 6d induction. But after DSCAM-siRNA was transfected into MSCs, expression of -III-tubulin obviously decreased 28.57%±2.91% 43.90%±12.31% after 3d and 6d induction.

Conclusions DSCAM might play an important role in MSCs differentiation into neurons. [Life Science Journal. 2010; 7(1): 5 – 8] (ISSN: 1097 – 8135).

Key Words: Down syndrome cellular adhesion molecule; marrow mesenchymal stem cells; neuron; RNA interfere

_____

1. Introduction

Down syndrome cell adhesion molecule DSCAM , which Gene is located at 21q22, if over-expressed (such as the chromosome 21 trisomy) , that is Down syndrome. It results in abnormality of nerve cell migration, proliferation, differentiation, leads to congenital intellectual maldevelopment [1]. Moreover, DSCAM is between nerve cells, and plays an important role in the the imperative cell adhesion molecule in connections formation and maintenance of the neural network [2]. In the process of inducing marrow mesenchymal stem cells (MSCs) to nerve cells in vitro, we firstly observed the changes of DSCAM expression and explored the function.

2 Materials and methods

2.1 The main reagents and animals

DMEM liquid medium, B_{27}, fetal calf serum, Trizol purchased from Gibco Company; basic fibroblast growth factor (basic fibroblast growth factor, bFGF) purchased from Pepro Tech EC Inc.; mouse anti-polyclonal DSCAM, nerve cell marker protein -III-tubulin antibody purchased from Abnova Corporation; goat anti-mouse-Cy3, goat anti-mouse-AP antibody purchased from Sigma company; Rat Rn-DSCAM-siRNA (FITC tags), transfection reagent HiPerFect, positive control Rn-MAPK1 Control siRNA, negative control AllStars Negative Control siRNA (FITC tags) purchased from Qiagen Inc.; RT-PCR kit purchased from Promega Corporation; The remaining biological and chemical reagents are imported or domestically analytical reagent. MSCs was extracted form femur of SPF-class Sprague-Dawley rats by the University Center, and passaged more than 10 generations, regular cryopreservation in liquid nitrogen.

2.2 Induction of MSCs to nerve cells in vitro

In the light of our approach [3], the culture and induction of MSCs differentiation was carried out. In accordance with the 2×10^4 cells / hole ratio, the 10th generation of MSCs was vaccinated in the 6-hole culture plate with plastic coverslip, cultured 3d, the induction experiment began when 80-90% was fused. After 3 washes with D-Hank's fluid, a pre-induction medium (DMEM medium, 10% fetal calf serum, 10ng/ml bFGF) added, cultured 24h. After pre-induced, induced 6h by adding liquid (DMEM medium, 200-400μM baicalin), then adding liquid (DMEM medium, 200-400μM baicalin, 10ng/ml bFGF, B27) to maintain 6d.

2.3 DSCAM-siRNA transfected MSCs

According to the Qiagen company's operating instructions for MSCs transfection as follows: 1250ng siRNA was dissolved in 100 μl DMEM medium (no serum) and then adding 12μl HiPerFect transfection reagents, and incubated 10m at room temperature after mixing; the complex was dropped on the surface of MSCs, and then added to the DMEM medium (containing 10% FBS), so that the final concentration of siRNA to achieve 24nM, incubated 12-24h. Positive control (Rn-MAPK-1 Control siRNA)and negative control (AllStars Negative Control siRNA) apply the same approach.

2.4 Immunocytochemistry method image collection and analysis

After washed with PBS, the cells were fixed 20 min at 4^oC in stationary liquid (4% paraformaldehyde),

reacted 10 min in 0.2% Triton, blocked 1h with 10% Bovine Serum Albumin (BSA), then incubated 24h at 4°C with Anti-DSCAM (1:200), Anti-CD90 (1:200) or Anti- -III-tubulin (1:800). The cells were stained and observed at room temperature with second antibody after 3 washs. The cells image were photoed 10x or 20× by microscope using 300dpi resolution. Every independent experiment collected more than 30 region of cells. Furthermore, the image collected in bright field contains the same counts of cells. Double person and double mind random method were counted positive cells and computed positive cells percentage.

2.5 Western Blot method

Collected cells of each group were cracked, degenerated, centrifuged in the cell lysate (50mM Tris-Cl, pH 6.8, 10mM EDTA, 2% SDS, 5mM DTT, 0.5mM PMSF) 100μl, collecting the supernatant protein samples and quantificating protein by Bradford method. Protein lysate was added in 4× gel upper sample buffer, and transferred to PVDF membrane after SDS-acrylamide gel electrophoresis ,blocked with 5% defatted milk (1 h at room temperature) and incubated overnight at 4 °C with TBST. The membrane was washed 3 times, and reacted 1h at room temperature with IgG tagged by horseradish peroxidase, then washed 3 times. ECL reaction was conducted, followed by exposure and development. The same experiment needs 3 repeats.

2.6 RT-PCR

Total cellular RNA was extracted with Trizol reagent and quantitated conventionally. RT-PCR amplification reaction was performed on the light of Promega kit manual, the reaction system was 50μl,

reverse transcription and PCR were accomplished in one step (35-40 cycles), 10μl of amplification product were added to 1.5% agarose gel, ultraviolet transilluminator was used to observe and photograph after electrophoresis. Primer was from Shanghai Public Health Synthesis Ltd.(Table 1)

2.7 statistical treatments

ImagePro Express software was used to collect and process all images. The data was expressed by $\bar{x}\pm s$. GraphPad Prism 5.01 was used to make picture. Analysis of variance was used to evaluate the data, the P value less than 0.05 was considered to be significantly different.

3 The results
3.1 Induction of bone marrow mesenchymal stem cells to differentiate into nerve cells in vitro

of rats cultured 10 generations are mainly spindle, squamous cells and expressed MSCs marker(Figure 1A). After 6h induction with Baicalin, some cells changed to a triangle, cell microfilament contracted, pseudopodium formed slender processes and interlaced locally , similar to nerve cells; After 6d the majority of cells changed to be cone-shaped, interlaced into a network, and formated typical nerve cell structure (Figure 1B). This study chose -III-tubulin as a marker of mature nerve cells, MSCs were not found to express -III-tubulin before the induction and after 6h induction (1.40% ± 0.79%). With the cells differentiation, -III-tubulin expression increased rapidly to (41.59% ± 3.17%) with 3d induction and (59.11% ± 4.76%, Figure 1C) with 6d induction. Western Blot also had similar results (Figure 2).

Table 1. Primer sequence

Gene name	Primer sequence	product
SCAM	Forward: 5'-AGAAGTGCCCACCAATTGAG-3'	135 bp
	Reverse: 5'-CACCCAGGTTCCTTCTGATC-3'	
-III-tubulin	Forward: 5'-TGCGTGTGTACAGGTGAATGC-3'	240bp
	Reverse: 5'-GGCTGCATAGTCATTTCCAAG-3'	
GADPH	Forward:5'-CCCACGGCAAGTTCAACGGCA-3'	430bp
	Reverse: 5'-TGGCAGGTTTCTCCAGGCGGC-3'	
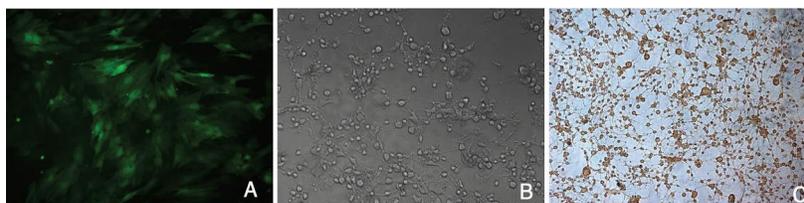
Figure 1. Induction of MSCs to neuron   A: pre-induction**,** the 10th generation of MSCs(CD90 staining, FITC,×200); **B :**6d after induction, change of cell morphology(×200),the cells were cone shaped, similar to neuron; **C:** 6d after induction, expression of -III-tubulin in differentiated cells(DAB coloration, ×100), most cells were cone shaped, interlaced to net, -III-tubulin was hyperexpressed.
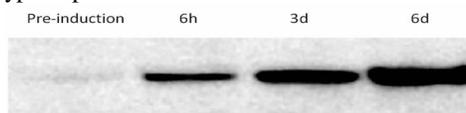
Figure 2. Changes of -III-tubulin expression before and after induction (Western blot)
 -III-tubulin expression increased rapidly with the time.

3.2 Changes of DSCAM expression

The rats MSCs did not express DSCAM before induction., MSCs began to express a small amount of DSCAM ($1.71\% \pm 0.67\%$) after 24h pre-induction and express partially on cell membrane and processes after 6h induction ($15.79\% \pm 4.24\%$); With the extension of time the expression continued increasing, and to the peak after 3d induction ($53.16\% \pm 5.94\%$). But DSCAM expression decreased significantly ($28.99\% \pm 6.72\%$) after 6d induction, and it was significantly different from 3d induction ($t = 8.516$, $P <0.01$). Western Blot method had similar results (Figure 3).

3.3 DSCAM-siRNA transfected MSCs

MSCs had no obvious morphological changes after DSCAM-siRNA transfection, Green fluorescent granules can be observed in cells by fluorescence microscope after 24h transfection and can express more than 1 week (Figure 4A, 4B). The efficiency is (78 ± 12.9) %. However, after baicalin induction, cell differentiation was poor, processes was short, straight .Branches and neural network formation were sparse (Figure 4C, 4D). Immunocytochemical stain (Figure 4E) and RT-PCR (Figure 5) prompted that DSCAM expression decreased significantly after DSCAM-siRNA transfection. But after DSCAM-siRNA transfection, with 3d or 6d induction, -III-tubulin expression decreased significantly ($28.57\% \pm 2.91\%$, $43.90\% \pm 12.31\%$), the difference was significant compared to untransfected cells ($P <0.01$, $P<0.05$).
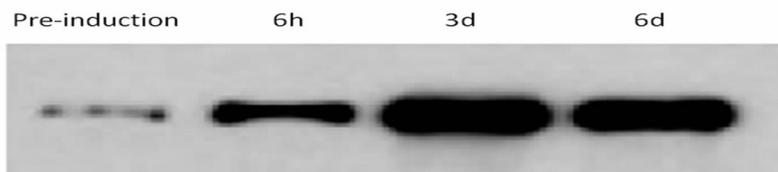
Figure 3 changes of DSCAM expression before and after induction(Western blot)
DSCAM expressed partially at 6h after induction. The expression increased gradually to the peak at 3d and decreased at 6d.
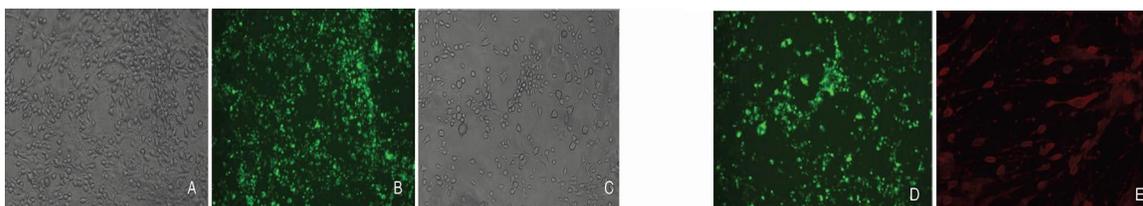
Picture 4 DSCAM-siRNA transfected MSCs A: Cell morphology of MSCS did not chang obviously after DSCAM-siRNA transfected MSCs($\times100$); **B:** Green fluorescent granules in cells can be observed in same visual field ($\times100$); **C:** 6d after DSCAM-siRNA transfection and induction ,the differentiation of transfected cells were poor, the neural networks were sparse($\times100$); **D:** Green fluorescent granules can be observed in differentiated cells in same visual field ($\times100$); **E:** 6d after siRNA transfection and induction, the change of DSCAM expression (immunofluorescence Cy3 staining,$\times200$) .
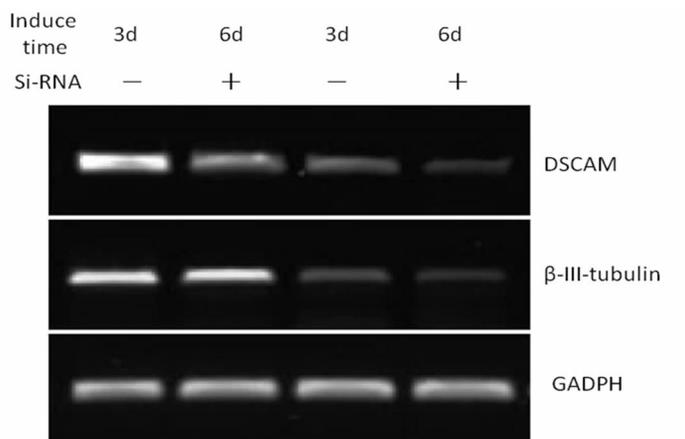
Picture 5 Changes of DSCAM mRNA expression before and after induction(RT-PCR)
DSCAM -III-tubulin expression decreased significantly than untransfected group after siRNA transfection($p<0.01$, $p<0.05$).

Discussion

DSCAM belongs to immunoglobulin super family. In 1998, Yamakawa isolated DSCAM gene and found that most of these genes expressed in the development phase of the nervous system [4]. Sequence analysis shows that, DSCAM consists of the N-end signal peptide, 10 immunoglobulin domain, 6 3-type fibronectin domains, a transmembrane domain and an intracellular domain. DSCAM can be cuted to 38,000 kinds of isomers through RNA, the protein may help nerve cells link exactly in the process of nerve network formation. Over-expression of DSCAM have the direct result of nerve cell migration, proliferation and abnormality of differentiation, this is the molecular genetics basis of Down's syndrome [1].

Nearly 10 years, the study found that MSCs can be directed to differentiate into nerve cells and glial cells. As a class of ideal "seed cells", MSCs have the advantages of proliferation, security, autologous transplantation without immunological rejection. It can be applied to the clinical therapy of cell transplantation in the nervous system injury and degenerative diseases [5].But the mechanism of MSCs differentiating to neural cells is not clear, it involves a number of signal transduction accesses. This study found that for the first time, the development of the nervous system as an important functional proteins, before the induction rat MSCs did not express DSCAM, with the induction time extending, expression of DSCAM gradually increased to the peak after 3d induction, and then began to decline. At the same time, the expression of nerve cell marker protein -III-tubulin increased in the differentiated cells. The results suggested that, the cells induced and differentiated from MSCs had a certain degree of nerve cell function, but the process may also be the recurrence of nerve cell development, and furthermore, DSCAM express mainly in the nervous system development phase, including the spinal cord, cerebral cortex, cerebellum and so on, it plays a vital role to ensure the accurate and close connections of nerve cells in growth and directed extension of its axon branches [6,7]. The expression of DSCAM increase gradually in the course of MSCs differentiation, it may be associated with growth of induced cell axon branches and establishment of cell junctions. Nduced cells have the network structure and function of nerve cell. Interference of DSCAM siRNA affected DSCAM expression and led to the decline of effect of induction and differentiation and reduce of nerve cell junction.

A recent study found that, DSCAM play a role in the formation of particular retinal layer. The other two adhesion molecules, that is, the Sidekick-1 and Sidekick-2, play a role in a similar manner. These elements are widely distributed in the nervous system, may be the components of adherence code in formation of brain nerve connection [8]. Therefore, whether the mechanism of MSCs induced to differentiate into neural cells is similar will be involved in an in-depth study.

Corresponding author.
Email: jiayanjie1971@yahoo.com.cn

References
1. Zinn K. Dscam and neuronal uniqueness [J]. Cell 2007, 129(3): 455-456.
2. Schmucker D. Molecular diversity of Dscam: recognition of molecular identity in neuronal wiring [J]. Nat Rev Neurosci 2007, 8(12): 915-920.
3.   ,   ,   ,   .
                                    [J].
   2002, 82(19): 1335-1339.
4. Yamakawa K, Huot YK, Haendelt MA, et al. DSCAM: a novel member of the immunoglobulin superfamily maps in a Down syndrome region and is involved in the development of the nervous system [J]. Hum Molecular Genetics 1998, 7(2): 227–237.
5. Dezawa M, Hoshino M, Ide C. Treatment of neurodegenerative diseases using adult bone marrow stromal cell-derived neurons[J]. Expert Opin Biol Ther. 2005, 5(3): 427-435.
6. Hughes ME, Bortnick R, Tsubouchi A, et al. Homophilic Dscam interactions control complex dendrite morphogenesis[J]. Neuron. 2007, 54(3): 417-427.
7. Ly A, Nikolaev A, Suresh G, et al. DSCAM is a netrin receptor that collaborates with DCC in mediating turning responses to netrin-1[J]. Cell 2008, 133(7): 1241-1254.
8. Yamagata M, Sanes JR. Dscam and Sidekick proteins direct lamina-specific synaptic connections in vertebrate retina [J]. Nature 2008, 451(7177): 465-469.

Assemblage structure of stream fishes in the Kumaon Himalaya of Uttarakhand State, India

Ram Krishan Negi and Tarana Negi*

Department of Zoology & Environmental Sciences, Gurukula Kangri University, Hardwar U.K. India 249404

*Department of Zoology, Govt. P.G. College, Panchkula (HR)

E mail: negi_gkv@rediffmail.com

Abstract

The fish assemblage structure was analyzed in the streams of Kumaon Himalaya of Uttarkhand State, India. Seven sites were sampled by using different fishing gears during Jan, 2007 to December 2008. The physical features like stream habitat, stream classifications, fish assemblage at different sites, habitat preference and riparian vegetations were registered for each site. In the present investigations a total of ten species belonging to three orders and four families were recorded, of which the cyprinides were the most dominant group at all the sites. According to Shannon Weaver diversity index the pool habitat support maximum fish diversity ('H' 0.164-0.292). [Life Science Journal. 2010;7(1):9 – 14] (ISSN: 1097 – 8135).

Keywords: Classification, cyprinids, fish diversity, substrate, preference

Introduction:

The highly complex functional and structural elements of running water are largely based on the system-inherent, dynamic genesis and development of those systems. Because of the very intricate interpretations with surrounding environments, running waters are among the most distinctive landscape elements. Especially in alluvial river floodplain systems, the high spatio-temporal heterogeneity and, therefore, the great diversity of complex habitat and ecotones in successional stages, represent key features. The diverse environment support species-rich fish communities that contribute to the overall high biodiversity of rivers/streams ecosystems (Schiemer & Waidbacher, 1992, Ward & Stanford, 1995a).

Importance of habitat is a major concern to fishery biologist. A common use of fish habitat indicates the physical and chemical characteristics of the environment, excluding biological attributed. Habitats for fish is place or for migratory fishes, a set place in which a fish population or fish assemblage can find the physical and chemical features needed for life, such as suitable water quality, migration routes, spawning grounds, feeding sites, resting sites and shelter from enemies and adverse weather. Habitat features have been identified as major determinants in the distribution and abundance of fishes from earlier times (Shelford, 1911) and later individual fish species as well as entire assemblage were studied for the patterns of North America (Smart and Gee, 1979; Baker and Ross, 1981). Fish species diversity is correlated with habitat complexity (Gorman & Karr, 1978; Schlosser, 1982) depth, flow and substrate types. The influence of these habitats attributes on the structure and function of fish assemblage in the streams has been studied in detailed at different latitudes (Mathew and Hill, 1980; Leveque, 1997). Extensive studies on freshwater fishes in India are available, but most of them are concern with taxonomy (Datta Munshi & Srivastava, 1988; Menon, 1992, Jayaram, 1999). Studies on fish assemblage structure and their requirements in Indian streams are lacking, though few initiatives started in the 1980's in south India (Arunachalam et al., 1988; 1997a), SriLanka streams (Moyle and Senanayake, 1984; Wickramanayake, 1990);Western Himalaya (Johal et al.,2002 and Kumaon Himalaya (Negi et al., 2007). The present study aims to describe the habitat structure, and its availability to fish assemblage, as well as habitat use and habitat suitability preference in seven streams of Kumaon Himalayas of Uttarakhand State, India.

Study area: Kumaon Himalaya lying the latitudes 280 44' and 300 49' and longitude 780 45' and 810 1' E is situated at the disjunction of Nepal, Tibet and India in the state of Uttarakhand. A natural water divide separates it from Tibet, the Kali river defines its eastern border with Nepal , High transverse mountain spurs , separate it from Chamoli and Pauri district of Garhwal and the southern limit of the Tarai belt demarcates its southern boundary. Geographically Kumaon has the four longitudinal physiographic subdivisions namely the outer Himalaya with Tarai and Bhabar belt and Shivalik ranges, the lesser

Himalayas and the Trans-Himalaya Tethyes domain of Bhotland. Seven study sites were selected for the present study. These sites varied in altitude from 800msl to 1098msl and varied geomorphologic characters, substrate and ecological conditions.

Material and methods:

The parameters like water source, channel materials, dominant habitat type and stream type were taken into consideration for the Kumaon Himalayan streams. The geographic location i.e. longitude, latitude and altitude were determined with the help of Magellan Trailblazer XL GPS system. The habitat type and substrate material were classified after Armantrout (1999). The stream under report were classified following the works of Rosgen (1996).

Stream classification: This classification is based on morphological arrangement of stream characters like entrenchment ratio, width/depth ratio and channel material in the various landforms at level 1 and 2.This is only broad level delineation of stream types. Entrenchment ratio has been considered primary criteria for the present stream classification. Whereas, water shed features, channel features, sediment sources, riparian vegetations and large wood debris were estimated on the spot by stream reach characterization field data sheet. Water temperature, air temperature and water velocity were measure on the spot as per standard methods APHA (1998)

Fish collection: The fishes were caught at each sites with the help of cast net, gill net, drag nets, scoop nets. Samples were carried out for ten times in each habitat on a fixed day every month from Jan. 2007 to December, 2008. The represented specimens were identified upto species level in the laboratory using standard references of Day (1878) and Jayaram (1999).

Results:

Fish diversity: A total of ten species belonging to three orders namely cypriniformes , Mastacembelis ,and perciformes were recorded during the present investigation Table 1. Of these cypriniformes comprises the dominant group represented by 8 species belonging to 7 genera. Tor putitora, Garra gotyla gotyla, Barilius bendelisis were the most abundant fishes in all the study sites. Higher species richness were recorded from Kosi, Saigad and Suyal streams respectively with an altitude range of 1027 to 1398msl and lower values were recorded from the altitude range 860 to 1120msl. This is chiefly because of the severity of anthropogenic activities in the form of extraction of boulders, cobbles from streams habitat in lower altitude leading to decrease in fish assemblage whereas, at higher altitude have greater species richness.

Habitat preference: In total 345 cyprinids fishes were recorded in pool, pool edges, run and edges of riffles. The cascade was least preferred habitat by majority of fishes. The maximum fish diversity was reported in pool habitat H' 0.845 followed by run H' 0.764 and riffle H'0.196 at Kosi stream Table 2. In Saigad stream, it was H' 0.760 in pool, H' 0.590 in run, H' 0.244 in riffle, In Suyal stream it was H' 0.464 in pool, H' 0.461 in run and H' 0.292 in riffle, in Busal stream, it was H'0.423 in pool and H' 0.292 in run, in Garur ganga stream it was H' 0.457 in pool, H' 0.386 in run and H' 0.210 in riffle, in Gagas stream, it was H' 0.581 in pool, H'0.196 in run and H'0.275 in riffle, whereas, it was H' 0.594 in pool, H' 0.454 in run and H' 0.164 in riffle at Gomti stream. In Garur ganga stream, Tor putitora, Barilius bendelisis and Schizothorax preferred deep and shallow pools, while, was found in the shallow pools with low velocity, whereas,Garra gotyla gotyla preferred shallow pool with low to medium velocity. In Gomti stream,Tor putitora and Barilius bendelisis and Barilius barla preferred shallow pools with medium velocity.

Fish species richness vs altitude: At level 1, the altitude had been considered as primary criteria for differentiating the streams. High correlation coefficient was observed between altitude r= 0.71. The high altitude site >1000m, had higher FSR (5-10) as compared to lower altitude site<1000m.i.e. Gomti stream which had lower FSR (5). This is because of anthropogenic activities occurring in lower altitude as compared to higher altitude. The relative abundance also inverse relation with altitude. At level 2, the streams were further delineated according to the source of water glacial or spring fed. In the present study streams under report were spring fed and had fish species richness (3-10 and H' 0.778-1.694).

Stream substrate: In Kosi stream, the dominant stream substrate were big boulders, small boulders, and cobbles in Saigad stream, small boulders and cobbles, in the Suyal stream, bed rock, big boulders edge and small boulders were prevalent. In Garur ganga streams, big boulders, bed rock edge and gravel, in the Gagas streams, small stream. Small boulders, cobbles and pebbles, and in Gomti stream, substrate was dominated by big boulders, small boulders and cobbles Table 3. The streams having cobbles as dominant bed materials along with small boulders lead to formation of a more variable types of habitat leading to the greater species richness (5-10).

Stream classification: There was a great variation in channel width almost all selected streams. The minimum cannel width was recorded as (6.3m) at Busal stream and maximum as (37.53m) at Gomti stream. Maximum depth was recorded at Suyal (0.76m) and minimum at Busal stream (0.25m). The depth width ratio was recorded maximum 63.46 at Kosi stream and minimum 16.93 at Garur ganga stream Table 3. In the present study, entrenchment ratio was considered as primary criteria for

the classification of streams. On the basis of entrenchment ratio all the streams has been classified as type 'B' streams with entrenchment ratio range from 1.46- 2.31. The width/depth ratio was very high in the streams of Kosi, Saigad, Gomti, whereas, rest of streams have moderate width/depth ratio.

Stream channel features: The channel features were found to be unstable at Kosi, Saigad, Garur Ganga and Gomti streams, whereas, they were moderately stable in Busal and Gagas streams. The proportion of stream reach morphology type was dominated by riffle, deep pools and runs at Kosi; shallow pools and run at Saigad and Busal;

deep pools, run and riffle at Suyal and riffle , run and cascade at Garur ganga; riffle, run and shallow pools at Gagas; run and riffles at Saryu and riffles and pools at Gomti streams. The local hydrological alterations in the form of channelization of water flow were more prominent in Kosi, Busal, Garur ganga and Saryu streams, leading to the formation of large side pools at different pockets of the streams reaches, which were responsible for sedimentation in the streams. The riparian vegetation was fragmentary with herbs, shrubs and trees at Kosi, Suyal Gagas and Gomti streams. Aquatic vegetation was mainly dominated by attach algae in most of the study sites. All the streams under reports were reported alkaline in nature.

Table 1. Fish species recorded from streams of Kumaun Himalaya of Uttarakhand State, India

	Kosi	Saigad	Suyal	Busal	Garurganga	Gagas	Gomti
Order:Cypriniformes							
Family:Cyprinidae							
Genus: Tor							
Tor putitora	++	+	+	-	+	+	+
Genus:Barilius							
Barilius bendelisis	++	++	++	++	++	++	++
Barilius barila	+	+	+	-	-	-	+
Genus:Puntius							
Puntius conchonius	+	+	-	-	-	-	-
Genus:Garra							
Garra gotyla gotyla	++	++	++	++	++	++	++
Genus:Chrosochelus							
Chrosochelus latius	+	-	-	-	-	+	-
Genus:Schizothorax							
Schizothorax richardsonii	+	+	+	-	+	+	+
Genus:Nemachelius							
Nemachelius montanus	+	+	+	-	-	+	-
Order:Mastacembeliformes							
Family: Mastacembelidae							
Genus: Mastacembelus							
Mastacembelus armatus	+	+	+	+	+	+	-
Order: Ophiocephaliformes							
Family:Ophiocephalidae							
Genus: Channa							
Channa punctatus	+	+	-	-	-	-	-

++: Dominant; +Abundant; -: Not recorded

Table 2. Physical characteristic and channel morphology in the streams of Kumaun Hamalaya of Uttrakhand State, India.

Name Of Stream	Stream Width(m)	Stream Depth (m)	Entren- chment ratio	Habitat	Substrate	Longitude	latitude	Altitude	Water velocity	Riparian Vegetation
Kosi	16.5	0.26	2.12	Deep pools,	Big boulders	79030'22.9"E	29046'55.3"N	1381	0.9	Fragmentary, trees and shrub,

				Riffles, Runs						Minimum encroachment in stream
Saigad	15.0	0.30	1.6	Shallow pool Runs	Cobbles, Pebbles, Sand	79036'03.2"E	29046'51.6"N	1398	0.43	Trees, shrubs, grasses, Moderate encroachment
Suyal	19.5	0.76	1.74	Deep pool, Cascade, Riffles	Dominant bed rock, Large boulders, Cobbles	79036'44.9"E	29033'21.5"N	1027	0.22	Shrub dominant, Fragmentary, Minimum encroachment
Busal	6.3	0.25	2.03	Runs, Pools	Cobbles, Pebbles	79036'59.9"E	29053'47.0"N	1122	0.39	Trees, shrubs, continuous, moderate encroachment
Garur ganga	8.3	0.49	2.31	Riffles, Cascade, Pool	Big boulders, Bed rock edge, gravels	79037'01.9"E	29053'49.2"N	1120	0.70	Shrubs, grasses dominant, Fragmentary
Gagas	7.8	0.36	2.05	Riffles, Runs, Shallow Pools	Cobbles, Small boulders	79027'28.2"E	29041'32.9"N	1061	0.51	Tress, shrubs, grasses, Fragmentary Minimum encroachment
Gomti	37.5	0.70	1.46	Runs, Riffles, pools	Big and small boulders	79046'10.9"E	29050'11.1"N	860	0.58	Trees, shrubs dominant, grasses, continuous, minimum encroachment

Table 3. Fish species diversity indices (Shannon and Weaver species Diversity) (H'), relative abundance and species richness in the streams of Kumaun Himalaya of Uttarakhand State, India

Streams	Pool	Riffle	Run	Relative Abundance	Species Richness
Kosi	0.845	0.196	0.764	11.62	10
Saigad	0.760	0.244	0.590	12.50	9
Suyal	0.464	0.292	0.461	13.20	7
Busal	0.423	--	0.292	4.91	3
Garur Ganga	0.457	0.210	0.386	8.33	5
Gagas	0.581	0.275	0.196	9.80	5
Gomti	0.594	0.164	0.454	8.62	5

Discussion

From the above observations it is clear that water depth and water velocity are the two major factors for the distribution of fish species in the different habitats. Similar observations were made by Gorman and Karr (1978); Moyle and Vondraceek (1985); Arunachalam (2000); Johal et al. (2002) and Negi et al.(2007). Harvey and Stewart (1991) reported that minnows survives longer in pools. The large numbers of small fishes becomes increasingly restricted to stream margins, because the mid stream reaches are fast or too deep or both (Bains et al., 1988). Most of the fishes in the small streams are habitat generalists (Horowitz, 1978). Other studies have also indicated a substantial overlap in the habitat utilizations in the cyprinid fishes communities. (Barker and Ross, 1981; Schlosser, 1987 a,b). The studies on the Western Ghats fishes assemblage structure (Arunachalm, 2000) and other parts of the world (Finger, 1982; Schlosser, 1982; Bains et al. 1988 and Schlosser 1987a) also reported that the diverse group of small fishes are found to be primarily restricted to habitat that are shallow in depth and slow in current velocity and are concentrated along the stream margin in pools and riffles. Scot and Hall (1997) have stated that fish assemblage as indicator of environmental degradation in Maryland coastal plain streams. The relationship between habitat diversity and fish communities has been analyzed by Gorman and Karr (1978) in temperate area in which they include the diversity of current, depth and substrate, which determines the riverian fish communities. Several studies have supported this generalization for fish communities (Werner and Hall, 1976; Schlosser and Toth, 1984; Bains et al. 1988; Aadland, 1993; Mathew et al. 1994; Arunachalam, 2000). Physical gradients from unstable shallow to deep, stable pool areas with stream fishes are common in temperate latitudes (Sheldon, (1968). Arunachalam,(2000) reported that non cyprinids such as Balitorids occur mostly in pool edges and cyprinids in big pools with varied habitat heterogeneity. Similar results were observed during the resent investigations having the diverse group of small fish species is restricted primarily to habitat which are shallow in depth and slow in water current velocity, which are the areas along stream margins in rifles and pools. In the Kumaun region of Wester Himalayas, small Puntius spp are confined to shallow low flow area and juveniles of big sized Tor putitora and Schizothorax used the shallow areas with the speed velocity of riffles and riffles-pool transition especially in Suyal stream. Stream assemblages dominated by short lived, rapidly maturing water column fishes generally show greater variability corresponding to environmental fluctuations, such as documented by Grossman et al (1982) and Ross et al (1987).

References

Aadland LP. Stream habitat type: Their fish assemblages and relationship to flow. North American Journal of Fisheries Management 1993; 13: 790-06.

APHA. Standared method for the examination of water and wasteland. 20th edition. Am.Public Health Assoc. Washington D.C. 1998.

Armantrout NB. Glossary of aquatic habitat inventory technology. American Fisheries Society. 1999; 150 pp.

Arunachalam, M. Assemblage structure of stream fishes in the Western Ghats (India). Hydrobiologia. 2000; 430: 1-31.

Arunachalam M, Johnson JA, Sankarnarayanan A Fish diversity in rivers of Northern Karnataka. Int. J. Ecol. Envir. Sci. 1997a; 23: 327-33.

Arunuchalam MKC, Madhusoodanan Nair, Vijverberg J, Kortmulder K. Food and feeding habitat usage of cyprinid fish assemblage in stream pools of a south river. Re., Limnological Institute of the Royal Academy of Science, The Netherland; 1998; 89pp.

Baker JA. Ross ST. Spatial and temporal resource utilization by south eastern cyprinids. Copiea 1981; 178-89.

Bain MB Finn JT Booke HE. Stream flow regulation and fish community structure. Ecology 1988; 69:382-392.

Datta Munshi JS, Srivatsava MS. Natural history of fishes and systematic of freshwater fishes in India. Narendra publishing Co. Delhi, India 1988; 421pp.

Finger TR. Fish community habitat relations in central New York stream. J. Freshwat. Ecol. 1982; 1: 343-52.

Gorman OT, Karr JR. Habitat structure and sream fish communities.Ecology 1978; 59:507-15.

Grossman GD, Moyle PB, Whittaker JO Jr. Stochasticity in structural and functional characteristics of an Indian stream fish assemblage a test of community theory. Am. Nat. 1982; 120:423-53.

Harvey BC, Stewart AJ. Fish size and habitat depth relationship in a headwater stream. Oecologia 1991; 87:336-342.

Horowitz RJ. Temporal variability patterns and the distributional patterns of stream fish. Ecological monogr. 1978; 48:307-21.

Jayaram KC. The freshwater fishes of the Indian region. Narendra Publishing House. Delhi 1999; pp 551.

Johal MS, Tandon KK, Tyor AK and Rawal YK. 2002. Fish diversity in different habitats in the streams of lower, middle Western Himalayas. Pol .J. Ecol. 50(1):45-56.

Leveque C. Biodiversity dynamics and conservation, the freshwater fish tropical Africa. Cambrige University Press, Cambrege 1997; pp 438.

Menon AGK. Conservation of freshwater fishes of Peninsular India. Final report submitted to Minist. Envir. Forest. (unpublished) 1992;137pp.

Mathew WJ, Hill LG. Habitat partitioning of fish community of a sourthwestern river. Southwest. Nat. 1980; 25:51-66.

Methew WJ, Harvey BC, Power ME. Spatial and temporal pattern in the fish assemblages of individual pools in a mid western stream (USA). Envir. Biol. Fishes 1994; 39:381-97.

Moyle PB, Senanayake FR. Resource partitioning among the fishes of rainforest streams in Sri Lanka. J. Zool. Soc. Lond. 1984; 202: 195-24.

Moyle PB, Vondracek B1. Persistence and structure of the fish assemblage in a small California stream. Ecology 1985; 65: 1-13.

Negi RK, Joshi BD, Negi Tarana, Chand P. A study on stream morphology of some selected streams hill streams of district Nainital with special reference to its biotic communities. Proceedings of National Seminar on Limnology at Jiapur, India. 2007;

Rosgen D.. Applied river morphology. Wild land Hydrology, Colorado, U.S.A. (Reprint edition) 1996

Ross ST, Baker JA, Clark KE. Microhabitat partitioning of south eastern streams fishes: temporal and spatial predictability. In: Methew WJ Heins WJ (ed) Community and Evolution Ecology of North American stream fishes. University of Oklahoma 1987; 42-51.

Schiemer F, Waidacher H. Strategies of conservation of a Danubian fish fauna. In: Boon, P.J.P. Carlow & G.E. Petts ed. River conservation and management. John Wiley & Son. 1992 ; 363-82.

Schlosser IJ. Fish community structure and function along two habitat gradients in headwater stream Ecol. Monogr. 1982; 52: 395-14.

Sheldon AL. Species diversity and longitudinal succession in stream fishes.Ecology1968; 9:193-98

Shelford VE. Ecological succession: stream fishes and the methods of physiographic analysis. Bio.Bull. 1911; 21: 9-35.

Smart HJ, Gee JH. Co-existence and resource partitioning in two species of darters (Percidae), Etheostoma nigrum and Percina maculate. Can.jk. Zool. 1979; 57: 2061-71.

Schlosser IJ. A conceptual framework for fish communities in small warm water streams ed. Mattews, WJ, Heins, DC In: Community and Evolutionary Ecology of North American Stream Fishes. University of Oklahoma Press, Norman. 1987b; pp 17-24.

Schlosser IJ, Toth LA. Niche relationships and population ecology of raibow (Etheostoma caeruleum) and fantil (E. flabellare) darters in a temporally variable environment. Oikos 1984; 42:229-38.

Scot MC, Hall LW jr. Fish assemblages as indicators of environmental degradation in Maryland coastal plain streams. Trans. Am. Fish Soc. 1997; 126:349-60.

Shannon CE, Weaver W. The Mathematical Theory of Communication. Urbana 243III. University of Illinois Press 1949

Ward JB, Stanford JA. Ecological: connectivity in alluvial rivers ecosystem and its distribution by flow regulation. Regul.Riv.Res. Manage. 1995b; 11: 105-19.

Ward JB, Stanford JA. The serial discontinuity concept: Extending the models of flood lai rivers. Regul. Riv. Res. Manage., 1995a; 10:159-68.

Werner EE, Hall JD. Niche shifts in sunfish: experimental evidence and significance Science 1976; 191:404-5.

Wikramanake ED. Ecomorphology and biogeography of a tropical stream fish assemblage: evolution of assemblage structure. Ecology 1990; 1756-64.

A Systematic Synthesis for High-OrderSquare-Root Domain Filters with Reduced Voltage

Gwo-Jeng Yu

Department of Computer Science and information Engineering, Cheng Shiu University Niaosong, Taiwan 833, R.O. China. gjyu@csu.edu.tw

Abstract

　　A systematic synthesis for high-order square-root domain filter (SRD) based on the quadratic *I-V* relationship for an MOSFET operated in saturation region is presented in this paper. Emphases are placed on the methodology of filter synthesis, the constructive settings of DC components for input signals, the DC voltages of the state-space variables, and the DC bias current I_0. The proposed prototypes of square-root domain filters are able to overcome the possible inequality between the input and output node of DC level, in which improve the reliability of high-order filter implementation. Furthermore, by means of adjusting the range of the DC bias current I_0 in the acceptable boundary, the center frequency f_0 or 3 dB frequency f_{3dB} of the proposed prototypical circuits of SRD filters are not only attainable at megahertz frequencies but also tunable electronically. Simulations are performed with the model of a 0.25 μm CMOS process at 1.5 V supply voltage. The simulated results, which provide that the average errors of frequency response are smaller than 1.0%, demonstrate the validity of the proposed synthetic technique. The synthesized filters have the features of high frequency operation, tuneability, extensibility, and low power consumption. [Life Science Journal. 2010; 7(1): 15-29] (ISSN: 1097 – 8135)

Key Words: high-order square-root domain filter; low-voltage level-shift current mirror; current-mode square-root circuit; electronically tunable; high frequency operation; extensibility

Introduction

　　Today, many researchers have dedicated to developing companding filters which comprise log-domain and square-root domain (SRD) filters. Log-domain filter which was originally proposed by Adams[1] is a nonlinear (exponential) mapping on the state variables of a state-space (SS) description of a linear transfer function and includes the characteristics of high-frequency operation and tuneability. Frey[2-3] further utilized the exponential transformation of the state-space description of a linear transfer function, in terms of bipolar circuits, to implement log-domain filters and in turn, was embedded in as forming part of a broader branch of structures by Tsividis[4]. Furthermore, Drakakis et al.[5-7] proposed a systematic synthesis method, based on "Bernoulli cell", to realize the log-domain filters.

　　Most of the IC fabrication technologies, however, trend to digital CMOS processes, and this is due to the fact that a similar I–V exponential relationship holds the concept of "log-domain filtering" has been extended to the MOS transistors in weak-inversion region. Thus, adopting a direct transformation of the corresponding implementations based on bipolar transistors into MOS transistors realizations. To meet such demand and change, Toumazou et al.[8]and Germanovix et al.[9] proposed log-domain filters in terms of MOSFET circuits that operate in weak inversion. The main drawbacks of these topologies are the increased effect of transistor mismatches and the limited operation frequency, both originated from the operation mode of MOS transistor. As a result, the problems of the above

methods are solved and enhanced via adopting the quadratic I–V relationship for the MOS transistor that operates in saturation region to implement log-domain filters-reducing fabrication cost while also lessening drawbacks such as high power supply voltage, high power consumption and low operation frequency. The methods are according to those of Eskiyerli et al.[10, 14], Yu et al.[11-12] and Lopez-Martin[13]. For this reason, these filters are also known as square-root domain filters. The basic building blocks for these filters include current mirrors, current-mode geometric-mean and multiplier-divider circuits. Different topologies for the geometric-mean circuits based on stacked MOS translinear loop[14-17]and up-down MOS translinear loop [18-19] are available in the open literature. Furthermore, both geometric mean and squarer blocks are used to implement the current-mode multiplier-divider[18-19].

　　For reliable operation of submicron digital CMOS integrated circuits, the continuous supply voltage decrease has become notable. Some current mirrors (CMs) are currently in use in most applications[20-22], whereas most of CMs either reveal severe performance degradation or are not functional at all in a low voltage supply environment. All high impedance CMs proposed by Mulder et al.[23], Zeki et al.[24] and Blalock et al.[25] require high input voltage, which provide the capability of high output voltage signal swing. The CMs proposed by[26-28] operate with low input voltage, whereas the main disadvantage of Prodanov et al.[26] has limited current range, Heim et al.[27] is not suitable for high frequency applications, and partial transistors of Itakura et al.[28] are biased in triode mode such that the mirror is sensitive to

geometry and threshold voltage mismatches.

Hence, Lopez-Martin et al.[29-30] proposed 1.5 V CMOS square-root domain low-pass and companding filters. The operation frequencies, nonetheless, remain low. In Yu et al.[31-32], an experiment based on 1.5 V square-root domain band-pass filter is proposed based on the MOSFET square law which contains the following characteristics and advantages: low cost, high frequency operation, low supply voltage operation, low power consumption, low noise, and electronically tunable of center frequency.

In this paper, based on the proposed prototypical circuits of SRD filters, a systematic synthesis method of high-order SRD filters is presented. Furthermore, in order to verify the extensibility of high-order filters, the synthetic procedures are also presented and discussed in which principles must be paid attention to at time of the syntheses for high-order filters, for example, the aspect ratios W/L of transistors, capacitance C, quality factor Q, DC bias voltages of driving MOSs, and DC bias current, etc. The main objectives are not only the demonstration of practicability of high-order low-voltage SRD filters, but also indicate the design matter requiring attention of the high-order filters.
Simultaneously, the simulated results of syntheses for several high-order low-voltage SRD filters are performed and compared with the specified values in which demonstrate the validity of the proposed synthetic technique and the high performances of the proposed prototypes of SRD filters.

Design Methodologies of Prototypes for Square-Root Domain filters

Square-root domain (SRD) filters feature a nonlinear (exponential) mapping on the state variables of a state-space description for a particular transfer function. In order to implement the filters, state equations must be further transformed to nodal equations at the nodes of grounded capacitors. Furthermore, based on the MOSFET square law relationship, the nodal equations are replaced by intermediate variables. Then, by means of interconnection of sub-circuits to realize the terms of nodal equation, the design procedures of square-root domain filters are achieved.

First, the transfer function of a band-pass filter (BPF) is introduced and shows how it is used to yield a SRD BPF. Assume that the transfer function of a second-order SRD BPF is expressed as

$$H(s) = \frac{\left(\dfrac{\omega_0}{Q}\right)s}{s^2 + \left(\dfrac{\omega_0}{Q}\right)s + \omega_0^2} \tag{1}$$

and by using the standard technique[33-35] for creating companion-form dynamical equations, Eq. (1) is realized by the system described by the following equations.

$$\begin{cases} \dot{x}_1 = -\omega_0 x_2 \\[2em] \dot{x}_2 = \omega_0 x_1 - \left(\dfrac{\omega_0}{Q}\right)x_2 + \left(\dfrac{\omega_0}{Q}\right)u \\[2em] y = x_2 \end{cases} \tag{2}$$

where x_1, x_2, y, and u are state variables, output and input signals, respectively. Let the node voltages V_1 and V_2 be the state variables x_1 and x_2, and a voltage signal U denotes the input u, then (2) is rewritten as follows

$$\begin{cases} C\dot{V}_1 = -C\omega_0 V_2 \\[2em] C\dot{V}_2 = C\omega_0 V_1 - (\dfrac{C\omega_0}{Q})V_2 + (\dfrac{C\omega_0}{Q})U \\[2em] y = V_2 \end{cases} \tag{3}$$

with C is a multiplying factor. Both of $C\dot{V}_1$ and $C\dot{V}_2$ in (3) are regarded as the time-dependent current through the two capacitors C connected between V_1 and ground and between V_2 and ground, respectively.
Assume that the drain current of an MOSFET transistor operated in saturation region is expressed as

$$I_D = \frac{\mu_0 C_{ox} W}{2L}\left(V_{GS} - V_T\right)^2 = \beta\left(V_{GS} - V_T\right)^2 \tag{4}$$

where β, V_{GS}, and V_T are the device transconductance parameter, the gate-to-source voltage, and the threshold voltage, respectively.
Hence, based on (4), the state equations of Eq.(3) are transformed into [11-12, 31-32]

$$\begin{cases} C\dot{V}_1 = -\sqrt{I_0 I_2} - I_T \\[2em] C\dot{V}_2 = \sqrt{I_0 I_1} - \dfrac{\sqrt{I_0 I_2}}{Q} + \dfrac{\sqrt{I_0 I_U}}{Q} + I_T \\[2em] y = V_2 \end{cases} \tag{5}$$

where

$$I_1 \equiv \beta\left(V_1 - V_T\right)^2 \tag{6}$$

$$I_2 \equiv \beta\left(V_2 - V_T\right)^2 \tag{7}$$

$$I_U \equiv \beta\left(U - V_T\right)^2 \tag{8}$$

$$I_T \equiv C\omega_0 V_T \qquad (9)$$

and

$$I_0 \equiv \frac{C^2 \omega_0^2}{\beta} \quad \text{or} \quad f_0 = \frac{\omega_0}{2\pi} = \frac{\sqrt{\beta I_0}}{2\pi C} \qquad (10)$$

Note that (6)-(10) are defined as the currents in the circuit corresponding to input voltages V_1, V_2, U, the DC compensation term of the threshold voltage V_T and the DC bias current, respectively. The SRD BPF is driven by the external applied input voltage U and DC bias current I_0. Hence, based on the given device parameters β and V_T of the transistors, the capacitance C, the DC bias current I_0, and the quality factor Q, the center frequency f_0 and the DC compensation current I_T can be calculated. Moreover, the current I_U is also yielded to correspond to the input voltage U. However, the currents I_1 and I_2 are changed according to the variations of the node voltages V_1 and V_2. The output is then taken from the node voltage V_2.

The center frequency f_0, defined in (10), is proportional to the square root of the DC bias current I_0, whereas is inversely proportional to the capacitance C. Therefore, the center frequency f_0 is tuned by using the capacitance C and the DC bias current I_0.

Similar to the above methodologies, the equivalent representations for first-order and second-order SRD filters may be derived as listed in Table 1.

Next, in order to achieve low voltage circuit operation, both of the n-type and n-type low-voltage (LV) current mirrors (CMs) in the proposed SRD filters are designed by means of LV level-shift technique, as shown in Fig. 1[32]. Simultaneously, Fig. 2[32] shows the DC biasing circuit diagrams of the proposed n-type and p-type LV level-shift CMs, respectively, where V_{N1}, V_{N2}, V_{P1}, and V_{P2} are connected to the corresponding bias terminals of the CMs, such that the overall supply voltage source is simplified to be only one supply voltage source V_{DD}.

Table 1.   Equivalent representations of the SRD filters.

Types of filters	Transfer functions	State equations	Equivalent equations of KCL
Second-order band-pass filter	$H(s) = \dfrac{\left(\dfrac{\omega_0}{Q}\right)s}{s^2 + \left(\dfrac{\omega_0}{Q}\right)s + \omega_0^2}$	$\begin{cases} \dot{x}_1 = -\omega_0 x_2 \\ \dot{x}_2 = \omega_0 x_1 - \left(\dfrac{\omega_0}{Q}\right)x_2 + \left(\dfrac{\omega_0}{Q}\right) \\ y = x_2 \end{cases}$	$\begin{cases} C\dot{V}_1 = -\sqrt{I_0 I_2} - I_T \\ C\dot{V}_2 = \sqrt{I_0 I_1} - \dfrac{\sqrt{I_0 I_2}}{Q} + \dfrac{\sqrt{I_0 I_U}}{Q} + I_T \\ y = V_2 \end{cases}$
First-order low-pass filter	$H(s) = \dfrac{\omega_0}{s + \omega_0}$	$\begin{cases} \dot{x} = -\omega_0 x + \omega_0 u \\ y = x \end{cases}$	$\begin{cases} C\dot{V}_1 = -\sqrt{I_0 I_1} + \sqrt{I_0 I_U} \\ y = V_1 \end{cases}$
Second-order low-pass filter	$H(s) = \dfrac{\omega_0^2}{s^2 + \left(\dfrac{\omega_0}{Q}\right)s + \omega_0^2}$	$\begin{cases} \dot{x}_1 = -\omega_0 x_2 + \omega_0 u \\ \dot{x}_2 = \omega_0 x_1 - \left(\dfrac{\omega_0}{Q}\right)x_2 \\ y = x_2 \end{cases}$	$\begin{cases} C\dot{V}_1 = -\sqrt{I_0 I_2} + \sqrt{I_0 I_U} \\ C\dot{V}_2 = \sqrt{I_0 I_1} - \left(\dfrac{\sqrt{I_0 I_2}}{Q}\right) + \left(1 - \dfrac{1}{Q}\right)I \\ y = V_2 \end{cases}$
Second-order biquad filter	$H_1(s) = \dfrac{y}{u_1}$ $= \dfrac{\omega_0^2}{s^2 + \left(\dfrac{\omega_0}{Q}\right)s + \omega_0^2}$ $H_2(s) = \dfrac{y}{u_2}$ $= \dfrac{\left(\dfrac{\omega_0}{Q}\right)s}{s^2 + \left(\dfrac{\omega_0}{Q}\right)s + \omega_0^2}$	$\begin{cases} \dot{x}_1 = -\omega_0 x_2 + \omega_0 u_1 \\ \dot{x}_2 = \omega_0 x_1 - \left(\dfrac{\omega_0}{Q}\right)x_2 + \left(\dfrac{\omega_0}{Q}\right) \\ y = x_2 \end{cases}$	$\begin{cases} C\dot{V}_1 = -\sqrt{I_0 I_2} + \sqrt{I_0 I_{U1}} \\ C\dot{V}_2 = \sqrt{I_0 I_1} - \dfrac{\sqrt{I_0 I_2}}{Q} + \dfrac{\sqrt{I_0 I_{U2}}}{Q} + I \\ y = V_2 \end{cases}$
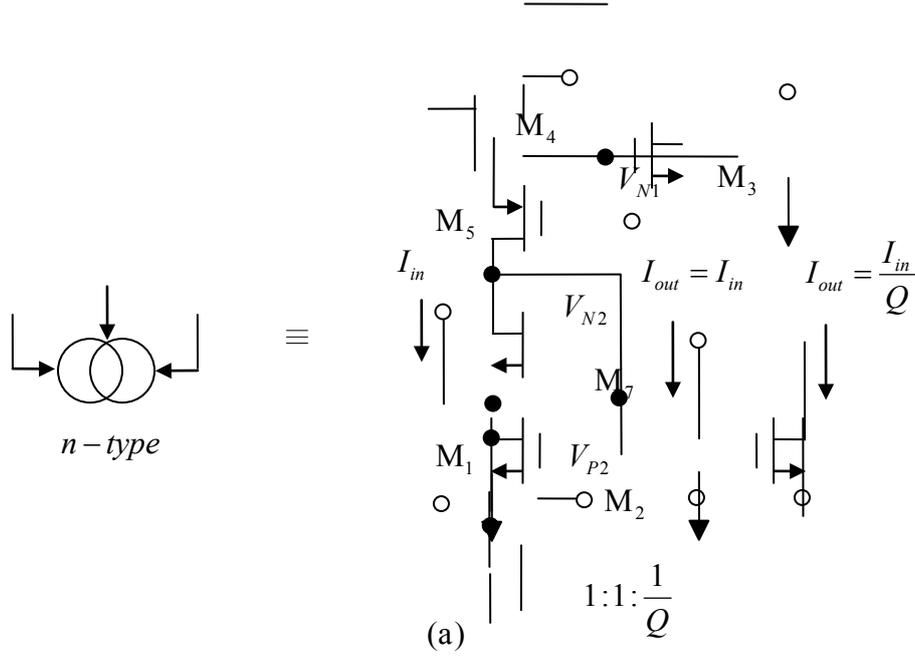
Fig. 1. (a) Symbol and circuit diagram of the n-type LV level-shift CM, (b) Symbol and circuit diagram of the p-type LV level-shift CM.
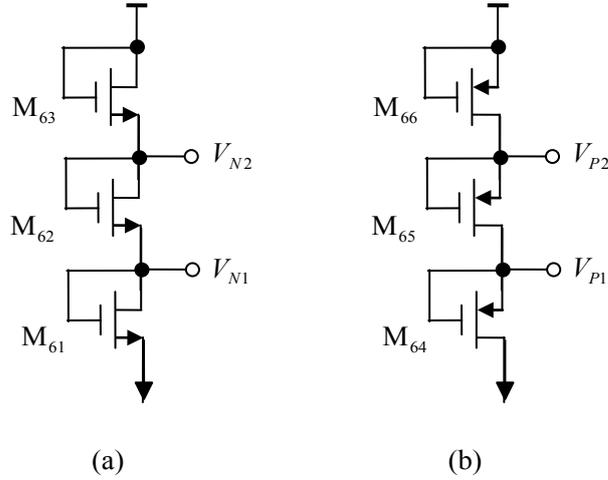
Fig. 2. DC biasing circuit diagram of (a) n-type and (b) p-type LV level-shift CMs.

Note that, in Fig. 1(a), the transistor M_5 biased by a voltage V_{N1} is acted as a current source. The V_{DS} voltage of transistor M_1 is fixed to a constant value by transistor M_4, current source transistor M_5, and voltage source V_{N2}. The transistor M_4 with bias voltage V_{N2} provides shunt feedback to form lower input impedance, which reduces the input voltage requirement.

Further, according to the MOSFET square law, the square-root of two currents is realized by the current-mode square-root circuit as shown in Fig. 3[32]. The core circuit is composed of transistors M_{31}, M_{32}, M_{33}, and M_{34}. The other transistors except M_{31}-M_{34}, which are

the LV level-shift CMs, are used to transmit current signals. Assume that the aspect ratios of the transistors in core circuit satisfy the following constraints:

$$\beta_{31} = \beta_{32} \equiv \beta \text{ and } \beta_{33} = \beta_{34} \equiv 2\beta \quad (11)$$

Thus, from the derivations of[31-32], we have

$$I_{out} = \sqrt{I_x I_y} \quad (12)$$

which conforms to the function of the current-mode square-root circuit.

18

(a)   (b)
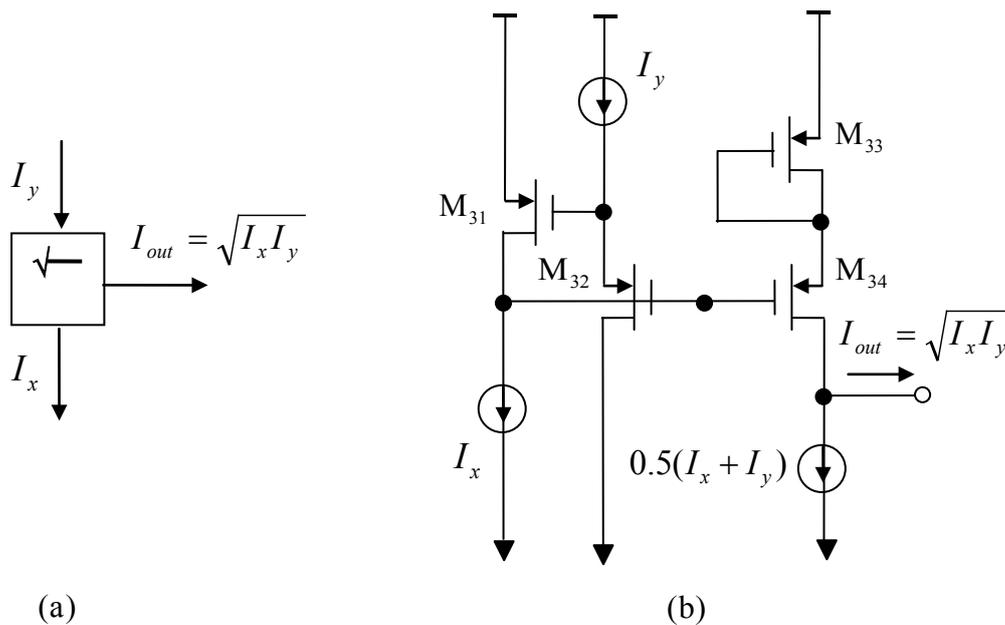
Fig. 3. (a) Symbol of the current-mode square-root circuit, (b) circuit diagram of the current-mode square-root circuit.
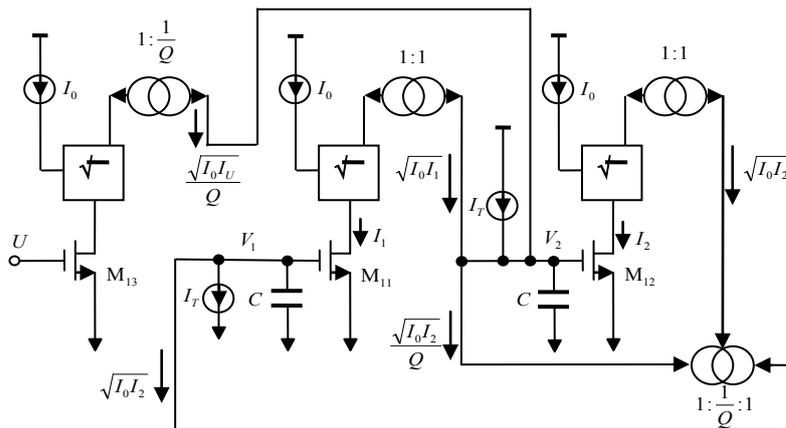
Fig. 4.   Prototypical circuit of the proposed second-order LV SRD BPF.
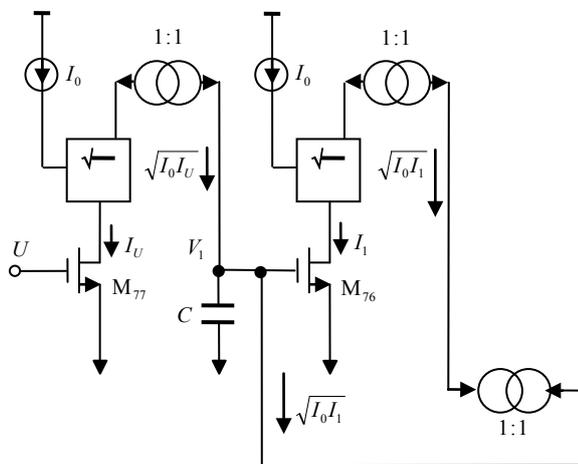
Fig. 5.   Prototypical circuit of the proposed first-order LV SRD LPF.
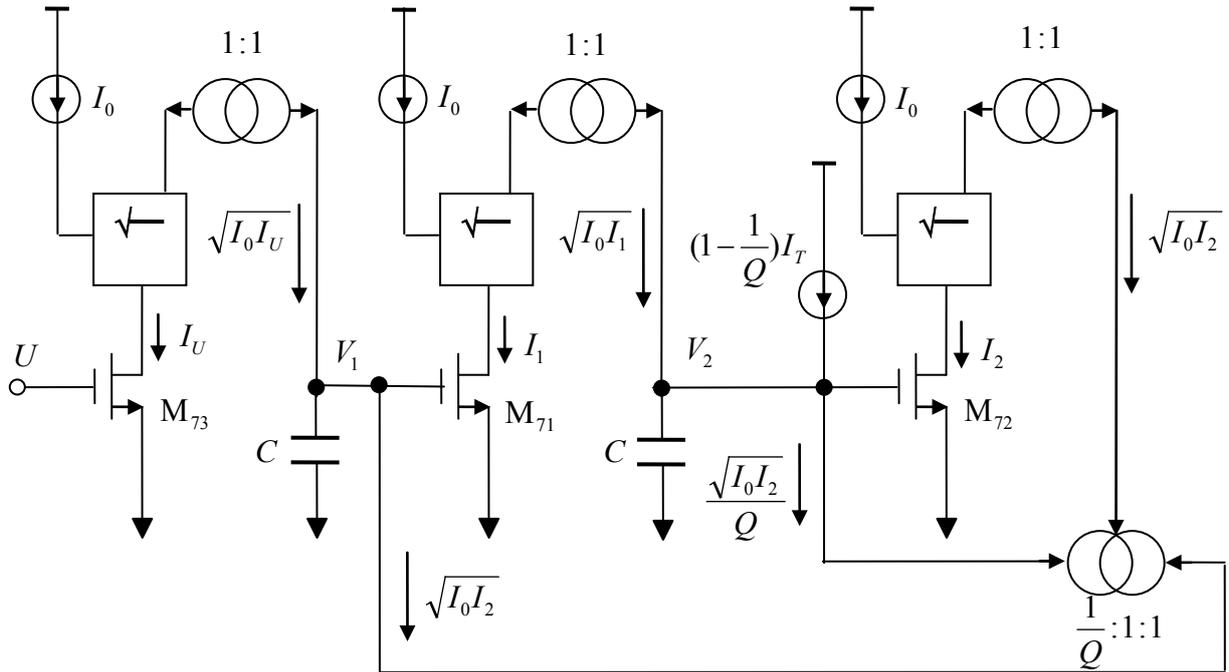
Fig. 6. Prototypical circuit of the proposed second-order LV SRD LPF.
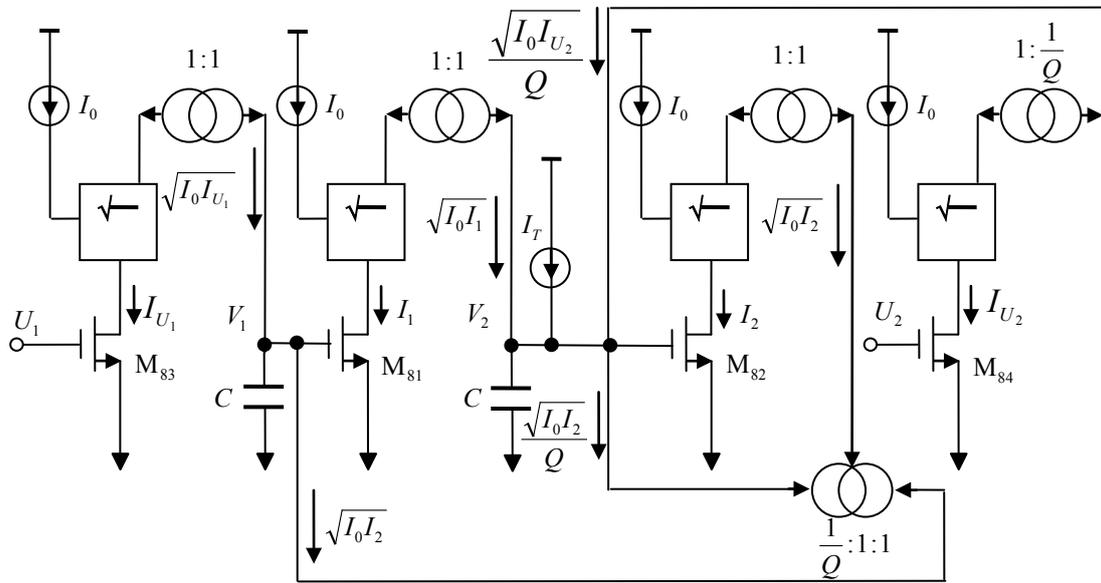
Fig. 7. Prototypical circuit of the proposed second-order LV SRD biquad.

Obviously, the constraint for the minimum power supply voltage V_{DD} is determined by following conditions,

$$V_{DD} \geq 2V_{EFP} + V_{EFN} \tag{13}$$

$$V_{DD} \geq 2V_{EFP} + |V_{TP}| \tag{14}$$

$$V_{N1} = \frac{V_{DD} + (\sqrt{(\frac{W}{L})_{61}/(\frac{W}{L})_{62}} + \sqrt{(\frac{W}{L})_{61}/(\frac{W}{L})_{63}} - 2)V_{TN}}{(\sqrt{(\frac{W}{L})_{61}/(\frac{W}{L})_{62}} + \sqrt{(\frac{W}{L})_{61}/(\frac{W}{L})_{63}} + 1)} \tag{15}$$

$$V_{N2} = V_{N1} + V_{TN} + (\sqrt{(\frac{W}{L})_{61}/(\frac{W}{L})_{62}})(V_{N1} - V_{TN}) \tag{16}$$

where V_{TN} and V_{TP} are the threshold voltage of the NMOS and PMOS transistor, respectively,

$$V_{EFN} \equiv V_{GSN} - V_{TN} \quad \text{and} \quad V_{EFP} \equiv V_{SGP} - |V_{TP}|$$

are defined as the minimum source-to-drain voltages required to sustain an NMOS transistor and PMOS transistor in saturation, respectively.

Hence, the prototypical circuit of the proposed second-order LV SRD BPF expressed as (5) is realized by using the LV level-shift CMs, three current-mode square-root circuit blocks, and two capacitors, as shown in Fig. 4[32], where U and I_0 are the external applied DC biasing input voltage and DC biasing current, respectively, and V_2 is the desired output voltage. Furthermore the currents I_U, I_1, and I_2 in the BPF are related to the corresponding input voltages U, V_1, and V_2, respectively. The DC bias current I_0 is used to control the position of center frequency of this BPF. As evident, the BPF having the expected transfer function may operate at lower supply voltage.

Similar to the above technologies, the prototypical circuits for proposed first-order LV SRD LPF, second-order LV SRD LPF, and second-order LV SRD biquad may be given, which are shown in Figs. 5, 6, and 7[32], respectively. Simultaneously, Figs. 1 to 7 are regarded as prototypes (or basic block diagrams) while carrying out the syntheses of high-order LV SRD filters.

Furthermore, consider the proposed circuits based on TSMC 0.25 μm 1p5m CMOS process with $V_{TN} = 0.53\,\text{V}$ and $|V_{TP}| = 0.58\,\text{V}$ to verify the functions of the proposed second-order LV SRD BPF. The maximum operation current is 200 μA, the power

supply voltage V_{DD} for the proposed LV SRD BPF as shown in Fig. 4 is set as 1.5 V, and two capacitors in this BPF are $C_1 = C_2 = 0.9$ pF. The DC biasing voltages of V_{N1}, V_{N2}, V_{P1}, and V_{P2} under $V_{DD} = 1.5$ V are measured to be 0.52 V, 1.02 V, 0.95 V and 0.46 V, respectively. The microphotograph of the proposed second-order LV SRD BPF is shown in Fig. 8 where the total area of this filter is 0.0175 mm^2.

Table 2 shows the measured and simulated results for the proposed LV SRD BPF and LPF, respectively; Table 3 shows the simulated results for the proposed LV SRD biquad filter[32]. Both of the measured and simulated results for the proposed LV SRD BPF are in well agreement and demonstrate that the center frequency f_0 are tunable electronically, further indicate that the proposed circuit is able to provide reliable operation at 1.5 V with low power consumption and high noise immunity.

Systematic Synthesis for High-Order Square-Root Domain Filters

Assume that the circuit diagrams of LV current-mode level-shift CMs, square-root circuit, the first-order and second-order LV SRD filters shown in Figs. 1 to 7 are regarded as the prototypes (or basic block diagrams), then the transfer function of a high-order LV SRD filter can be decomposed into the product of several first-order and second-order ones, which can be implemented by cascading the corresponding prototypes.

Note that every individual pole frequency of the first-order or the second-order LV SRD filter must be adjusted to meet the specified pole frequency. Simultaneously, for realizing the high-order filter, the possible inequality between the input, output node, and grounded capacitors of DC level which will induce the incomplete power propagation and seriously degrade the frequency response of the filter all must be improved. Hence, in the course of designing, additional condition will be joined by setting the DC components of input signals and state-space variables to be a same DC voltage value, in order to guarantee that the DC levels of the input node, the output node, and the grounded capacitors are equal. Fig. 9 shows the synthetic procedures of high-order LV SRD filters in which the aspect ratios W/L of transistors for the current-mode CMs and square-root circuit shown in Table 4 are assumed to be fixed, while those of transistors and C for the current-mode LV SRD filters shown in Table 5 are allowed to be adjustable such that the DC bias current I_0 may fall into the acceptable boundary which are demonstrated in the simulated and measured results of[32].
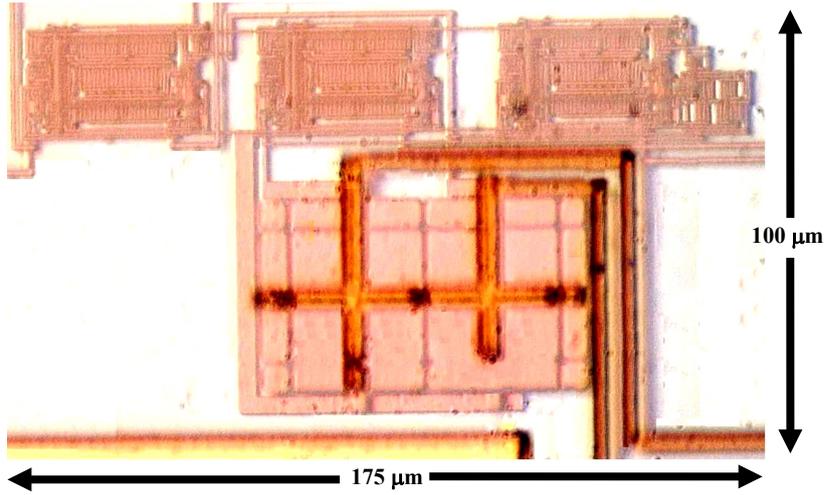
Fig. 8.   The microphotograph of the proposed second-order LV SRD BPF.

Table 2.   Measured and simulated results for the proposed LV SRD BPF and LPF.

Parameters	LV SRD BPF Measured results	LV SRD LPF Simulated results	LV SRD LPF Simulated results
Technology	TSMC 0.25 μm 1p5m		
Order of the filter	2	1	2
Q	21.3	1	1
C	0.9 pF	1 pF	1 pF
Supply voltage	1.5 V	1.5 V	1.5 V
Power consumption (average)	1.598 mW	0.366 mW	0.633 mW
f_0 or f_{3dB} tuning range	f_0 = 4 - 10 MHz	f_{3dB} = 1.2 – 21.2 MHz	f_{3dB} = 1.1 – 22.5 MHz
IM3 (V_{pp} = 0.1 V)	-44.67 dB (5.35 MHz and 5.4 MHz (in band))	-45.3 dB (4 MHz and 5 MHz (in band))	-38.6 dB (4 MHz and 5 MHz (in band))
THD (V_{pp} = 0.1 V)	-26.7 dB (5.38 MHz)	-27.6 dB (1 MHz)	-26.0 dB (1 MHz)
Output noise power	-45.2 dBm	-46.2 dBm	-44.2 dBm
SFDR	35.0 dB	37.1 dB	34.6 dB
Measured and simulated conditions			
I_0	90 μA	20 μA	20 μA
f_{3dB}	5.52 MHz	13.7 MHz	14.4 MHz
f_0	5.66 MHz		

Table 3.   Simulated results for the proposed second-order LV SRD biquad filter.

Parameters	Simulated results Band-pass section	Low-pass section
Technology	TSMC 0.25 μm 1p5m	TSMC 0.25 μm 1p5m
Order of the filter	2	2
Q	1	1
Supply voltage	1.5 V	1.5 V
Power consumption (average)	1.42 mW	1.27 mW
f_0 or f_{3dB} tuning range	f_0 = 1.9 – 17.0 MHz	f_{3dB} = 1.2 – 22.2 MHz
IM3 (V_{pp} = 0.1 V)	-33.2 dB (10 MHz and 11 MHz (in band))	-34.1 dB (5 MHz and 6 MHz (in band))
THD (10 MHz, V_{pp} = 0.1V)	-25.2 dB	-24.8 dB
Output noise power	-43.7 dBm	-44.0 dBm
SFDR	32.7 dB	31.6 dB
Simulated conditions		
I_0	20 μA	20 μA
f_{3dB1}, f_0, f_{3dB2}	6.7 MHz, 10.2 MHz, 13.5 MHz	f_{3dB} = 14.1 MHz

Synthesis of a specified
High-order SRD filter

Given specifications
of a specified
High-order SRD filter

Decomposing into the product
of 1st and 2nd-order filter
transfer functions

Selecting the corresponding
basic block diagram of 1st and
2nd-order filters

Including :
(a) Figs 3.1 - 3.5   for V_{DD} = 2.5V
(b) Figs 3.8 - 3.14 for V_{DD} = 1.5V

Cascading the selected
basic block diagram of 1st and
2nd-order filters

Selecting the specified CMOS
process and the relative
threshold volatges

Including :
V_{TN} and V_{TP}

Setting initial conditions

Including :
(a) V_{DD} and Q
(b) Acceptable boundaries of I_0 , C and W/L

Setting DC component of
input signal and state-space
variables to be same

Including :
(a) U, V_1 and V_2 for 2nd order BPF & LPF
(b) U and V_1 for 1st order LPF
(c) U_1 , U_2 , V_1 and V_2 for 2nd order Biquad

Setting the initial values
C = 1 pF
W/L = 20 μm/ 2 μm

C < min.
acceptable boundary ?   no   yes

(W/L>max.)or
(W/L<min.)acceptable
boundary ?   no   yes

Changing the values of
C = C - 0.1 pF
W/L = 20 μm/ 2 μm

Calculating the corresponding
β , I_T and I_0

Changing the values of
W/L = W/L + 5 μm/ 0 μm

Changing the values of
W/L = W/L - 5 μm/ 0 μm

Does I_0 fall
into the acceptable
boundary ?   no

($I_0 \geqq$ max.) and
($C \geqq$ min.) acceptable
boundary ?   no

($I_0 \leqq$ min.) and
($C \geqq$ min.) acceptable
boundary ?   no

yes   yes   yes

Evaluating the frequency
response and error

The synthesis of the
High-order SRD filter fails

Completing the synthesis of
the High-order SRD filter

End of the synthesis of the
High-order SRD filter

Fig. 9.   The synthetic procedures of a specified high-order LV SRD filter.

Table 4. The aspect ratios of transistors for the LV current-mode level-shift CMs and square-root circuit shown in Figs. 1 to 3

Prototypes	The aspect ratios (W/L)
The proposed LV level-shift CMs (Fig. 1)	W/L = 20 μm/ 2 μm
The DC biasing circuits (Fig. 2)	$(W/L)_{61}$= 2 μm/ 0.25 μm, $(W/L)_{62}$ = 0.3 μm/ 0.25 μm, $(W/L)_{63}$ = 0.3 μm/ 0.25 μm, $(W/L)_{64}$ = 2 μm/ 0.25 μm, $(W/L)_{65}$ = 4 μm/ 0.25 μm, $(W/L)_{66}$ = 30 μm/ 0.25 μm
The proposed LV current-mode square-root circuits (Fig. 3)	W/L = 7 μm/ 0.7 μm except W/L = 14 μm/0.7 μm for M_{33} and M_{34}

Table 5. The acceptable boundaries of C, W/L, and I_0 of the LV current-mode LV SRD filters shown in Figs. 4 to 7 operated at V_{DD} = 1.5 V.

Type of filters	Prototypes	C	W/L		I_0
Second-order LV SRD BPF	Fig. 4	0.5 – 1.0 pF	10 for M_{11} - M_{13}	μm/ 2 μm	60 - 200 μA
First-order LV SRD LPF	Fig. 5	0.5 – 1.0 pF	10 for M_{76} - M_{77}	μm/ 2 μm	2 - 40 μA
Second-order LV SRD LPF	Fig. 6	0.5 – 1.0 pF	10 for M_{71} - M_{73}	μm/ 2 μm	2 - 40 μA
Second-order LV Low-pass section of SRD biquad	Fig. 7	0.5 – 1.0 pF	10 for M_{81} - M_{84}	μm/ 2 μm	2 - 40 μA
Second-order LV Band-pass section of SRD biquad	Fig. 7	0.5 – 1.0 pF	10 for M_{81} - M_{84}	μm/ 2 μm	2 - 40 μA

Simulated Results of High-Order Square-Root Domain Filters

Consider the proposed prototypical circuits based on TSMC 0.25 μm 1p5m CMOS process with $V_{TN} = 0.53\,\text{V}$ and $|V_{TP}| = 0.58\,\text{V}$ to verify the functions of the proposed high-order LV SRD filters.
Synthesis of Third-Order LV SRD Low-Pass Filter
For an attempt to synthesize a third-order low-voltage square-root domain low-pass filter specified in Table 6, the synthetic configurations have two types that contain one stage of second-order LV SRD LPF cascaded one stage of first-order LV SRD LPF or one stage of second-order LV low-pass section of SRD biquad cascaded one stage of first-order LV SRD LPF shown in Fig. 10(a) and (b), respectively, whereas, the synthetic methods for the two configurations are similar. Thus, accordingly, only one of the synthetic configurations, one stage of second-order LV SRD LPF cascaded one stage of first-order LV SRD LPF, is provided in the following.

Table 6. Specifications of a third-order LV SRD LPF.

| Parameters	Specifications
Technology	TSMC 0.25 μm 1p5m
Order of the filter	3
Type of filter	Low-pass filter
Q	1
Supply voltage	1.5 V
3 dB frequency f_{3dB}	1.5 MHz

(a)

(b)
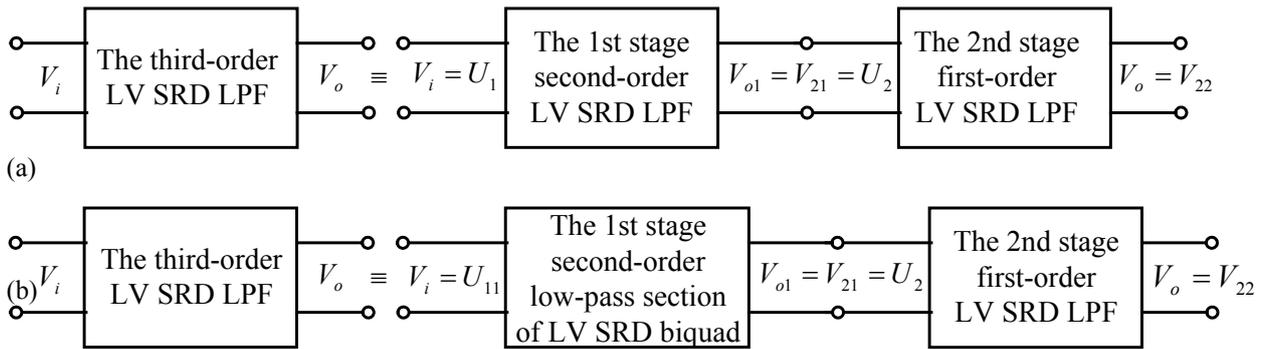
Fig. 10.   Synthetic configurations of the specified third-order LV SRD low-pass filter.

Firstly, the prototypical circuits of second-order LV SRD LPF and first-order LV SRD LPF are given in Fig. 6 and 5, respectively, which the boundaries of I_0, C, and W/L are rewritten and given in Table 7. Thus, according to the synthetic procedures shown in Fig. 9, the initial values of C and W/L for the corresponding circuits are set to be C = 1 pF and W/L = 20 respectively, and let the DC components of input signal and state-space variables be $U = V_1 = V_2 = 0.65$ V. Next, the corresponding values of β, I_T, and I_0 defined in (4), (9), and (10), respectively, are identical for the two prototypical circuits as

$$\beta \equiv \frac{1}{2}\mu_0 C_{ox}\left(\frac{W}{L}\right) \approx 30.81 \ \mu A \Box V^2$$

$$I_T \equiv C\omega_0 V_T = C(2\pi f_0)V_T \approx 5.00 \ \mu A$$

$$I_0 \equiv \frac{C^2\omega_0^2}{\beta} = \frac{C^2(2\pi f_0)^2}{\beta} \approx 2.88 \ \mu A \Box$$

where the DC bias current I_0 falls into the acceptable $\Box m \Box 2 \Box$ boundary shown in Table 7. Hence, the simulated frequency response of third-order LV SRD LPF may be evaluated as shown in Fig. 11 in which the simulated 3 dB frequency f_{3dB} is approximately 1.486 MHz. Obviously the error of frequency response is approximately 0.933%, while compared with the specified 3 dB frequency f_{3dB} = 1.5 MHz

Table 7.   The acceptable boundaries of C, W/L, and I_0 of second-order LV SRD LPF and first-order LV SRD LPF.

| Type of filters	Prototypes	C	W/L	I_0
Second-order LV SRD LPF	Fig. 6	0.5 – 1.0 pF	10 μm/ 2 μm - 40 μm/ 2 μm for M_{71} - M_{73}	2 - 40 μA
First-order LV SRD LPF	Fig. 5	0.5 – 1.0 pF	10 μm/ 2 μm - 40 μm/ 2 μm for M_{76} - M_{77}	2 - 40 μA

Fig. 11.   The simulated frequency response of the third-order LV SRD LPF.

Synthesis of Eighth-Order LV SRD Band-Pass Filter

Similarly, by means of combining four stages second-order LV SRD BPF or LV band-pass section of SRD biquad cascaded, an eighth-order low-voltage square-root domain band-pass filter specified in Table 8 may be synthesized. Further, simply only the synthetic method of adopting four stages of second-order LV SRD BPF cascaded is described.

Table 8.   Specifications of an eighth-order LV SRD BPF.

Parameters	Specifications
Technology	TSMC 0.25 μm 1p5m
Order of the filter	8
Type of filter	Band-pass filter
Q	1
Supply voltage	1.5 V
Center frequency f_0	5 MHz

The adopted prototype of second-order LV SRD BPF shown in Fig. 4 and Table 9 is then the corresponding boundaries of I_0, C, and W/L. Furthermore, according to the synthetic procedures of Fig. 9, the initial values of C and W/L for the corresponding prototype are set to be 1 pF and 20 □m/ 2 □m, respectively, and assume the DC components to be $U = V_1 = V_2 = 0.65$ V. Hence, the corresponding values of β, I_T, and I_0 for the second-order LV SRD BPF are calculated as

$$\beta \approx 30.81 \qquad I_T \approx 16.65, \text{ and} \qquad I_0 \approx 32.03 \quad \square$$

Table 9.   The acceptable boundaries of C, W/L, and I_0 of second-order LV SRD BPF.

Type of filters	Prototypes	C	W/L	I_0
Second-order LV SRD BPF	Fig. 4	0.5 – 1.0 pF	10 μm/ 2 μm - 40 μm/ 2 μm for M_{11} - M_{13}	60 - 200 μA

However, the DC bias current I_0 is smaller than the acceptable lower limit 60 μA□specified in Table 9. Thus, according to the synthetic procedures of Fig. 9, the aspect ratio W/L must be decreased to be W/L = 10 μm/ 2 □m. The resultant quantities are

$$\beta \approx 15.41 \ \mu A\square V^2, \quad I_T \approx 16.65, \text{ and} \quad I_0 \approx 64.05 \ \mu A$$

which indicate DC bias current I_0 satisfies the acceptable boundary specified in Table 9. Hence, the simulated frequency response of the eighth-order LV SRD BPF is performed and shown in Fig. 12 in which the simulated center frequency f_0 approximates at 4.97 MHz and suffers from 0.6% error of frequency response, while compared with the specified center frequency $f_0 = 5$ MHz.
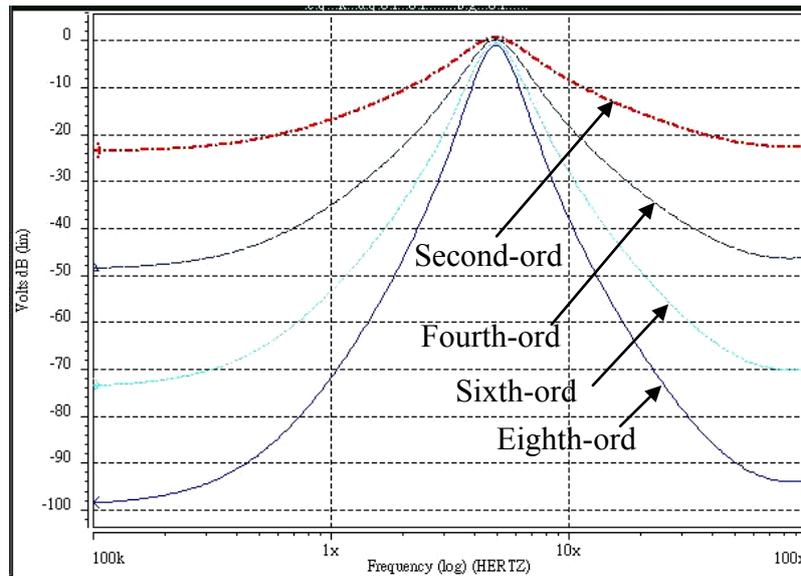
Fig. 12.   The simulated frequency response of the eighth-order LV SRD BPF.

Synthesis of Ninth-Order LV SRD Low-Pass Filter

Next, in order to design a ninth-order LV SRD low-pass filter specified in Table 10, two schemes are used. Each contains four stages of second-order LV SRD LPF cascaded one stage of first-order LV SRD LPF or four stages of second-order LV low-pass section of SRD biquad cascaded one stage of first-order LV SRD LPF, respectively, are provided in below and demonstrated.

Table 10.   Specifications of a ninth-order LV SRD LPF.

Parameters	Specifications
Technology	TSMC 0.25 μm 1p5m
Order of the filter	9
Type of filter	Low-pass filter
Q	1
Supply voltage	1.5 V
3 dB frequency f_{3dB}	2 MHz

Four Stages of Second-Order LV LPF Cascaded One Stage of First-Order LV SRD LPF. The prototypes of second-order LV SRD LPF and first-order LV SRD LPF are given in Fig. 6 and 5, respectively, and the corresponding boundaries of I_0, C, and W/L are rewritten and given in Table 11. Simultaneously, the initial values of C and W/L for the corresponding prototypes are also set to be 1 pF and 20 μm/ 2 μm, respectively. Thus, the corresponding values of β, I_T, and I_0 for the two prototypes are all identical, result in

$\beta \approx 30.81$ μA□V², $I_T \approx 6.66$ μA, and $I_0 \approx 5.13$ μA

where the DC bias current I_0 meets the acceptable boundary shown in Table 11. Fig. 13 shows the simulated frequency response of the ninth-order LV SRD LPF. The simulated 3 dB frequency f_{3dB} approximates at 2.018 MHz and results in approximately 0.9% error of frequency response.

Table 11.   The acceptable boundaries of C, W/L, and I_0 of the second-order LV SRD LPF and first-order LV SRD LPF.

Type of filters	Prototypes	C	W/L	I_0
Second-order LV SRD LPF	Fig. 6	0.5 – 1.0 pF	10 μm/ 2 μm - 40 μm/ 2 μm for M_{71} - M_{73}	2 - 40 μA
First-order LV SRD LPF	Fig. 5	0.5 – 1.0 pF	10 μm/ 2 μm - 40 μm/ 2 μm for M_{76} - M_{77}	2 - 40 μA

Fig. 13.   The simulated frequency response of the ninth-order LV SRD LPF.

Four Stages of Second-Order LV Low-Pass Section of SRD Biquad Cascaded One Stage of First-Order LV SRD LPF

Similarly, Figs. 7 and 5 are adopted as the prototypes of second-order LV low-pass section of SRD biquad and first-order LV SRD LPF, respectively. Table 12 is the corresponding boundaries of I_0, C, and W/L. Next, the initial values of C and W/L for the corresponding prototypical circuits are set to be 1 pF and 20 μm/ 2 μm, respectively, and let the DC components be $U_1 = U_2 = V_1 = V_2 = 0.65$ V. Hence, the corresponding values of β, I_T,

and I_0 for the two prototypical circuits are also identical and calculated as

$\beta \approx 30.81$ μA□V², $I_T \approx 6.66$ μA, and $I_0 \approx 5.13$ μA

The DC bias current I_0 also falls into the acceptable boundary shown in Table 12. Hence, the simulated frequency response of the ninth-order LV SRD LPF is shown in Fig. 14. The simulated 3 dB frequency f_{3dB} approximates at 2.02 MHz and suffers from approximately 1.0% error of frequency response.

Table 12. The acceptable boundaries of C, W/L, and I_0 of the second-order LV low-pass section of SRD biquad and first-order LV SRD LPF.

| Type of filters	Prototypes	C	W/L		I_0
Second-order LV low-pass section of SRD biquad	Fig. 7	0.5 – 1.0 pF	10 μm/ 2 μm - 40 μm/ 2 μm for M_{81} - M_{84}		2 - 40 μA
First-order LV SRD LPF	Fig. 5	0.5 – 1.0 pF	10 μm/ 2 μm - 40 μm/ 2 μm for M_{76} - M_{77}		2 - 40 μA

Fig. 14. The simulated frequency response of the ninth-order LV SRD LPF.

Conclusion

Based on the MOSFET square law, a systematic synthesis method for high-order square-root domain filter with reduced voltage is presented in this paper. This work is based on the MOSFET square law. Emphases are given on synthesizing filters. The keys to this work are the constructive settings of DC components for input signals, the DC voltages of the state-space variables, and the DC bias current I_0. The proposed prototypical circuits of low-voltage square-root domain filters are able to overcome the possible inequality of DC level between the input and output node. It is a significant and necessary improvement for the convenient and reliability of high-order filter realization since the inequality of input and output node of DC voltage will induce the incomplete power propagation and seriously degrade the frequency response of the filter. Moreover, by means of adjusting the range of the DC bias current I_0 in the acceptable boundary, which may be established and attainable during the process of designing for the proposed prototypical circuits of SRD filters, it provides that the center frequency f_0 or 3 dB frequency f_{3dB} are not only attainable at megahertz frequencies but also tunable electronically. Simulations for the proposed high-order LV SRD filters, based on 0.25 μm CMOS process and operated with 1.5 V power supply voltage, were provided and discussed throughout this paper. Simulated results, which indicate that the average errors of frequency response are less than 1.0%, demonstrate the validity of the proposed synthetic technique and the high performances of the proposed prototypical circuits of LV SRD filters. Hence, the proposed synthetic technique provides an alternative for performing high-order square-root domain filter implemented by standard digital CMOS technology.

References

1. Adams RW. Filtering in the log-domain. 63rd AES Conf, New York, 1979, 1470.
2. Frey DR. Log-domain filtering: an approach to current-mode filtering. IEE Proc. Pt. G, 1993;140 (12):406-416.
3. Frey DR. Exponential state space filters: A generic current mode design strategy. IEEE Trans. Circuits Syst. I, 1996;43(1): 34-42.
4. Tsividis Y. Externally linear, time-invariant systems and their application to companding signal processors. IEEE Trans. Circuits Syst. II, 1997;44(2): 65–85.
5. Drakakis EM, Payne AJ, Toumazou C. Log-domain state-space: a systematic transistor-level approach for log-domain filtering. IEEE Trans. Circuits Syst. II, 1999;46(3):290-305.
6. Drakakis EM, Payne AJ, Toumazou C. Log-domain filters, translinear circuits and the Bernoulli cell. IEEE ISCAS, Hong Kong, 1997;1:501–504.
7. Drakakis EM, Payne AJ, Toumazou C. Log-domain filtering and Bernoulli cell. IEEE Trans. Circuits Syst. I, 1999;46(5):559-571.
8. Toumazou C, Ngarmnil J, Lande TS. Micropower log-domain filter for electronic cochlea. Electron. Lett, 1994; 30(10):1839–1841.
9. Germanovix W, O'neill G, Toumazou C, et al. Analogue micropowered log-domain tone controller for auditory prostheses. Electron. Lett,

1998;34(11):1051-1052.

10. Eskiyerli MH, Payne AJ, Toumazou C. State-space synthesis of biquads based on the MOSFET square law. IEEE Int. Symp. Circuits and Syst, 1996;1: 321-324.

11. Yu GJ, Liu BD, Hsu YC, *et al.* 'Design of log domain low-pass filters by MOSFET square law,' in Proc. The Second IEEE Asia Pacific Conf. on ASICs, 2000; 9-12.

12. Yu GJ, Huang CY, Chen JJ, *et al.* Design of Square-Root Domain Filters. Analog Integrated Circuits and Signal Processing, (Accepted), 2004.

13. Lopez-Martin AJ, Carlosena A. A 3.3V tunable current-mode square-root domain biquad. IEEE Int. Symp. On Circuits and Systems, 2000;5-8.

14. Eskiyerli MH, Payne AJ, Toumazou C. State-space synthesis of integrators based on the MOSFET square law. Electron. Lett, 1996;32(6):505-506.

15. Mulder J, van der Woerd AC, Serdijn WA, *et al.* Current-mode companding √x-domain integrator. Electronics Lett,1996;32(3):198-199.

16. Mulder J, van der Woerd AC, Serdijn WA, *et al.* A 3.3 V current-controlled √x-domain Oscillator. Analog Integrated Circuits and Signal Processing, 1998;16(1):17-28.

17. Eskiyerli MH, Payne AJ, Square-root domain filter design and performance. Analog Integrated Circuits and Signal Processing, 2000;22(2-3):231-243.

18. Lopez-Martin AJ, Carlosena A. Systematic design of companding systems by component substitution. Analog Integrated Circuits and Signal Processing, 2001;28(3):91-106.

19. Lopez-Martin AJ, Carlosena A. Current-Mode Multiplier-Divider Circuits Based on the MOS Translinear Principle. Analog Integrated Circuits and Signal Processing. 2001;28(3):265-278.

20. Steyaert M, Crols J, Gogaert S, *et al.* Low-voltage analog CMOS filter design. IEEE Int. Symp. On Circuits and Systems, ISCAS '93, 1993;2: 1447-1450.

21. Rajput SS, Jamuar SS. Low voltage, low power, high performance current mirror for portable analogue and mixed mode applications. IEE Proc. Circuits, Devices and Systems, 2001;148: 273-278.

22. Ramirez-Angulo J, Carvajal RG, Torralba A, *et al.* The flipped voltage follower: a useful cell for low-voltage low-power circuit design. IEEE Int. Symp. On Circuits and Systems, ISCAS 2002, 2002;3:615-618.

23. Mulder J, Van der Woerd AC, Serdijn WA, *et al.* High-swing cascode MOS current mirror. Electronics Lett, 1996;32(14):1251 – 1252.

24. Zeki A, Kuntman H. Accurate and high output impedance current mirror suitable for CMOS current output stages. Electronics Lett, 1997;33(12):1042-1043.

25. Blalock BJ, Allen PE, Rincon-Mora GA, Designing 1-V op amps using standard digital CMOS technology. IEEE Trans. Circuits and Systems II, 1998;45(7):769-780.

26. Heim P, Jabri MA. MOS cascode-mirror biasing circuit operating at any current level with minimal output saturation voltage. Electronics Lett, 1995;31(9):690 – 691.

27. Prodanov VI, Green MM. CMOS current mirrors with reduced input and output voltage requirements. Electronics Lett, 1996;32(2):104 – 105.

28. Itakura T, Czamul Z. High output-resistance CMOS current mirrors for low- voltage applications. IEICE Trans. 1997; E80-A(1):230-232.

29. Lopez-Martin AJ, Carlosena A. A 1.5 V CMOS square-root domain filter. IEEE Int. Conf. On Electronics, Circuits and Systems, 2001;1465-1468.

30. Lopez-Martin AJ, Carlosena A. A 1.5 V CMOS companding filter,' Electron. Lett, 2002;38(10): 1346-1348.

31. Yu GJ, Chen JJ, Lin HY, *et al.* A low-voltage low-power log-domain band-pass filter. IEEE Int. Symp. On VLSI Technology, Systems, and Applications, 2003;219-222.

32. Yu GJ, Huang CY, Chen JJ, *et al.* Design of Current-Mode Square-Root Domain Band-Pass Filter with Reduced Voltage. Analog Integrated Circuits and Signal Processing, (Accepted), 2004.

33. Chen CT. Linear system theory and design. (CBS College Publishing, Holt, Rinehart & Winston, New York, 1984).

34. Sinha NK. Control Systems. (CBS College Publishing, Holt, Rinehart & Winston, New York, 1986).

35. Nise NormanS. Control Systems Engineering. (John Wiley & Sons, Inc., New York, 2000).

Low Voltage Tunable Square-Root Domain Band-Pass Filter with Translinear Loop Technique in Biomedical Engineering

Gwo-Jeng Yu[1], Yu-Shian Lin[2]

[1]*Department of Computer Science and information Engineering, Cheng Shiu University Niaosong, Taiwan 833, R.O. China*

[2]*Department of Electronic Engineering, Cheng Shiu University, Niaosong, Taiwan 833, R.O. China.* gjyu@csu.edu.tw

Abstract

A low voltage square root domain filter based on the MOSFET square law is proposed in this thesis. Through HSPICE simulation, the extendibility and the reliability of the design procedure are verified. Furthermore, the supply voltage is successfully reduced down to 0.9V by the Flipped Voltage Follower (FVF) low-voltage technique without regarding the performance of the filters. The proposed filter structure has the merits of low-power voltage supply operation, high frequency operation, and the wide range of pole frequency tuning capability. The proposed circuit has been simulation with the TSMC 0.18 μm CMOS technology. The experimental results have demonstrated that the center frequency f0 of the band-pass filter can be electronically tunable in 774-914kHz with tunable bias-current, 1.78% total harmonic distortion (THD), and the power dissipation is less than 387μW at a 0.9V supply voltage. [Life Science Journal. 2010; 7(1): 30 – 33] (ISSN: 1097 – 8135).

1. Introduction

Recently, there is a growing interest in the field of translinear filters. Main advantages of regarding to these various filters are large dynamic range and low-voltage/low power operation capability. Since the voltage swings of internal capacitors are compressed, DC power supply voltage will be less restrictive to the maximum input signal. Initially, a subclass of translinear filters was the log-domain filters introduced by Adams[1]. On the other hand, a subclass of translinear filters, named "square-root domain filter" was introduced. Toumazou[2] proposed state-space synthesis of the second filter which was the first filter structure using the MOSFET square law. Although an alternative biasing of MOS translinear loops based on the application of the Flipped-Voltage Follower (*FVF*) was proposed[3-5], it allowed a significant reduction in the voltage supply requirements. In order to improve the problem of Germanovix'a [6] method, Psychalinos[7], Yu [8] and Lopez-Martin[9-10] also adopted MOSFETs operating in saturation region to implement the square-root domain filters.

In this paper, a square-root domain filter with voltage supply down to 0.9V has been proposed. The paper is organized as follows: In Section 2, the principle and architecture of the square-root domain filter using state-space approach are derived and explained. Then in Section 3, the most supply-voltage critical block, i.e. the square-root circuit, which performs the geometric-mean function, is proposed to operate at a supply as low as 0.9V. By using the proposed circuit implementation as well as the state-space approach, several filter prototypes are designed for the purpose of verification highlighted in Section 4. Finally, a brief conclusion is given at the end of this paper.

2. Principle and Architecture

The transfer function of a second-order band-pass filter can be expressed as

$$H(s) = \frac{(\omega_0)s}{s^2 + \left(\frac{\omega_0}{Q}\right)s + \omega_0^2} \tag{1}$$

By using the standard technique for deriving companion-form dynamical equations, Eq. (1) is realized with the system described by the following equations.

$$\begin{cases} \dot{x}_1 = -\omega_0 x_2 \\ \dot{x}_2 = \omega_0 x_1 - \left(\frac{\omega_0}{Q}\right)x_2 + \left(\frac{\omega_0}{Q}\right)u \\ y = x_2 \end{cases} \tag{2}$$

where x_1, x_2, y, and u are state variables, output and input signals, respectively. If the node voltages V_1 and V_2 are assumed to be the state variables, x_1 and x_2, and a voltage signal U denotes the input u, the Eq.(2) can be rewritten as

$$\begin{cases} C\dot{V}_1 = -C\omega_0 V_2 \\ C\dot{V}_2 = C\omega_0 V_1 - \left(\frac{C\omega_0}{Q}\right)V_2 + \left(\frac{C\omega_0}{Q}\right)U \\ y = V_2 \end{cases} \tag{3}$$

where C is a multiplicatioin factor. $C\dot{V}_1$ and $C\dot{V}_2$ in Eq.(3) can be regarded as the time-dependent current through the two capacitors C connected from V_1 to ground and from V_2 to ground, respectively.

The drain current of a MOSFET transistor operating in saturation can be expressed as

$$I_D = \frac{\mu_0 C_{ox} W}{2L}(V_{GS} - V_{th})^2 = \beta(V_{GS} - V_{th})^2 \tag{4}$$

where β, V_{GS} and V_{th} are the device trans-conductance parameter, the gate-to-source voltage and the threshold

voltage, respectively. Thus, the state-space equation becomes

$$\begin{cases} C\dot{V}_1 = -\sqrt{I_0 I_2} - I_T \\ C\dot{V}_2 = \sqrt{I_0 I_1} - \dfrac{\sqrt{I_0 I_2}}{Q} + \dfrac{\sqrt{I_0 I_U}}{Q} + I_T \\ y = V_2 \end{cases} \quad (5)$$

According to Eq. (4), and while supposing $Q=1$, the state equations in Eq. (3) can be written as

$$\begin{cases} C\dot{V}_1 = -\sqrt{I_0 I_2} - I_T \\ C\dot{V}_2 = \sqrt{I_0 I_1} - \sqrt{I_0 I_2} + \sqrt{I_0 I_U} + I_T \\ y = V_2 \end{cases} \quad (6)$$

where

$$\begin{cases} I_1 = \beta(V_1 - V_T)^2 \\ I_2 = \beta(V_2 - V_T)^2 \\ I_U = \beta(U - V_T)^2 \end{cases} \quad (7)$$

and

$$\omega_0 = \frac{\sqrt{\beta I_0}}{C} \quad (8)$$

$$I_0 = \frac{C^2 \omega_0^{\,2}}{\beta} \quad (9)$$

Note that ω_0 is inversely proportional to the capacitance C and is proportional to the square root of I_0; hence the cutoff frequency ω_0 is dominated by the capacitance C and I_0 is used to tune the cutoff frequency.

3. Circuit Implementation

3.1 Flipped-Voltage Follower Circuit

Fig. 1[3-5] shows a flipped voltage follower (*FVF*), which consists of a current source and two transistors. One transistor is cascaded with another. The current source supplies the drain current of M_1, and the voltage at the drain of M_1 connecting to the gate of M_2 can be expressed as
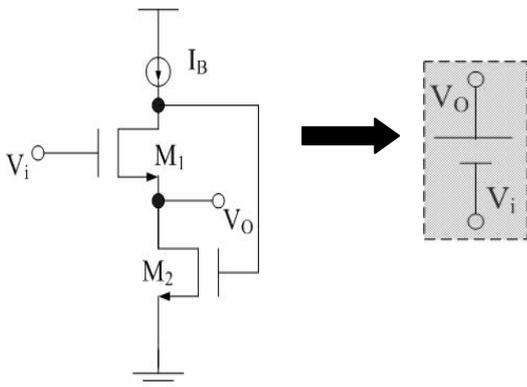
Fig.1. Current-mode Flipped-Voltage Follower (*FVF*) circuit

$$\begin{cases} V_{iO} = V_{GS1} + V_{th} \\ V_{GS1} = \sqrt{\dfrac{I_B}{\beta}} \end{cases} \quad (10)$$

3.2 Current-Mode Square-Root Circuit

The proposed current-mode square-root circuit is shown in Fig. 2 operates as follows: I_X and I_Y are input currents, and these currents generate the corresponding voltage, V_X and V_Y through the current to voltage conversion of diode-connected MOS. The matched transistors M_2-M_5 which are forced to operate in saturation region and the DC current sources, depicted as I_C altogether to construct a voltage-averaging circuit.
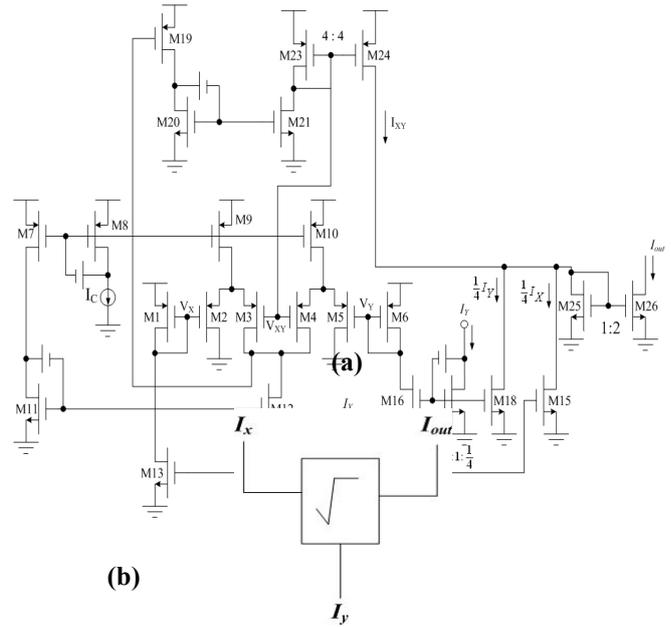
Fig. 2. Current-mode square-root circuit (a) Circuit diagram(b) Equivalent block diagram

The voltage averaging circuit produces a gate voltage V_{XY}, which is manipulated to be equal to the average of the gate voltage of M_1 and M_6 as $V_{XY} = (V_X+V_Y)/2$. The detailed operation of the averaging function circuit can be explained with a few simple steps. The well-known I-V relationship between the drain current and gate-source voltage for a MOS operating in saturation region can be formulated as the following equation:

$$I_D = \beta(V_{GS} - V_{th})^2 \quad (11)$$

We can easily find the following equation holds since $I_{D2}+I_{D3}=I_{D4}+I_{D5}=I_C$

$$I_{D2} = I_{D4} \quad (12)$$

Substitute Eq.(11) into Eq.(12) , the equation can be rewritten as

$$\beta(V_{S1} - V_X - V_{th})^2 = \beta(V_{S3} - V_{XY} - V_{th})^2 \quad (13)$$

From Eq.(13) we can derive the result :

$$V_{XY} = V_{S3} - V_{S1} + V_X \qquad (14)$$

with the similar manner, we can obtain the following result.

$$V_{XY} = V_{S1} - V_{S3} + V_Y \qquad (15)$$

According to Eq.(14) and Eq.(15), we can state the following Eq.(16).

$$V_{XY} = \frac{V_X + V_Y}{2} \qquad (16)$$

According to the translinear loop formed by transistors M_X, M_Y, and M_{XY}, it is realized under the assumption of $\beta_{M23} = \beta_{M24} = 4\beta$ and $\beta_{M1} = \beta_{M6} = \beta$ where β is the aspect ratio, and the following equation can be derived.

$$I_{XY} = I_X + I_Y + 2\sqrt{I_X I_Y} \qquad (17)$$

We narrow current I_X and I_Y by 1/4 times to give supply voltage of low power, so we can prove the following Eq.(17).

$$I_{XY} = \frac{1}{4} I_X + \frac{1}{4} I_Y + \frac{1}{2}\sqrt{I_X I_Y} \qquad (18)$$

Again by writing the KCL equation at output node of this circuit, the equation can be reduced to the follows:

$$I_{XY} = \frac{1}{2}\sqrt{I_X I_Y} \qquad (19)$$

Hence if the ratio of the output stage current mirror in Fig. 2 is set to be 1:2 the output current I_{out} can be derived as:

$$I_{out} = \sqrt{I_X I_Y} \qquad (20)$$

Fig. 3 shows a circuit diagram of the proposed band-pass filter. The band-pass is realized by using current mirrors, three current-mode square-root circuit blocks and two capacitors. V_2 is the desired output voltage and U is a DC biased input voltage.
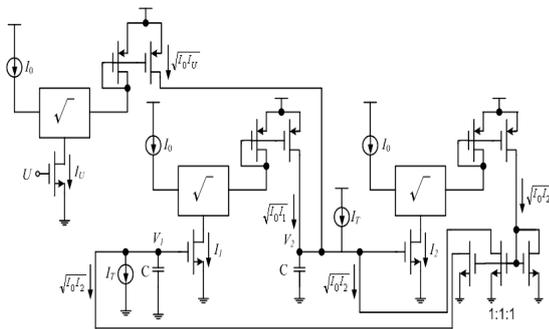
Fig. 3. Circuit diagram of the second-order band-pass filter

4. Simulation Results

Fig. 4 illustrates the simulated result of the current-mode square-root circuit while V_{DD} = 0.9V, I_X and I_Y are a triangular wave current with values between 20 to 30 μA and a 30 μA DC current, respectively.
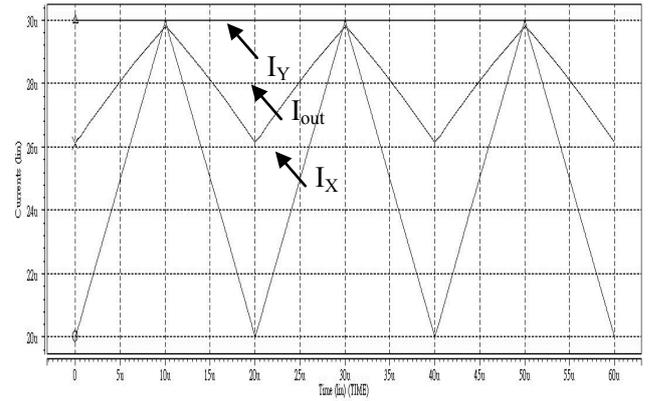
Fig. 4. Simulated result of the square-root circuit

The simulated frequency responses of the second-order band-pass filter with V_{DD} = 0.9V, C = 5 pf, Q = 1, I_0 is changed from 20 to 30 μA, shows the tunble center frequency f_0 of the band-pass filter from 776 to 914 kHz shown in Fig. 5.
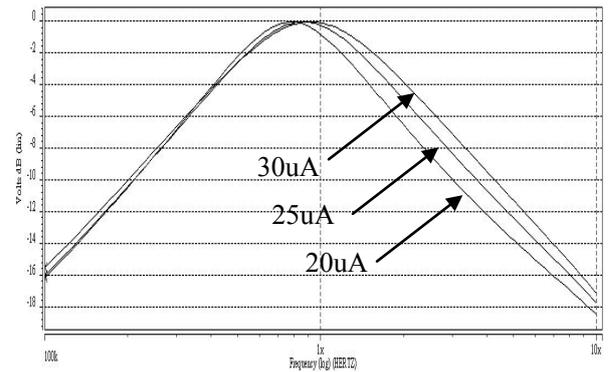
Fig. 5. Frequency response of the second-order band-pass filter

The total harmonic distortion (*THD*) with a 4MHz 100mV peak-to-peak sinusoid is 1.78%. The specifications of a second-order band-pass filter are summarized in Table 1.

Table 1. Specifications of the second-order band-pass filter

Parameters	Simulation conditions
Order of filter	2
Technology	TSMC 0.18μm
Power supply voltage	0.9V
Load capacitance	5 pf
I_0	20μa, 25μa, 30μa
Parameters	**Simulation results**
f_0 (I_0=20μa, 25μa, 30μa)	776kHz, 871kHz, 914kHz
Power dissipation (I_0=20μa, 25μa, 30μa)	387μW, 452μW, 487μW
THD (V_{PP}=0.1V) (I_0=20μa, 25μa, 30μa)	1.78%, 1.61%, 1.25%

32

5. Conclusion

In this paper, based on the MOSFET square law, a square-root domain band-pass filter with low voltage and low power operation is proposed. Operating at 0.9V power supply voltage, band-pass filter has been simulation in 0.18μm CMOS technology.

The proposed circuit, thus, has the advantages of high frequency operation, low supply voltage operation and low power consumption. Furthermore, implementation via standard digital CMOS technology for the proposed filter is feasible for system-on-a-chip (SOC) application.

References

1. RW Adams. Filtering in the log-domain. *AES Conj*, 1979, preprint 1470.
2. MH Eskiyerli, AJ Payne, C Toumazou. State-space synthesis of biquads based on the MOSFET square law. IEEE Int. Symp. Circuits and Syst, 1996;1:321–324.
3. Ramirez-Angulo I, Carvajal RG, Torralba A, *et al.* The flipped voltage follower: a useful cell for low-voltage low-power circuit design. lSCAS ,2002, Phoenix, AZ, pp. 111 615.618,
4. CA De La Cruz-Blas, AJ Lopex-Martin, A Carlosena. 1.5V tunable square-root Domain filter. *Electron. Lett*, 2004 ; 40.
5. J Ramirez-Angulo, S Gupta, RG. Carvajal, *et al.* New improved CMOS class AB buffers based on differential flipped voltage followers. *IEEE Int. Symp*. Circuits Syst., Kos, Greece, May 21–24, 2006; 3914-3917.
6. W Germanovix, G. O'Neill, C Toumazou, *et al.* Analogue micropowered log-domain tone controller for auditory prostheses. *Electron. Lett*, 1998; 34: 1051-1052.
7. C Psychalinos, S Blassis. A systematic design procedure for square-root-domain circuits based on the signal flow graph approach. *IEEE Trans. Circuits Syst. I*, 2002;49:1702-1712.
8. G. J Yu, BD Liu, YC Hsu, *et al.* Design of log domain low-pass filters by MOSFET square law. *In Proc. The Second IEEE Asia Pacific Conf. on ASICs*, 2000, pp. 9–12.
9. AJ Lopez-Martin, A Carlosena. A 1.5 V CMOS companding filter. *Electron Lett*, 2002; 38: 1346–1347.
10. AJ Lopez-Martin, A Carlosena. A 3.3V tunable current-mode square-root domain biquad. *In Proc. IEEE Int. Symp. Circuits and Syst.*,2000; 5:375–378.

The Effects of 17 -estradiol on Neuronal PC12 Cells Injuried by OGD-R and NO/iNOS System Mechanism

Yu Wang[1], ZhengTang[2], Xiufang Chen[3], Jing Zhang[4], Guanxun Zhang[5]

1 Department Of Neurosurgery Of the First People's Hospital Of Zhengzhou, Zhengzhou, Henan, China nice2836@sina.com; 2 Xinxiang Medical University, Xinxiang, Henan, China; 3 Modern Medical Research Institute Of Henans, Zhengzhou, Henan, China; 4 Zhengzhou Children's Hospital, Zhengzhou, Henan, China; 5 Emergency Center of Zhengzhou Xinzheng International Airport Management Co., Ltd., Xinzheng, Henan, China.

Abstract

Estrogen also plays an important role in normal development or differentiation of the brain. It's found recently that estrogen can not only affect reproductive activity through the regulation of serving Gn-RH inferior colliculus neurons, but also affect the other neurons of the brain in electrophysiology, neurological nutrition and metabolism. And, what concern most is the protection to central neuron of it. Through establishing the model of PC12 cells injuried by OGD-R, investigating the effect of Estrogen receptor antagonist ICI182780 Intervention on 17 -estradiol of PC12 cells injuried by OGD-R and ON/iNOS system. [Life Science Journal. 2010; 7(1): 34– 40] (ISSN: 1097 – 8135).

1. Objectives

Through establishing the model of PC12 cells injuried by OGD-R, investigating the effect of Estrogen receptor antagonist ICI182780 Intervention on 17 -estradiol of PC12 cells injuried by OGD-R and ON/iNOS system. For more, explore further the neuro-protective mechanism of 17 -estradiol on PC12 cells injuried by OGD-R, so as to provide the theoretical basis for clinical therapeutic application of 17 -estradiol in acute brain injuries induced by ischemia or reperfusion injury.

2. Methods

PC12 cells were cultured in DMEM medium, and then were induced to differentiate in DMEM medium containing 50ng/ml NGF for 5 days. These cells were named neuronal PC12 cells after exhibiting characteristic neuronal morphology. These neuronal PC12 cells which grew well and were well induced, and were dissected into suspension and then were inoculated on well plates with the cell concentration according to the necessity of different experiments. After induced to differentiate with NGF for 48 hours, they attached the wall and completely expanded. These cells were randomly divided into five groups Table 1 : the normal control group, the OGD-R group, the 17 -estradiol group, the ICI182780 Intervention group and the ICI182780 control group. PC12 cells in the normal group did not receive OGD-R and were cultured in DMEM medium recovered glucose as usual during oxygen-glucose deprivation and during reperfusion. While PC12 cells in OGD-R group were cultured in medium without glucose. Cells in 17 -estradiol group containing 10ng/ml 17 -estradiol and medium without glucose during OGD-R. The ICI182780 intervention group containing 10ng/ml 17 -estradiol and medium without glucose during OGD-R. adding 100ng/ml ICI182780. The ICI182780 control group was cultured in 100ng/ml ICI182780 DMEM without glucose. Then were put into the chamber in which oxygen was driven off, after receiving oxygen-glucose deprivation for 30 minutes, PC12 cells in the groups were taken out and were changed into medium with glucose, 10ng/ml 17 -estradiol and medium with glucose, 10ng/ml 17 -estradiol and 100ng/ml ICI182780 DMEM with glucose and 100ng/ml ICI182780 DMEM with glucose respectively. They were put back to cells culture incubator and cultured successively during reperfusion. Cellular morphological changes were observed after oxygen-glucose deprivation.

The viability of cells and the concentration of NO in the culture medium were measured at each time point of 2h, 4h, 8h, 16h, and 24h after reperfusion. Cell apoptosis and cell death were detected with flow cytometry 24 hours after oxygen-glucose deprivation. The expression level of iNOS and protein were examined by Western Blotting 24 hours after oxygen-glucose deprivation. The expression level of iNOS mRNA and protein were examined by RT-PCR analysis 24 hours after oxygen-glucose deprivation.

Table 1:   group experiments and the experimental process

groups	period of oxygen-glucose deprivation 30min	period of reperfusion
normal control group	were cultured in DMEM medium and did not receive OGD-R in the chamber	were cultured in DMEM medium
OGD-R group	were cultured in medium without glucose and receive OGD-R in the chamber	were cultured in DMEM medium
17 -estradiol group	containing 10ng/ml 17 -estradiol and medium without glucose during OGD-R in the chamber	10ng/ml 17 -estradiol and medium with glucose
ICI182780 Intervention group	containing 10ng/ml 17 -estradiol and medium without glucose during OGD-R, adding 100ng/ml ICI182780	10ng/ml 17 -estradiol and 100ng/ml ICI182780 DMEM with glucose
ICI182780 control group	were cultured in 100ng/ml ICI182780 DMEM without glucose	100ng/ml ICI182780 DMEM with glucose and receive OGD-R in the chamber

3. Results

(1) The morphological observation of PC12 cells after oxygen- glucose deprivation for 30 minutes

The PC12 cells in normal control group grew well as usual Figure 1 . After oxygen-glucose deprivation for 30 minutes, the PC12 cells in OGD-R group   Figure 2 and the ICI182780 control group   Figure 5   became round because of serious edema and their prominence completely disappeared.
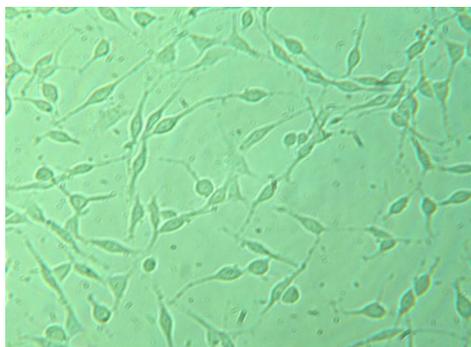
The PC12 cells in 17 -E$_2$ group   Figure 3   reserved the neuron-like characteristics, but the cell body of them had slighter edema and their prominence became thinner and shorter. the PC12 cells in the ICI182780 Intervention group Figure 4   seem similar with that in 17 -E$_2$ group. The PC12 cells in five different groups had a very different appearance.
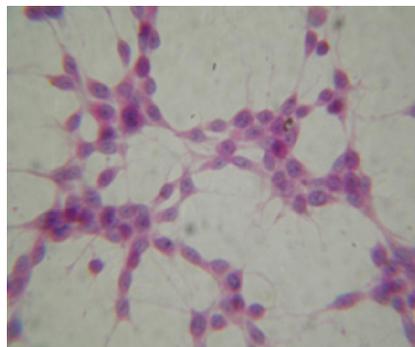
Figure 1: The characteristics of PC12 cells in normal control group are very similar to these of neurons. The right figure is HE staining. (Observed under the microscope 10×40)
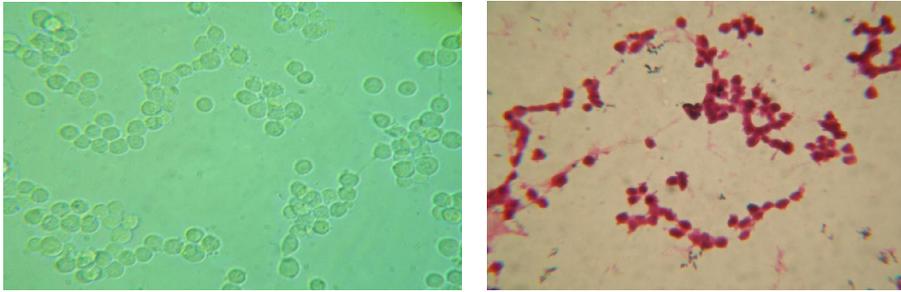
Figure 2: After oxygen-glucose deprivation for 30 minutes, the PC12 cells in OGD-R group became round because of serious edema and their prominence completely disappeared. They group gathered. The right figure is HE staining. (Observed under the microscope 10×40)
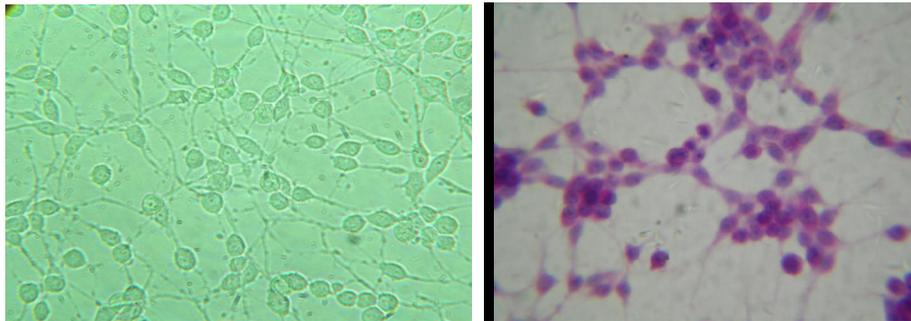
Figure 3: After oxygen-glucose deprivation for 30 minutes, most PC12 cells in 17 -E$_2$ group retained the spindle-shaped cells, but the cell body of them had slighter edema and their prominence became thinner and shorter. Small number of cells became round and their prominence disappeared; the group gathered is not obvious. The right figure is HE staining. (Observed under the microscope 10×40)
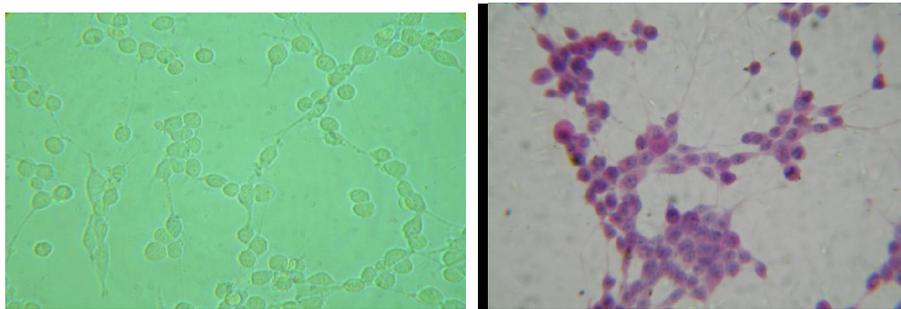
Figure 4: After oxygen-glucose deprivation for 30 minutes, most PC12 cells in the ICI182780 Intervention group retained the spindle-shaped cells, but the cell body of them had slighter edema and their prominence became thinner and shorter. Small number of cells became round and their prominence disappeared, the group gathered is not obvious. A small number of cells floated. The right figure is HE staining. (Observed under the microscope 10×40)
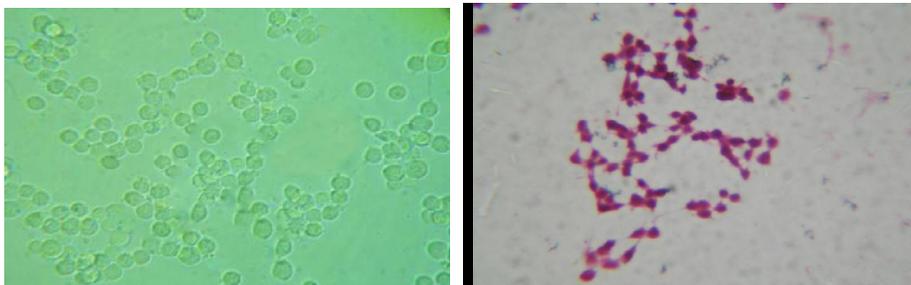
Figure 5: After oxygen-glucose deprivation for 30 minutes, the PC12 cells in the ICI182780 control group became round because of serious edema and their prominence completely disappeared. They group gathered. Their characteristics are very similar to these of OGD-R group. The right figure is HE staining. (Observed under the microscope 10×40)

(2) The determination of NO in cell medium

The concentration of NO in cell medium was measured respectively at each time point of 2h, 4h, 8h, 16h, and 24h after reperfusion. At each time point, the concentration of NO was highest in OGD-R group or Fulvestrant control group, and lowest in normal control group, and the concentration of NO in 17 -E$_2$ group and ICI182780 Intervention group was between the two. The differences among five groups were obvious ($P<0.01$). Along with the reperfusion time, the differences of the concentration of NO among five groups changed more significantly.   Table 2

Table 2: The concentration of NO in cell medium of every group in each time ($\bar{x} \pm s$)

groups	n	The concentration of NO μM				
		2h	4h	8h	16h	24h
the normal control group	6	0.566±0.212	0.605±0.178	0.606±0.178	0.645±0.122	0.685±0.130
OGD-R group	6	1.830±0.415	2.027±0.277	2.146±0.193	2.303±0.245	2.422±0.178
17 -E$_2$ group	6	1.080±0.178	1.159±0.130	1.238±0.178	1.356±0.245	1.435±0.193
the ICI182780 Intervention group	6	1.372±0.156	1.405±0186	1.532±0.179	1.631±0.185	1.746±0.253
the ICI182780 control group	6	1.790±0.451	1.998±0.321	2.120±0.213	2.259±0.241	2.389±0.117

Annotate: Compare with the normal control group, $P<0.01$ compare with OGD-R group $P<0.01$ compare with the ICI182780 control group, $P<0.01$.

(3) Detecting the expression of iNOS protein in neuronal PC12 cells after 24 hours of reperfusion

The iNOS protein in the cytoplasm of PC12 cells after 24 hours of reperfusion was showed by Western Blotting method, and then was measured by computer picture analysis software. The expression of iNOS protein was lowest in normal control group and highest in OGD-R group and ICI182780 control group, but the expression of iNOS protein in 17 -E$_2$ group and ICI182780 Intervention group was between the two Figure6.7 . The differences of the expression of iNOS protein among five groups were obvious ($P<0.05$) Table 3 .
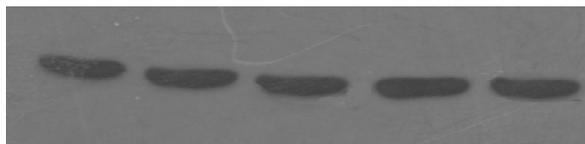
Figure 6
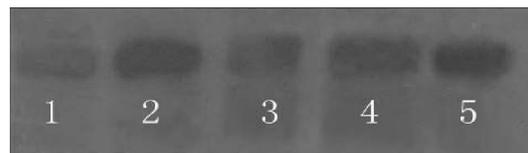
Figure 7

Figure 6: After oxygen-glucose deprivation for 30 minutes and after 24 hours of reperfusion, the expression of protein. (-action). Figure 7: After oxygen- glucose deprivation for 30 minutes and after 24 hours of reperfusion, the expression of iNOS protein in five groups. In the figure, 1 is for the normal control group, 2 is for the OGD-R group, 3 is for the 17 -estradiol group, 4 is for the ICI182780 Intervention group, 5 is for the ICI182780 control group.

Table 3: Comparison of iNOS protein gray level ($\bar{x} \pm s$)

groups	n	iNOS
normal control group	3	0.31±0.01
OGD-R group	3	0.62±0.01
17 -E$_2$ group	3	0.45±0.02
the ICI182780 Intervention group	3	0.39±0.01
the ICI182780 control group	3	0.61±0.02

Annotate: Compare with the normal control group, *P*<0.05; compare with OGD-R group *P*<0.01; compare with the ICI182780 control group, *P*<0.01.

(4) The expression of iNOS mRNA examined by RT-PCR after 24 hours of reperfusion. Figure 8, 9 The level of iNOS mRNA was expressed as ratio expression rate of iNOS gene/ -actin according to RT-PCR. The level of iNOS gene expression was 0.640±0.028 in normal control group, 1.322±0.094 in OGD-R group, 1.361±0.065 in ICI182780 control group, 0.772±0.032 in 17 -E$_2$ group and 0.764±0.0453 in ICI182780 Intervention group. The expression of iNOS mRNA was different among five groups (*P*<0.05). The difference between OGD-R group and normal control group was more significant (*P*<0.01) Table 4 .
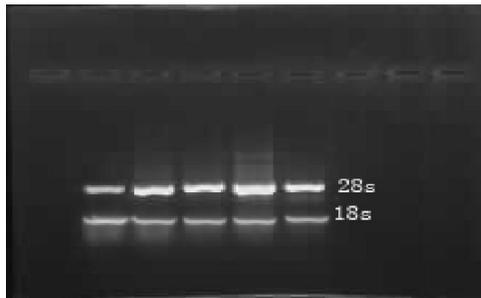
Figure 8
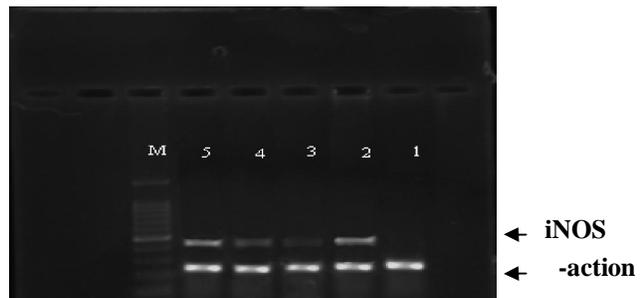
Figure 9

Figure 8: The expression of iNOS mRNA examined by RT-PCR after 24 hours of reperfusion. Figure 9: **A**fter oxygen-glucose deprivation for 30 minutes and after 24 hours of reperfusion, the expression of iNOS mRNA in five groups. In the figure, M is for mark, 1 is for the normal control group, 2 is for the OGD-R group, 3 is for the 17 -estradiol group, 4 is for the ICI182780 Intervention group, 5 is for the ICI182780 control group.

Table 4: Comparison of iNOS mRNA gray level ($\bar{x} \pm s$)

groups	n	iNOS mRNA
the normal control group	3	0.630±0.028
the OGD-R group	3	1.342±0.094
the 17 -estradiol group	3	0.772±0.032
the ICI182780 Intervention group	3	0.869±0.029
the ICI182780 control group	3	1.361±0.065

Annotate: Compare with the normal control group, *P*<0.05 compare with the OGD-R group, *P*<0.01 compare with the ICI182780 control group, *P*<0.01.

4. Discussions and Conclusions

In the experiment, oxygen glucose deprivation and reperfusion injury of PC12 cells model is more realistic than a simple lack of oxygen, or lack of sugar, and even oxygen-glucose deprivation period of application of sugar-free Earle's solution in the simulation of cerebral ischemia-reperfusion in which nerve cells ischemic perfusion environment [1]. After numerous pre-tests we found that the model repeatability and stability. It can meet the needs of this experiment [2]. Through inhibiting NO / iNOS system, 17 -estradiol can reduce the injury of PC12 cells in oxygen-glucose deprivation and reperfusion, also, it reduce their early apoptosis as a neuroprotective role [3]. However, the exact mechanism of action and role of the target is not clear [4]. In order to further understand the mechanism of estrogen action, we introduced estrogen receptor (ER) of the specific antagonist ICI182780 (Faslodex) [5] to interfere in the 17 -estradiol treatment, with its observation of the object as a control study was to investigate estrogen receptor ER [6, 7], in the cerebral protective effect of estrogen in the meaning. In this experiment, five groups, in the oxygen-glucose deprivation and reperfusion 2h, 4h, 8h, 16h, 24h of each time point. We found NO concentration in the supernatant of the cells in the experimental group; the cell activity was reduced reverse. We can see that high concentrations of NO have obvious cytotoxicity[8]. So NO / iNOS system activation may lead to oxygen-glucose deprivation-reperfusion injury in PC12 nerve cell injury and early apoptosis [9, 10]. It's one of the important reasons [11, 12]. Detection of RNA and protein expression levels of the test results also prompted that iNOS gene and protein expression have a consistency in all experimental groups[3], and directly related to the measured NO concentrations; compared with the normal group, the iNOS gene and protein expression of PC12 cells in the 24h oxygen-glucose deprivation-reperfusion model group is the highest. The cell activity in microscopic observation is the worst. ICI182780 followed by the group below. While the iNOS gene and protein expression of estrogen-treated PC12 cells is the lowest, activity of microscopic cells is the closest to the

normal group. The ICI182780 Intervention group is between model group and treatment group. So we can see through inhibiting NO / iNOS system, 17 -estradiol can reduce the injury of PC12 cells in oxygen-glucose deprivation and reperfusion, and reduce their early apoptosis as a neuroprotective role [13]. In this experiment, the iNOS gene, protein expression, NO concentration and cell activity observations of PC12 cells have shown that the ICI182780 intervention groups still have a certain protection to PC12 cells on oxygen-glucose deprivation and reperfusion [14]. Using enough high-purity of estrogen receptor antagonist can not make an effective rivalry to the protection of estrogen. So, we speculate that the neuroprotective effect of estrogen is multipath. We point out it may play a neuroprotective effect through means other than its receptor [15].

This experiment was successfully prepared by oxygen-glucose deprivation-reperfusion injury model PC12 cells, the application interfere with estrogen receptor antagonist[16.17], estrogen treatment, compared to observe the protective effect of estrogen, and further explored 17 -estradiol on the oxygen-glucose deprivation and then reperfusion injury in PC12 cells[18.19], and NO / iNOS system, the impact mechanism, draw the following conclusions:

(1) High concentrations of NO has a strong cytotoxic, NO / iNOS system activation is the important cause of PC12 cells injuried by OGD-R.

(2) 17 -E2 can effectivly inhibit NO/iNOS system from activating and performing in PC12 cells of OGD-R. It can relieve cell edema, preserve cell morphous and enhance cell activity.

(3) Estrogen receptor antagonist ICI182780 could not effectively block the 17 -estradiol inhibited NO / iNOS system in neuroprotection.

(4) The protective effects of estrogen are probably many ways, and 17 -E_2 can exert neuroprotective effects and relieve injuries on neuronal PC12 cells injuried by OGD-R through other means other than receptor.

References

[1] Plaschke K, Yun SW, Martin E, *et al*. Linear

relation between cerebral phosphocreatine concentration and memory capacities during permanentbrain vesselocclusions in rats [J]. Ann N Y Acad Sci. 2000; 903:299-306.

[2] Al-Abdulla NA, Martin LJ. Apoptosis of retrogradely degenerating neurons occurs in association with the accumulation of perikaryal mito-chondria and oxidative damage to the nucleus [J]. American Journal of Pathology. 1998; 153:447-456.

[3] Neil Howell; James Dykens; Walter H Moos. Estrogens and Neuroprotection: Desperate Housewives, Lost, and Survivor [J]. Drug Development Research, 2005, 66(2):51-52.

[4] Mattson MP. Presenilin-1 mutation increases neuronal vulnerability to focal ischemia in vivo and to hypoxia and glocuse deprivation in cell culture: involvement of perturbed calcium homeostasis [J]. The Journal of Neuroscience, 2000, 20: 1358.

[5] Varshochi R, Halim F, Sunters A, et al. ICI182,780 induces P21 waf 1 gene transcription through realeasing histone deacytylase1 and Eralpha from SP1 sites to induce cell cycle areest in MCF-7 breast cancer cellline [J].JBiolChem, 2005, 280(5): 3185-3196.

[6] Shughrue P J, Merchenthaler I. Estrogen is more than just a "sex hormone": novel sites for estrogen action in the hippocam-pus and cerebral cortex [J]. Front Neuroendocrinol, 2000; 21(1):95-101.

[7] Osuka K, Feustel PJ, Mongin AA, Tranmer BI, Kimelberg HK. Tamoxifen inhibits nitrotyrosine formation after reversiblemiddle cerebral artery occlusion in the rat [J]. J Neurochem, 2001; 76(6):1842-50.

[8] Dawson VL, Dawson TM, Bartley DA, et al. Mechanisms of nitric oxide- mediated neurotoxicity in primary brain cultures [J]. J Neurosci, 1993, 13(6): 2651-2661.

[9] Iadecola C, Zhang F, Casey R, et al. Inducible nitric oxide synthase gene expression in vascular cells after transient focal cerebral ischemia[J]. Stroke, 1996, 27(8):1373-1380.

[10] Ikeno S, Nagata N, Yoshida S, et al. Immature brain injury via peroxynitrite production induced by inducible nitric oxide synthase after hypoxia-ischemia in rats[J]. J Obstet Gynaecol Res, 2000, 26(3):227-234.

[11] Jiang H, Koubi D, Zhang L, et al. Inhibitors of iNOS protect PC12 cells against the apoptosis induced by oxygen and glucose deprivation [J]. Neurosci Lett, 2005, 375(1):59-63.

[12] Tehranian R, Rose ME, Vagni V, et al. Disruption of baxprotein prevents neuronal cell death but produces cognitive impairment in mice following traumatic brain injury [J].J Neurotrauma, 2008, 25(7):755-767.

[13] Chen Z, Yuhanna IS, Galcheva-Gargova Z, et al. Estrogen receptor alpha mediates the nongenomic activation of endothelial nitric oxide synthase by estrogen [J]. J Clin Invest, 1999, 103(3):401-406.

[14] Liaudet L, Soriano FG, Szabo C. Biology of nitric oxide signaling [J]. Crit Care Med, 2000, 28(Suppl 4):37-52.

[15] Toran-Allerand CD, Guan X, MacLusky NJ, et al. ER-X: a novel, plasma membrane-associated, putative estrogen receptor that is regulated during development and after ischemic brain injury [J]. J Neurosci, 2002, 22(19): 8391-8401.

[16] Kim HP, Lee JY, Jeong JK, et al. Nongenomic stimulation of nitric oxide release by estrogen is mediated by estrogen receptor alpha localized in caveolae[J]. Biochem Biophys Res Commun, 1999, 263(1):257-262.

[17] Hurn PD, Macrae IM. Estrogen as a neuroprotectant in stroke [J]. J Cereb Blood Flow Metab, 2000, 20(4):631-652.

[18] McCullough LD, Alkayed NJ, Traystman RJ, et al. Postischemic estrogen reduces hypoperfusion and secondary ischemia after experimental stroke [J]. Stroke, 2001, 32(3):796-802.

[19] Shafer TJ, Atchison WD. Transmitter, ion channel and receptor properties of pheochromocytoma (PC12) cells: a model for neurotoxicological studies [J]. Neurotoxicology, 1991, 12(3):473-492.

The agkistrodon acutus venom componets of X in vitro anti-tumor effect and mechanism

Zhaoxia Pang; Wenqing Lu; Ruiren Zhai

Tongji Medical College, Huazhong University of Science and Technology School of Public Health, Department of Occupational and Environmental Health, Wuhan, Hebei, China
zgy@zzu.edu.cn; Received Oct, 20, 2009

Abstract

Objective To observe the agkistrodon acutus venom componets of X(FX) on human colonic adenocarcinoma cell HCT-8 inhibition and to explore its mechanism. **Method**: From the cells, protein and gene of the three levels of the agkistrodon acutus venom componets of X(FX) of HCT-8 cell inhibition and to explore its anti-tumor. mechanism. Using colony formation assay detection of the agkistrodon acutus venom components of X of HCT-8 cell proliferation effect, using RT-PCR detection of apoptosis-related genes Caspase, survivin, Bax, bcl-2mRNA level changes, using flow cytometry FX After the effects of different time, HCT-8 cells, Caspase-3 protein and Survivin protein expression. **Results**: FX on the HCT-8 cells significantly inhibited the proliferation, FX up-regulated caspase-3, reduced survivin, Bax, bcl-2mRNA gene expression, FX acting on the HCT-8 cells, Caspase-3 protein expression increased and then gradually decreased to below normal, Survivin protein in the role of PF-II expression after 6-48 h sustained reductions in. **Conclusion** The agkistrodon acutus venom components of X can be raised to promote apoptosis-related genes, down-induced apoptosis genes inhibited apoptosis in HCT-8. [Life Science Journal. 2010; 7(1): 41 – 45] (ISSN: 1097 – 8135).

Key words: apoptosis; gene; the agkistrodon acutus venom; anti-tumor

Anti-tumor effect of snake venom has gradually been recognized and applied, however anti-tumor mechanism of snake venom is not yet clear. We extracted from the agkistrodon acutus venom anti-tumor componets and to research its anti-tumor mechanism.

1. Materials and methods:

Main materials: The agkistrodon acutus venom componets of X(FX),in our laboratory using monoclonal antibody technology extraction, Purity of more than 95%; HCT-8 cells, this experiment preservation; Caspase3 McAb polyclonal antibodies, rabbit anti-human survivin monoclonal antibody (Santa Cruz, USA), RNA inhibitor (Promega, USA), RNA enzymes (Sigma, USA).

Methods:

1.2.1 Colony formation assay

Logarithmic growth phase of the HCT-8 tumor cells, With 0.25% trypsin digestion,.and made into single cell suspension count, transfer cell concentration of $3 \times 103/ml$, were inoculated on 24-well plate (3×102 / hole), cells cultured 16 h to be fully adherent to join after the snake venom and its components X, to continue to develop 72 h, supernatant was washed two times with culture medium, to continue to foster exchange of fresh culture medium 7 ~ 14 d. Methanol at room temperature a fixed 15 min, Giemsa stain at room temperature 30 min, tap water wash away the residual dye liquor, counting colonies (including more than 50 cells, namely, diameter 0.5 mm of the cell colony) number, and calculate the average colony number of each group.

1.2.2 Determination of apoptosis-related genes

(1) primer design

According to four kinds of gene mRNA sequences, are designed for caspase-3, bcl-2, GAPDH, Bax, and survivin, PCR primers (designed by Shanghai Bio-engineering and synthetic.)

caspase-3 primers
Forward 5' TTT TTC AGA GGG GAT CGT TG 3 '
Backward 5' GCC TCC ACT GGT ATT TTA TG 3'
bel-2 primers
Forward5'CCA GAT CCC AGA GTT TGA GC 3'
Backward 5'ATG ATG GCT GCT GCT GGT TG 3' 29
GAPDH primers
Forward5'TAT TGG GCG CCT GGT CAC CA 3'
Backward 5' CCA CCT TCT TGA TGT CAT CA 3'
Bax primers
Forward5' TTT GCT TCA GGG TTT CAT CC 3'
Backward 5' CAG TTG AAG TTG CCG TCA GA 3'
survivin primers
Forward5' GGA CCA CCG CAT CTC TAC AT 3'
Backward 5' GAC AGA AAG GAA AGC GCA AC 3'

(2) Tumor cell total RNA extraction and quantification

(a) Equipment ready: Plastic equipment with 1% DEPC distilled water soak1-2 h after the high-pressure sterilization, back to dry, Glass equipment at 180   high temperature dry roasted 5 hours standby

(b) Cell preparation: Logarithmic growth phase HCT-8 cells, with 0.25% trypsin digestion, made into single cell suspension counted, transfer cell concentration of $1 \times 106/ml$, inoculated 6-well plate (5×105 / hole), cultured 16 h to be fully adherent cells , 400μg/ml of each hole to join the PF-II, final volume of 1.5 ml, 0,2,6,12,24 and 48 h post-training,Cells were collected, respectively, using Trizol kit from the total RNA, reverse transcriptase synthesized DNA, synthesized by the PCR double-stranded DNA, while synthesis of mouse glyceraldehyde 3 phosphate dehydrogenase (GAPDH) as internal reference.

(c) Trizol extraction of total cellular RNA: the collection of cells, transferred to 1.5 ml eppendorf tube, add 800μl Trizol, a gun repeatedly pumping blending, at room temperature 5 min, by adding 200μl chloroform volatility in 30 sec, room temperature for 3 min,12,000 rpm centrifugation at room temperature 5 min, the supernatant absorption to another 1.5 ml eppendorf tube, add an equal volume of isopropyl alcohol mixing at room temperature 30min, centrifuged 12,000 rpm at room temperature 5 min,supernatant was washed with 70% ethanol twice, centrifuged 12,000 rpm at room temperature 2 min, discard supernatant, vacuum drying, precipitation dissolved in 50μl DEPC water.

(d) RNA Quantitative: Lessons 2μl RNA, 50-fold diluted by UV spectrophotometer OD260 and OD260/OD280 value, OD260/OD280 value between 1.8 to 2.0, indicating RNA of high purity, this time, 1 OD is equivalent to 50μg/ml double-stranded DNA , 40μg/ml single-stranded DNA or RNA. RNA concentration determined by the formula: Concentration (μg / ml) = OD260 × dilution factor × 40, quantitative after -70   to save.

(3) RT-PCR method

2μg RNA,1μl RNase inhibitor(20 units/μl),3μl 25 pmol/L Oligo dT,2μl 10 mmol/L dNTP,4μl 25 mmol/L Mg2+,0.5μl AMV(10 units/μl), Oligo dT, 2μl 10 mmol / L dNTP, 4μl 25 mmol / L Mg2 +, 0.5μl AMV (10 units / μl), 42   , 60 min after 95   , 5 min inactivation of reverse transcriptase enzymes and destruction of mRNA-DNA hybrids, ice bath 5 min after PCR amplification. PCR reaction system containing both ends of each primer, 25 pmol, reverse transcriptase product of 5μl, Taq enzyme 1μl (5unit/μl). Reaction conditions: 94   1 min, 57   1 min, 72   90 sec, 35 cycles after the end of the last cycle, 72   extension of 10 min, 1% agarose gel electrophoresis, PCR analysis of the results of UV lamp.

(4)Agarose gel electrophoresis and gray-scale analysis

With 0.5 × TBE running buffer (0.045 mol/LTris-boric acid, 0.001 mol / LEDTA) with 0.8 ~ 1.2% (W / V) agarose gel electrophoresis, liquid, heated to agarose completely dissolved, add EB (10 mg / ml) to a final concentration of 0.5μg/ml; sealing a good adhesive, after mixing into the mold, insert the appropriate comb, comb of about 1.0 mm from the floor until the glue completely solidified, crefully remove the comb, the gel into the electrophoresis containing 0.5 × TBE electrophoresis buffer tank,take apropriate sample and a proper volume of loading buffer (0.25% bromophenol blue, 0.25% xylene blue FF, 40% sucrose) blending, mcro-plus with the comb-like device added to the hole to 5 V / cm voltage electrophoresis, when the electrophoresis to the appropriate location, in the long-wave UV lamp observations and photographed.After the photographed analyzed with the purpose of image analysis of the gray zone and GAPDH, and calculate the ratio between the two.

1.2.3 FCM detection of Survivin and Caspase-3 protein expression

(1) cell culture

Logarithmic phase were collected from HCT-8 cells were treated with 0.25% trypsin digestion made into single cell suspension, counting, transfer cell concentration of 1×106/ml, were inoculated on 6-well plate (5×105 / hole),cells cultured 16 h to be fully adherent, each hole by adding 400μg/ml of the PF-II, final volume of 1.5 ml, cultured 0,6,12,24 and 48 h respectively after the cells were collected, fixed in 70% cold ethanol, and placing -20   preservation within a week with the FCM assay.

(2) monoclonal antibody

Washing the cells with PBS twice, plus an anti-(rabbit anti-Caspase-3, Santa Cruz Company, USA) 3150μl (1:50 dilution) at 4   for the role of 45 min,plus serum (1:20 dilution) 50μl closed 30 min, PBS washed cells twice, plus wo anti-(FITC tag goat anti-rabbit IgG, Santa Cruz Company, USA) 50μl (1:100 dilution) at 4   for the role of 45 min, PBS washed cells twice.

(3) protein expression detected by flow cytometry

Add 300μl PBS, protein expression detected by flow cytometry, 104 cells per sample collected, Cellquest software analysis. Results The positive cells expressed as a percentage.

1.2.4 Statistical Methods

Two samples were used to compare the number of Student's t test.

2 Results

2.1The agkistrodon acutus venom componets of X on cell HCT-8 colony formation.

Test results showed that when the concentration of 400μg/ml, 800μg/ml, when, FX process after 72 h, HCT-8 cells, the number of colony formation were significantly reduced compared with control group were significantly different (respectively P <0.01). Showed that snake venom and its components on the HCT-8 colon adenocarcinoma cells significantly inhibited the proliferation. The results shown in Table 1 and Figure 1.

2.2 The snake venom component X on the HCT-8 cells, apoptosis-related genes.

Using RT-PCR detection of mRNA level changes. The results showed that, FX process after 2 ~ 12h, HCT-8 cells, caspase-3 mRNA on average higher than that of water. The results in Table 2.

Table 1. Effect of snake venom and traction X on colony formation of HCT-8 cells

| Group	Concentration ()	Number of colonies	Rate of colony formation (%)
Control	0	199±7.35	100
SV	400	173±6.98	86.9
Fraction X	400	132±9.83**	66.3
Control	0	197±6.91	100
SV	800	196±7.24	99.5
Fraction X	800	69±6.47**	35.3

**P<0.01, vs control
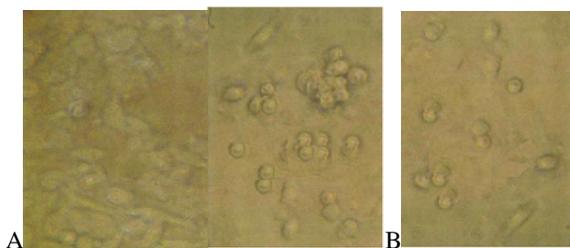
Figure 1. Venom X-component of the HCT-8 cell line A as the control group, B is 400ug/ml, C for 800ug/ml (× 40)

Table 2. Changes in Caspase-3 mRNA level of HCT-8 cells at different time points after treatment with 400μg/ml FX

Time(h)	Ratio%
0	0.93±0.02
2	1.27±0.01
6	1.11±0.04
12	1.08±0.02

2.2.2 snake venom components FX pairs of HCT-8 cells, Bax mRNA levels in

Using RT-PCR detection of mRNA level changes. The results showed that, PF-II process after 2 ~ 24h, HCT-8 Cells, Bax mRNA levels decreasing. The results in Table 3.

2.2.3 snake venom components FX pairs of HCT-8 cells, bcl-2 mRNA expression in

Using RT-PCR detection of mRNA level changes. The results showed that, FX process after 2h, HCT-8 cells, bcl-2 mRNA levels began to decrease, the role of post-24h, bcl-2 mRNA levels reduced to minimum. The results in Table 4.

2.2.4 snake venom components FX pairs of HCT-8 cells, expression of survivin mRNA

Using RT-PCR detection of mRNA level changes. The results showed that, FX process after 2 ~ 24h, HCT-8 cells, survivin mRNA were lower than the control group. The results in Table 5.

Table 3. Changes in Bax mRNA level of HCT-8 cells at different time points after treatment with 400μg/ml FX

Time(h)	Ratio%
0	0.94±0.04
2	0.73±0.04
6	0.92±0.04
12	0.58±0.02
24	0.78±0.04

Table 4. Changes in bcl-2 mRNA level of HCT-8 cells at different time points after treatment with 400μg/ml FX

Time(h)	Ratio%
0	1.635±0.055
2	1.290±0.030
6	1.120±0.060
12	1.005±0.025
24	0.840±0.050

Table 5. Changes in survivin mRNA level of HCT-8 cells at different time points after treatment with 400μg/ml FX

Time(h)	Ratio%
0	1.31±0.03
2	1.09±0.04
6	1.07±0.03
12	0.96±0.02
24	1.17±0.04

Table 6. Changes in Caspase-3 protein expression of HCT-8 cells after treatment with 400μg/ml FX

Time (h)	Percentage of positive cells (%)
0	37.29±7.00
6	42.45±6.54
12	20.76±2.43*
24	15.58±1.24**
48	6.09±0.6*

2.3.Apoptosis-related changes in protein expression
2.3.1 snake venom components FX pairs of HCT-8 cells, Caspase-3 protein expression

FX effect detected by flow cytometry at different times after, HCT-8 cells, Caspase-3 protein expression changes. The results show that, FX process after 6 h, HCT-8 cells, Caspase-3 protein expression increased and then gradually decreased to below normal levels. The results in table 6.

2.3.2 snake venom components FX pairs of HCT-8 cells, Survivin protein expression

FX effect detected by flow cytometry at different times after, HCT-8 cells of Survivin protein. The results show that, FX process after 6 h, HCT-8 cells, Survivin protein expression began to decrease continued lower (P <0.05), 48 h to a minimum value (P <0.01). The results in Table 7.

Table 7. Changes in Survivin protein expression of HCT-8 cells at differ points after treatment with 400μg/ml FX

Time(h)	Percentage of positive cells (%)
0	42.20±3.99
6	31.74±5.75
12	34.53±2.85
24	27.17±6.99*
48	12.29±1.43**

*P<0.05,**P<0.01 vs 0 h

3. Discussion

Venom from the snake's venom gland secretion of a natural toxic protein complex composition, mainly of protein, peptide, and a number of enzymes, with a wide range of biological activity, can be used as a natural medicinal resources. As the pharmacology, toxicology, pharmacology development of many components of snake venom have been a more in-depth study and found that their anti-thrombosis, hemostasis, analgesic and anti-tumor aspects of great potential.

The exact anti-tumor mechanism of snake venom has yet to clear, the current point of view include: interference with membrane transport mechanisms; affect cellular energy metabolism; affect the body's immune system; Inducing Interferon; affect the blood hypercoagulability; -induced apoptosis; inhibit angiogenesis [1-7], In this study, cells, proteins genes on the, the agkistrodon acutus venom componets of X of three levels induced apoptosis in the mechanism study.

Apoptosis is an extremely complex and sophisticated process, involving many events, including the expression of apoptosis-related genes such as increased or reduced. In general apoptosis need to undergo initiation, effector and degradation period of three stages. In the initial stage, the cells are from outside of the various types of apoptotic signals stimulated a series of biochemical reactions; In effect stage, the cells showed a variety of biochemical reactions to form one or more of the signal transduction pathway; Finally, the cells enter the degradation phase, performance for a variety of hydrolytic enzymes (including the specific protease Caspases and nucleic acid enzymes) are activated, cell DNA degradation, nuclear chromatin condensation, cells membrane permeability and cell surface molecules change, as well as the cytoplasm of reactive oxygen substances (reactive oxygen species, ROS) increased and a series of apoptosis. Has confirmed that apoptosis occurs mainly through two ways. First, receptor-mediated pathway, from receptor-mediated activation of Caspase-8 launched the protease cascade to apoptosis; The other one is the mitochondrial pathway by the mitochondrial release of cytochrome C-mediated activation of Caspase-3 induced apoptosis [8]. Endogenous pathway, cytochrome C release in the center of apoptosis. Stage of apoptosis, due to internal and external mitochondrial membrane permeability change, led to disappearance of mitochondrial membrane potential and cytochrome C and other pro-apoptotic factor release, these pro-apoptotic factor released into the cytoplasm can lead to apoptosis cascade reaction, including Caspase-3 and other substances in activation of proteolytic enzymes and DNA fragments appear, in this process, the mitochondrial membrane permeability transition pore (PTP) opening and closing is to determine whether the cells the key to apoptosis [9]. But Bcl-2 family members on the regulation of apoptosis mainly through regulation of mitochondrial PTP opening and closing to achieve. Bcl-2, Bcl-xL inhibited the PTP opening such as to inhibit the release of apoptotic factors and prevent the occurrence of apoptosis, but Bax, Bad, Bak, Bik, Bcl-xS etc. as the role of the contrary, hey promote PTP opening, thereby promoting the release of apoptotic factors.

Cells in Bax protein can form a homodimer their own,and easily Bcl-2 protein in the formation of heterodimer complex, So that Bax inactivation. Bcl-2 expression increased when the relative increase in Bcl-2/Bax dimers, make the elimination of the pro-apoptotic effect of Bax, but the relative increase in expression of Bax, when Bax / Bax homodimers increase, Increase pro-apoptotic effect. This study is based on snake venom-induced apoptosis of tumor cells results, selected two kinds of human tumor cells in colon adenocarcinoma cell line HCT-8 and ovarian cancer cells SKOV-3 pathway in the regulation of the PTP opening and closing of two key factors Bax and bcl-2 gene, downstream ffector caspase-3 and a newly discovered inhibitor of apoptosis gene survivin levels of mRNA detection, as well as one of the pro-apoptotic gene caspase-3 and apoptosis inhibiting gene survivin protein levels were detected,to discuss the possible mechanism of snake venom-induced apoptosis of tumor cells. China have not seen the similar report on the the agkistrodon acutus venom-induced molecular mechanisms of tumor cell apoptosis. We have detected that the HCT-8 cells treated with FX at different times after treatment, apoptosis promoting gene Bax, caspase-3 and apoptosis-suppressing gene Bcl-2, survivin transcription level changes. The results showed that, FX dealing with HCT-8 cells after 2-24 h, Bax mRNA level was no higher, Caspase-3 mRNA levels in the PF-II dealing with 2-12h showing a rising trend, pro-apoptotic gene expression increased; At the same time, suppressing apoptosis gene bcl-2 mRNA levels in the 2-24h after treatment showed sustained reductions in trend, survivin mRNA levels at all time points were lower than the control group, and at 2-12h after treatment continued to decrease, that is, reduced gene expression of apoptosis suppression. These results suggest that, FX can induce increased expression of certain pro-apoptotic genes, the suppression of apoptosis gene expression decreased, and thus can promote the HCT-8 tumor cells apoptosis, thus inhibit tumor cell growth. Furthermore we were selected one of the pro-apoptotic gene and an inhibition of apoptosis gene, that is pro-apoptotic gene caspase-3 and apoptosis inhibiting gene survivin, using fluorescent antibody staining by FCM to detect Caspase-3 and Survivin protein expression levels.The results showed that, FX acting on the HCT-8 cells after 6 h, Caspase-3 protein expression increased, and then gradually decreased to normal levels below, Survivin protein in the role of PF-II expression after 6-48 h sustained reductions (P <0.05 ~ P <0.01),note the agkistrodon acutus venom inhibit the growth of HCT-8 tumor cells through the regulation of apoptosis-related gene expression achieved. Based on the above results suggested that, the agkistrodon acutus venom componets of the role of HCT-8 cells, by down-regulating bcl-2 expression to make irreversible PTP opening, outer mitochondrial membrane of small molecules into the membrane, mitochondria transmembrane potential loss, membrane damage, between the inside and outside the membrane leading to mitochondrial cytochrome C and other pro-apoptotic

factor release, the cytochrome C and apoptosis protein-activating factor 1 (Apaf1) combined, activatd Caspase-9, activation of Caspase-3 and then the cells underwent apoptosis, Survivin protein expression in the same time, down to the role of Caspase-3 inhibition reduced, Caspase-3 activity was enhanced cell apoptosis.

References

1. Weijie Zhu:Jing RUI: snake venom anti-tumor cell apoptosis mechanism of research, practical general Medicine, 2007,5 (5) :456-457
2. Hongliang Li: Xianda REN:Yingru Luo etc. NNAV oral serum preparation on HepG2 cell apoptosis [J]. CHINESE JOURNAL OF PATHOPHYSIOLOGY, 2002, 18 (2):199-200.
3. Ruping Yan:Jiansong Wang:Hongyi Xu: snake venom toxin anti-tumor mechanism of membrane research, Yunnan Medicine, 2007,28 (4) :404-408
4. GALLAGHER PG, BAO Y, SERRANO SM, et al. Use of microarrays for investigating the subtoxic effects of snake venoms: insights into venom-induced apoptosis in human umbilical vein endothelial cells [J]. Toxicon, 2003, 41(4): 429-440.
5. Yue Zhang,Jing. RUI: snake venom disintegrin anti-tumor research. Chinese Journal of C Yinical Pharmacology and Therapeutics 2007, 12 (9):984-988.
6. Chung KH, Kim SH, Han KY, et al. Inhibitory effect of sal-mosin, a Korean snake venom-derived disintegrin, on the integrin alphav-mediated proliferation of SK- Mel-2 human melanoma cells[J] . Pharm Pharmacol , 2003 ;55 :1577 - 1582.
7. Stragies R, Osterkamp F, Zischinsky G, et al. Design and synthesis of a new class of selective integrin alpha5beta1 antagonists [J]. Med Chem, 2007;50 :3786 - 3794.
8. Kiechle FL,Zhang X.Apoptosis:biochemical aspects and clinical implications.Clinica Chimica Acta 2002,326(1-2):27-45.
9. Feixiang Wu, Caspase-3 apoptosis pathway involved in neuropathic pain and its related mechanism of [D], 2008.

The changes of corneal biochemical properties after simulated ejection on the ground

Han-Yin Sun[1], Mu-Hsin Chen[2], Chih-Hung Lin[2], Ming-Jen Lee[3], Ming-Liang Tsai[4] ,
Cheng-Shu Yang[5], Chi-Ting Horng[6,7*]

[1] School of Optometry, Chung Shan Medical University. Taichung, Taiwan 402, R.O. China .[2]Department of Optometry, Chung Hwa University of Medical Technology, No.89, Wunhua 1st St., Rende Township, Tainan County, Taiwan, Taiwan 717, R.O. China. [3]School of Medical Imaging and Radiological Sciences, Chung Shan Medical University Taichung, Taiwan 402, R.O. China [4] Department of Ophthalmology, Tri-Service General Hospital. Taipei, Taiwan 114, R.O. China .[5] Aviation Physiology Research Laboratory. Kaohsiung, Taiwan 802, R.O. China. [6] Department of Ophthalmology. Kaohsiung Armed Force General Hospital. Kaohsiung, Taiwan 830, R.O. China. [7] Department of Pharmacy, Tajen University, Pintung, Taiwan 907, R.O. China. h56041@gmail.com.tw

February, 2009

Abstract

Ejection in high acceleration force may result in several physiologic responses and injuries. However, little is known about the effects of ejection on corneal rigidity and elasticity when pilots ejected from the cabinet after high + Gz acceleration. The aim of this study was to determine the changes of corneal biomechanical properties after simulated ejection. Thirty male pilots were enrolled in the study. The ejection seat training system at the Aviation Physiology Research Laboratory (Taiwan) was used to simulate ejection process at 8 times of gravitational force in head to toe Z-axis direction (+8 Gz force). Ocular Response Analysis (ORA) was applied to detect the dynamic bi-directional changes of cornea in the subjects who underwent simulated ejection. The related parameters were evaluated before ejection such as corneal hysteresis (CH), corneal resistance factor (CRF), and central corneal thickness (CCT). The bare visual acuity and refraction were also recorded. At instant, 15mins and 30mins after ejection, the parameters were detected as well. Two hours after ejection, the anterior chamber and relative position of lens were observed under the slit lamp. All the bare visual acuity and refractive errors remain unchanged during the study. There were no significant change of CH and CRF before and after ejection. However , the CCT increased significantly immediately after(548.5 ± 18.7 vs 590.8 ± 15.4, $p < 0.005$) and 15 min after (548.5 ± 18.7 vs 587.5 ± 16.2, $p < 0.005$) compared with the values before ejection. No hyphema, sub-location, or dislocation of the lens, or any rupture of the anterior lens surface were observed. After safe ejection on the ground, the main corneal biomechanical properties had no significant change. Besides, the refraction and bare visual acuity remained stable. We concluded that the rigidity and elasticity of the cornea, the stability of lens and the anterior segment of ocular structure were not apparently affected by high G-force. Nevertheless, our experiments were performed on the ground. During real high altitude ejection, true environmental factors such as windblast, low temperature, and hypoxia remained challenger to pilots. We need further studies in the future. [Life Science Journal. 2010; 7(1): 46 – 50] (ISSN: 1097 – 8135)

Key Words: Corneal hystresis, Corneal resistance factor, G-force

Introduction

The ejection seat has been responsible for saving the lives of thousand of pilots around the world since its introduction in the later 1940's. Escape system in fighters is a device which was first developed by German Air Force and designed to rescue the pilot in crisis (1). In early stage of World War II, military aircrafts flied at lower altitudes and slower speeds in combat. When an emergency occurs, they can use manual parachutes and make rapid escapes in time (2). With increasing in speed of modern vesicle developed, older manual methods might induce more risks during ejections associated with downward acceleration (3). For that reason, new equipment is necessary and ejection seat system developed. The ejection seat is the main component of the modern emergency rescue system. When the military pilots must leave the aircraft immediately, they should push the button at once. One aircrew with his seat may eject by an explosive cartridge stowed beneath a rocket system from the cabinet under high acceleration force around 6-12 times of G (gravitation)(4).

However, ejection in high acceleration force may result in several physiologic responses (5). The cornea has been a subject of interest to ophthalmologist and other eye careers because it playa a critical role in human undergoing high-acceleration movement. To our knowledge, there were no related articles to evaluate the effects of ejection after high-acceleration force exposure on human corneal rigidity and elasticity (so called biomechanical properties). The goal of this study was to investigate the influence of ejection on corneal biomechanical characteristics. In our experiment, Fig. 1 shows a simulated ejection seat on the ground was used to elicit an acceleration force set at eight times of gravitational force in head-to-toe Z-axis direction of (+8 Gz force). The ORA (Ocular Response Analyzer) was applied to evaluate the changes of corneal biomechanical properties.

Materials and Methods

The subjects were 30 healthy male pilots between 20 and 28 (mean = 24.5) yr of age. Informed consent was obtained from each volunteer before participation in the

studies began. All experimental protocols were conducted in accordance with the Declaration of Helsinki. Ethical approval for this study in advance was obtained from the institution review board. All the subjects with history of ocular or systemic diseases, such as hypertension, diabetes, cataracts, glaucoma, or uveitis were excluded from the study. They were instructed to not to take any medication within 72 hours. In Fig 2, the simulated ejection seat system at the Aviation Physiology Research Laboratory (Kaohsiung, Taiwan) was used to elicit an acceleration force set at +8Gz on the ground level. The total height of the instrument was 8 meters. When ejected, the subject within the seat reached the highest point (8 meters in height). Then the subject sent back by machine within 5 seconds.

Before ejection, each volunteer underwent a series of examinations including corneal biochemical properties, refraction and bare visual acuity. The Ocular Response Analyzer (ORA, Reichert, Buffalo, NY, USA) are the new instrument that measures the main corneal biomechanical properties including cornea hysteresis (CH), cornea resistance factor (CRF) and central corneal thickness (CCT). Bare visual acuity was tested were at 4 meter distance and recoded by EDTRS (Early Treatment of Diabetes Retinopathy) logMAR chart. Refractive errors were gained by Auto-refractometer (AR310, Nidek, Tokyo, Japan). Due to the limitations of time, only the left eyes of all subjects (total 30 eyes) were enrolled.

After the investigation, one subject sat on the ejection seat. At the instant of ejection (the seat may be sent back by automobile machine within 5 seconds, and now we represent the data as the immediate time after ejection), 15 minutes, and 30 minutes after ejection, the above series of examinations should be repeated again. All results are corrected and analyzed. Two hours after ejection, we checked the anterior chamber and its 360 degree of angle (hemorrhage or not) by the three-mirror gonioscopy and the relative position of the lens (dislocation, sub-dislocation or not) from full-dilated pupils with cyclopegia under the slit-lamp examination.
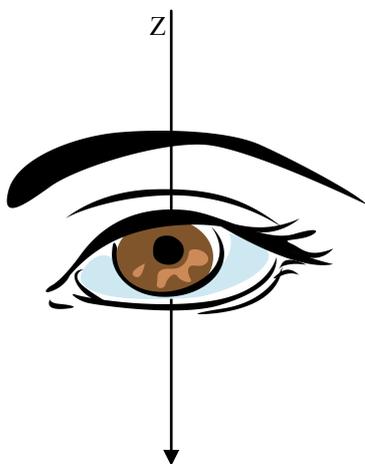
Fig 1：The direction of gravitational force is from head to toe in Z-axis direction (+ Gz force) after ejection. .
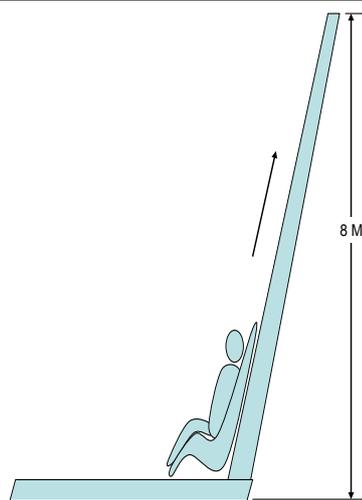
Fig 2：The simulated ejection seat system at the Aviation Physiology Research Laboratory (Kaohsiung, Taiwan) was used to elicit an acceleration force set at +8Gz on the ground.
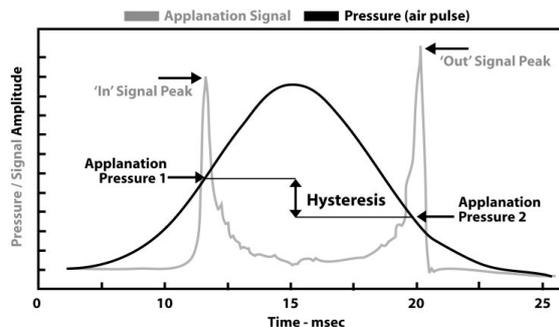
Fig 3: Explanation of corneal hystresis by the ocular response analyzer. By applying air-puff, a light reflex from the corneal surface changes and is detected by a sensitive sensor. There is a "delay time" in recovery from the convex condition, which is an indicator of absorbed energy during the deformation processes (corneal hystresis).

All results are expressed as the mean ± standard deviation (SD). Bare visual acuity is indicated as LogMAR (The chart has five letters per low ranging in size from + 1.0 to -0.3 log MAR). A paried t-test was used to compare the physiological parameters before and after ejection associated with +8 Gz. $P < 0.005$ was accepted as significant.

Results

All the data were collected for 30 eyes. In Table 1, there were no significant changes of CH and CRF before and after ejection associated with +8Gz. However ,in Table 2, the CCT increased significantly immediately after(548.5 ± 18.7 vs 590.8 ± 15.4, $p < 0.005$) and 15 min after (548.5 ± 18.7 vs. 587.5 ± 16.2, $p < 0.005$) compared with the values before ejection. Remarkable central corneal thickness increase was observed and persisted at least for 15 mins after

ejection.

The bare visual acuity of all the pilots were 0.05 ± 0.03 (logMAR) and the mean refraction of subjects were -0.50 ± 0.25 diopters (D) before ejection. In Table 3, two parameters of visual acuity remained un-change after simulated ejection at the same time.

Two hours after ejection, no hyphema or apparent blood clots tin the anterior chamber, and its 360 degrees of angles b y the Goldmann gonioscopy. In addition, we failed to find out the sub-location or dislocation of the lens or any rupture of the anterior lens surface under slit lamp examination.

Discussion

We can not commonly kwon the effects of high force around several times of gravitation (G-force) on the ground level. Meanwhile, every pilot especially the military aircrews had the special experience. Now ejection seats are installed in most military fighter and training aircraft around the world, and have saved the lives of many pilots. In time of crisis, they may survive with the eject system from high-speed fighter/attack by 8 times or higher of G gravitation on the sky. Now the egress systems of these weapon platform (such as F-15, F-16 and A-10), which use the Advanced Concept Ejection Seat (ACES-II), were developed and deployed after the Vietnam conflicts. The engineering design of the ACES-II provides for an escape envelope (system) of o to 600 KIAS(Knots Indicated Air Speed) and safe ejections up to high altitude, by mean of versatile operation depending upon both speed and altitude. During Operation Desert Storm, USAF lost four F-16 aircraft while mission on combat missions over Iraq and Kuwait, with four pilots ejecting safety (4). Today the simulated seat ejection system is very popular in the worldwide. Many military aircrews will receive well-training programs on the ground in peacetime. In the experiment, we use the system to create the impact of ejection safely to investigate corneal biomechanical properties and visual acuity of the volunteers in the ground level in Taiwan.

The emergencies that required ejection were obtained form accident records in which ejections were involved in the Japan Air Self-Defense Force between 1956 and 2004 (6). Engine failure was the most frequent reason. Mid-air collision, fire, and explosion, pilots' loss of human error, and fuel exhaustion comprised the majority of reasons for deciding to eject. Ejection under high acceleration force may result in several physiologic responses (7, 8), injuries and even fatality. The fatality rate ranged between 2.4% (Germany)(1) and 17.7% (USA) (9). They may die from cervical fracture, cardiac injury (10), and traumatic asphyxia. The other major and minor injuries including chronic subdural hematoma, spinal fracture (11), atlanto-axial dislocation (12), head injury, long bone fracture, rib fracture, burn, abrasion, limb injuries and neck sprain (13,14,15).

The abnormal ocular findings under different circumstance after ejection were sub-conjuctival hemorrhage, temporary loss of vision, and peri-ocular edema. It was caused by the high decelerative forces of abrupt onset applied from the rear while the blood vessels of the head and face are congested by high hydrostatic pressure. In addition, contusions and laceration over the eyes were ever reported (15,16). However, the impact of the corneal biomechanical properties after ejection was never surveyed in the past. Understanding corneal biomechanics is important for the accurate prediction of refractive surgery outcomes (17, 18), the use of contact lenses to change corneal topography, and the development of reliable correct factors for tonometry measurement .

In the past, we only use the concept of central corneal thickness (CCT) to investigate the corneal rigidity/elasticity and its function. In the last few decades, corneal biomechanics received more attention to define the corneal hyper-elasticity, the effects and hydration. Until 2005, the ocular response analyzer (ORA) was introduced as devices capable of acquiring an IOP measurement by Luce (19). The machine offers a new metric, corneal hystresis, it represents visoelastic properties. In addition, we can measure the corneal resistance factor and central corneal thickness (an ultrasound pachymetry attach to ORA) together. Now the CH and CRF were widely used by the ophthalmologists to predict the probability of ecstatic cornea after LASIK (20) as well as the early detection and difference diagnosis of glaucoma (21).

The ORA release a precisely metered air pulse that cause central 3mm of the cornea to move inwards. Thus, the cornea passes through applanation- inward applanation(P_1), then the past applanation phase where its shape becomes slightly concave. Twenty milliseconds after applanation, the air puff shuts off resulting in pressure decrease in a symmetrical fashion. During this phase the cornea shape tries to gain its normal shape. During this process the cornea again passes through an applanation phase-outward applnation(P_2). Theoretically, these two pressures should be the same, but this is not the cause. It is described as the bi-dynamic response that is the resistance to applanation manifested by the corneal tissue due to the viscoelastic properties. In Fig 3, the difference between the outward and inward pressure (P_1-P_2) is termed corneal hystresis (23) and is measured in mmHg. The P_1 is normally higher than P_2 where P_1 and P_2 are arbitrary units. The conversion formula of CRF by Luce (19) is that CRF $= \{ 0.1324 〔 (P_1 -0.7) 〕 P_2 \} -7.46$. In general, CH was refers to the viscosity of cornea. Luce (19), however, regards that CH is the absorbing and dispersing ability of cornea and CRF represents the elastic properties of cornea. Ortiz (24) defined CRF as the sum of the corneal rigidity to resist the external force and the ability to prevent from deformation of the cornea.

However, it has never been reported in any studies about corneal biomechanics change after ejection in literatures review. In our experiment, we could not find the significant change of CH and CRF after ejection. We know that the cornea has viscoelastic characteristics due to its numerous fibers thickness, hydration, and the crossed distribution of collagenous fibers (22). The effect of high gravitational force on human including cardiovascular system was well-known. Meanwhile, the

rigidity and elasticity of cornea may absorb and disperse the external G-force. Then the changes of CH and CRF were not significant after ejection. We suggested that if the military aircrew ejected on the sky, the CF and CRF may remain unchanged under high G force exposure.

Our experiment also revealed that the thickness of central cornea (CCT) increased significantly immediate and 15 mins after ejection. It means that the signs persisted at least for 15 mins after ejection. The values returned to the pre-ejection normal range 30 min after exposed to + 8 Gz. The minor changes may result from fiber arrangement or corneal edema after exposure to G-force, meanwhile because of the rebounding ability of the cornea, it returns to the value before ejection. We had ever observed a 10 % increase in CCT after + 9 Gz for exposure created by human centrifugation (25). The transient hydrostatic pressure may explain that findings. When the subject exposed to high gravity, the hydrostatic pressure of the ocular anterior chamber may increase. Then it may push the aqueous humor to flow across the corneal endothelium into the stroma, which may increase the corneal thickness (26).

In this experiment, we also found that the bare visual acuity remain stable even just immediately after ejection. Previous reports concerned with the occurrence of pathology in human during + Gz exposures have suggested some adverse effects including temporary vision, chest pain, dyspnea, motion sickness, nonpathological changes in the electrical activity of the brain, various cardiac arrhythmias, and unconscious (27). Some reasons of that symptoms and signs may be due to the hemodynamics changes of the pilots. It is the tendency that massive peripheral blood stasis in the lower extremities and the difficulty in returning to the heart and brain were noted under high G-force (8-12G). However, that effect may be apparent during a longer time (always persisted for 8 to 15 seconds). The exposed time was only 1 to 3 seconds after injection. Then the visual acuity of the military pilots may remain unchanged. Nevertheless, our experiments were performed on the ground. During the real ejection in crisis in the sky , the pilots may loss their helmet by the massive force (1). The strong effects of the windblast should be take into consideration. If the corneal biomechanics properties and visual function were affected by severe windblast or not, further studies are necessary in future.

The weight of human lens at 1 yr of age is about 140 mg. As it grows with age, it eventually weighs about 250 mg at the age of 80 yr of age (28). Till now, no previous studies have showed that the position of the lens of pilots will change under high speed flying or even after ejection. The structure and relative position of the lens play a important role in refraction. In our experiment, we also found that the refractive errors of the subjects remain stable after ejection. It is well known by ophthalmologists that if the relative position of lens had changed (such as dislocated into the vitreous cavity or anterior chamber of the eye, or sub-dislocation) after massive external forces, the zonules of the lens may tear. Then the refraction of the patient may be change and myopic shit is the predominant sign under auto-refractometer. Meanwhile, we checked the angle of anterior chamber and the relative position of the lens from full-dilated pupils two hours after ejection. No hyphema or apparent blood clots in the anterior chamber and its 360 degrees of angles. At the same time, we failed to find out the sub-location or dislocation of the lens or any rupture of the anterior lens surface. Although little platelet aggregation on the endothelium of Schlemm's canal under transmission electron microscopy (29), we could easily make the diagnosis of hyphema after stress under the slit-lamp examination. We should be able to make a conclusion that the stability of human lens and the anterior segment of ocular structure were not apparently affected by high G-force.

Table 1: The corneal hystresis and corneal resistance factor before and after ejection

	Before	Immediate after	After 15 min	After 30 min
CH(mmHg)	9.11 ± 1.86	10.22 ± 2.54	10.18 ± 1.49	9.19 ± 2.13
CRF(mmHg)	11.04 ± 2.05	12.11 ± 2.08	11.84 ± 1.56	11.12 ± .098

N=30 eyes
*Statistically significant difference ($P<0.005$).

Table 2: The central corneal thickness before and after ejection

	Before	Immediate after	After 15 min	After 30 min
CCT(μm)	548.5 ± 18.7	590.8 ± 15.4*	587.5 ± 16.2*	550.5 ± 20.4

N=30 eyes
*Statistically significant difference ($P<0.005$).

Table 3: The refraction and bare visual acuity before and after ejection

	Before	Immediate after	After 15 min	After 30 min
Refraction (D)	-0.50±0.25	-0.25±0.25	-0.25±0.25	-0.50±0.25
Bare visual acuity (LogMAR)	0.05±0.03	0.05±0.08	0.04±0.07	0.06±0.05

N=30 eyes

* Statistically significant difference ($P<0.005$)

Correspondence:

Chi-Ting Horng, Ph.D.

email: h56041@gmail.com.tw

References

1   Werner U. (1999) Ejection associated with injuries within the German Air Force form 1981-1997. *Aviat Space Environ Med.* 70(12): 1230-7.

2   Nelson P. (1990) Escape systems evolution. *Areomed Train Dig.* 4: 23-5.

3   Craig SC, Lee T. (2000) Attention to detail: Injuries at altitude among U.S. line parachutists. *Mil Med.* 165(4):268-71.

4   William CS. (1993) F-16 pilots experience with compact ejections during the Persian Gulf. *Aviat Space Environ Med.* 64(9):845-7.

5   Guill FC. (1989) Ascertaining the causal factors for ejection-associated injuries. *Aviat Space Environ Med.* 60(10,Suppl.): 44-71.

6   Nakamura A. (2007) Ejection experience 1956-2004 in Japan: An Epidemiological study. *Aviat Space Environ Med.* 78: 54-8.

7   Snyder RG. (1963) Human tolerances to extreme impacts in free-fall. *Aerospace Med.* 34:695-709.

8   Stapp JP. (1955) Effects of mechanical force on living tissues I. Abrupt deceleration and windblast. *J Av Med.* 26:268-88.

9   Campbell B. (2003) Ejection summary. *Flying Safety.* January/ February: 54.

10 Krefft S. (1974) Cardiac injuries resulting from ejection. *Aerospace Med.* 45(8):948-53.

11 Lewis ME. (2002) Spinal injuries caused by the acceleration of ejection. *J R Army Med Corps.* 148:22-6.

12 Boos N, Khazim R, Werslake RW, Webb JK, Mehdian H. (1997) Atlanto-axial dislocation with fracture. Case report of an ejection injury. *J Bone Joint Surg.* 79-B: 204-5.

13 Fleming C. (1979) Ejection problem and injury: Their cause , effects and treatment, and suggestions for preventive measurement. *Aviat Space Environ Med.* 50(8): 829-33.

14 Newman DG. (1995) The ejection experience of the Royal Australian Air Force: 1951-92. *Aviat Space Environ Med.* 66: 45-9.

15 Rowe KW, Brooks CJ. (1984) Head and neck injuries in Canadian Forces ejection. *Aviat. Space Environ Med.* 55(4):313-5.

16 Visuri T, Aho J. (1992) Injuries associated with the use of ejection seat in Finnish pilots. *Aviat. Space Environ Med.* 63:727-30.

17 Chen MC, Lee N, Bourla N, Halmilton DR. (2008) Corneal biomechanical measurement before and after laser in situ keratomileusis. *J Cataract Refract Surg.* 34:1886-91.

18 Deenadayalu C, Mobasher B, Rajan SD, Hall GW. (2006) Refractive changes induced by the LASIK flap in a biomechanical finite element model. *J Refract Surg.* 22:286-92.

19 Luce DA. (2005) Determining in-vivo biomechanical properties of the corneal with an ocular response analyzer. *J Cataract Refract Surg.* 31(3):156-62.

20 Kerautret J. Colin J, Touboul D, Robert C. (2008) Biomechanical characteristics of the ecstatic cornea. *J Cataract Refract Surg.* 34:510-3.

21 Ann GS, Bochmann F, Townend J, Azuara-Blanco A. (2008) Corneal biomechanical properties in primary open angle glaucoma and normal tension glaucoma. *J Glaucoma.* 17(4): 259-62.

22 Boote C, Hayes S, Abahassin M, Meek KM. (2006) Mapping collagen organization in the human cornea: left and right eyes are structurally distinct. *Invest Ophthalmol Vis Sci.* 47:901-8.

23 Kirwan C, O'Malley D, O'Keefe M.(2008) Corneal hystersis and corneal resistance factor in keratoectasia: Findings using the Reichert Ocular Analyzer. *Ophthamologica.* 222(5):334-7.

24 Ortiz D, Piñero D, Shabayek MH, Arnalich-Montiel F, Aliŏ JL. (2007) Corneal biomechanical properties in normal post-laser in situ keratomileusis and keratoconic eyes. *J Cataract Refract Surg.* 33(8):1371-5.

25 Tsai ML, Liu CC, Wu YC, Wang CH, Shieh PH, Lu DW, Chen JT, Horng CT.(2009) Ocular responses and visual performance after high-acceleration force exposure. *Invest Ophthalmol Vis Sci.* 50: 4836-9.

26 Muir KW, Jin J, Freedman SF. (2004) Central corneal thickness and its relationship to intraocular pressure in children. *Ophthalmology.* 111: 2220-3.

27 Burton RR, Leverett SD, Michaelson ED. (1974) Man at high sustained +Gz acceleration: a review. *Aerospace Med.* 45(10):1115-36.

28 Smith PA, Ivan D, LoRusso F, MACKersie D, Tredici T. (2002) Intraocular lens and corneal status following aircraft ejection by a USAF aviator. *Aviat Space Environ Med.* 73: 1230-4.

29 Hamanaka T, Bill A. (1994) Platelet aggregation on the endothelium of Schlemm's canal. *Exp. Eye Res.* 59:249-56.

30 Rissanen S, MÄkiken T, RintamÄki H, Aatsalo O, Kuronen P. (2002) Simulated parachute descent in the cold: Thermal responses and manual performance. *Aviat Space Environ Med.* 73: 1100-5

There were 74 subjects who were diagnosed with dental fluorosis. All of them lived in EFV, the prevalence of dental fluorosis was 51.7 (74/143) and dental fluorosis index was 1.35 in EFV and 0.021 in NEFV respectively. There were nearly 89.2% (66/74) of cases whose urinary fluoride levels exceeding 1.5mg/L. The exceeded rate of urinary fluoride was 84.6% (55/69) and 9.6% (9/94) in controls of EFV and NEFV respectively. The dental fluorosis cases were older than controls from EFV (P 0.05).

3.2 The distribution of genotypes for the *ER Rsa*I polymorphism in peripheral blood and its relationship with children's dental fluorosis

Figure 1 shows the target fragments of ER RsaI. No significant differences were found in the distribution of genotypes for the *ER Rsa*I polymorphism among these three groups (P 0.05; Table 2). No significant differences were found in the prevalence rate of dental fluorosis for different gender Children in EFV (P 0.05; Table 3). The distribution of genotypes for the ER RsaI polymorphism in boys and girls with dental fluorosis was no significant difference (P 0.05; Table 4). Urinary fluoride of children in these three groups have statistically significant differences ($P<0.05$). The level of urine fluoride was significantly lower in controls from NEFV compared with cases and control from EFV($P<0.05$ respectively) However, no significant difference was observed in the level of urinary fluoride between cases and controls from EFV ($P=0.668$; Table 5). When comparing the *ER Rsa*I genotype of children who has high-loaded fluoride status, no significant difference was found in children with or without dental fluorosis ($P>0.05$; Table 6).
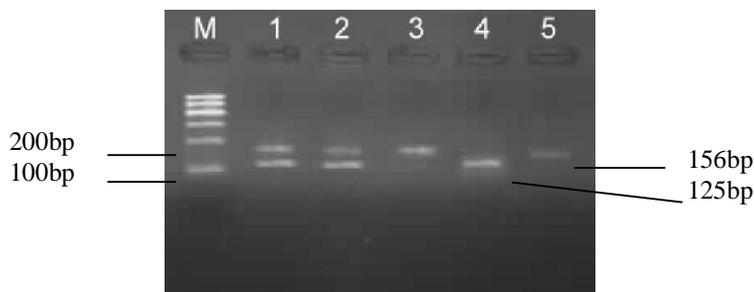
Figure 1. PCR-RFLP of ER target fragments. Lane 1 and 2: heterozygote (Rr); Lane 4: mutant homozygote (RR); Lane 3 and 5: wild-type homozygote (rr).

Table 2. Association between dental fluorosis and *ER Rsa*I polymorphisms

Polymorphisms	Cases N=74	EFV controls		NEFV controls	
		N=69	OR(95%CI)	N=94	OR(95%CI)
rr	45(0.608)	51(0.739)	1.00	60(0.638)	1.00
Rr	20(0.270)	14(0.202)	1.705(0.452-6.435)	32(0.340)	3.955(0.761-20.541)
RR	9(0.121)	4(0.058)	1.235(0.290-5.263)	2(0.021)	5.294(0.960-29.193)

Adjusted for age and gender.

Table 3. The comparison of dental fluorosis in boys and girls(%)

gender	Cases	Controls in EFV	Prevalence	^{2}	P
boys	33	41	44.6	3.14	0.076
girls	41	28	59.4		

Table 4. Comparison of ER RsaI polymorphisms in boys and girls with dental fluorosis

gender	rr	Rr	RR	total	^{2}	P
boys	22(0.667)	6(0.182)	5(0.151)	33	1.757	0.415
girls	23(0.561	13(0.317)	5(0.122)	41		
total	45	20	9	74		

Table 5. Comparison of urine fluorosis in groups

Groups	n	The scope of urinary fluoride	median	P
Cases	74	1.049~5.706	2.445	
EFV controls	69	1.143~5.135	2.419	0.000
NEFV controls	94	0.110~2.299	0.702	

Table 6. Comparison of ER RsaI genotypes in high-loaded fluoride status children with or without dental fluorosis

Groups	rr	Rr	RR	Total	^{2}	*P*
Cases	44(0.667)	16(0.242)	6(0.091)	66	0.275	0.872
Non-dental fluorosis	39(0.709)	12(0.218)	4(0.072)	55		
Total	83	28	10	121		

4 Discussion

Endemic fluorosis is a major public health concern in Henan province due to the excessive consumption of fluoride in drinking water. To date, the role of genetic susceptibility in relation to fluorosis, particularly dental fluorosis, has been unclear. Huang et al. found that children with homozygous P allele of COL1A2 PvuII had about five times the risk of dental flouorosis compared to children with homozygous p allele after adjusting for age and gender [8]. The results above indicated that genetic factor plays a role in the formation of Children's dental fluorosis. Estrogen plays an important role in stimulating osteoblast activity, promoting the deposition of calcium and phosphate in bone. Therefore, *ER* genetic polymorphism may be have an impact on the combination of estrogen and biological activity. There are some similarities between the formation of teeth and bones. Furthermore, the pathological change of dental fluorosis is the same as skeletal fluorosis, and it related to osteoblast activities, secreted structural matrix proteins and multiple proteases, and fluid composition including calcium ions and fluoride ions. As such, we speculate that *ER* gene polymorphism may be associated with pathological changes in bone, at the same time it may influence the formation of Children's dental fluorosis in Endemic fluorosis areas.

*Rsa*I polymorphism of *ER* gene is located on the codons 328, and resulting in synonymous mutation[9]. Studies suggested that the synonymous mutation may affect the expression of mRNA at synthesis, editing, sophisticated, transit, translation, degradation, etc, and thus may have an impact on protein function [10-12]. Sundarrajan et al.[13]suggested that ERß gene RsaI polymorphisms may be associated with ovulatory defects in some patients. On the other hand, Lau and Bagger also reported that *ER* gene *Rsa*I polymorphism was not associated with bone mineral density[14,15]. In the current study, no relationship was found between ER gene Rsa polymorphism and dental fluorosis although children with dental fluorosis had about two times higher of the proption of carrying homozygous H allele of *ER Rsa*I compared to children without dental fluorosis. The above results indicated that *ER* gene polymorphism may not be obvious associated with dental fluorosis..

Our study showed that no significant differences were found in urinary fluoride levels between cases and controls from the EFV (*P*>0.05). It means that, in the endemic fluorosis area, nearly half of children (45.5) with higher interior exposure levels (urinary fluoride>1.5mg/L) did not suffer from dental fluorosis. The result shows that there has individual susceptibility

under the same exposure conditions. However, no statistically significant difference in the distribution of *ER Rsa*I genotype among these groups (*P*>0.05). The reasons here, on the one hand, *ER* gene RsaI polymorphism may be not the fluoride-sensitive polymorphism marker. On the other hand, dental fluorosis is a complex disease and it is likely that several genes influence dental malformations. Therefore, further investigation on other polymorphisms of *ER* gene and other candidate genes related to calcium-metabolism may be useful.

Correspondence to:
Dr. Yue Ba,
Department of Envirnmental Health,
Zhengzhou University School of Public Health,
Zhengzhou, Henan 450001, China
Tel: +86 371 6778 1797
Fax: +86 371 67781868
E-mail: bayue1963@hotmail.com

References:
[1] Aoba T, Fejerskov O. Dental fluorosis: chemistry and biology. Crit Rev Oral Biol Med 2002;13 (2):155-70.
[2] Deng HW, Chen WM, Conway T, Zhou Y, Davies KM, Stegman MR, Deng H, Recker RR. Determination of bone mineral density of the hip and spine in human pedigrees by genetic and life-style factors. Genet Epidemiol 2000;19 (2):160-77.
[3] Riancho JA, Zarrabeitia MT, Valero C, Sanudo C, Mijares V, Gonzalez-Macias J. A gene-to-gene interaction between aromatase and estrogen receptors influences bone mineral density. Eur J Endocrinol 2006;155 (1):53-9.
[4] Zhang Wen-lan GSZD. Chronic fluorosis and osteoblastic activation. Chinese Journal of Control of Endemic Diseases 2003;18 (4):210-2.
[5] Yuan R, Le Ai-wen, Gen L, Xia EL, Yao ZW. The study on the relationship between Rsa I, Alu I polymorphism of the estrogen receptor beta gene and unknown aetiology hypomenorrhea. Zhonghua Yi Xue Yi Chuan Xue Za Zhi 2007;24 (4):425-7.
[6] Health MO. Manual control of endemic fluorosis.

Beijing: People's Health Publishing House, 1991.

[7] Valero C, Zarrabeitia MT, Hernandez JL, Zarrabeitia A, Gonzalez-Macias J, Riancho JA. Bone mass in young adults: relationship with gender, weight and genetic factors. J Intern Med 2005;258 (6):554-62.

[8] Huang H, Ba Y, Cui L, Cheng X, Zhu J, Zhang Y, Yan P, Zhu C, Kilfoy B, Zhang Y. COL1A2 gene polymorphisms (Pvu II and Rsa I), serum calciotropic hormone levels, and dental fluorosis. Community Dent Oral Epidemiol 2008;36 (6):517-22.

[9] Setiawan VW, Hankinson SE, Colditz GA, Hunter DJ, De Vivo I. Estrogen receptor beta (ESR2) polymorphisms and endometrial cancer (United States). Cancer Causes Control 2004;15 (6):627-33.

[10] Aschim EL, Giwercman A, Stahl O, Eberhard J, Cwikiel M, Nordenskjold A, Haugen TB, Grotmol T, Giwercman YL. The RsaI polymorphism in the estrogen receptor-beta gene is associated with male infertility. J Clin Endocrinol Metab 2005;90 (9):5343-8.

[11] Duan J, Wainwright MS, Comeron JM, Saitou N, Sanders AR, Gelernter J, Gejman PV. Synonymous mutations in the human dopamine receptor D2 (DRD2) affect mRNA stability and synthesis of the receptor. Hum Mol Genet 2003;12 (3):205-16.

[12] Almeida S, Franken N, Zandona MR, Osorio-Wender MC, Hutz MH. Estrogen receptor 2 and progesterone receptor gene polymorphisms and lipid levels in women with different hormonal status. Pharmacogenomics J 2005;5 (1):30-4.

[13] Sundarrajan C, Liao WX, Roy AC, Ng SC. Association between estrogen receptor-beta gene polymorphisms and ovulatory dysfunctions in patients with menstrual disorders. J Clin Endocrinol Metab 2001;86 (1):135-9.

[14] Lau HH, Ho AY, Luk KD, Kung AW. Estrogen receptor beta gene polymorphisms are associated with higher bone mineral density in premenopausal, but not postmenopausal southern Chinese women. Bone 2002;31 (2):276-81.

[15] Bagger YZ, Jorgensen HL, Heegaard AM, Bayer L, Hansen L, Hassager C. No major effect of estrogen receptor gene polymorphisms on bone mineral density or bone loss in postmenopausal Danish women. Bone 2000;26 (2):111-6.

An Integrated Investigation of CAD/CAM for the Development of Custom-made Femoral Stem

Jeng-Nan Lee[1] and Kuan-Yu Chang[2*]

1. *Department of Mechanical Engineering, Cheng Shiu University, Kaohsiung County, Taiwan 833, R.O. China.*
2. *Mackay Memorial Hospital Taitung Branch, Taitung, Taiwan 833, R.O. China.*
    mmhadm@ttms.mmh.org.tw

_____

Abstract: In this paper, an integrated approach of CAD/CAM was presented for the concurrent development of custom-made femoral stem. The femoral stem is developed on a prescription basis and is unique for each patient. The geometric parameters and the necessary constrains based on surgical experience were integrate into the CAD system. The rapid prototyped model was built as the reference for review. Through the application of CAM software, the interference-free toolpath and the cutter location for multi-axis NC machining are generated. The cutting simulations with solid model are performed to verify the generated toolpath. It is also verified through the trial-cut with model material on a five-axis machine tool. [Life Science Journal. 2010; 7(1): 56 – 61] (ISSN: 1097 – 8135).

Keywords   custom-made, femoral stem, CAD/CAM, rapid prototyping

_____

1. Introduction

Over the last 25 years, major advancements in hip replacement have improved the outcome of the surgery greatly. Hip replacement surgery is becoming more common as the population of the world. The main reason for replacing any arthritic joint with an artificial joint is to stop the bones from rubbing against each other. Degenerative and arthritic problems result in very painful or nonfunctional joint movement. Replacing the painful and arthritic joint with an artificial joint gives the joint a new surface, which moves smoothly without causing pain [1].

Each year, over two million osteoarthritis joints are replaced with artificial joints worldwide. A primary concern of these devices for the hip and knee is to eliminate pain and improved mobility. However, products for other areas such as the shoulder, ankle, elbow, wrist, etc. are also available as well as trauma and sports medicine devices [2].

A total hip prosthesis replaces both the ball and the socket of the natural joint, in most cases, with a femoral component inserted in the upper end of the femur and an acetabulum component placed in the pelvis. Most modern implants are fabricated from (a) Ti-6Al-4V alloy, (b) ASTM F-75 cobalt-chrome alloy, or (c) 315 stainless steel alloy that are attached to prepared bony structures and surfaces. Ultra high molecular weight polyethylene bearings are used between the mating joint surfaces. The components are often anatomically shaped or contoured designs versus basic geometric shapes. They are produced as a family in a range of sizes that can be selected at surgery to match the patient requirements.

Total hips may be classified in two basic types: cemented and press fit. Cemented implants use a polymethyl methacrylate-based grout for fixation, whereas press-fit implants have a rough, porous surface intended for bone to grow into. They are fixed directly to bone. This rough surface can be manufactured by plasma spray operations, by sintering metal beads to the implant surface. These kinds of implants are often used in patients that are younger and more active, since their bone is better able to grow than those of older, more sedentary patients [3, 4].

The orthopedic industry consults with surgeons in the development of new implant systems and related instrumentation. Their expertise and medical training coupled with bioengineering and manufacturing capability provides the collaboration to advance the state of the art of these implants. It is a very complex design environment. The soft tissue integrity and bone remodeling all relate to the success of the implant. Thus, solid modeling and rapid prototyping can bridge the gap between the designers and the manufacturing engineers which is essential for concurrent engineering [4].

In the study of tool orientation for multi-axis machining, Choi et al. [5] proposed a method to generate optimal cutter location data for free-form surface. The optimization problem is formulated as a 2D constrained minimization problem. There are three constraints, viz., joint limits, gouging, and collisions on cutter location. Rao and Sarma [6] described an exact method for the detection and elimination of local gouging in five-axis machining using a flat-end tool. Lee [7] presented a method to find the admissible tool orientation by considering gouging. The drawback of these methods mentioned above is that they cannot guarantee a collision-free and gouge-free 5-axis toolpath.

This paper describes a design system combining clinical experience and engineering knowledge for the manufacture of custom-made femoral stem. The femoral stem is developed on a prescription basis and is unique for each patient. Rapid prototyped models are fabricated from three-dimensional CAD models for concurrent development. The generated toolpath from CAM is converted to the NC code. The trial cut is also performed with model material and demonstrates the practical application. Figure 1 shows the flowchart of the integrated research for design and manufacture of femoral stem.
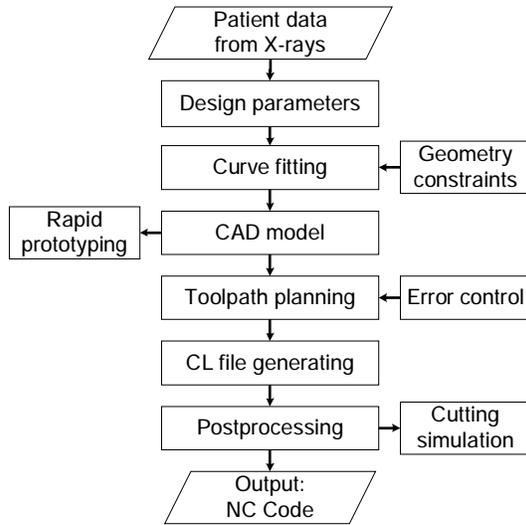
Figure 1. Flowchart of the integrated research for design and manufacture of femoral stem.

2. Geometry of femoral stem

The hip joint is one of the true ball-and–socket joints of the body. The hip socket is called the acetabulum and forms a cup that surrounds the ball of the upper thigh bone, known as the femoral head. The thick muscles of the buttock at the back and the thick muscles of the thigh in the front surround the hip. A hip that is painful as a result of osteoarthritis (OA) can severely affect your mobility. Custom-made femoral stem is necessary for those situations when an off-the-shelf standard size stem is not suitable. To develop the stem, the surgeon and the engineer determine the basic requirements and design criteria use either patient X-rays, the computer tomography (CT) scans or magnetic resonance image (MRI) as shown in Figure 2. To provide the best fill and fit femoral stem to each individual patient, the shape is of major concern.

The relationship of femoral size between proximal and distal diameters in most people is not proportional but wide distributed. According to the canal flare index, the femur shape can be divided into three types, stovepipe, normal, and champagne flute. The goal for the hip stems design was to define a product that met manufacturing requirements and surgical expectations.

The design features of a femoral stem are specified as shown in Figure 3, A is the head offset; χ is the neck-shaft angle; B is the proximal diameter; C and D are the diameters of intramedullary; D_1 and D_2 are the curve fitting points of intramedullary; E is the distal diameter; Stem length is the amount of X and J. Figure 4 is the design parameters of femoral stem model related to the features of intramedullary. By inputting a group of geometric data measured from X-ray, a CAD model of femoral stem which satisfies the design rules can be created.

3. Rapid prototyping of femoral stem

The conception invented by the engineer or surgeon

may start off as hand drawn sketches. The engineers understand how to interpret the engineering drawing with its geometric dimensions and tolerances. They can envision the actual shape by observing the orthogonal views. The surgeons try to communicate a complex three-dimensional concept in this two-dimensional views is very difficulty. Features that seem insignificant on a sketch can become very expensive manufacturing challenges. The goal of rapid prototyping is to bridge this gap by providing actual full-scale models. The physical model of a part is made directly from a three-dimensional CAD model by rapid prototyping. The rapid prototyped model can be the important bases of revision, process planning and cost analysis. Figure 5 shows the computational steps in producing a stereolithography file of the femoral stem.
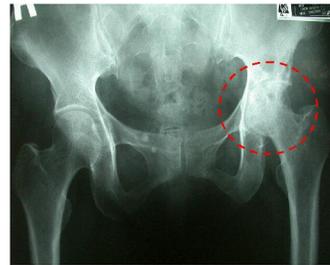
Figure 2. Degenerative osteoarthritis [8]
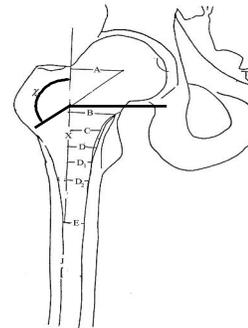
Figure 3. The features of femoral stem on X-ray.
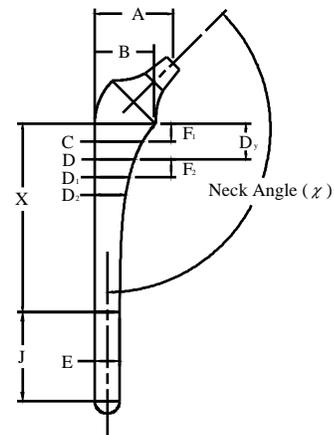
Figure 4. The design parameters of femoral stem model.
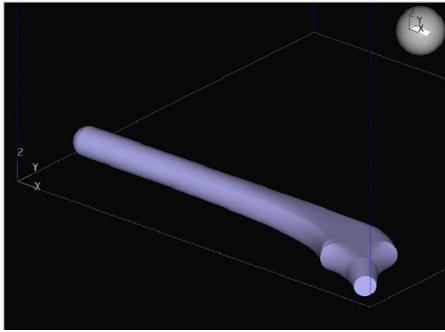
(a) Three dimensional description of the femoral stem.
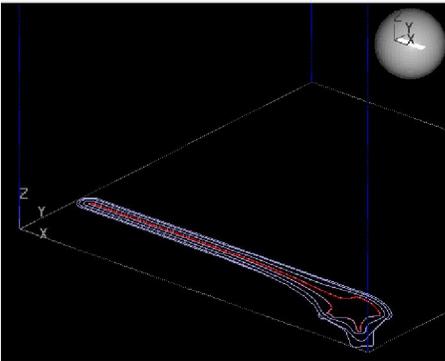
(b) Support structure is planed.
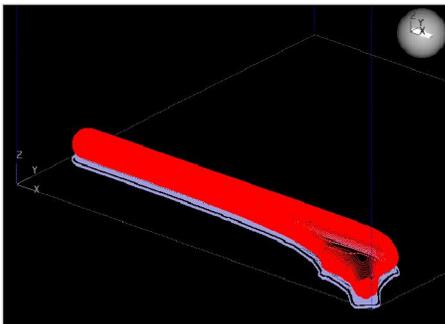
(c) The stem is divided into slices.
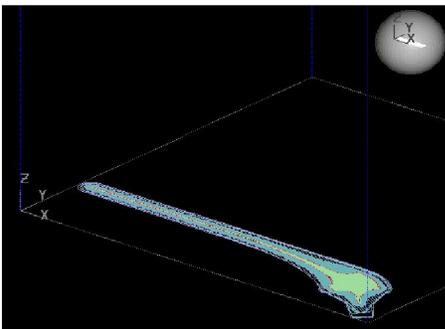
(d) A set of tool path is determined for manufacturing each slice.
Figure 5. The computational steps in producing a stereolithography file.

3.1 Fused-deposition modeling

After the simulation of slicing and the extruder path, a stereolithography file is imported into rapid prototype machine. The process of additive manufacturing is used to build part in layers. The technique of fused-deposition modeling (FDM) is applied in this paper. In the FDM process, as shown in Figure 6, parts are built layer by layer. The extrusion heads move in two principal directions over a table. The table can be raised and lowered as needed. A thermoplastic filament is extruded through the small orifice of a heated die. The initial layer is placed on a foam foundation by extruding the filament at a constant rate while the extrusion heads follow a predetermined tool path. When the first layer is completed, the table is lowered so that subsequent layers can be superposed. Whilst the part is completely created, support structures are dissolved in a water-based solution or snapped off by hand.
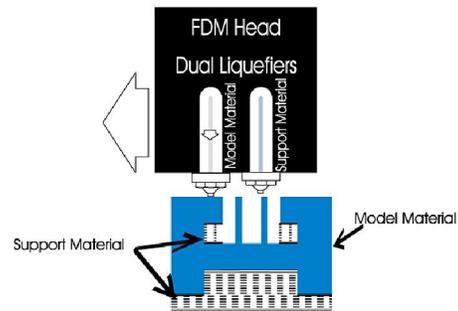
Figure 6. Schematic illustration of the fused-deposition modeling process [9].

4. CAM for the femoral stem

The femoral stems have to be machined on multi-axis CNC machine tools because of their complex shapes. The interference-free toolpath is the major consideration for multi-axis machining of the stem. Machining sequences and cutter location (CL) files can be created in the manufacturing module of UniGraphics NX software, which is the same CAD/CAM environment that the solid model was created in. In order to clamp and manufacture the stem, the design model was modified to become the manufacturing model and a workpiece model can be created for cutting simulation.

In the set up environment of manufacturing module for the stem, a cylindrical workpiece is built first and than assembled with the manufacturing model, as shown in Figure 7. The operation of multi-axis milling is used to machine the complex surface. The machining features are selected based on the Surface Area drive method. The position and the orientation of the milling tool, also known as the cutter location, can be specified by the functions of Tool Axis and Projection Vector. The cutting and non-cutting parameters are chosen for the actual cutting conditions. The toolpath sequences created can be displayed on the system separately or serially. The generated CL file can be verified through the function of solid cutting simulation built in this module. Figure 8 shows the cutting simulation of finish machining by multi-axis machining operation.
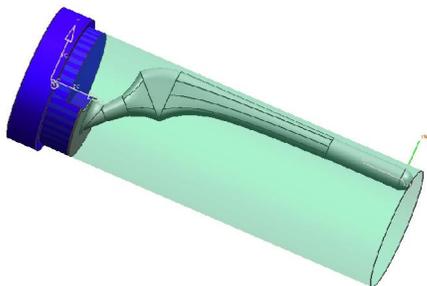
Figure 7.   Manufacturing model is assembled with the workpiece model.
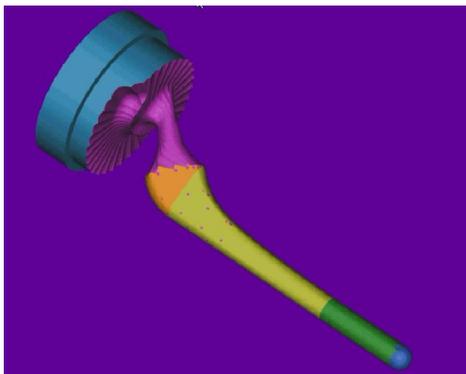
Figure 8.   Cutting simulation of finish machining for the femoral stem.

5. Results and discussions
5.1 Geometric modeling and rapid prototyping
The design parameters of a femoral stem as shown in Table 1, is used to verify the validity and effectiveness of the proposed approaches. Using these parameters in CAD system, the surface geometry of the femoral stem is created. Two solid models of custom-made femoral stem built by Unigraphics NX software are shown in Figures 9,10,11,and 12. After the computational steps in producing two stereolithography files respectively, the FDM process is adopted to obtain the rapid prototyped models (Figures 13 and 14). The rapid prototyped models can be sent to the surgeon for review and approval prior to fabricating the actual stem.

Table 1.   Design parameters of the femoral stem.

A,*mm*	χ	B, *mm*	C, *mm*	D, *mm*
35	137°	29.5	26	24
D_1, *mm*	D_2, *mm*	X, *mm*	J, *mm*	E, *mm*
22	20.3	85	50	15

Figure 9.   Solid model of a femoral stem built by Unigraphics NX. (Type I)
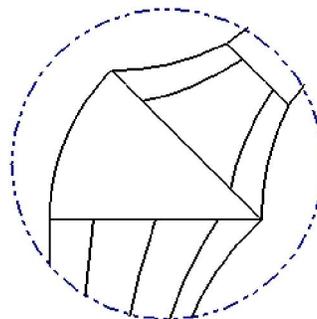
Figure 10.   Detail view of a femoral stem. (Type I)

Figure 11.   Solid model of a femoral stem built by Unigraphics NX. (Type II)
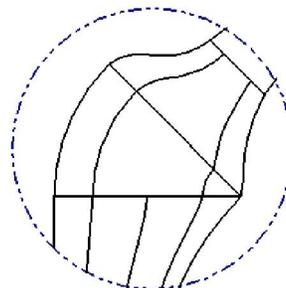
Figure 12.   Detail view of a femoral stem. (Type II)
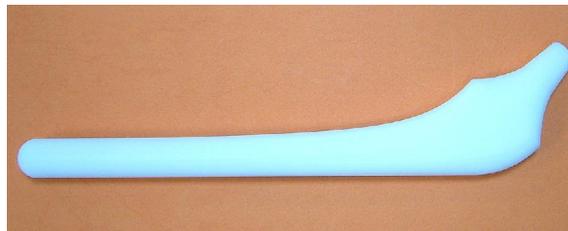
Figure 13.   Rapid prototyped model of a femoral stem produced through FDM process. (Type I)

Figure 14.   Rapid prototyped model of a femoral stem produced through FDM process. (Type II)

5.2 Toolpath simulation and trial-cut

To avoid collision between all machine tool components and the risk of human error, the generated toolpath is verified before actual machining through solid cutting simulation. Table 2 shows the used machining parameters corresponding to various machining process. Figure 15(a) reveals the toolpath generation of rough machining with ball end mill simulated by UniGraphics NX. Figure 15(b) shows the result of solid cutting simulation for rough machining using CL file. The toolpath generated from UniGraphics NX is converted into NC program by the postprocessor. The NC program is verified via VERICUT® software. Figure 16(a) presents the cutting simulation of rough machining. Figure 16(b) shows the result of finish machining. The simulation results demonstrate that the machining process works well and the collision between the shank and workpiece surface does not occur. After the simulation and the verification, the NC program is transferred to controller through Internet. The five-axis machine tool is used to perform the actual machining. Figure 17 shows the multi-axis machining of model material.

Table 2. Machining parameters for femoral stem.

Machining Process	Cutting Tool	Chordal Deviation	Scallop height	Cutting Method	Out-Toleance
Rough Machining	$\phi14R7$	0.1 mm	0.1 mm	Zig-zag	0.5 mm
Finish Machining	$\phi14R7$	0.01 mm	0.01 mm	Zig-zag	0.0 mm

(a) Toolpath generation; (b) Cutting simulation.

Figure 15. Multi-axis toolpath for rough machining of the femoral stem. (UniGraphics NX)
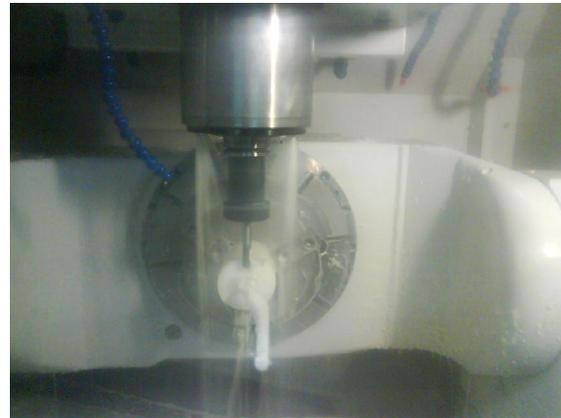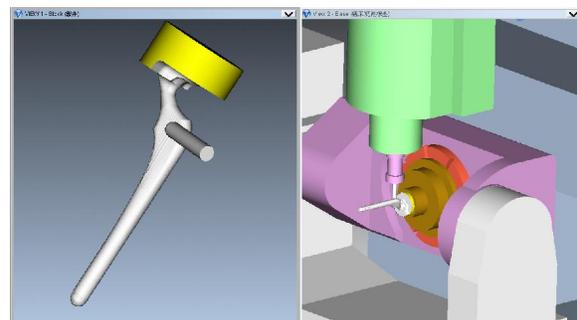
(a) Rough machining.

(b) Finish machining.
Figure 16. Simulation of femoral stem cutting by the ball end mill. (VERICUT®)
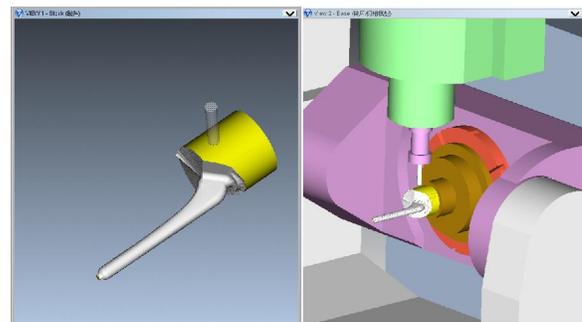
Figure. 17. The multi-axis machining of model material on five-axis machine tool.

6. Conclusion

A design system combining clinical experience and engineering knowledge was developed for the manufacture of custom-made femoral stem. The system implemented is from surgeon requirements to the completion of manufacturing. The solid modeling and rapid prototype are used in the system to establish the interface among conception, design and manufacture. The CAD/CAM techniques are applied to develop the complicated surface and multi-axis machining by inputting a group of geometric data provided from surgeon. The designed hip stems will meet the manufacturing requirements and surgical expectations.

_____

Corresponding Author
Kuan-Yu Chang, MD
E-mail : mmhadm@ttms.mmh.org.tw

References
1. http://www.eorthopod.com
2. Huang BW. Medical Devices Industry Yearbook, Industrial Economics & Knowledge Center, Taiwan, 2007.
3. Kalpakjian S and Schmid SR. Manufacturing Processes for Engineering Materials, Pearson Education, New Jersey, 2003.
4. Jacobs Paul F. Rapid Prototyping & Manufacturing Fundamentals of StereoLithography, Socity of Manufacturing Engineers, 1992.
5. Choi BK, Park JW and Jun CS. Cutter-location data optimization in 5-axis surface machining. Computer-Aided Design, 1993, 25(6): 377-386
6. Rao A and Sarma R. On local gouging in five-axis sculptured surface machining using flat-end tools. Computer-Aided Design, 2000, 32: 409-420
7. Lee YS. Admissible tool orientation control of gouging avoidance for 5-axis complex surface machining. Computer-Aided Design, 1997, 29(7): 507-521
8. http://www.postal.com.tw
9. http://www.stratasys.com

Mechanical Stimulation Effect on Proliferation of Murine Osteoblast Cell

Bo Wun Huang[1], Feng-Sheng Wang[2], Jih-Yang Ko[2], Wun-Han Jhong[1], Ke-Tien Yen[1], Jung-Ge Tseng[*1]

[1]Graduate Institute of Mechatronics Engineering, Cheng Shiu University, Kaohsiung, Taiwan 833, R.O. China
[2]Chang Gung Medical Foundation, Kaohsiung Branch, Kaohsiung, Taiwan 833, R.O. China
james.tseng@csu.edu.tw

_____

Abstract: Age-related diseases, such as osteoporosis, arthritis, accidental fracture, etc., are increased dramatically due to rapid progressing modern medical science and technology push the early arrival of aging society of mankind. How to increase osteoid of the healthy cell, restrain the malignant cell, and fast recovery from bone fracture are becoming major research subjects in the medical community. The growth of bones is proved in medical research to have some relationship with external strength, such as direct current, electromagnetic field, coupled electrical field, ultrasound, etc., and all such researches have their effectiveness in different level. However, few people study the mechanical excitation (vibrating shaker) onto the cell directly in subsonic frequency range. This research studies the culture of mice MC3T3 osteoblast cell in vitro, stimulate the growing cell with mechanical broad range subsonic frequency with or without temperature factor and investigate the effect of different amplitude, repeated number of times, and excitation durations of the stimulation. The cell concentration are then measured by MTT assay by fluorescence spectrometer and RNA assay by electrophoresis diagram and compared with the control (nature growing cell) set. Comparison of different parameters are obtained together with mechanical setup are ready to provide the information about the proliferation of osteoblast for medical community reference. [Life Science Journal. 2010; 7(1): 62 – 67] (ISSN: 1097 – 8135).
Keywords: Osteoblast cell; **Mechanical Stimulation**; **Broadband** Frequency; **MTT assay**; **RNA assay**.
_____

1. Introduction

The rapidly progressing modern medical science and technology push the early arrival of aging society of mankind. However, Age-related diseases are increased dramatic accordingly. Osteoporosis, so called "Silent Disease" in medical community, is one of the major problems for elderly people. The occurrence probability of osteoporosis induced fracture is more than three times of heart attack, stroke, and breast cancer within women. There are over 1.6 million hipbone fracture patients per year all over the world due to osteoporosis.

Lots of studies aim on how to improve or restrain the proliferation of osteoblast cell (human and/or animal model, in vitro or in vivo) by employing the external energy and/or combined with different physical/chemical treatment, co-culture with different materials, etc.

Chang [1] investigates the effect of physical stimulation on osteoporosis in osteoporotic animal models including the effect of: 1) whole body vibration (WBV) on osteoporotic SD rats model, and 2) pulsed electro- magnetic field (PEMF) and high magnetic single pulsed electromagnetic field (HMSP-EMF) on osteoporotic BALB/C mice model.

Tsai [2] studies the effects of low frequency pulsed electromagnetic fields on treatment or prevention of osteoporosis by inducing osteoclast (cocultured with osteoblast cell) apoptosis.

Rutten et al. [3, 4] employ low-intensity pulsed ultrasound (LIPUS), histology and histomorphometric analysis to determine bone formation and bone resorption parameters for bone healing at the tissue level in patients with a delayed union of the osteotomized fibula and find out that in both areas of new bone formation and cancellous bone, LIPUS significantly increased osteoid thickness, mineral apposition rate, and bone volume.

Tsui [5] discovered that the correlation coefficient, amplitude, and conduction velocity of the compound action potential (CAP) of the nerve tissue of a bullfrog are affected by ultrasonic stimulation which were postulated due to the mechanism of opening and closing ion channel gate causing modification of ion permeability of cell membrane in experiments.

Reher et al. [6] discover that Long wave ultrasound (LWU, 45 kHz) is capable of inducing a comparable or even higher enhancement of bone formation compared with traditional ultrasound (1 MHz), which, with LWU's greater penetration, may accelerate the healing effect of ultrasound on osteoradionecrosis. Li et al. [7] compare the mechanisms of ultrasound on osteoblast proliferation with those of pulsed electromagnetic field (PEMF), by different signal transduction pathway inhibitors. Myrdycz et al. [8] evaluate the adhesion between cells and various substrates by ultrasounds [9]. Tanimoto et al [10] indicate that osteoblast-like cell proliferation increased with increasing sintering temperature and the biological stability of the sintered tricalcium phosphate (TCP) sheet surface was considered to have affected cell proliferation. Some researchers study how to culture the osteoblast cell on metallic support, phosphate ceramics, other surface or material, etc. [11~17].

Dumas et al. [18] identify that low-amplitude, high-frequency strain regimen is able to increase major matrix proteins of bone tissue and to regulate the expression of vascular endothelial growth factor (VEGF) variants, which shows that an appropriate combined loading has the potential to function cellularized bone-like constructs.

Bochu et al. [19] find that the mechanical vibration can distinctly enhance the growth of Gerbera jamesonii acrocarpous callus at 3 Hz in frequency, and its quality is higher than the controls. Meanwhile, after stimulation by mechanical vibration, the fibers direction in the cell wall was unclear, the degree of accumulation of fibers in the

cell wall was high and the cytoskeleton rearranged.

Tanaka et al. [20] indicate that MC3T3-E1 osteoblasts cells are more sensitive to low amplitude, broad frequency (0 to 50Hz) strain, and this kind of strain could sensitize osteoblasts to high amplitude, low frequency strain, which also implies a potential contribution of stochastic resonance to the mechanical sensitivity of osteoblasts. Mechanical static stretching or strain are also employed for osteoblast cell proliferation [21~25].

Frias et al. [26] conduct the experiments to grow osteoblasts on the surface of a piezoelectric material, both in static and dynamic conditions at low frequencies (1 and 3Hz, respectively), and total protein, cell viability and nitric oxide measurements shows that both static and dynamic affect cell viability and proliferation negatively.

Henriksen et al. [27] investigate mechanical stimulation of human osteoblast like cell through intercellular calcium wave propagation.

When the vibrating wave propagate though a biological tissue, bioeffects including those induced by heat and vibration could result constructive and destructive effect for physiotherapy according to previous study. Also, the study of microscopic cell can assist to more understanding the macroscopic dynamic characteristic of bone structure [28].

This purpose of research is find the influence of mechanical stimulation over broad range of frequency onto mice MC3T3 osteoblast cell in vitro with different amplitude, time, excitation durations, and with or without temperature factor.

2. Cell Cultivation

The growth of bones is proved in medial research to have some relationship with external strength, such as direct current, electromagnetic field, coupled electrical field, ultrasound, etc., and all such researches have their effectiveness in different degree.

This research studies the culture of mice MC3T3 osteoblast cell in vitro, stimulate the growing cell with mechanical broadband frequency with or without temperature factor and investigate the effect of different amplitude, time, and excitation durations of the stimulation. The cells are then counted by MTT test and RNA extraction method and compared with the control (nature growing cell) set.

The flow chart of culture and stimulation of murine osteoblast cell is shown in Fig. 1.
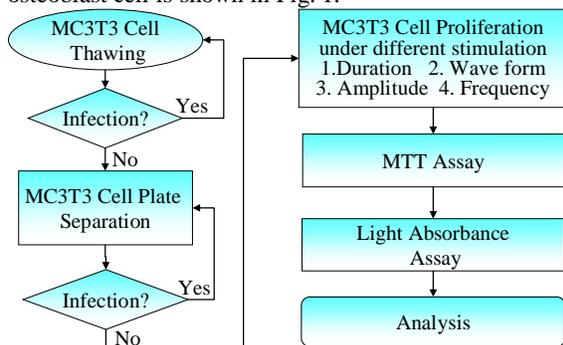
Fig. 1. The flow chart of culture and stimulation of murine osteoblast cell

3. MTT Assay

The MTT assay is a laboratory test and standard colorimetric assay (an assay which measures changes in color) to estimate the survival rate of the cell by measuring the reduction of yellow 3-(4,5-dimethythia-zol-2-yl)-2,5-diphenyl tetrazolium bromide (MTT) by mitochondrial succinate dehydrogenase. The procedures are as follows:

1. Preparation
 (1) PBS
 (2) MTT (5 mg/ml in PBS) – filter and prepare freshly
 (3) Acidic isopropanol (0.1N HCl in absolute isopro-panol)
 (4) 96-well plate (flat bottom)
2. Procedure
 (1) Plate cells (104-106 cells) in 200 ml PBS in 96-well (flat bottom).
 (2) Add 20 ml of MTT solution, mix well.
 (3) Incubate for 4 hour in 37°C
 (4) Remove aliquot for analysis; add 200 ml acidic isopropanol and mix well.
 (5) Incubate additional 1 hour in 37°C
 (6) Read absorbance intensity of the cell from Fluorescence spectrometer.

4. RNA Assay

The flow chart of RNA assay is shown in Fig. 2.
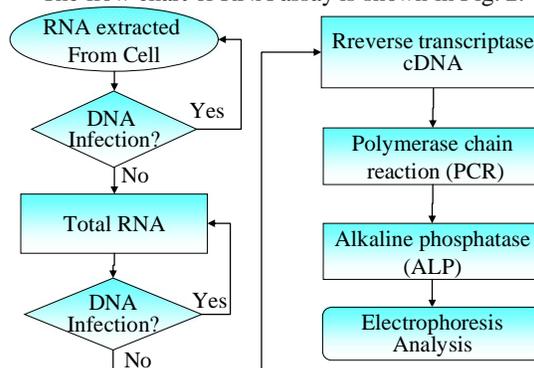
Fig. 2. The flow chart of RNA assay

4.1. RNA Extraction

1. Pipetting up the upper layer solution of the osteoblast cell, add 1 ml TRIZOL to suspend the cell.
2. Pipetting TRIZOL suspension solution to centrifuge tube, add 220 ul (BCP) excited for 15 seconds, wait for 2 minutes.
3. Place into 12,000 rpm, 4°C centrifuge for 15 minutes.
4. Pipetting upper layer solution 400 ul to new centrifuge tube and mixed with 550 ul isopropanol.
5. Place into -80°C container for 30 minutes.
6. Direct place into 12,000 rpm, 4°C centrifuge from cryo-status and spin for 20 minutes.
7. Empty the solution, mixed with 1cc, 75% alcohol (0.1%DEPC water treated)
8. Place into 8,000 rpm, 4°C centrifuge spinning for 5 minutes.
9. Pipetting the solution from the tube, dry up in the air (the cells are stuck tightly on the tube and will not come off from the tube, can use paper to such the

remaining solution).
10. Add 0.1%, 15 ul (0.015 cc) DEPC water, mixed for 15 minutes. The RNA (appeared in sticky state since it contains nucleic acid) is ready for the assay.

4.2. Reverse Transcriptase cDNA
1. Quantitative total RNA, dilute to 500 ng/ul, pipetting 2 ul around 1 ng/ul. Calculate when the ph value is greater than 1.6 then can be used for experiment.
2. Reverse Transcriptase (RT) response: RT Polymerase Chain Reaction (PCR) is a widely used transformation. In RT-PCR, one RNA chain can be RT to complimentary DNA (cDNA), then use this template and PCR to proceed DNA duplication.

5. Experimental setup
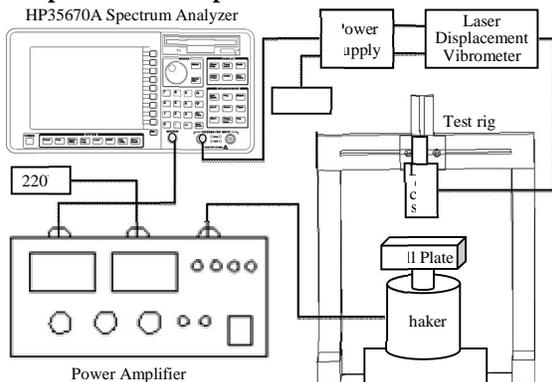
Fig. 3. Mechanical stimulation setup for MC3T3 cell

The experimental set up is shown in Fig. 3 to investigate the proliferation effects of osteoblast cell (MC3T3) under mechanical stimulation with different parameters: broad range of frequencies, amplitude, duration, repeated times, and temperature effects, etc. The MC3T3 cell culture plate is fixed at the center tip of a vibration shaker which is excited by one channel of HP 35670A spectrum analyzer through a 220V power amplifier. The sensor of a Laser Displacement Vibrometer is hanged on the test rig and placed around 3 cm apart from the top of the cell culture plate to measure actual cell vibration signal. This Laser Displacement Vibrometer is connected to the other channel of HP 35670A spectrum analyzer through 110V power supply.

6. Results and Discussion
The SEM (Scanning Electron Microscope) photos of just seeded and 80% growing of MC3T3 cell are shown in Fig. 4, 5.
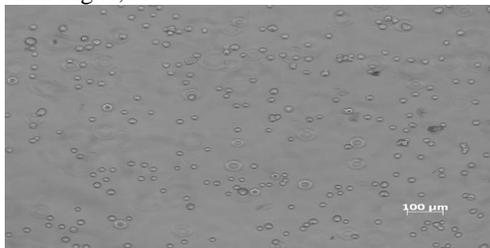
Fig. 4. The new seeded MC3T3 cell
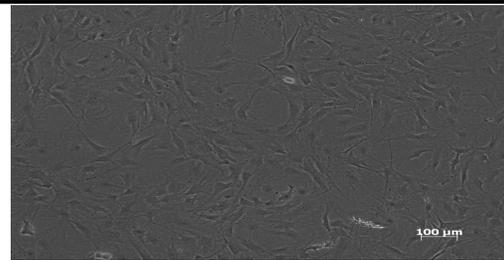
Fig. 5. 80% growing of the new seeded MC3T3 cell

Two major categories, under and avoid temperature, are described as follows:

6.1. Under temperature influence
6.1.1. Varying frequency
There are seven sets of cell culture plates, control_1, control_2 and five different excitation frequencies: 100 to 2000 Hz with wave form, amplitude (1 VPK, peak to peak), duration (20 min) keep the same. When one set of the culture plate is taking the stimulation in room temperature, all other six plates are kept inside the 37°C incubator. Therefore, each set has different exposure period to the temperature. Since MTT and RNA assays will cause the death of the cell, hence, it needs two control sets (used in all experiments of this study) to evaluate the initial and final cell concentration under nature growth without any external stimulation. The cell proliferation varied through different frequencies is shown in Fig. 6. 500 and 1000 Hz excitation are restraining the growth of cell, while 2000 Hz excitation plate has the same proliferation rate with the nature growth.
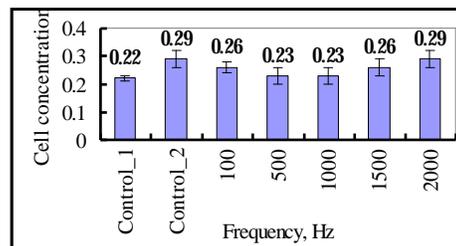
Fig. 6. Cell affected by excitation frequencies

6.1.2. Varying duration
The effect of cell growth on different excitation duration, with fixed frequency (2KHz), amplitude (1 VPK), and sine wave form, from 5 to 60 minutes is shown in Fig. 7. 40 minutes of excitation has increased the cell concentration almost 50% of the nature growth and over 50 minutes seams not affect much.
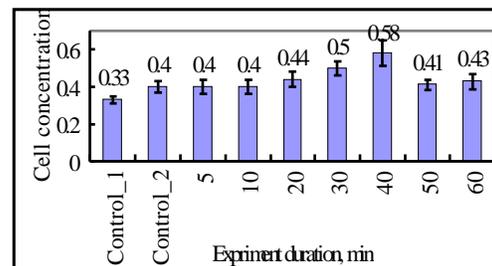
Fig. 7. Cell growth affected by excitation duration

6.1.3. Varying amplitude
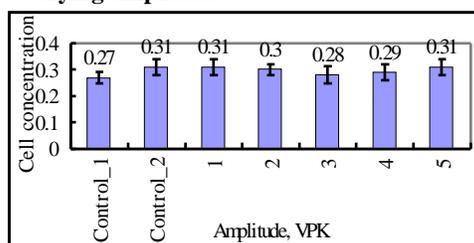
Fig. 8. Cell growth affected by excitation amplitude

The effect of cell growth on different excitation amplitude, with fixed frequency (2KHz), duration (40 min), and sine wave form, from 1 to 5 VPK (peak to peak voltage) is shown in Fig. 8. In the case, excitation amplitude seams not affect cell growth very much.

6.1.4. Varying number of repeated experiments

The effect of cell growth on different number of repeated experiments, with fixed frequency (2KHz), amplitude (1VPK), duration (40 min), and sine wave form, from once to five times is shown in Fig. 9. This experiment takes total 3 days to accomplish. Control_2 specimen is kept in the incubator without any disturbance while other sets are taken in and out of the incubator up to five times. Hence, no repeated experiment is growing faster than the nature growing cell in $37^{\circ}C$ 5% CO_2 incubator.
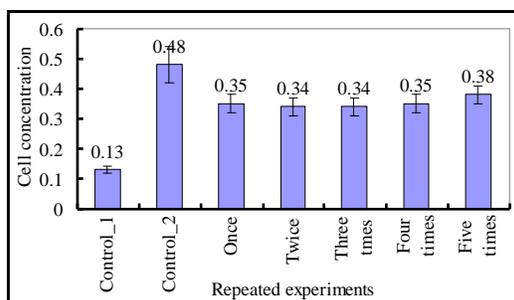
Fig. 9. Cell growth affected by repeated experiments

6.2. Avoid temperature influence

In this category, all cultured plates are taken out of the incubator when each of them has been proceeded the experiment in room temperature.

6.2.1. Varying frequency

The cell proliferation varied through different frequencies with fixed amplitude (1 VPK), duration (20 min), and sine wave form, is shown in Fig. 10. Similar to Fig. 6, 500 and 1000 Hz excitation are restraining the growth of cell, while 2000 Hz excitation plate has the same proliferation rate with the nature growth.
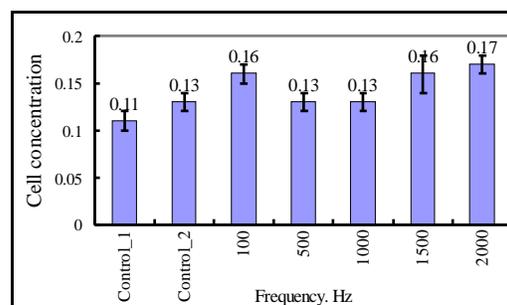
Fig. 10. Cell affected by excitation frequencies without temperature effects.

The electrophoresis diagram, shown in Fig.11, presents similar results as Fig.10, which is the more cell concentration (1.5K, 2KHz in Fig.10) measured by Fluorescence spectrometer, the lighter on electrophoresis bar (4, 5 in Fig.11).
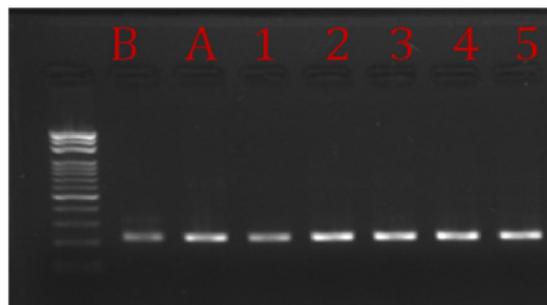
Fig. 11. Electrophoresis diagram with different excitation frequencies without temperature effects

6.2.2. Varying duration
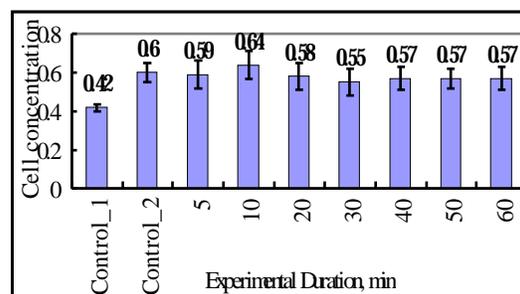
Fig. 12. Cell growth affected by excitation duration without temperature effects

The effect of cell growth on different excitation duration, with fixed frequency (2KHz), amplitude (1 VPK), and sine wave form, from 5 to 60 minutes is shown in Fig. 12. It is different from Fig. 7, 10 minutes of excitation has increased the cell concentration the most, but only about 7% of the nature growth and over 20 minutes seams not affect much.

6.2.3. Varying amplitude
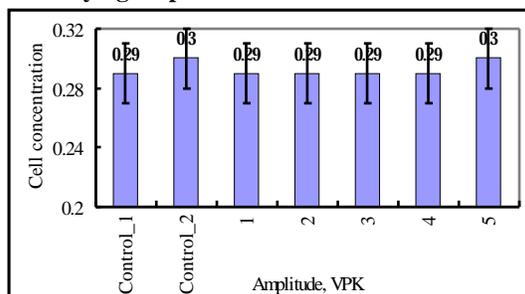
Fig. 13. Cell growth affected by excitation amplitude

The effect of cell growth on different excitation amplitude, with fixed frequency (2KHz), duration (40 min), and sine wave form, from 1 to 5 VPK (peak to peak voltage), and without temperature effect is shown in Fig. 13. It is similar to Fig. 6, excitation amplitude seams not affect cell growth very much.

6.2.4. Varying number of repeated experiments

The effect of cell growth on different number of repeated experiments, with fixed frequency (2KHz), amplitude (1VPK), duration (40 min), and sine wave form, from once to five times is shown in Fig. 14. This shows significant difference from Fig. 9. All the cell specimens including nature growing one, are not cultivated well enough compared to the plate always stays in the incubator (control_2) in Fig. 9. This result suggests that the culture environment, temperature, humidity, atmosphere with 5% CO_2, etc. are crucial to cultivate the osteoblast cell.
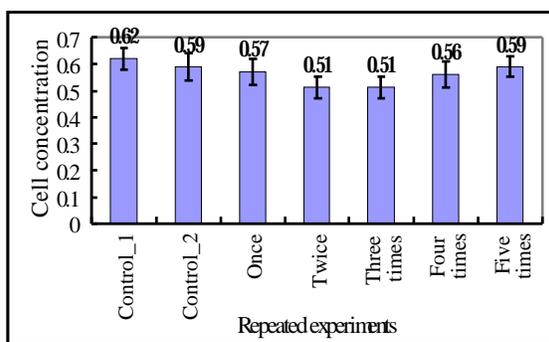
Fig. 14. Cell growth affected by repeated experiments without temperature effects

7. Summary

This research investigates the mechanical stimulation affects the proliferation of osteoblast cell. Different excitation parameters, temperature, broad range of frequencies, amplitude, duration, repeated number of experiments, etc., are compared for the cultivation of cells. The aim for this research is to understand the vibration stimulation of the murine osteoblast cell first and then use this model to analyze the related parameters of real human osteoblast or other cells in the future. Therefore, the result of this research is quite useful for physician's reference.

Several aspects are discovered during this research and listed as follows:

1. Different frequencies of the stimulation have different effects onto the proliferation of the cell. Some frequencies (500, 1KHz) will suppress the proliferate of the cell, while others (1.5K, 2KHz) will increase the number of cell.
2. In subsonic range of frequencies excitation, the amplitude plays no significant role in the cultivation of cell.
3. The culture environment, including temperature, humidity, atmosphere with 5% CO_2, etc. are crucial and will help to cultivate the osteoblast cell.

References

1. Yu-Ting Chang, Investigate the Effect of Physical Stimulation on Osteoporosis Using Animal Models, 2009. Master Thesis, National Cheng Kung University, Tainan, Taiwan, R.O.C.
2. Ming-Ci Tsai, Effects of Different Stimulation Time of sPEMF on Apoptosis of Osteoclast-Like Cells Developed from Coculture of Osteoblast Cells and Bone Marrow Cells, 2002, Master Thesis, Chung Yuan Christian University, Tao Yuan, Taiwan, R.O.C.
3. Sjoerd Rutten, Peter A. Nolte, Clara M. Korstjens, Marion A. van Duin, Jenneke Klein-Nulend, Low-intensity pulsed ultrasound increases bone volume, osteoid thickness and mineral apposition rate in the area of fracture healing in patients with a delayed union of the osteotomized fibula, Bone, 2008, 43: 348–354.
4. Sjoerd Rutten, Peter A. Nolte, Clara M. Korstjens, Jenneke Klein-Nulend, Low-intensity pulsed ultrasound affects RUNX2 immunopositive osteogenic cells in delayed clinical fracture healing, Bone, 2009, 45: 862–869.
5. Bo-Shiang Tsui, Studies on the response of neural tissues following ultrasonic stimulation, 2001. Master Thesis, Chung Yuan Christian University, Tao Yuan, Taiwan, R.O.C.
6. P. Reher, N. Doan, B. Bradnock, S. Meghji, M. Harris, Therapeutic Ultrasound for Osteoradio-necrosis: an In Vitro Comparison Between 1MHz and 45 kHz Machines, European Journal of Cancer, 1998, 34 (12): 1962-1968.
7. Jimmy Kuan-Jung Li, James Cheng-An Lin, Hwa-Chang Liu, Jui-Sheng Sun, Rouh-Chyu Ruaan, Chung Shih, Walter Hong-Shong Chang, Comparison of ultrasound and electromagnetic field effects on osteoblast growth, Ultrasound in Medicine & Biology, 2006, 32 (5): 769-775.
8. A. Myrdycz, Dorothee Callens, K. Kot, F. Monchau, E. Radziszewski, A. Lefebvre, H.F. Hildebrand, Cells under stress: a non-destructive evaluation of adhesion by ultrasounds, Biomolecular Engineering,

2002, 19: 219-225.
9. Yong Pan, Yong Hao, Tongwei Chu, Changqing Li, Zhengfeng Zhang, Yue Zhou, Ultrasonic-assisted extraction, chemical characterization of polysaccharides from Yunzhi mushroom and its effect on osteoblast cells, Carbohydrate Polymers, In Press, Corrected Proof, Available online 4 February 2010.
10. Yasuhiro Tanimoto, Yo Shibata, Yu Kataoka, Takashi Miyazaki, Norihiro Nishiyama, Osteoblast-like cell proliferation on tape-cast and sintered tricalcium phosphate sheets, Acta Biomaterialia, 2008, 4: 397–402.
11. M. Lewandowska-Szumiel, K. Sikorski, A. Szummer, Z. Lewandowski, W. Marczynski, Osteoblast response to the elastic strain of metallic support, Journal of Biomechanics, 2007, 40: 554–560.
12. Takahiro Suzuki, Mika Hukkanen, Ryo Ohashi, Yoshiyuki Yokogawa, Kaori Nishizawa, Fukue Nagata, Lee Buttery, Julia Polak, Growth and Adhesion of Osteoblast-Like Cells Derived from Neonatal Rat Calvaria on Calcium Phosphate Ceramics, Journal of Bioscience and Bioengineering, 2000, 89 (1): 18-26.
13. Tetsuya Yuasaa, Youji Miyamoto, Kunio Ishikawa, Masaaki Takechi, Yukihiro Momota, Seiko Tatehara, Masaru Nagayama, Effects of apatite cements on proliferation and differentiation of human osteoblasts in vitro, Biomaterials, 2004, 25: 1159–1166.
14. Xue Qu, Yuqing Wan, Hanwei Zhang, Wenjin Cui, Jianzhong Bei, Shenguo Wang, Porcine-derived xenogeneic bone/poly (glycolide-co-lactideco-caprolactone) composite and its affinity with rat OCT-1 osteoblast-like cells, Biomaterials, 2006, 27: 216–225.
15. Zhongli Shi, Xin Huang, Yurong Cai, Ruikang Tang, Disheng Yang, Size effect of hydroxyapatite nanoparticles on proliferation and apoptosis of osteoblast-like cells, Acta Biomaterialia, 2009, 5: 338–345.
16. Heidi A. Declercq, Ronald M.H. Verbeeck, Leo I.F.J.M. De Ridder, Etienne H. Schacht, Maria J. Cornelissen, Calcification as an indicator of osteoinductive capacity of biomaterials in osteoblastic cell cultures, Biomaterials, 2005, 26: 4964–4974.
17. Ilse Y. Pieters, Natasja M.F. Van den Vreken, Heidi A. Declercq, Maria J. Cornelissen, Ronald M.H. Verbeeck, Carbonated apatites obtained by the hydrolysis of monetite: Influence of carbonate content on adhesion and proliferation of MC3T3-E1 osteoblastic cells, Acta Biomaterialia, 2010, 6 (4): 1561-1568.
18. Virginie Dumas, Anthony Perrier, Luc Malaval, Norbert Laroche, Alain Guignandon, Laurence Vico, Aline Rattner, The effect of dual frequency cyclic compression on matrix deposition by osteoblast-like cells grown in 3D scaffolds and on modulation of VEGF variant expression, Biomaterials 2009, 30: 3279–3288.
19. Wang Bochu, Long Xuefeng, Liu Yiyao, Duan Chuanren, A. Sakanishi, The effects of mechanical vibration on the microstructure of Gerbera jamesonii acrocarpous callus, Colloids and Surfaces B: Biointerfaces, 2002, 23: 1–5.
20. Shigeo M. Tanaka, Jiliang Li, Randall L. Duncan, Hiroki Yokota, David B. Burr, Charles H. Turner, Effects of broad frequency vibration on cultured osteoblasts, Journal of Biomechanics, 2003, 36: 73–80.
21. In Sook Kim, Yun Mi Song, Tae Hyung Cho, Je Yeon Kim, Franz E. Weber, Soon Jung Hwang, Synergistic action of static stretching and BMP-2 stimulation in the osteoblast differentiation of C2C12 myoblasts, Journal of Biomechanics, 2009, 42: 2721–2727.
22. Lin Tang, Zhu Lin, Yong-ming Li, Effects of different magnitudes of mechanical strain on Osteoblasts in vitro, Biochemical and Biophysical Research Communications, 2006, 344: 122–128.
23. L.A. Viscontia, E.H.K. Yenb, R.B. Johnson, Effect of strain on bone nodule formation by rat osteogenic cells in vitro, Archives of Oral Biology, 2004, 49: 485-492.
24. Ludwika Kreja, Astrid Liedert, Sofia Hasni, Lutz Claes, Anita Ignatius, Mechanical regulation of osteoclastic genes in human osteoblasts, Biochemical and Biophysical Research Communications, 2008, 368: 582–587.
25. Katerina K. Papachroni, Demetrios N. Karatzas, Kostas A. Papavassiliou, Efthimia K. Basdra and Athanasios G. Papavassiliou, Mechanotransduction in osteoblast regulation and bone disease, Trends in Molecular Medicine, 2009, 15 (5): 208-216.
26. C. Frias, J. Reis, F. Capela e Silva, J. Potes, J. Simoes, A.T. Marques, Polymeric piezoelectric actuator substrate for osteoblast mechanical stimulation, Journal of Biomechanics, In Press, Corrected Proof, Available online 8 February 2010.
27. Zanne Henriksen, Jeffrey F. Hiken, Thomas H. Steinberg, Niklas R. Jorgensen, The predominant mechanism of intercellular calcium wave propagation changes during long-term culture of human osteoblast-like cells, Cell Calcium, 2006, 39: 435–444.
28. Bo Wun Huang, Huang Kuang Kung, Kuan-Yu Chang, Bo Kai Hsu, Jung-Ge Tseng, Human Cranium Dynamic Analysis, Life Science Journal, Vol. 6, No.4, pp.15-22.

Temperature rise of alveolar bone during dental implant drilling using the finite element simulation

Ching-Chieh Huang [1], Yau-Chia Liu [1], Li-Wen Chen [2] and Yung-Chuan Chen [2*]

1 Medical Device Section, Metal Industries Research & Development Centre, Kaohsiung, Taiwan 91201, R.O. China. 2 Department of Vehicle Engineering, National Pingtung University of Science and Technology, Pingtung, Taiwan 91201, R.O. China. chuan@mail.npust.edu.tw; Received , February 2010

Abstract: In this study, a three-dimensional elastic-plastic dynamic finite element model is used to simulate the alveolar bone temperature rise during dental implant drilling. An experimental setup was designed to verify the feasibility of the proposed dynamic finite element model. The peak bone temperature within the alveolar bone is investigated through both simulations and experiments. The results indicate that the proposed elastic-plastic dynamic finite element model can provide a good prediction of the alveolar bone temperature rise during the implant drilling. The result also indicated that the peak bone temperature occurs at the interface of cortical bone and cancellous bone for a fixed feeding rate. [Life Science Journal. 2010; 7(1): 68 – 72] (ISSN: 1097 – 8135).

1. Introduction

Dental implant is an artificial dental root used to replace a natural one. It is generally made of pure titanium or titanium alloy. At present, the dental implantology has been considerably matured, but how to improve the success rate of implantation is still the major direction in the relevant research field.

The study by Alberktsson et al [1] indicated that the success of endosteal implants depends on the primary healing capability of alveolar bones. The temperature rise within the alveolar bone during bone drilling is the one critical factor that affects the primary healing capability of alveolar bone. Many researchers [2-5] showed that heat generation is an important problem during bone drilling since the heat is not easily conducted away from the drill site and thus the bone is at significant risk of thermal damage. The literatures indicated that temperatures ranging from $56\,^{\circ}C$ to $70\,^{\circ}C$ are harmful to bone tissue because alkaline phosphatase (AP) is transformed at that level [5-9]. Eriksson and Albrektsson [10] inferred that temperatures below the transference point of AP ($53\,^{\circ}C$) could be considered unfavorable to the reparative capability of bone, as burning and resorption of fat cells together with sluggish blood flow were observed. The above-mentioned phenomena are called osseous necrosis. Eriksson and Albrektsson [10-12] reported in their studies that bone would bear a threshold temperature ranging from $44\,^{\circ}C$ to $47\,^{\circ}C$ for 1 minute without defective bony regeneration. Finally, Tehemar concluded that heating up to $47\,^{\circ}C$ could be considered as the optimal limit that bone can withstand without necrosis [12].

As mentioned above, decreasing the temperature rises caused by surgical drillings can enhance the primary healing capability of alveolar bones and further increase the success rate of implantation. The temperature rise measurement of surgical drilling can be generally divided into two types, infrared rays [13-14] and thermocouples [15-16], both of which have certain limitations. Infrared rays can only be applied to measure the temperature distribution on the bone surface. In experiments, the thermocouple can be placed no closer than 0.5 mm from the edge of the drilled hole to avoid the damage of thermocouple [17]. Since the frictional heat generated by the drilling process is not easily conducted away by the bone, the temperature measurements obtained using the thermocouple are not able to provide a true indication of the peak temperature in the immediate vicinity of the drilled hole. Accordingly, the present study proposes a dynamic finite element model to simulate the thermal contact behavior between the bone and the drill bit during bone drilling. Both the temperature rise and the temperature distribution near the drilled hole to be effectively reproduced through these simulations.

2. Experimental measurement of bone temperature rise

Figure 1 presents a schematic illustration of the experimental setup used to measure the temperature rise within the bone during drilling. As shown, the major components include a drilling machine, a dental drill bit, a biomechanical test block, an electronic data acquisition system (model 2680A, Fluke Corporation), a computer system, thermal couples (K-type), a torque sensor, a load cell, a motor controller, and a jig. Biomechanical test blocks supplied by Sawbones [18] are used to replace human alveolar bone in this study. The mechanical properties of biomechanical test blocks and human bones are similar. The pilot drill bit (Straumann, Swiss) used in experiments is made of stainless steel with a diameter of 2.2 mm. Figure 2 shows two thermocouples placed at positions x=0.5 mm from the edge of the drilled hole. The depths or the vertical positions of the two thermocouples are at z= 1 and z= 6 mm (z= 0 indicates the upper surface of the bone), respectively. The drilling speed and the feeding rate in all the experiments were fixed at 800 rpm and 0.9 mm/s, respectively.
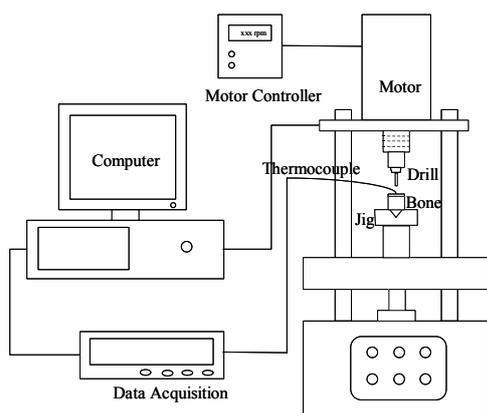
Figure 1. Experimental setup for bone temperature rise measurement
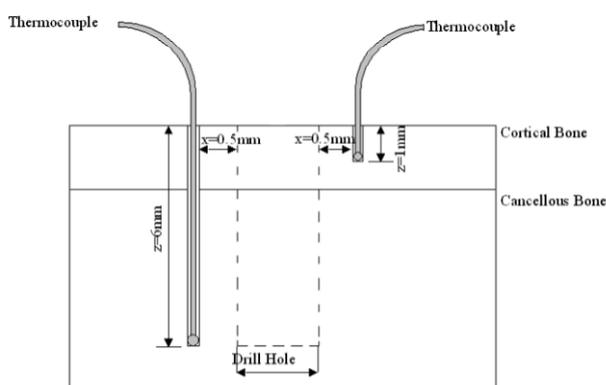
Figure 2. Schematic illustration of thermocouple embedded positions

3. Finite Element Model

A three-dimensional elastic-plastic dynamic temperature-displacement coupled finite element model (FEM) is used to simulate the thermo-mechanical behavior of the contact region between the drill bit and the alveolar bone during drilling. The simulations are performed using the commercial ABAQUS/Explict package (2008), and a dynamic failure criterion is applied to control the element removal during the drilling operation. In performing the simulations, the thermal contact behavior between the drill bit and the alveolar bone is modeled using contact elements.

The shape of alveolar bone is extremely complicated, but the region of particular interest is in the immediate vicinity of the drilled hole for a single implantation. Thus, without loss of generality, the domain for the numerical simulations is simplified as a circular disc. The alveolar bone model used in this study is 10 mm in diameter and 20 mm in height. As shown in Fig. 3, the thicknesses of cortical bone and cancellous bone are taken as 2 mm and 18 mm, respectively. These dimensions are taken according to the maximum width of the single edentulous zone as well as the relevant dimensions of human alveolar bone. The drill bit and bone contact geometry considered in this study is shown in Fig. 4. The finite element model comprises a total of 241,296 eight-node hexagonal elements and 250,975 nodes. The

contact behavior between the drill bit and the bone is simulated using 25,800 contact elements. According to the previous study [19], the coefficient of friction is taken as 0.3. Figure 4 shows the enlarged view of the drill bit and bone contact finite element model.
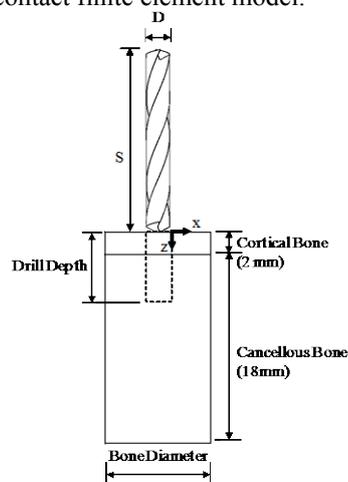
Figure 3. Configuration of a drill bit and bone contact model
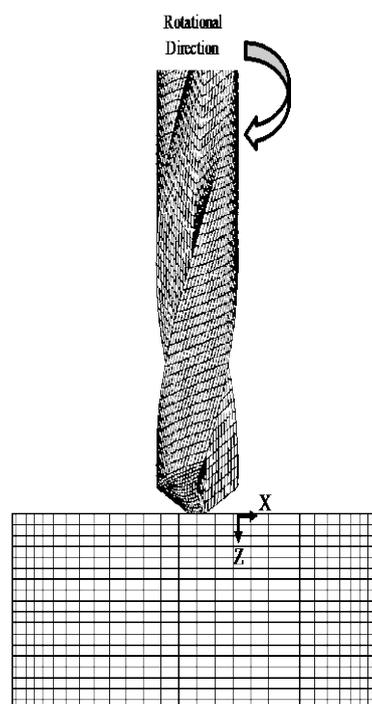
Figure 4. A enlarge view of the drill bit and bone contact finite element model

The alveolar bone used in this study is a biomechanical test block supplied by Sawbones [18] according to the testing standards of ASTM D-1621, D-1623, and D-273. The material of drill bit is SUS420 stainless steel. The mechanical properties of the drill bit and bone used in finite element simulations are summarized in Table 1. The initial temperatures of the drill bit and the bone in simulations are both taken as $25\,^{\circ}$C

Table 1. Mechanical properties of the drill bit and bone used in FE simulations

Material properties	Biomechanical test blocks [18]		Drill bit [20]
	Cortical	Cancellous	
Density(kg / m³)	1640	320	7800
Young's Modulus(MPa)	16000	2840	200000
Poisson's Ratio	0.30	0.06	0.24
Yielding Stress(MPa)	106.99	5.69	585.00
Tensile Stress(MPa)	107.00	5.70	760.00
Specific Heat (J /kg-℃)	1640	1570	460
Thermal Conductivity (W / m-k)	0.45	0.05	24.90
Thermal Expansion (k⁻¹)	6.30×10^{-5}	6.30×10^{-5}	1.03×10^{-5}

4. Results and Discussions

The feasibility of the proposed dynamic FEM model was confirmed by comparing the numerical solutions for the variations of bone temperature with the experimental results. Figure 5 and 6 present the simulation and experiment results of the temperature variation during drilling at the positions of x=0.5, z=1.0 mm and x=0.5, z=6.0 mm, respectively. The I-bars represent the temperature range of experimental results and the empty symbols are the corresponding mean values. The solid symbols indicate the numerical results obtained from the proposed dynamic finite element model. Both figures show good agreements exist between the simulation results and the experimental mean values. The largest deviation between the simulation and experimental results is less than $2\,^{\circ}C$. Thus, the validity of the proposed dynamic FEM model is confirmed.
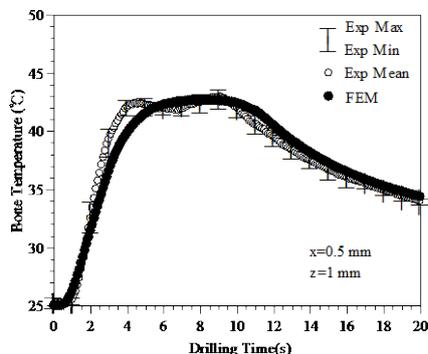
Figure 5. Comparison of experimental and numerical results for variation of bone temperature with drilling time at depth z=1 mm
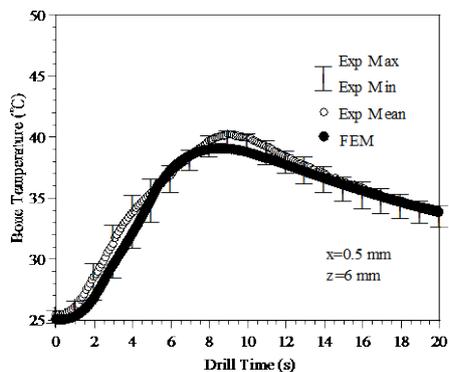
Figure 6. Comparison of experimental and numerical results for variation of bone temperature with drilling

time at depth z=6 mm

It is important to decide what the peak temperature is and where it is occurred during dental implant surgical drilling. However, because of the technical reason, the thermocouple can be placed no closer than 0.5 mm from the edge of the drilled hole. In the following, the proposed dynamic finite element is used to investigate the peak bone temperature during drilling. The drilling speed and the feeding rate in all the finite element simulations were fixed at 800 rpm and 0.9 mm/s. Figure 7 shows that the bone temperature distribution at five different distances from the edge of the drilled hole, i.e. x=0.1 ~0.5 mm. The measurement depth in Fig. 7 is at z= 1 mm. The results show that the bone temperature increases rapidly in the region adjacent to the drilled hole (i.e. x=0.1 mm). It can be observed that the peak temperatures at measurement positions x = 0.1, 0.2 and 0.5 mm are found to be 55.3, 54.3 and 50.3 $^{\circ}C$, respectively. The peak temperature varies by as much as $5\,^{\circ}C$ within a distance of 0.5 mm from the drilled hole. It also can be found that the drilling time taken to have the peak temperature occurred is different for different measurement positions.
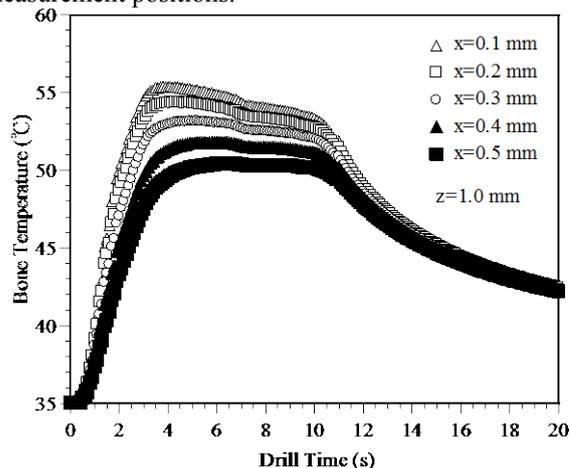
Figure. 7. Variation of bone temperature with drilling time at different measurement distances from the drill hole with a depth of z=1 mm

In the following, the bone temperature distribution along the drilling depth is explored by finite element simulations. The drilling depth of the drill bit is taken as 6 mm. The measurement distance from the drill hole is taken as x = 0.1 mm. Firstly, the variation of bone temperature within the cortical bone is discussed. The thickness of the cortical bone used in this study is 2.0 mm. Figure 8 shows the variation of bone temperature with drilling time at four different measurement depths, i.e. z= 0.2, 0.4, 0.6, 1.0 mm. The bone temperature rise at various depths of z= 1.2 to 2.0 mm is shown in Fig. 9. These two figures show that the bone temperature increases as the depth increases. The peak bone temperature within the cortical bone is 63.5 $^{\circ}C$ occurred at the depth of z=2.0 mm.
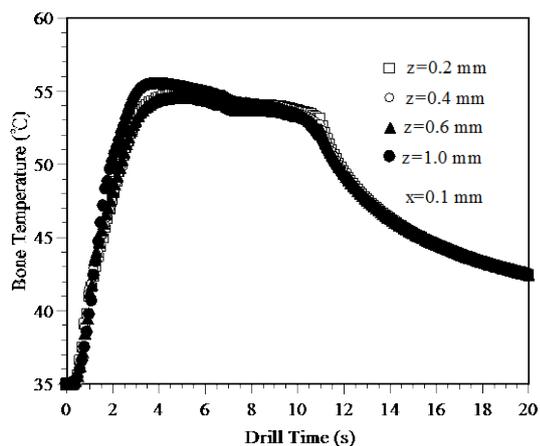
Figure 8. Variation of bone temperature with drilling time at measurement depths of z= 0~ 1.0 mm
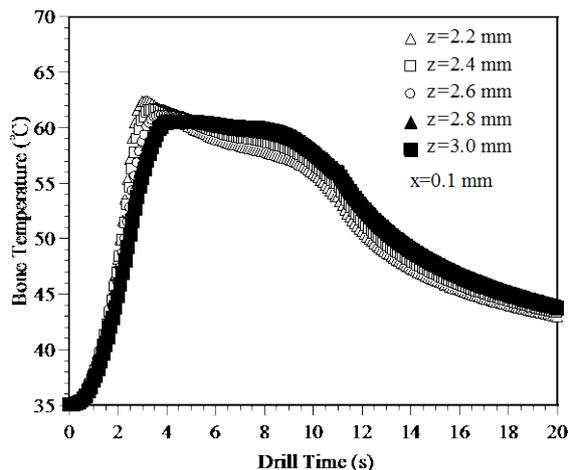
Figure 10. Variation of bone temperature with drilling time at measurement depths of z= 2.2~ 3.0 mm
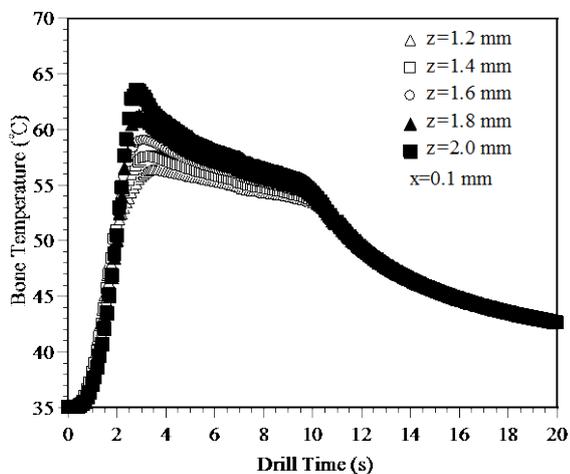
Figure 9. Variation of bone temperature with drilling time at measurement depths of z= 1.2~ 2.0 mm
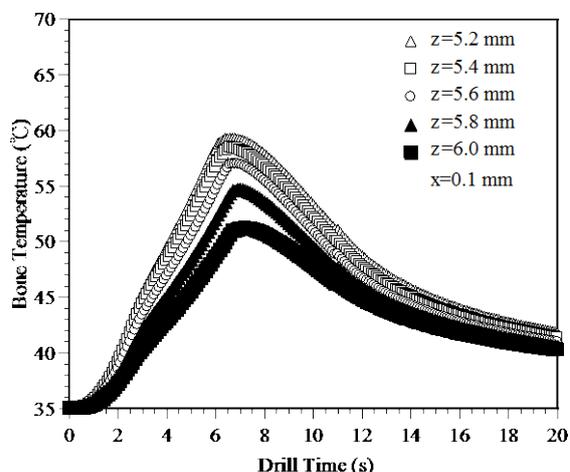
Figure 11. Variation of bone temperature with drilling time at measurement depths of z= 5.2~ 6.0 mm

However, the profile of bone temperature distribution within the cancellous bone is different to the one in the cortical bone. Figures 10 and 11 present the variation of bone temperature within the cancellous bone for depths of z=2.2 ~ 3.0 mm and z=5.2 ~6.0 mm, respectively. It can be found in Figs. 10 and 11 that the peak bone temperature decreases as the depth increases. The peak bone temperature is found to be 62.3 and 51.2 $^\circ$C in Figs. 10 and 11, respectively. To summarize the results shown in Figs. 8 to 11, it can be found that the peak bone temperature occurs at the interface of cortical bone and cancellous bone for a constant feeding rate. According to the simulation data, the peak bone temperature is 63.5 $^\circ$C occurred at drilling time of 3 seconds in this study.

5. Conclusion

In this study a 3D elastic-plastic dynamic finite element model is proposed to simulate the bone temperature rise during a dental implant drilling process. An experimental setup was designed to verify the feasibility of the proposed dynamic FEM model. The numerical results support the following major conclusions:

1. The proposed elastic-plastic dynamic FEM model can provide a good prediction of the alveolar bone temperature rise in the implant drilling process.
2. Because of the technical reason, the thermocouple is not able to detect the peak temperature in the immediate vicinity of the drilled hole. This problem is effectively resolved in the elastic-plastic dynamic FE model proposed in this study.
3. The temperature rise within the cortical bone is higher than what within the cancellous bone.
4. The peak bone temperature occurs at the interface of cortical bone and cancellous bone for a fixed feeding rate.

Corresponding Author:
Professor Yung-Chuan Chen
chuan@mail.npust.edu.tw

References
1. Alberktsson T, Branemark PI, Hansson HA, Lindstrom J. Osseointegrated titanium implants: requirements for ensuring a long-lasting, direct bone-to-implant anchorage in man. Acta Orthopedica Scandinavica, 1981, 52: 155-170.
2. Collins DH. Surgical changes around nails and screws in bone. Journal of Pathology, 1953, 65: 109-121.
3. Moss RW. Histopathologic reaction of bone to surgical cutting. Journal of Oral Surgery, 1964, 17: 405-414.
4. Lavelle C, Wedgwood D. Effect of internal irrigation on frictional heat generated from bone drilling. Journal of Oral Surgery, 1980, 38: 499-503.
5. Tehemar S. Factors affecting heat generation during implant site preparation: a review of biologic observations and future considerations. The International Journal of Oral & Maxillofacial Implants, 1999, 14: 127-136.
6. Matthews LS, Hirsch C. Temperatures measured in human cortical bone when drilling. Journal of Bone and Joint Surgery, 1972, 54: 297-308.
7. Ludewig R. Temperaturmessungen beim Knochensagen [thesis]. Gissen: Univ of Gissen, 1972.
8. Rhinelander F, Nelson CL, Stewart RD, Stewart CL. Experimental reaming of the proximal femur and acrylic cement implantation: vascular and histologic effects. Clinical Orthopaedics and Related Research, 1979, 141: 74-89.
9. Berman AT, Reid JS, Yaniko DR, Sih GC, Zimmerman MR. Thermally induced bone necrosis in rabbits. Relationship to implant failure in humans. Clinical Orthopaedics and Related Research, 1984, 186: 284-292.
10. Eriksson RA, Albrektsson T, Grane B, McQueen D. Thermal injury to bone. A vital microscopic description of heat effects. International Journal of Oral Surgery, 1982, 11: 115-121.
11. Eriksson RA, Albrektsson T. Temperature threshold levels for heat induced bone tissue injury: a vital microscopic study in rabbit. Journal of Prosthetic Dentistry, 1983, 50: 101-107.
12. Eriksson RA, Albrektsson T. The effect of heat on bone regeneration: An experimental study in the rabbit using the bone growth chamber. Journal of Oral and Maxillofacial Surgery, 1984, 42: 705-711.
13. Watanabe F, Tawada Y, Komatsu S, Hata Y. Heat distribution in bone during preparation of implant sites: heat analysis by real-time thermography. The International Journal of Oral & Maxillofacial Implants, 1992, 7: 212-219.
14. Benington IC, Biagioni PA, Crossey PJ, Hussey DL, Sheridan S, and Lamey PJ. Temperature changes in bovine mandibular bone during implant site preparation: an assessment using infrared thermography. Journal of Dentistry, 1996, 24: 263-267.
15. Eriksson RA, Adell R. Temperatures during drilling for the placement of implants using the osseointegration technique. Journal of Oral and Maxillofacial Surgery, 1986, 44: 4-7.
16. Yacker M, Klein M. The effect of irrigation on osteotomy depth and bur diameter. The International Journal of Oral & Maxillofacial Implants, 1996, 11: 634-638.
17. Cordioli G, Majzoub Z. Heat generation during implant site preparation: an in vitro study. The International Journal of Oral & Maxillofacial Implants, 1997, 12: 186-193.
18. http://www.sawbones.com
19. Mellal A, Wiskot HW, Botsis J, Scherrer SS, Belser UC. Stimulating effect of implant loading on surrounding bone : comparison of three numerical models and validation by in vivo data. Clinical Oral Implants Research, 2004, 15: 239-241.
20. http://www.matweb.com

Rapid Prototyping and Multi-axis NC Machining for The Femoral Component of Knee Prosthesis

Jeng-Nan Lee[1*], Hung-Shyong Chen[1], Chih-Wen Luo[1] and Kuan-Yu Chang[2]

1 Department of Mechanical Engineering, Cheng Shiu University, Kaohsiung County, Taiwan 833, R.O. China.
2 Mackay Memorial Hospital Taitung Branch, Taitung, Taiwan 833, R.O. China.
jengnan@csu.edu.tw

_____

Abstract: In this paper, a design system combining clinical experience and engineering knowledge was developed for the manufacture for femoral component of knee prosthesis. The femoral component is developed on a prescription basis and is unique for each patient. The medical image of the femoral component obtained according to the patient CT. The necessary constrains based on surgical experience were integrate into the CAD system. The rapid prototyped model was built as the reference for review. In the process planning, the fixture is designed and the cutting sequence for rough and finish machining is arranged. Through the application of CAM software, the interference-free toolpath and the cutter location file for multi-axis NC machining are generated. The cutting simulations with solid model are performed to verify the generated toolpath and NC program. The result of this work can be of crucial benefit in research and development. [Life Science Journal. 2010; 7(1): 79 – 83] (ISSN: 1097 – 8135).

_____

1. Introduction

The biomedical engineering has great advancements in the health care of patient. Many of these are related to various technologies such as imaging systems, reverse engineering, rapid prototyping, and multi-axis NC machining. These technologies allow users to increase productivity and decrease the cycle time for product development. The medical industry has certain applications which are well suited to these technologies.

Artificial knee replacement surgery is becoming more common as the population of the world. Each year, over two million osteoarthritis joints are replaced with artificial joints worldwide. The main reason for replacing any arthritic joint with an artificial joint is to stop the bones from rubbing against each other [1]. A primary concern of these devices for the hip and knee is to eliminate pain and improved mobility [2].

Artificial knee replacements may be classified in two basic types: cemented prosthesis and cementless prosthesis. Cemented prosthesis is held in place by a type of epoxy cement for fixation, whereas cementless prosthesis has a rough, porous surface intended for bone to grow into and attach the prosthesis to the bone [3, 4].

In the knee prosthesis design, Sathasivam and Walker [5] determines the femoral and tibial bearing surface geometries which will induce the least destructive fatigue mechanisms in the polyethylene whilst conserving the laxity of the natural knee. Sixteen knee designs were generated by varying four parameters systematically to cover the range of contemporary knee designs. Liau et al. [6] investigates the effects of malalignment on stresses in tibial polyethylene component of total knee protheses. The greatest increase of contact stress and von Mises stress was occurred in the high conformity flat-on-flat design of knee prosthesis under the severest malalignment condition. The high conformity curve-on-curve design of knee prosthesis has the minimal risk of polyethylene wear under the

malalignment conditions. The orthopedic industry consults with surgeons in the development of new implant systems and related instrumentation. Their expertise and medical training coupled with bioengineering and manufacturing capability provides the collaboration to advance the state of the art of these implants. The soft tissue integrity and bone remodeling all relate to the success of the implant. Thus, solid modeling and rapid prototyping can bridge the gap between the designers and the manufacturing engineers which is essential for concurrent engineering [4].

Gouging is a very important problem in finishing complicate surface. Gouging occurs when portions of the profile of cutting tool penetrate the designed surface. Two types of gouging problems, local gouging and rear gouging, need to be considered in the process of toolpath generation. The mismatch in curvatures between the cutting tool and the designed surface can cause local gouging. Rear gouging occurs as a result of the interference between the tool geometry and the local surface shapes. Rao and Sarma [7] described an exact method for the detection and elimination of local gouging in five-axis machining using a flat-end tool. Lee [8] presented a new methodology for determining feasible tool orientation of toroidal milling cutter with collision and gouging avoidance in five-axis machining of free-form surface.

In this paper, the femoral component of knee prosthesis is developed based on the CAD/CAM system and rapid prototyping. Rapid prototyped model is fabricated from three-dimensional CAD model for concurrent development. The generated multi-axis toolpath from CAM is converted to the NC code. Figure 1 shows the flowchart of the integrated research for solid modeling, rapid prototyping, and NC machining of femoral component.
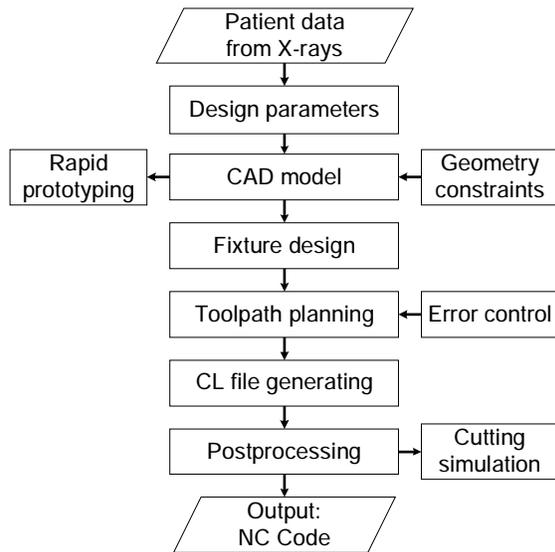
Figure 1. Flowchart of the solid modeling and manufacture for femoral component of knee prosthesis.

2. Geometry of femoral component

Artificial knee replacement is made up of three main parts. The femoral component (top portion) replaces the bottom surface of the femur and the groove where the patella fits. The tibial component (bottom portion) replaces the top surface of the tibia. The patella component (kneecap potion) replaces the surface of the patella where it glides in the groove on the femur, as shown in Figure 2. The components are often anatomically shaped or contoured designs versus basic geometric shapes. They are produced as a family in a range of sizes that can be selected at surgery to match the patient requirements.

A painful knee as a result of osteoarthritis (OA) can severely affect your mobility. Custom-made femoral component is necessary for those situations when an off-the-shelf standard size implant is not suitable. To develop the implant, the surgeon and the engineer determine the basic requirements and design criteria use either patient X-rays, the computer tomography (CT) scans or magnetic resonance image (MRI). To provide the best fill and fit femoral component to each individual patient, the shape is of major concern. The goal for the femoral component design was to define a product that met manufacturing requirements and surgical expectations. The first step is computer-aided design. The design features of a femoral component are specified as shown in Figure 3. The geometry of femoral component may also be modeled to serve as a reference.
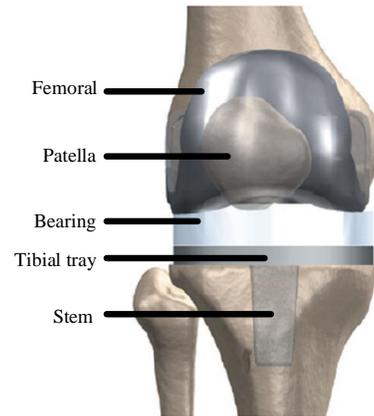
Figure 2. Schematic illustration of the anatomy of total knee prosthesis [1].

(a) Front view.   (b) Left side sagittal view.

(c) Right side sagittal view.
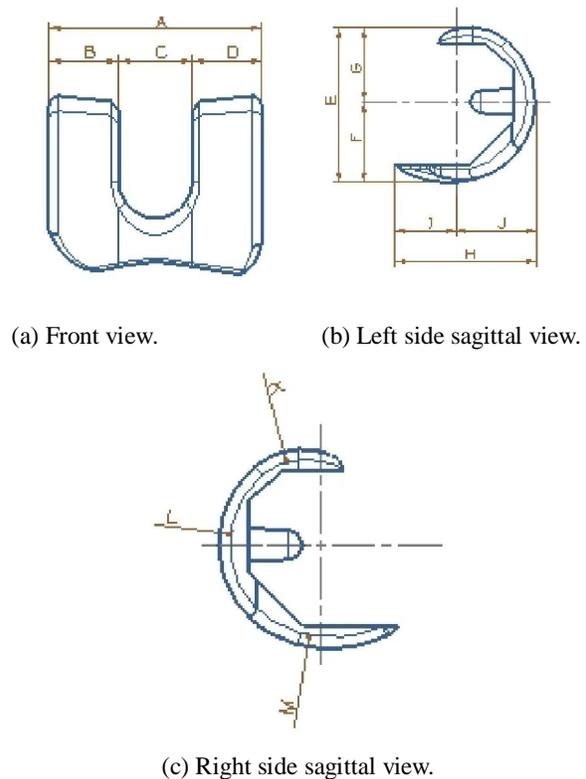
Figure 3. The design parameters of femoral component model.

3. Rapid prototyping of femoral component

Rapid prototyping and manufacturing technology was developed in the late 1970s and early 1980s. The benefits of rapid prototyping (RP) are the enhanced visualization capability and the decrease of cycle time required to produce prototype parts. The physical model of a part is made directly from a three-dimensional CAD model by rapid prototyping. The materials used include liquid resin, fusing powdered thermoplastic materials, ceramics, ABS, investment wax, etc. The layer creation

techniques comprise liquid-layer curing, extrusion of melted plastic, binder-droplet deposition onto powder layer, laser-driven, electron-beam, etc. The RP primitives provided actual full-scale models that can be handled, analyzed, and used for future development.

The RP process begins with a CAD model. A preferably solid modeling CAD system is a key component of success. Most popular solid model CAD systems require translated processors to create the stereolithography (STL) file for a RP system. The degree of resolution for the model surfaces must be specified by entering a quality value in the interface of CAD system. This step assures that the CAD data is input to the RP machine in the tessellated STL surfaces of the object are represented as numerous tiny triangles. After creating STL model files, the next step is to simulate the process of build prototype via Catalyst[®] software (pre-process). The simulation software automatically slices, calculates support structures, and creates toolpaths. Figure 4 shows the computational steps in producing a stereolithography file of the femoral component.
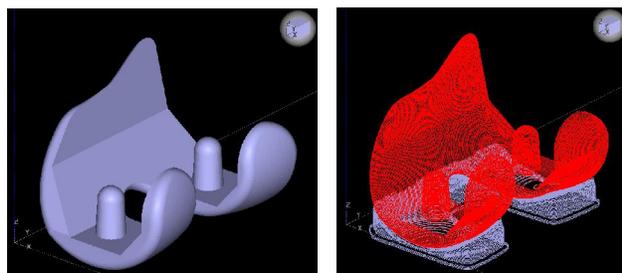
(a) Three dimensional structure is description of the femoral component.

(b) Support planed.
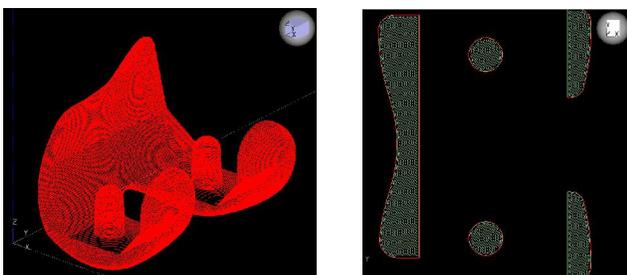
(c) The femoral component path is is divided into slices.

(d) A set of tool determined for manufacturing each slice.

Figure 4. The computational steps in producing a stereolithography file.

3.1 Fused-deposition modeling

After the simulation of slicing and the extruder path, a stereolithography file is imported into rapid prototype machine. The process of additive manufacturing is used to build part in layers. The technique of fused-deposition modeling (FDM) is applied in this paper. In the FDM process, as shown in Figure 5, parts are built layer by

layer. The extrusion heads move in two principal directions over a table. The table can be raised and lowered as needed. A thermoplastic filament is extruded through the small orifice of a heated die. The initial layer is placed on a foam foundation by extruding the filament at a constant rate while the extrusion heads follow a predetermined tool path. When the first layer is completed, the table is lowered so that subsequent layers can be superposed. Whilst the part is completely created, support structures are dissolved in a water-based solution or snapped off by hand. The RP prototype can be sent to the surgeon for review and approval prior to fabricating the femoral component.
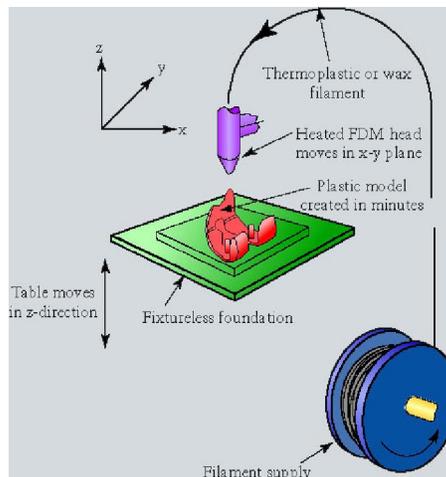
Figure 5. Schematic illustration of the fused-deposition modeling process [3].

4. CAM for the femoral component

The femoral component has to be machined on multi-axis CNC machine tools because of their complex shapes. Machining sequences and cutter location (CL) files can be created in the manufacturing module of UniGraphics NX software, which is the same CAD/CAM environment that the solid model was created in. In order to clamp and manufacture the femoral component, the design model was modified to become the workpiece model for cutting simulation.

In the set up environment of manufacturing module for the femoral component, an alike femoral component workpiece (red portion) is built first and than assembled with the manufacturing model, as shown in Figure 6. The operation of multi-axis milling is used to machine the complex surface. In specifying tool orientation for multi-axis machining within CAD/CAM software, two constraints, i.e. collision and gouging, are the major consideration. The generated CL file can be verified through the function of solid cutting simulation built in this module. Figure 7 shows the cutting simulation of finish machining by multi-axis machining operation.
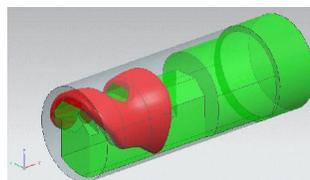
Figure 6. Manufacturing model is assembled with the workpiece model.

(a)   (b)
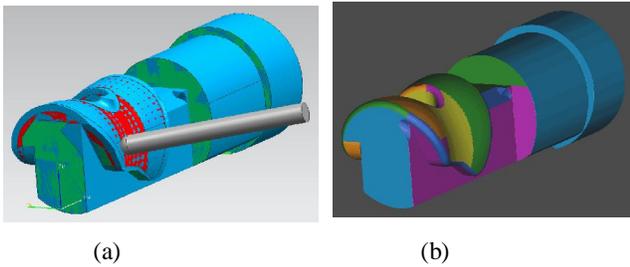
Figure 7. Cutting simulation of finish machining for the femoral component.

4.1 Linear tolerance

Once five-axis machine tools where rotary and linear motion takes place simultaneously, the trajectory of the cutting tool point will deviate from a straight line between adjacent points derived from CL file. This will result in gouging of the part. The amount and direction of deviation depends upon the configuration of the machine tool and the part geometry. To avoid gouging, the function of linear tolerance set in CL file is to interpolate the additional machine coordinate (MCD) points between those derived from the CL file to ensure that this deviation does not exceed the tolerance (Figure 8). The format revealed in the CL file is LINTOL / {ON | OFF | tol}.
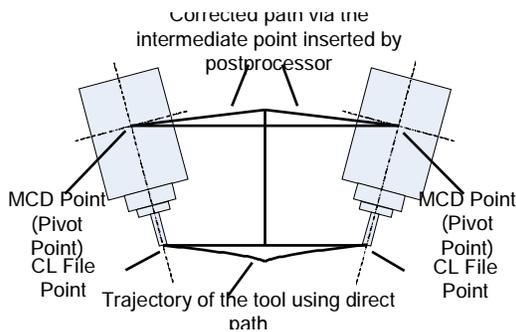
Figure 8. Schematic illustration of the linear tolerance.

5. Results and discussions
5.1 Geometric modeling and rapid prototyping

Using the commercial CAD/CAM system, the complicated surface geometry of the femoral component of knee prosthesis is developed. The solid model of custom-made femoral component built by Unigraphics NX software is shown in Figure 9. After the computational steps in producing a stereolithography file, the FDM process is adopted to obtain the rapid prototyped model (Figure 10).
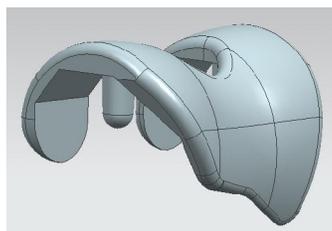
Figure 9. Solid model of a femoral component built by Unigraphics NX.
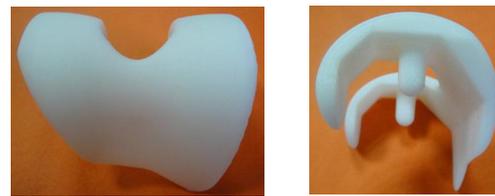
(a) Front view   (b) Side view

Figure 10. Rapid prototyped model of a femoral component produced through FDM process.

5.2 Toolpath simulation and virtual-cut

To avoid the risk of human error, the generated toolpath is verified before actual machining through solid cutting simulation. Table 1 shows the used machining parameters corresponding to various machining process. Figure 11 reveals the toolpath generation and the cutting simulation of finish machining with ball-end mill simulated by UniGraphics NX.

The toolpath generated from UniGraphics NX is converted into NC program by the postprocessor of table-tilting type five-axis machine tool. The NC program is verified via VERICUT® software. The CNC machine tool and controller are modelled to perform realistic 3D simulation. Figure 12(a) presents the cutting simulation of rough machining. Figure 12(b) shows the result of finish machining. The simulation results demonstrate that the collision between the shank and workpiece surface does not occur.

Table 1. Machining parameters for femoral component.

Machining Process	Cutting Tool	Chordal Deviation	Scallop height	Cutting Method	Out-Toleance
Rough Machining	$\phi10$	0.1 *mm*	0.1 *mm*	Zig-zag	0.5 *mm*
Finish Machining	$\phi10R5$	0.01 *mm*	0.01 *mm*	Zig-zag	0.0 *mm*
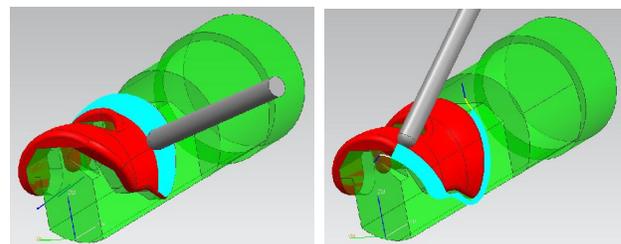
(a) Finish machining of tibiofemoral surface.
(b) Finish machining of fillet surface.

Figure 11. Multi-axis toolpath generation for the femoral component. (UniGraphics NX)

solid cutting simulation and virtual-cut. The results are useful for the development of the femoral component.

_____

Corresponding Author
Jeng-Nan Lee, PhD
E-mail: jengnan@csu.edu.tw

References

1. http://www.eorthopod.com
2. Huang BW. Medical Devices Industry Yearbook, Industrial Economics & Knowledge Center, Taiwan, 2007.
3. Kalpakjian S and Schmid SR. Manufacturing Processes for Engineering Materials, Pearson Education, New Jersey, 2003.
4. Jacobs Paul F. Rapid Prototyping & Manufacturing Fundamentals of StereoLithography, Socity of Manufacturing Engineers, 1992.
5. Sathasivam S and Walker PS. The conflicting requirements of laxity and conformity in total knee replacement. Journal of Biomechanics, 1999, 32: 239-247
6. Liau JJ, Cheng CK, Huang CH and Lo WH. The effect of malalignment on stresses in polyethylene component of total knee prostheses – a finite element analysis. Clinical Biomechanics, 2002, 17:140-146
7. Rao A and Sarma R. On local gouging in five-axis sculptured surface machining using flat-end tools. Computer-Aided Design, 2000, 32: 409-420
8. Lee RS. And Lee JN. Interference-free tool orientation determination by virtual enveloping element for 5-axis machining of free-form surface. Journal of Engineering Manufacture, Proceedings of the Institution Mechanical Engineers, 2001, 215(B): 1683-1693

Figure 12. Simulation of femoral component cutting by the end mill. (VERICUT®)

6. Conclusion

This paper presents the integrated approach of computer-aided design and computer-aided manufacturing for the design and manufacture for femoral component of knee prosthesis. The system implemented is from surgeon requirements to the completion of manufacturing. The solid modeling, rapid prototype and virtual machining are used in the system to establish the interface among conception, design and manufacture. The CAD/CAM techniques are applied to fulfill the design of complicated surface and multi-axis NC machining. The NC programs are verified through

Effects of Vibration Training Combined with Plyometric Training on Muscular Performance and Electromyography

Yen Ke Tien[1], Tsai Chun Bin[1] and Chang Kuan Yu[2]

[1] Cheng Shiu University, Kaohsiung, Taiwan 833, R.O. China; [2] Mackay Memorial Hospital Taitung Branch, Taitung, Taiwan 833, R.O. China. ktyen@csu.edu.tw

Abstract: backgrounds: Complex training has been recommended as a method of incorporating plyometrics with strength training. However, there are some safety issues during heavy strength training. Purpose: To investigate whether the vibration stimulation can instead strength training as pre-loading method when perform Complex training. **Methods**: there were two experiments. Division I: 12 Subjects are accepted by three kinds of different vibration frequency (20, 30, 40Hz) respectively by two kinds of different amplitude (2-4, 4-6mm). The isokinetic (peak torque) and electric physiological activation (integral EMG, iEMG) are measured for deciding which frequency and amplitude were most suitable in vibration training. Division II: 24 male collegiate athletes were randomly assign to three groups: complex training group (CT, vibration+ plyometrics); plyometrics training group (TP, plyometrics only); control group (C). After eight weeks training, we compared isokinetic strength, power performance and synchronized electromyography activity before and after the period of training separately. **Results:** There were significantly enhancement of the peak torque, and power both in CT and TP. However, iEMG was significantly difference between two experimental groups. **Conclusion**: With 20Hz (frequency) and 4-6mm (amplitude) vibration stimulation are most suitable in vibration training; the vibration stimulation can instead strength training as pre-loading method when perform Complex training; Plyometrics training (depth jump on sandlot) can significantly improve leg muscular performance. [Life Science Journal. 2010; 7(1): 78 – 82] (ISSN: 1097 – 8135).

Keywords: post-activation potentiation, complex training, vibration training, plyometric training, depth jump, muscular performance, Electromyography.

1. Introduction

Twitch torque is increased after a brief submaximal or maximal voluntary contraction (MVC). This occurrence has been attributed to as post-activation potentiation (PAP) [1] enhanced twitch potentiation and reflex potentiation has been reported following contractile activity such as a series of evoked twitches. The probable mechanism responsible for PAP is the phosphorylation of myosin regulatory light chains during the conditioning activation that raises sensitivity of actin-myosin to Ca2+ released by the sarcoplasmic reticulum[2].

In performance conditioning fields, based on the opinion of PAP, alternating a high-load weight training exercise with a dynamic exercise such as plyometrics performance has been used [4]. For example, Young et al. [3] have observed that loaded vertical height was Significant increased 2.8% by achieving a 5 repetitive maximum (RM) half-squat exercise previous to the jump test.

Two methods, resistance and plyometric training, are usually referred to the literature as improving the most powerful strength characteristics (explosive strength). Several investigations have demonstrated the "Complex training" that result from the application of these methods, reporting higher increases in the explosive strength indicators [4].

Complex training has been recommended as a method of unifying plyometrics with strength training. [5] Some research propose that plyometric performance is strengthened after the strength training. Strength training can evoke higher PAP of more motor units to increasing plyometric training effects.

Acute vertical whole-body vibration (WBV), inducing rapid eccentric/concentric effects of the leg extensors [6], improves performance of these muscles in the short-term [7]. This transient effect is thought to be mediated by a rapid reflex-mediated stretch-shortening likely to involve the tonic vibration reflex (TVR), which stimulates the muscle spindles [8]. Nearly, WBV application leads to enhanced anaerobic power [8]. It is possible that acute WBV enhances muscular performance consequently, in part, through PAP; however, this theory remains untested.

Therefore, the aim of this study was to investigate whether the vibration stimulation can instead strength training as pre-loading method when perform Complex training, in terms of PAP and strength effect of conditioning contraction, through recording of power characteristics, voluntary torque, and electromyographic activities of the muscles involved. We hypothesized that PAP affects dynamic torque production performed voluntarily and improving of voluntary dynamic performance.

2. Materials and Methods
2.1 Subject

24 collegiate athletes subjects with no history of orthopedic or neuromuscular disorders volunteered for this study. Basically all the subjects had the squatting ability more than 1.5 times body weight. The subjects were fully informed of the procedures used, the possible risks, and the purpose of the study. Written informed consent was obtained from all subjects prior to the investigation. This study was approved by the ethical committee of the Faculty of Sport Sciences at National

Taiwan Collage of Physical Education and was consistent with their requirement for human experimentation.

2.2 Experimental Protocol
Division I: Optimal vibration combination (frequency × amplitude)

12 Subjects are accepted by three kinds of different vibration frequency (20, 30, 40Hz) respectively by two kinds of different amplitude (4-6mm, 2-4mm). The isometric (peak torque) and electric physiological activation (iEMG) are measured for deciding which frequency and amplitude were most suitable in vibration training. Maximal voluntary contractions of the hamstring and quadriceps muscles occurred in a seated position utilizing the Isokinetic Biodex system 3 (Shirley, NY, USA) testing dominant isometric strength. One MVC was performed before the treatment, and one MVC was performed after the treatment. Single MVC trials were utilized to prevent any confounding effect of additional MVC trials on fatigue and PAP. All MVCs were 3 seconds in duration, and for all trials, subjects were instructed to develop maximal force as quickly as possible.

Division II: Vibration stimulation instead strength training as pre-loading application

24 male collegiate athletes were randomly assigned to three groups: complex training group (CT, vibration+ plyometrics); plyometrics training group (TP, plyometrics only); control group (C). There were twice training courses on Tuesday and Friday every week. The vibration parameters were developed from Division I optimal combination. The depth jump program was dropped from 70 cm height platform to sandlot, whenever feet reached the ground jumping up as high as possible. After eight weeks training, we compare isokinetic strength, power performance and synchronized electromyography activity before and after the period of training separately.

2.3 Isokinetic test

Isokinetic concentric/eccentric knee extension and flexion were measured using a calibrated Biodex system 3 (Shirley, NY, USA). A specially designed chair was used which allowed for the various thigh lengths of the subjects. At all testing sessions, a standardized procedure included a warm-up of 2-min cycling on a Monark cycle ergometer 814E (Monark, Varberg, Sweden) at a moderate intensity and 2 minutes of stretching the hamstring and rectus femoris muscles before the knee test. The dominant limb, determined from kicking preference, was used for assessment. Subjects were prepared for a seated position and the axis of rotation of the dynamometer lever arm was aligned with the lateral epicondyle of the knee. The force pad was placed approximately 3 cm superior to the medial malleolus with the foot in a plantar flexed position. The subject was asked to relax their leg so that passive determination of the effects of gravity on the limb and lever arm could be measured. Ranges of motion (ROM) for the knee test during concentric actions were 90 degrees and 15degrees

for eccentric actions, due to the need for an applied preload torque of the eccentric limits. This reduction in ROM for eccentric actions was made necessary by the need for the preload activation torque that could not be performed at the terminal of the ROM, especially in the aged subjects. To ensure full extension, anatomical 0 deg was determined as maximal voluntary knee extension for each subject. Testing occurred at 30 deg·s–1. Subjects were guided to push the lever up, and pull it down, as hard and as fast as possible with extension/flexion undertaken first for concentric actions. For eccentric actions, subjects were instructed to opposing the lever arm with extension as the first movement. The subjects performed three maximal efforts to determine maximal peak torque during CON/CON and ECC/ECC cycles. A 2-min rest period was given between cycles with CON actions tested before ECC actions. All subjects were encouraged to give a maximal effort for each action by using both visual feedback and strong verbal encouragement.

Division I: Optimal vibration combination (frequency × amplitude)

operation	W	S	R	V	R	V	R	V	R	V	R	Knee isometric test
time	5'	5'	2'	1'	2'	1'	2'	1'	2'	1'	2'	+ EMG

Division II: Vibration as pre-loading application

operation	W	S	V	R	V	R	V	R	V	R	P	R	P	R	P	R	P
time	5'	5'	1'	2'	1'	2'	1'	2'	1'	2'	1'	2'	1'	2'	1'	2'	1'

TP
CT

Ps. W, cycling warming up; S, stretch; V, vibration(optimal vibration combination (frequency × amplitude) in Division I); R, rest; P, plyometrics; F,finish.
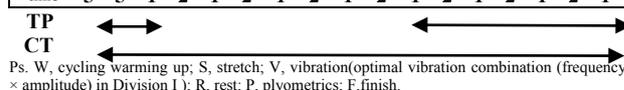
Figure 1. Experimental protocols in optimal vibration combination and vibration as pre-loading application.

2.4 Vertical Jumping Testing.

Vertical jump height was determined using a force platform with specifically designed software (jymmy jump platform, Kistler, Switzerland). Jump height was determined as the centre of mass displacement calculated from force development and measured body mass. Two types of vertical jumps were performed: squat (SJ) and counter-movement (CMJ) jumps. SJ was started from a static semi-squatting position with a knee angle of 90 deg of knee flexion, followed by subsequent action, during which the leg and hip extensor muscles contracted concentrically. In CMJ, each subject stood erect on the force platform and performed a preparatory movement down to approximately 90 deg of the knee flexion, stretching the leg extensor muscles (eccentric contraction), followed by an explosive maximal extension in the opposite direction (concentric contraction).

2.5 Electromyography recording.

During the different experimental operation, EMG from the hamstring and quadriceps muscles was measured. The myoelectric signal was collected through the use of a telemetry transmitter (8 channel, 12-bit analog to- digital converter; Noraxon USA, Inc., Scottsdale, AZ). The amplified myoelectric signal was detected by a receiver– preamplifier and then sent to an

A/D card. The signal was full-wave rectified and filtered (6-pole Butterworth notch filter 60 Hz, band pass filter 10–200 Hz). The integrated value (mVɘs) was calculated and then averaged to determine IEMG (mV) for the working operation. Custom designed EMG programs written in Noraxon package program (Noraxon USA, Inc., Scottsdale, AZ) were used for recording and analyzing the EMG data.

2.6 Statistical analyses

Statistic analyses were performed using SPSS for Windows (Version 10.0, SPSS, Inc., and Chicago, Illinois, U.S.A.). Using data from a similar study, the sample sizes in the present study were deemed to be adequate based on the calculated effect sizes (ES = [Post-measurement mean – pre-measurement mean]/pooled standard deviation) [9] and a minimum statistical power of 0.80. Each parameter that had multiple trials was subject to 1-way repeated measures analysis of variance (ANOVA) to produce the most stable representation for that parameter. Bonferroni pairwise comparisons were used as a post hoc analysis if significant differences were found (p<0.05). The initial analysis included a 1-way ANOVA to explore baseline (pretest) values for each parameter of interest. If there was a significant group effect, then a Bonferroni pairwise comparison was utilized as a post hoc analysis. Repeated measures (Group*Time point, percent change) analysis of covariance (ANCOVA) performed on percent change values were used if significant group differences were found at baseline for any of the jump parameters to allow for relevant covariates to be added to the analysis. Because the depth jump and squat jump parameters (height [cm], peak power [W], peak power/kg [W/kg], and mean power [W]) were assessed pre– post vibration for three groups, 2-way ANOVA or ANCOVA was used to compare group percent changes in these variables. Percent change was calculated as ([[Post value – pre value]/pre value] ×100). Bonferroni corrections were used when multiple comparisons were calculated to account for inflation of alpha. Statistical significance was set at p <0.05.

3. Results
3.1 Optimal Vibration Combination

The isometric force of dominant leg measured in different combinations (20Hz×2-4mm, 20Hz×4-6mm, 30Hz×2-4mm, 30Hz×4-6mm, 40Hz×2-4mm, 40Hz×4-6mm) the first were not different (253.2 Nm, 262.4 Nm, 251.6 Nm, 258.6 Nm, 254.8 Nm, 256.1 Nm; F=1.203, p ＞ .05） between operation. There were significant different between the means iEMG of rectus femoris (0.296 mV, 0.327 mV, 0.286 mV, 0.267 mV, 0.273 mV, 0.299mV; F=7.546, p＜.05). 20Hz×4-6mm increased significantly

3.2 Vibration as pre-loading application

The isokinetic tests of the knee extensors results indicated statistically significant effects in the same group including maximal concentric force (P=.040; P=.038), and maximal eccentric force (P=.035; P=.062) after 8 weeks CT and TP training. The isokinetic tests of

the knee flexors results indicated similar statistically trend. As expected, 8 weeks of training enhance power performance of the muscle: post-training verse pre-training and C values of CT/TP were increased significantly. However, there was no significant indication of improved muscle activation between post-CT and post-TP in flexor.

TABLE 1. Comparision muscular parameters of knee extensor after 8 weeks training.

Parameter	CT(n=8)		TP(n=8)		C(n=8)	
	pre	post	pre	post	pre	post
Maximal concentric force (Nm)	213.0 (49.7)	248.7[ab] (43.9)	221.1 (65.3)	247.2[ab] (50.3)	235.9 (68.8)	237.5 (69.2)
Maximal eccentric force (Nm)	244.3 (44.5)	279.1[ab] (42.1)	249.2 (48.6)	276.3 (56.8)	26.1.4 (73.0)	263.6 (73.4)
Fatigue index (%)	45.2 (6.1)	47.1 (5.9)	44.3 (6.8)	46.6 (5.4)	47.8 (7.2)	48.9 (6.4)
SJ(cm)	44.4 (4.7)	55.5[ab] (7.3)	46.8 (6.7)	51.7[ab] (5.6)	44.6 (7.3)	46.1 (6.3)
CMJ(cm)	51.0 (5.7)	58.3[ab] (7.4)	46.7 (7.1)	53.8[ab] (6.8)	49.5 (6.2)	49.6 (7.5)

Ps. Values are Mean (SEM).

a: vs.pre-in the same group, p<.05; b: vs. post-C, p<.05.

TABLE 2. Comparision muscular parameters of knee flexor after 8 weeks training.

Parameter	CT(n=8)		TP(n=8)		C(n=8)	
	pre	post	pre	post	pre	post
Maximal concentric force (Nm)	115.3 (32.2)	139.8[ab] (38.4)	117.5 (26.3)	138.8[ab] (27.5)	120.2 (41.0)	124.0 (40.9)
Maximal eccentric force (Nm)	128.1 (37.4)	158.8[ab] (41.5)	138.6 (34.3)	163.7[ab] (35.7)	138.7 (41.5)	139.6 (42.1)
Fatigue index (%)	42.5 (5.3)	44.1 (5.1)	44.6 (6.5)	45.4 (5.8)	46.8 (7.5)	47.1 (6.6)

Ps. Values are Mean (SEM).

a: vs.pre-in the same group, p<.05; b: vs. post-C, p<.05.

TABLE 3. Comparision iEMG of knee muscles after 8 weeks training.

Parameter	CT(n=8)		TP(n=8)		C(n=8)	
	pre	post	pre	post	pre	post
rectus femoris (mV ·s)	0.284 (0.066)	0.385[abc] (0.083)	0.276 (0.079)	0.311[ab] (0.081)	0.308 (0.095)	0.294 (0.087)
hamstring (mV ·s)	0.275 (0.082)	0.297[ab] (0.075)	0.278 (0.065)	0.301[ab] (0.075)	0.274 (0.062)	0.270 (0.077)

Ps. Values are Mean(SEM).a: vs.pre-in the same group, p<.05;

b: vs. post-C, p<.05; c: vs. post-TP, p<.05.

4. Discussions

The aim of this study was to investigate the vibration stimulation can instead strength training as pre-loading method when perform complex training. We

hypothesized that continuous acute WBV would potentiate the muscle twitch response compared to a centrally mediated effect that would potentiate WBV-induced PAP and perform the plyometrics training effects. Our results support our hypothesis that 20Hz×4-6mm WBV combining explosive power training (CT) induces a higher iEMG level compared to plyometrics only (TP) and Control(C) interventions.

PAP recommended as an increase in muscle performance led by a muscle contractile activity [10] and is estimated by twitch potentiation (TP), or reflex potentiation (RP) [11]. To our knowledge, this is the first time following WBV as pre-loading to enhance explosive power training. The results showed that CT and TP increased muscular concentric/eccentric force and SJ/CMJ, but with no change in fatigue index compared to C. We refer other research that the time approach of TP reached a maximal level 90 s after WBV and returned to base levels after 10 min [12]. It is described that acute WBV improves short-term muscular performance above cycling-only exercise [13]. It means that WBV has the potential to be considered as warm-up modes before explosive power training such as strength, speed and power [13]. Likewise the increase in rate of force development (RFD) from acute WBV is supported by other studies that have reported increases in RFD following high stimulation frequencies (>100 Hz) [14]. However, as a result of enhancing RFD, explosive activities such as jumping may be improved if TP is heightened [10, 11]. We set plyometrics training after WBV combined lower frequency (20-40 Hz) and interval 1 minute rest in the complex training.

It is well documented that heavy pre-loading exercise regimes such as 3–5 repetition maximum (RM) or MVCs are often implemented prior to short-term activities to induce PAP[3, 16]. Therefore it seems that the pre-loading activity of WBV and plyometrics are needed to be greater magnitude to elicit TP and RP. Our mechanism should be integrated TP and RP. On the basis of molecular level, the solution for PAP has formed around twitch potentiation (TP) and reflex potentiation (RP) [11]. TP is considered to involve the phosphorylation of myosin regulatory light chains making actin and myosin more sensitive to the intracellular Ca2+ signal [15]. This would react more cross-bridge interaction under the same intracellular Ca2+ concentration, which raises the muscle tension for the same absolute level of neural stimulus [16]. However if calcium homeostasis was involved, then one would expect an unbalance change in RFD and PF. It means that WBV could enhance muscle power output.

RP is evoked reflex activity in the spinal cord, by expanding synaptic capacity between Ia afferent terminals and α motoneurones of the muscle [11]. WBV lead muscle contractions through spinal reflexes [6, 13]. It should be intended that WBV is a combination of muscle vibration and voluntary exercise contractions. Therefore, our findings suggest that RP from CT may be more important than TP. Further, it should be noted that using a tendon tap under lower frequency to elicit a stretch reflex response does necessarily provide a extensive measure of spindle sensitivity or its

contribution, as there are several factors from which the stretch reflex can be modified either by the excitatory or inhibitory factors of the motoneurone pool and/or the mechanical sensitivity of the muscle spindle itself [17]. We consider that changes in muscle performance from CT are in part caused by neurogenic factors from possible changes in muscle spindle sensitivity [7].

5. Conclusion

In conclusion, we measured the neuromuscular response of working muscles, and our results suggest that CT causes iEMG increasing. Muscular performances studies have shown that weight training induce PAP by heavy pre-load activity which enhances muscular activity [3]. Similarly, CT-WBV is also capable of inducing higher loads through vibration frequency and amplitude that act as a pre-loading movement to activate PAP. With 20Hz (frequency) and 10mm (amplitude) vibration stimulation are most suitable in WBV training; the vibration stimulation can instead strength training as pre-loading method when perform Complex training; Plyometrics training (depth jump on sandlot) can significantly improve leg muscular performance.

Corresponding Author:
Ke-Tien Yen, PhD
E-mail : ktyen@csu.edu.tw

References
1. Baudry S, Duchateau J. Postactivation potentiation in a human muscle: effect on the rate of torque development of tetanic and voluntary isometric contractions. Journal of Applied Physiology, 2007, 102: 1394–1401.
2. Palmer BM, Moore RL. Myosin light chain phosphorylation and tension potentiation in mouse skeletal muscle. The American Journal of Physiology, 1989, 257: C1012–C1019.
3. Young WB, Jenner A, Griffiths K. Acute enhancement of power performance from heavy load squats. Journal of Strength and Conditioning Research, 1998, 12: 82–84.
4. Hedrick A. Strength and power training for basketball. National Strength and Conditioning Association Journal, 1993, 15: 31–35.
5. Ebben W P. Complex training: A brief review. Journal of Science and Medicine in Sports, 2002, 1: 42-46.
6. Cochrane DJ, Stannard SR, Walmsley A, Firth EC. The acute effect of vibration exercise on concentric muscular characteristics. Journal of science and medicine in sport, 2008, 11:527–534.
7. Cardinale M, Bosco C. The use of vibration as an exercise intervention. Exercise and Sport Sciences Reviews, 2003, 31: 3–7.
8. Komi P V. Physiological and biomechanical correlates of muscle function, effects of muscle

structure and stretch-shortening cycle on force and speed. Exercise and Sport Sciences Reviews, 1984, 12: 81-121.

9. Ronnestad, B. Comparing the performance-enhancing effects of squats on a vibration platform with conventional squats in recreationally resistance-trained men. Journal of Strength and Conditioning Research, 2004, 18: 839–845.

10. Sale, DG. Postactivation potentiation: role in human performance. Exercise and Sport Sciences Reviews, 2002, 30: 138–143.

11. Hodgson, M, Docherty, D, Robbins, D. Post-activation potentiation: underlying physiology and implications for motor performance. Sports Medicine, 2005, 35: 585–595.

12. Baudry S, Duchateau J. Postactivation potentiation in human muscle is not related to the type of maximal conditioning contraction. Muscle Nerve, 2004, 30: 328–336

13. Cochrane DJ, Stannard SR. Acute whole body vibration training increases vertical jump and flexibility performance in elite female field hockey players. British Journal of Sports Medicine, 2005, 39: 860–865

14. Abbate F, Sargeant AJ, Verdijk PWL, De Haan A. Effects of high-frequency initial pulses and posttetanic potentiation on power output of skeletal muscle. Journal of Applied Physiology, 2000, 88: 35–40

15. Zhi G, Ryder JW, Huang J, Ding PG, Chen Y, Zhao YM, Kamm KE, Stull JT. Myosin light chain kinase and myosin phosphorylation effect frequency-dependent potentiation of skeletal muscle contraction. Proceedings of the National Academy of Sciences of the United States of America, 2005, 102: 17519–17524

16. Yen KT, Chang KY. Tai chi exercise affects the isokinetic torque but not changes hamstrings: quadriceps ratios. Life Science Journal, 2009, 6: 50-55.

17. Hopkins JT, Fredericks D, Guyon PW, Parker S, Gage M, Feland JB, Hunter I. Whole body vibration does not potentiate the stretch reflex. International Journal of Sports Medicine, 2008, 30: 124–12

Intelligence and academic achievement: an investigation of gender differences

Habibollah. Naderi[1], Rohani. Abdullah[2], H. Tengku Aizan[3], Jamaluddin. Sharir[4]

1. Department of Educational Studies, University of Mazandaran, Street of Pasdaran, Babolsar, Iran
2. Department of Human Development & Family Studies, University Putra Malaysia, Serdang43400, Malaysia
3. Institute of Gerontology, University Putra Malaysia, Serdang, 43300, Malaysia
4. Department of Educational Psychology and Counseling, University of Malaya, 50603 Kuala Lumpur, Malaysia
naderihabibollah@yahoo.com

Abstract

The objective of this research is to examine if a relationship exists between intelligence and academic achievement and if the relationship differs between males and females. Two research questions are examined in this paper: (1) what is the relationship between different aspects of intelligence and academic achievement? (2) Is there any significant gender differences regarding the relationship between different aspects of creativity and academic achievement? Participants (N=153; male=105 and female=48) completed creativity test. Cumulative grade point average (CGPA) was used to select the participants. Intelligence was measured using the Catell Culture fair Intelligence Test (CFIT-3a & b). Pearson Correlation analysis indicated that aspects of intelligence were not related to academic achievement for both males and females. However, implications of the findings for this study in intelligence and academic achievement are discussed. [Life Science Journal. 2010;7(1): 83 – 87] (ISSN: 1097 – 8135).

1. Introduction

Is intelligence related to academic achievement? Historically this question has been addressed by researchers. The relationship between measures of intelligence and achievement is significant to research, if there is a strong relation between them, it might be deduced that the intelligence test has an important contribution in connection with other variables for instance the curriculum, study program, the teacher, the characteristics of the school, and others in scholastic performance (Naglieri & Bornstein, 2003).

In current years, several researchers have shown more interest in the relationship between intelligence and academic achievement. Researchers mentioned that there are empirical evidence for a strong association between general cognitive ability and academic achievement, there is still anywhere from 51% to 75% of the variance in academic achievement that is unaccounted for by measures of general cognitive ability alone(Rohde & Thompson, 2007). Additionally, understanding the nature of the relationship between general cognitive ability and academic achievement has widespread implications for both practice and theory(Rohde & Thompson, 2007).

Academic achievement of students in high school strongly correlates (.50 to .70) with intelligence scores(Jensen, 1998), but in another study researchers experienced the hypothesis that the relationship between general intelligence and academic achievement was in large part associated with a mental speed component. At the beginning, the divided variance between general intelligence and academic achievement was nearly 30%(Luo, Thompson, & Detterman, 2003). On the other hand, after controlling for the mental speed component, the shared variance between general intelligence and academic achievement was decrease to approximately 6% (Luo et al., 2003) . This result is strong shows to be

true that the items of intelligence (such as mental speed component and maybe other substances) are a significant intervener between intelligence and academic achievement.

In another study, (Watkins, Lei, & Canivez, 2007) stated there has been considerable debate regarding the causal precedence of intelligence and academic achievement. Some researchers view intelligence and achievement as identical constructs. Others believe that the relationship between intelligence and achievement is reciprocal. Still others assert that intelligence is causally related to achievement (Laidra, Pullmann, & Allik, 2007) reported that students' achievement relies most strongly on their cognitive abilities through all grade levels.

Gender differences in IQ have been examined in adolescent and adult samples with respect to different of intelligence measures. (Colom & Garc a-L pez, 2002) reported some researchers (Allik, Must, & Lynn, 1999; Hattori & Lynn, 1997; Richard Lynn, 1994; R Lynn, 1998) have challenged the observations that there is no gender difference in intelligence. Their findings are based on the summation of the gender differences in several aspect of intelligence.

Although during the almost period of one hundred years a general agreement has been reached that there is no sex difference in overall general intelligence (Douglas and Rushton, 2006) but several studies have been reported gender differences in intelligence (Furnham et al., 1999). They support gender differences in specific cognitive abilities; some support females and some support males (Hyde, 2005; Lynn et al., 2002) but many of studies find no sex differences in intelligence (Halpern and LaMay, 2000).

Several investigators found gender differences in intelligence. (Deary et al., 2003) studied also the cognitive ability distribution in 80,000+ students. There

were no significant mean differences in cognitive test scores between genders but there was a highly significant difference in their standard deviations. Boys were more at the low and high extremes of cognitive ability (Douglas and Rushton, 2006). Douglas and Rushton (2006) found a point of biserial size of 0.12 favoring males on the SAT, which provides a good measure of general intelligence as manifested through school of learned abilities in high school graduating samples.

Researchers have also examined gender differences in intelligence in 20 countries, studies from China trough to Germany and Scotland have shown males give significantly and higher estimates than females for general over intelligence (Adrian and Buchanan, 2005). Adrian and Buchanan (2005) stated also this difference is consistent across countries and populations although there are wide differences in level. Sophie et al. (2006) investigated whether sex differences observed on the subtests of the intelligence test were attributable to sex difference in general intelligence. Males outperformed than females on 3 out of the 10 subtests (information, arithmetic and matrix reasoning), while females` performance was better than males only on 1 subtest, called digit of symbol substitution.

Wendy and Johnson (2007) investigates 436 (188 males, 248 females) participants (ages were between 18-79 from Australia, Great Britain and North America). Their result have shown that there was a very small gender difference in general mental ability but males clearly performed better on Visio-spatial tasks while females performed better on tests of verbal usage and perceptual speed. Rammstedt and Rammsayer (2000) have been investigated on 105 German students and concluded that male self-estimates were significantly higher for logical-mathematical and spatial intelligences, while female estimates were significantly higher for musical and interpersonal intelligences. Reilly and Mulhern (1995) estimated the intelligence of 125 (45 male and 80 female) of students at Queen`s University using the WAIS. They found there was no gender significant difference in their measured intelligence. However, men in the sample appeared to overestimate their intelligence, while the women were quite accurate in estimating their intelligence. Habibollah, et,. al (2008) reported there were no significance between males and females on intelligence but the result shows males' means are higher than females.

The current study reported here suggested studying the relationship between intelligence and academic achievement, especially to see if the relationship could be different for females and males by Catell Culture Fair Intelligence Test. Because few researches have been done on the basis of this instrument and previous research used other instruments, so this instrument has been employed by this research. Another reason for this study is that the previous research studied in certain cultures and researchers stated the need of study in different cultures and nations. So, due to the lack of research in this field on the basis of CCFIT test, in Iranian population, this research addressed this issue in overseas Iranian students by this test. In line with the aim of this investigate, the research questions were as follows: What is the relationship between different aspects of intelligence and academic achievement? Are there any differences for females and males in terms of the relationship between different aspects of intelligence and academic achievement?

2. Methodology
Sample

One hundred and fifty three Iranian undergraduate students in Malaysian Universities (31.4% females and 68.6% males) were recruited as respondents in this study. Their ages ranged from 18-27 years for females and 19-27 years for males.

Measures
Catell Culture Fair Intelligence Test

To evaluate the intelligence, every student was administered by a Scale 3 of the Catell Culture fair Intelligence Test (CFIT-3a & b). Roberto Colom, Botella, & Santacreu (2002) reported that this test is a well-known test on fluid intelligence (GF). Participants completed Cattell's culture fair intelligence test battery to assess individual differences in fluid intelligence. Cattell's Culture Fair Intelligence Test (1971), which is a nonverbal test of fluid intelligence or Spearman's general of intelligence. This test contained four individually timed subsections a) Series, b) Classification, c) Matrices, d) Typology, each with multiple-choice problems progressing in difficulty and incorporating a particular aspect of visuospatial reasoning. Raw scores on each subtest are summed together to form a composite score, which may also be converted into a standardized IQ.

Cumulative Grade Point Average (CGPA)

For the purposes of this study, Cumulative Grade Point Average (CGPA) was used as a proxy of academic achievement. The CGPA was calculated by dividing the total number of grade points earned by the total number of credit hours attempted. A student's academic achievement was based on their mid-year examination results. Academic achievement was the aggregate or the total number of grade points in the mid-year examinations. In these examinations, each university subject was graded along a one hundred (or four) point scale, the best grade point being one hundred (or four) and the lowest being zero. Hence the aggregate would range from 75 to 100 (3 to 4); notably the lower the aggregate, the better the academic achievement. This approach was used because other researchers have used the measure and found it an acceptable one for measuring academic achievement Palaniappan (2007) cited several researchers (Nuss, 1961; Parker, 1979; Taylor, 1958; Wilson, 1968).

Procedure

The students who participated in this study were all undergraduates. The research questions posed for the study required the students to identify and analyze the distributions and correlations of certain

creativity perception were best addressed in the form of a descriptive study. Creativity levels were assessed by self-report instruments and were confirmed by consideration of the results from the administration offices of the universities (described below). They were then divided by gender, with the total scores and subscales calculated for each male and female. The participant sample, women (18-27 years) and men (19-27years), was asked to respond during the regular course time. Both written and oral instructions were given to all participants, and the subjects were ready to answer upcoming questions in the class. Multiple significance tests were conducted, and the data were analyzed by t-test. Participants answered the tests either using their name or anonymously (whichever they preferred). They received no rewards for participating but were advised they would be given information of their results in the form of a self-referenced level of abilities at a later date. Scores for the creativity scale and its factors, were entered into the SPSS statistical program.

3. Result
Descriptive Statistics

The data were analyzed on the basis of the relationship between intelligence and academic achievement among males and females, and the results are reported in the Table and Figure below. SPSS for Windows Version 16.0 was used to conduct the analysis.

Table 1 shows descriptive statistics of intelligence (The A form). The finding of this result [intelligence (The A form)] indicated that the females' mean score was not different from the males (male = 104.63, female =104.38, but standard deviation of the males (SD=16.35) were greater than the females' standard deviation (14.35). As it is shown in the table for intelligence (The B form), the males' mean score (100.86) was a little more than the females' mean score (97.54) for intelligence. The standard deviations between females and males were not so high different (15.69 = females & 15.91= Males). This table shows also a descriptive statistical intelligence between genders total of intelligence (Both A & B forms). It shows that males' mean score was higher than the females' on intelligence (Both A& B Forms), but the standard deviations between females and males were a little different, However, we had different results about the Intelligence (A&B forms) scores; the males' mean scores (103.05) were more than the females' mean scores (101.12) for the generally as well as the Intelligence (A& B forms). The standard deviations between females and males were a little different (14.09= females & 14.57 = Males).

Table 3 reveals that the females' mean (2.89) score for cumulative grade point average was lower than the males' mean score (3.00), but the standard deviations between females and males were not very different from each other (males=0.53 & females=0.56).

TABLE 1. Descriptive Statistics CGPA

Variables	N	Mean	Std. Deviation
CGPA	153	2.97	0.54
Male	105	3	0.53
Female	48	2.89	0.56

TABLE 2. Descriptive Statistics Intelligence

Variables	N	Mean	Std. Deviation
Intelligence (The A Form)			
Total Score	153	104.54	15.70
Male	105	104.63	16.35
Female	48	104.38	14.35
Intelligence (The B Form)			
Total Score	153	99.82	15.87
Male	105	100.86	15.91
Female	48	97.54	15.69
Intelligence (The A & B Form)			
Total Score	153	102.45	14.40
Male	105	103.05	14.57
Female	48	101.12	14.09

TABLE 4. Pearson Correlation Results a

Variables	r	p	N
Intelligence (The A Form)	.101*	.213	153
Intelligence (The B Form)	.011*	.889	153
Intelligence (The A & B Form)	.063*	.438	153

Dependent Variable; CGPA. * Correlation is not significant at the 0.05 level (2-tailed).

TABLE 5. Pearson Correlation Results for Males a

Variables	r	p	N
Intelligence (The A Form)	.088*	.372	105
Intelligence (The B Form)	- .032*	.749	105
Intelligence (The A & B Form)	.034*	.731	105

Dependent Variable; CGPA. * Correlation is not significant at the 0.05 level (2-tailed).

TABLE 6. Pearson Correlation Results for Females a

Variables	r	p	N
Intelligence (The A Form)	.133*	.368	48
Intelligence (The B Form)	.074*	.619	48
Intelligence (The A & B Form)	.109*	.461	48

Dependent Variable; CGPA. * Correlation is not significant at the 0.05 level (2-tailed).

Data Analysis
Pearson Correlation

This part presents the results from Pearson Correlation of intelligence and academic achievement variables for the males and the females, respectively. Table 3 shows the relationship between intelligence with academic achievement and the differences between males and females. Analyses of the relationships between intelligence and academic achievement among students were undertaken using Pearson Correlations for males and females. These correlations were not significantly related to Academic Achievement for [intelligence (The A&B forms)] (r=.101, p>0.05), [intelligence (The A form)] (r=.011, p>0.05), on the other hand, the [intelligence (The B form)] were not also significantly but negatively related to Academic Achievement (r=- .063, p>0.05).

Males: These correlations were not significantly related to Academic Achievement for [intelligence (The A&B forms)] (r=034, p>0.05), [intelligence (The A form)] (r=.088, p>0.05), on the other hand, the [intelligence (The B form)] were not also significantly but negatively related to Academic Achievement (r=- .032, p>0.05).

Female: These correlations were not significantly related to Academic Achievement for [intelligence (The A&B forms)] (r=.109, p>0.05), [intelligence (The A form)] (r=.133, p>0.05), on the other hand, the [intelligence (The B form)] were not also significantly related to Academic Achievement (r=- .074, p>0.05).

4. Discussion and conclusion

The majority interesting finding of this research is that when student's intelligence was measured by three of intelligence test, the result imply that there existed no significantly relation between males and females regarding which aspect of intelligence related to academic achievement, although intelligence was shown not be related to academic achievement for both genders. Hence, different aspect of intelligence and academic achievement doesn't matter for males and females when looking at the relation between intelligence and academic achievement. This could be one reason previous study yielded not decisive results respecting the relation between intelligence and academic achievement. One possible interpretation for this result is that males and females which has not been excelled in different aspect of intelligence.

Findings from this study are consistent with those of others (Deary et al., 2003) Wendy and Johnson (2007) Mulhern (1995) Habibollah, et. al (2008). The present study challenges strong statements by several researchers and psychologists. Adrian and Buchanan (2005) noted that there is gender difference on intelligence. Their result has been shown males give significantly and higher estimates than females for general over intelligence. Study's Sophie et al. (2006)

also revealed sex differences on the subtests of the intelligence test were attributable to sex difference in general intelligence. Males outperformed than females on subtests (information, arithmetic and matrix reasoning), while females` performance was better than males only on digit of symbol substitution. Of course, this research has some limitations. One is the measure of academic achievement. Measure of academic achievement for this study was cumulative grade point average. Another limitation was the number of this study's subjects there were 153 Iranian students only. To conclude this study shows that the relation between intelligence and academic achievement is complex. It may vary by gender and by the intelligence masseur used. If could be, follow-up study must look at other issues that are significant for a improve understanding of intelligence.

Acknowledgment

Corresponding Authors:

Dr Rohani Abdullah
Department of Human Development & Family Studies
University Putra Malaysia, Serdang 43400, Malaysia
Email: naderihabibollah@yahoo.com
Tel; +6038946538

References

1. Allik, J., Must, O., & Lynn, R. (1999). Sex differences in general intelligence among high school graduates: Some results from Estonia. Personality and Individual Differences, 26(6), 1137-1141.
2. Cattell, R. B. (1971). Abilities: Their structure, growth, and action. New York: Houghton Mifflin.
3. Colom, R., & Garc a-L pez, O. (2002). Sex differences in fluid intelligence among high school graduates. Personality and Individual Differences, 32(3), 445-451.
4. Habibollah, N., Abdullah, R., & Tengku Aizan, H. (2008). Male Versus Female Intelligence among Undergraduate Students: Does Gender Matter? Asian Journal of Scientific Research, 1(5), 539-543.
5. Hattori, K., & Lynn, R. (1997). Male--female differences on the Japanese WAIS-R. Personality and Individual Differences, 23(3), 531-533.
6. Horn, J. L. (1985). Remodelling old models of intelligence. In: B.B.Wolman,Hanbook of Intelligence. Willy, New York.
7. Jensen, A. R. (1998). The g factor: The science of mental ability. Westport, CT: Praeger.
8. Kline, P. (1998). The new psychometrics: Science, psychology and measurement. London: Routledge.
9. Laidra, K., Pullmann, H., & Allik, J. (2007). Personality and intelligence as predictors of academic achievement: A cross-sectional study from elementary to secondary school. Personality and Individual Differences, 42(3), 441-451.
10. Luo, D., Thompson, L. A., & Detterman, D. K. (2003). The causal factor underlying the correlation between psychometric g and scholastic performance. Intelligence, 31(1), 67-83.
11. Lynn, R. (1994). Sex differences in intelligence and brain size: A paradox resolved. Personality and Individual Differences, 17(2), 257-271.
12. Lynn, R. (1998). Sex differences in intelligence: some comments on Mackintosh and Flynn. Journal of Biosocial Science 30, 555-559.
13. Naglieri, J. A., & Bornstein, B. T. (2003). Intelligence and achievement: Just how correlated are they? Journal of Psychoeducational Assessment 21, 244-260.
14. Nuss, E. (1961). An Exploration of relationships between creativity and certain Personal-Social variables among Eight Grade Pupils. Unpublished Unpublished Doctoral Dissertation
15. University of Maryland.
16. Palaniappan, A. K. (2007). Academic Achievement of Groups Formed Based on Creativity and Intelligence. Paper presented at the The 13th International Conference on Thinking Norrköping. from http://www.ep.liu.se/ecp/021/vol1/020/index.html
17. Parker, J. P. (1979). The predictive validity of creativity and intelligence tests administered at age five. Unpublished Dissertation Abstract International, 39A, 345.
18. Rohde, T. E., & Thompson, L. A. (2007). Predicting academic achievement with cognitive ability. Intelligence, 35(1), 83-92.
19. Taylor, C. W. (1958). Variables related to Creativity and Productivity Among men in two research Laboratories. Paper presented at the Second Utah Creativity Research Conference on the identification of creative Scientific Talent, Salt Lake City, University of Utah Press.
20. Watkins, M. W., Lei, P.-W., & Canivez, G. L. (2007). Psychometric intelligence and achievement: A cross-lagged panel analysis. Intelligence, 35(1), 59-68.
21. Wilson, M. P. (1968). The relationship of sense of humor to Creativity, Intelligence and Achievement. Unpublished Unpublished Ph.D. Dissertation, University of Southern California.

A Secure DoS-resistant User Authenticated Key Agreement Scheme with Perfect Secrecies

Jeng-Ping Lin[1], Jih-Ming Fu[2]

[1]*Department of Information Network Technology Chihlee Institute of Technology, Niaosong, Taiwan 833, R.O. China.*
Email: jplin@mail.chihlee.edu.tw
Corresponding author
[2]*Department of Computer Science & Information Engineering, Cheng Shiu University, Niaosong, Taiwan 833, R.O.*
China.
Received February 2, 2008

Abstract

The goal of a denial-of-service (DoS) attack is to deplete the resource of a targeted server in order that its intended clients cannot obtain the services. Recently, Hwang *et al.* proposed an ID-based password authentication scheme using smart cards against the DoS attack. In their scheme, the major merits include: (1) mutual authentication; (2) the password guessing attack; (3) the replay attack; (4) the impersonation attack; (5) session key establishment; and (6) the server resources exhaustion attack. However, two basic and the most important security properties of a session key establishment are not satisfied in their scheme. One is the perfect forward secrecy. If the long-term secret key is compromised, the previous session key should not be derived. The other is the perfect backward secrecy. If a used session key is compromised, subsequent communications should not be damaged. The intentions of this paper are to show that the above weaknesses exist in Hwang *et al.*'s scheme and to propose a security-enhanced user authentication scheme. The proposed scheme not only can achieve the above admired security requirements, but also can solve the smart card loss problem which is a troublesome security threat in our life and cannot be solved in most authentication and key agreement schemes. [Life Science Journal. 2010;7(1): 88 – 94] (ISSN: 1097 – 8135).

Keywords   Authentication; Client puzzles; Perfect forward secrecy; Perfect backward secrecy

1 INTRODUCTION

IN today, most on-line services over the Internet are based on the client/server architecture. In the architecture, there is a single server to serve a lot of clients. Authentication is basic and is the first step to identify whether a remote client is authorized or unauthorized. After the verification of the identity, the client can be held accountable and the system can decide to give a specific access privilege. Moreover, the system generates a session key to protect their future communications [1-5] [Bellar and Rogaway, 1993; Juang, Feb. 2004;Juang, March 2004;Juang, May 2004;Juang, 2006].

Password is widely adopted into authentication and session key generation schemes since a password-based scheme is easily implemented for many applications. Relatively, the entropy of a memorial password is low and is easily suffered from the guessing attack. Therefore, many password-based authentication schemes with the key agreement scheme were proposed to provide robust security requirements [6, 7] [Juang, 2008; Wen *et al.*, 2005].

Owing to the openness of the Internet, a goal of malicious attackers is to make that the service from the remote server is unavailable. One of the tricks is that the attackers can launch a denial of service (DoS) attack or a distributed denial of service (DDoS) attack to deplete the resource of the remote server by sending a huge service requests[8,9] [Agah and Das, 2007;Peng *et al.*, 2007]. Hence, the DoS and DDoS attacks should be taken into consideration in the design of a secure user authentication scheme.

By sending a large connection requests to a targeted victim, the attack will cause that the server exhausts the resource to reply the response due to the innateness of the TCP/IP protocol principle. As we know, the DoS or DDoS attacks are easily implemented, but the attacks are hard to be prevented for the server. In general, the defense mechanisms of the DoS/DDoS attacks can be divided into four types [9] [Peng *et al.*, 2007]: attack prevention, attack detection, attack source identification, and attack reaction. Most previous schemes addressed the works in the network layer and tried to analyze the information of incoming and outgoing packets. The major ideas are to install firewall, intrusion detection system, and intrusion prevention system on the entrance of systems.

Recently, the idea of adopting a puzzle game is paid more attention for defeating the DoS/DDoS attacks [10, 11][Aura *et al.*, 2001;Bocan, 2004]. The intention of the idea is to prevent the resources of the server from being exhausted and the sincerity of the client has been shown to the server by performing some expensive cryptographic operations. The goal is to design an acceptable solution of a puzzle for legal clients, but the computation cost is high for malicious outsiders. In general, a puzzle is designed that the challenge is to seek out the miss materials of a hashed value [12, 13] [Juels and Brainard, 1999; Laurens *et al.*, 2006]. For instance, z is a digest value of two variables x and y. Given z and y, the goal is to seek out x' to satisfy $z = h(x', y)$. As we know, if x and y are known, it is computationally fast for the server from computing the digest value of x and y. Without the knowledge of x and y, the computation cost is heavy for the client. The computation cost is disequilibrium between the client and the server because the client could only perform the brute-force search to

seek out the solution of a puzzle.

In 2009, Hwang *et al*. proposed a password-based user authentication scheme with session key establishment against the server resource exhaustion attacks and some well-known attacks [14] [Hwang *et al*., 2010]. Unfortunately, two basic and important security properties of a secure key establishment scheme are not taken into their consideration and we introduce them as follows:

1) **Perfect Forward Secrecy.** A key establishment scheme is said to provide the perfect forward secrecy if the compromise of long-term keys for communicated parties cannot damage past session keys.

    The idea of the perfect forward secrecy is that previous traffics can be locked securely in the past. A widely adopted method is to employ the concept of Diffie-Hellman key agreement to generate distinct session keys, wherein the exponentials are chosen randomly as short-term keys. If long-term secret keys are compromised, previous sessions are not affected by an active adversary [15] [Schneier, 1996]. An admired key agreement should provide this property.

2) **Perfect Backward Secrecy (Known-key Attack)**. A key establishment scheme is said to be secure against a known-key attack if the compromise of past session keys cannot allow that either a passive adversary learns the future session keys, or an active adversary impersonates one of the communicated parties successfully in the future. The perfect backward secrecy on a key establishment scheme is analogous to the known-plaintext attack [16, 17] [Minier *et al*., 2009; van Oorschot and Wiener, 1991] on an encryption algorithm. Firstly, from implementation and engineering decisions point of view, scholars consider that, the probability of the compromise of session keys which were established previously may be larger than that of long-term keys. Secondly, in terms of cryptographic techniques, if a key establishment scheme only took moderate strength into consideration, past session key may be recovered over time. Finally, for some reasons of applications, it is necessary that past session keys may be deliberately uncovered. A secure key agreement should be against this threat.

Another serious security threat is also not taken into consideration in most smart card-based authentication schemes. In a real life, we always worry about the damage of smart cards loss. In 1998 and 2002, Kocher *et al*.[18] [Kocher *et al*., 1999] and Messerges *et al*. [19][Messerges *et al*., 2002] stated that this security threat happened by monitoring the power consumption and analyzing the leaked information in the smart card. A secure and admired smart card-based authentication scheme should blockade this threat.

In this paper, we propose a user authentication with key agreement scheme where the perfect forward secrecy and the perfect backward secrecy can be satisfied at the same time and the merits in Hwang *et al*.'s scheme are also taken into our consideration. Apart from that, our proposed scheme also can be secure against the smart card loss threat. Most smart card-based schemes cannot solve this threat. It implies that if previous schemes want to withstand this threat, their schemes must rely on a tamper-resistant smart card [20] [Nordin, 2004]. As we know, in a tamper-resistant smart card-based scheme, the system cost is high.

In the next section, we first review Hwang *et al*.'s scheme and show their weakness. In Section 3, we present our method. In Section 4, we analyze the security of the proposed scheme and compare the satisfaction of some security criteria between our scheme and Hwang *et al*.'s scheme. Finally, we conclude this paper in Section 5.

I. HWANG *ET AL*.'S SCHEME

In this section, we briefly review Hwang *et al*.'s scheme [14][Hwang *et al*., 2010]. Before we introduce the scheme, we first notify the used parameters as follows.

A. Notations

l v_s is a solution of the puzzle which is decided by the server S.

l N_s and N_i denote the nonces and are generated by the server and the smart card, respectively.

l q_i is a session and is chosen by the smart card.

l $h()$ is a 128bits one-way hash function.

l SK is the secret key of the server.

l sk_s is also a secret key of the server and is used for puzzle verification.

l $puzzle(p, x_1, x_2, …, x_n)$ denotes that given ($p, x_1, x_2, …, x_n$) to find v such that $h(x_1, x_2, …, x_n, v) = p$.

B. Registration Phase

Client U_i sends the identity ID_i and the chosen password PW_i for registration. Upon receiving the request, the server generates a smart card's identifier CID_i and calculates $S_i = ID_i^{SK} \bmod n$, $h_i = g^{PW_i * SK} \bmod n$, and $W_i = h(ID_i, SK)$ where n is a large prime number and g is a generator of Z_n^*. The server stores ($n, g, ID_i, CID_i, S_i, h_i, W_i$) into a smart card and issues it back to the client. The phase is finished through a secure channel and the smart card adopted a fingerprint technology to verify the fingerprint of the client.

C. Login Phase

Client U_i enters the password PW_i and imprints the personalized fingerprint through a fingerprint input device. If it succeeds, the card performs the following steps:

1) The card extracts the content (ID_i, CID_i), generates a random nonce N_i and forwards them to the server as its login request.

2) Upon receiving the request (ID_i, CID_i, N_i), the server determines a puzzle solution v_s and calculates $p = h(ID_i, N_i, N_s, v_s)$ and $token_i = h(p, ID_i, N_i, N_s, v_s, sk_s)$. The server sends ($p, N_s, token_i$) back to the card.

3) The cards tries to seek out the solution v_s to satisfy $h(ID_i, N_i, N_s, v_s) = p$. It should apply a brute-force method to find of the solution without the knowledge of the solution. After the solution is found, the card calculates $X_i = g^{r_i * PW_i} \bmod n$,

$Y_i = S_i * h_i^{r_i * token_i} \bmod n$, $Z_i = W_i \oplus q_i$, and $T_i = h(X_i, Y_i, token_i, q_i)$, where q_i is a chosen session key for future communications. The card sends $(ID_i, X_i, Y_i, Z_i, T_i, v_s, N_i, N_s)$ to the server.

4) The server checks the validity of (ID_i, N_i, N_s) and verifies whether $token_i$ is equal to $h(p, ID_i, N_i, N_s, v_s, sk_s)$ for proving the solution of the puzzle. If the above verification holds, the server extracts $q_i = Z_i \oplus h(ID_i, SK)$ and verifies whether T_i is the same as $h(X_i, Y_i, token_i, q_i)$. If it is also true, the server checks whether $Y_i^{SK^{-1}}$ is equal to $ID_i * X_i^{token_i} \bmod n$. If the verification is also correct, the server sets q_i as the session key and sends $h(q_i)$ back to the card for the mutual authentication.

5) Similarly, the card verifies the correctness of $h(q_i)$. If it is true, the card sets q_i as the session key.

D. Perfect Forward Secrecy

Since the communications $(ID_i, X_i, Y_i, Z_i, T_i, v_s, N_i, N_s)$ are always eavesdropped from outsiders, if the attacker compromises the long-term secret key SK, all the session keys can be derived.

1) The attack can construct all the secret keys of clients, $W_i = h(ID_i, SK)$

2) Then the attacker can derive all the session keys $q_i = Z_i \oplus W_i$.

E. Perfect Backward Secrecy

Similarly, the communications $(ID_i, X_i, Y_i, Z_i, T_i, v_s, N_i, N_s)$ are always eavesdropped from outsiders, if the attacker compromises a used session key q_i, we can show that the attacker can impersonate the client U_i to communicate with the server.

1) Firstly, the attacker employs q_i to extract the long-term secret key $W_i = h(ID_i, SK) = Z_i \oplus q_i$.

2) Now, the attacker sends a login request (ID_i, CID_i, N_i) to the server. Without loss of generality, the server will return $(p_{new}, N_{snew}, token_{inew})$ back to the attacker.

3) The goal of the attacker is to forge $(ID_i, X_{inew}, Y_{inew}, Z_{inew}, T_{inew}, v_{snew}, N_i, N_{snew})$ for passing the verifications of the servers.

  I. For simplicity, we assume that the attacker have unlocked the solution v_{snew} of the puzzle p_{new}.

  II. Find an integer a to satisfy $a * token_{new} \equiv token \bmod n$, where $a \equiv token_i * token_{inew}^{-1} \bmod n$.

  III. Select a new session key q_{inew}.

  IV. Calculate $X_{inew} = X_i^a \bmod n$, $Z_{inew} = W_i \oplus q_{inew}$, and $T_{inew} = h(X_{inew}, Y_{inew}, token_{inew}, q_{inew})$

  V. Send $(ID_i, X_{inew}, Y_{inew} = Y_i, Z_{inew}, T_{inew}, v_s, N_i, N_{snew})$

4) Without loss of generality, the server will verify:

  I. Check the validity of (ID_i, N_i, N_s);

  II. Verifies whether $token_{inew}$ is equal to $h(p, ID_i, N_i, N_{snew}, v_{snew}, sk_s)$ for proving the solution of the puzzle.

  III. Extract $q_{inew} = Z_{inew} \oplus h(ID_i, SK)$;

  IV. Verify whether $T_{inew} = h(X_{inew}, Y_{inew}, token_{inew}, q_{inew})$. If it is also true, the server checks whether $Y_{inew}^{SK^{-1}}$ is equal to $ID_i * X_{inew}^{token_{inew}} \bmod n$. If the verification is also correct, the server sets q_{inew} as the session key and sends $h(q_{inew})$ back to the card for the mutual authentication.

  V. The forged request will pass the verification of server and the server will believe the session key is q_{inew}.

5) Correctness.

(1) $Y_{inew}^{SK^{-1}} = Y_i^{SK^{-1}} = (S_i * h_i^{r_i * token_i})^{SK^{-1}} \bmod n$

$= (ID_i * g^{PW_i * r_i * token_i}) \bmod n$

(2) $(ID_i * X_{inew}^{token_{inew}}) = (ID_i * X_i^{a * token_{inew}}) \bmod n$

$= (ID_i * g^{PW_i * r_i * token_i}) \bmod n$

II. OUR SCHEME

In this section, we propose a novel user authentication scheme with key agreement. The proposed scheme not only can keep the same merits of Hwang *et al*.'s scheme, but also can add more admired security properties. The used parameters are the same Hwang *et al*.'s scheme.

A. Registration Phase

Client U_i sends the identity ID_i and the chosen password PW_i for registration. Upon receiving the request, the server generates a smart card's identifier CID_i and calculates $S_i' = (ID_i^{SK} \bmod n) \oplus h(PW_i)$, $h_i' = (g^{PW_i * SK} \bmod n) \oplus h(PW_i)$, and $W_i' = h(ID_i, SK) \oplus h(PW_i)$. The server stores $(n, g, ID_i, CID_i, S_i', h_i', W_i')$ into a smart card and issues it back to the user. The phase is finished through a secure channel.

B. Login Phase

User U_i enters the password PW_i into a card reader. Then the smart card performs the following steps to achieve the mutual authentication with the server.

1) The card extracts the content $(ID_i, CID_i, S_i = S_i' \oplus h(PW_i), h_i = h_i' \oplus h(PW_i), W_i = W_i' \oplus h(PW_i))$, generates a random number N_i and calculates $g^{N_i * PW_i} \bmod n$. Then the card forwards $(ID_i, CID_i, g^{N_i * PW_i} \bmod n)$ to the server as its login request.

2) Upon receiving the request, the server determines a puzzle solution v_s and calculates $g^{N_s} \bmod n$ and $p = h(ID_i, g^{N_i * PW_i} \bmod n, g^{N_s} \bmod n, v_s)$. The server also calculates $p = h(ID_i, g^{N_i * PW_i} \bmod n, (g^{N_s} \bmod n) \oplus h(ID_i, SK), v_s)$ and $token_i = h(p, ID_i, g^{N_i * PW_i} \bmod n, (g^{N_s} \bmod n) \oplus h(ID_i, SK), v_s, sk_s)$ and sends $(p, (g^{N_s} \bmod n) \oplus h(ID_i, SK), token_i)$

back to the card.

3) The cards employs W_i to extract $g^{N_s} \bmod n$ and tries to seek out the solution v_s to satisfy $h(ID_i, g^{N_i * PW_i} \bmod n$, $(g^{N_s} \bmod n) \oplus h(ID_i, SK)$, $v_s) = p$. It should apply a brute-force method to find of the solution without the knowledge of the solution. After the solution is found, the card calculates $Y_i = S_i * h_i^{N_i * token_i} \bmod n$, $Sess = g^{N_s * N_i * PW_i} \bmod n$, and $T_i = h(Y_i, token_i, Sess, v_s)$. The card sends ($ID_i$, $token_i$, Y_i, T_i) to the server.

4) The server checks the validity of ID_i and verifies whether $token_i$ is equal to $h(p, ID_i, g^{N_i * PW_i} \bmod n$, $g^{N_s} \bmod n$, v_s, sk_s) for proving the solution of the puzzle. If the above verification holds, the server

verifies whether $Y_i^{SK^{-1}}$ is equal to $ID_i * g^{N_i * PW_i * token_i} \bmod n$. If it holds, the server calculates $Sess = g^{N_i * PW_i * N_s} \bmod n$ and verifies whether T_i is the same as $h(Y_i, token_i, Sess, v_s)$. If all of the conditions are held, the server authenticate the identity of the user and sets the session key $SK_{US} = h(Sess)$ as their session key. The server sends $h(Y_i, token_i, Sess+1, v_s)$ back to the card.

5) Similarly, the card verifies the correctness of $h(Y_i, token_i, Sess+1, v_s)$. If it is true, the card also sets the session key $SK_{US} = h(Sess)$ as their session key. We use Figure I to introduce our scheme.
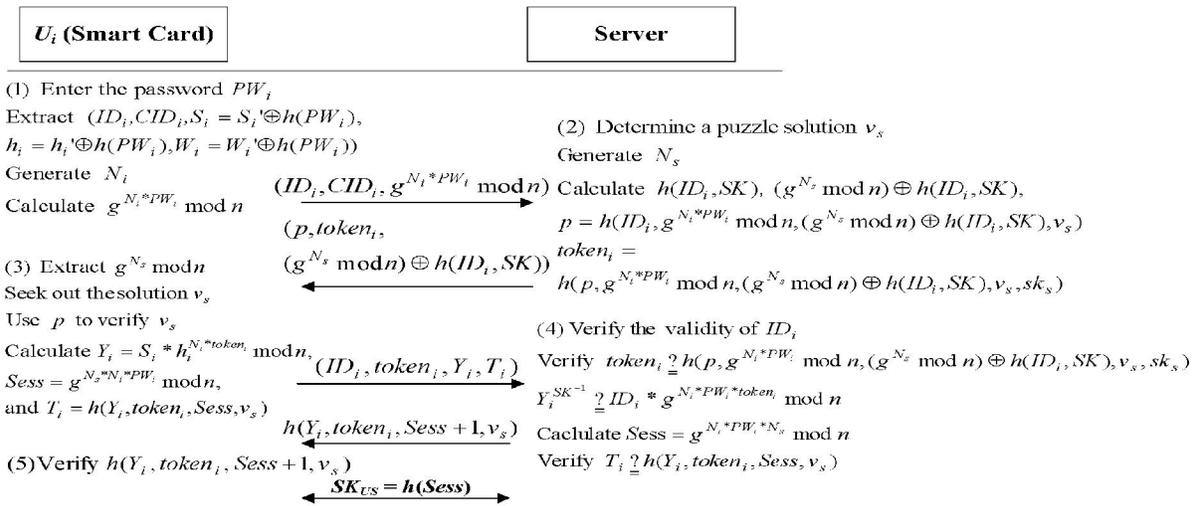
Figure I. The Proposed Scheme

III. DISCUSSIONS

A. Security Analysis

We analyze that the proposed scheme is secure against some well-known security threats.

1) **Mutual Authentication.** The goal of the mutual authentication is to establish an agreed session key SK_{US} between U_i and the server. Let $U_i \xleftrightarrow{SK_{US}} S$ denote that U_i shares a secret key SK_{US} with the server S. The mutual authentication is complete between U_i and S if there is a session key SK_{US} such that U_i believes $U_i \xleftrightarrow{SK_{US}} S$, and S also believes $U_i \xleftrightarrow{SK_{US}} S$. A strong mutual authentication may lead to the following statement [21][Burrows *et al*., 1990]:

I. U_i believes that S believes $U_i \xleftrightarrow{SK_{US}} S$, and

II. S believes that U_i believes $U_i \xleftrightarrow{SK_{US}} S$.

U_i and S can do mutual authentication in the login phase.

I.   Upon receiving $h(Y_i, token_i, Sess+1, v_s)$ in Step

4, U_i will verify whether the received hashed value is correct or not. If it holds, U_i will believe that $(g^{N_s} \bmod n) \oplus h(ID_i, SK)$ is generated by S and believe $U_i \xleftrightarrow{SK_{US}} S$.

II. Since N_i is generated by U_i, U_i believes N_i is fresh and believes that S believes $U_i \xleftrightarrow{SK_{US}} S$.

III. Using the same way, upon receiving (ID_i, $token_i$, Y_i, T_i) in Step 3, S will verify the validity of $token_i$, Y_i and T_i. If all the conditions hold, S believes that $g^{N_i * PW_i} \bmod n$ is generated by U_i and believe $U_i \xleftrightarrow{SK_{US}} S$.

IV. Since N_s is generated by S, S believes N_s is fresh and believes that U_i believes $U_i \xleftrightarrow{SK_{US}} S$.

2) **The Replay Attack.** The attack could be classified into two categories. Firstly, if the attacker re-submits a used message (ID_i, CID_i, $g^{N_i * PW_i} \bmod n$) to the server as a new login request. Without loss of generality, the server responses (p_{new},

$(g^{N_{snew}} \bmod n) \oplus h(ID_i, SK), token_{inew})$ back. The attacker cannot retrieve $(g^{N_{snew}} \bmod n)$ without W_i. It implies that the attacker has no ability to send the response to the server in Step 3. Secondly, if the attacker re-submits a used message $(p, (g^{N_s} \bmod n) \oplus h(ID_i, SK), token_i)$ back to the card. The card believes that the received message is fresh. Based on the difficulty of the computational Diffie-Hellman problem, without the knowledge of N_s, the attacker still has no ability to send the response $h(Y_i, token_i, Sess+1, v_s)$ back in Step 4.

3) **The Impersonation Attack without the Smart Card.** Consider that the attacker can send a forged request $(ID_i, CID_i, g^{N_i} \bmod n)$ and will get an honest response $(p, (g^{N_s} \bmod n) \oplus h(ID_i, SK), token_i)$ back. Without the secret key W_i, the attacker cannot retrieve $g^{N_s} \bmod n$. It implies that the attacker has no ability to forge a valid $T_i = h(Y_i, token_i, Sess, v_s)$ to the server based on the difficulty of the computational Diffie-Hellman problem.

4) **The Guessing Attack / Impersonation Attack with the Smart Card.** Consider that the attacker has the ability to extract the content of the smart card, $(S_i' = (ID_i^{SK} \bmod n) \oplus h(PW_i), h_i' = (g^{PW_i * SK} \bmod n) \oplus h(PW_i)$, and $W_i' = h(ID_i, SK) \oplus h(PW_i))$. Owing to the openness of the Internet, the attacker also can eavesdrop the communicated messages $(ID_i, CID_i, g^{N_i * PW_i} \bmod n$, p, $token_i = h(p, ID_i, g^{N_i * PW_i} \bmod n, (g^{N_s} \bmod n) \oplus h(ID_i, SK),$ $v_s, sk_s), Y_i = S_i * h_i^{N_i * token_i} \bmod n$, $T_i = h(Y_i, token_i, Sess, v_s), h(Y_i, token_i, Sess+1, v_s))$.

   I. **Case 1.** The attacker guesses the password PW_i' and tries to verify whether the guessed value is correct on the eavesdropped messages. By the difficulty of the discrete logarithm and the computationally Diffie-Hellman problems and without the knowledge of sk_s, it is hard for the attacker to launch the off-line guessing attack on the messages $(g^{N_i * PW_i} \bmod n$, $token_i$, $Y_i = S_i * h_i^{N_i * token_i} \bmod n)$.

   II. **Case 2.** The attacker guesses the password PW_i' and tries to verify whether the guessed value is correct on the response of the server.
      l The attacker calculates a forged request $(ID_i, CID_i, g^{N_i'*PW_i'} \bmod n)$ and sends it to the server.
      l Without loss of generality, the server sends $(p = h(ID_i, g^{N_i'*PW_i'} \bmod n, (g^{N_s} \bmod n) \oplus h(ID_i, SK), v_s)$ and $token_i = h(p, ID_i, g^{N_i'*PW_i'} \bmod n, (g^{N_s} \bmod n) \oplus h(ID_i, SK), v_s, sk_s)$ back to

the card.
      l The primary goal of the attacker is to retrieve $g^{N_s} \bmod n$ from $(g^{N_s} \bmod n) \oplus h(ID_i, SK)$. Without the correct password, the attacker must employ the guessed value to retrieve $h(ID_i, SK)'$ and $g^{N_s'} \bmod n$. Then the attacker uses $g^{N_s'} \bmod n$ and $g^{N_i'*PW_i'} \bmod n$ to construct $Sess' = g^{N_s'*N_i'*PW_i'} \bmod n, Y_i' = S_i * h_i^{N_i'*token_i} \bmod n, T_i' = h(Y_i', token_i, Sess', v_s)$. If the guessed password is correct, the server sends the response $h(Y_i', token_i, Sess+1', v_s)$ back; otherwise, the server no response. Obviously, this is an on-line detectable guessing attack. The server must join the attack and can detect whether the received messages are valid or not. Most password-based can prevent this attack by limiting an acceptable fails attempts such as three. This method also can be adopted into our scheme.

5) **The Perfect Forward Secrecy.** If the long-term secret key SK of the system is compromised, the session key is still secure in the proposed scheme. Following the scheme, the client sends $g^{N_i * PW_i} \bmod n$ to the server in Step 1 and the server sends $(g^{N_s} \bmod n) \oplus h(ID_i, SK)$ back in Step 3. Then the client and the server can establish the same session key $SK_{US} = h(Sess = g^{N_s * N_i * PW_i} \bmod n)$. Based on the difficulty of the computationally Diffie-Hellman problem and without the knowledge of the ephemeral keys N_s and N_i, the attacker cannot derive the session key SK_U.

6) **The Perfect Backward Secrecy.** Assume that a used session key $SK_{US} = h(Sess = g^{N_s * N_i * PW_i} \bmod n)$ with the communicated messages $(ID_i, CID_i, g^{N_i * PW_i} \bmod n$, p, $token_i = h(p, ID_i, g^{N_i * PW_i} \bmod n, (g^{N_s} \bmod n) \oplus h(ID_i, SK),$ $v_s, sk_s), Y_i = S_i * h_i^{N_i * token_i} \bmod n$, $T_i = h(Y_i, token_i, Sess, v_s), h(Y_i, token_i, Sess+1, v_s))$ are compromised by the attacker. The goal of the attacker is to do the following cases successfully.

   I. **Case 1.** The attacker eavesdrops the communications and tries to compromise the future session keys. Since the ephemeral keys N_s and N_i are chosen randomly, based on the difficulty of the computationally Diffie-Hellman problem, it is infeasible to derive the session key $SK_{US} = h(Sess = g^{N_s * N_i * PW_i} \bmod n)$.

   II. **Case 2.** The attacker sends a forged login request $(ID_i, CID_i, g^{N_i'} \bmod n)$ to the server and gets a response $(p, (g^{N_s} \bmod n) \oplus h(ID_i,$

SK), $token_i = h(p, ID_i, g^{N_i * PW_i} \bmod n$,

$(g^{N_s} \bmod n) \oplus h(ID_i, SK), v_s, sk_s))$ back. Without the knowledge of the system key SK or the secret keys S_i and h_i, it is computationally infeasible to find out Y_i' and T_i' to pass the equation $Y_i'^{SK^{-1}} = ID_i * g^{N_i * token_i} \bmod n$ and $T_i' = h(Y_i', token_i, Sess', v_s)$.

B. Comparisons

1) Satisfaction of the Criteria

In this subsection, we compare some admired security criteria with the related schemes and show the result in Table I.

2) Computation Cost

We denote that T_H is the time of one hash function operation; T_{MUL} is the time for one modular multiplication; $T_{\oplus}$ is the time for one exclusive OR operation; and T_{EXP} is the time for one modular exponentiation operation.

We show the comparison of the computation cost in Table II. To provide the perfect forward secrecy and the perfect backward secrecy properties and to solve the smart card loss problem, we add a slight computation cost in client and server sides respectively.

Table I. Satisfaction of the security criteria between our scheme and the related schemes

	Kim et al. [22] [Kim et al., 2003]	Hwang et al. [14][Hwang et al., 2010]	Our Scheme
Mutual authentication	No	Yes	Yes
On-line password guessing attack	Yes	Yes	Yes
Off-line password guessing attack	Yes	Yes	Yes
Message replay attack	Yes	Yes	Yes
Impersonation attack	No	Yes	Yes
Server resource exhaustion attack	No	Yes	Yes
Session key establishment	No	Yes	Yes
Perfect forward secrecy	Not supported	No	Yes
Perfect backward secrecy	Not supported	No	Yes
Security against the smart card loss problem	Not supported*	Not supported*	Yes

*: even if the schemes follow our idea, the schemes still cannot achieve the same requirement.

Table II. Comparison of the Computation Cost

	Computation Cost	
	Client Side	Server Side
Our Scheme	$(n^*+7)T_H + 4T_{\oplus} + 5T_{MUL} + 3T_{EXP}$	$6T_H + 4T_{MUL} + 3T_{EXP}$
Kim et al.'s scheme [22][Kim et al., 2003]	$3T_{MUL} + 2T_{EXP}$	$1T_H + 1T_{MUL} + 2T_{EXP}$
Hwang et al.'s scheme [14][Hwang et al., 2010]	$(n^*+3)T_H + 1T_{\oplus} + 3T_{MUL} + 2T_{EXP}$	$6T_H + 1T_{\oplus} + 1T_{MUL} + 2T_{EXP}$

*: n is the number of hash function operations that is used to solve the puzzle.

Conclusions

We have proposed a security enhanced password-based user authentication scheme with key agreement. By Tables I and II, the proposed scheme not only satisfies the same security criteria with Hwang et al.'s scheme, but also uses a slight computation cost to provide more admired security requirement such as the perfect forward secrecy, the perfect backward secrecy and the smart card loss problem.

References

[1] Agah A. and Das S. K., Preventing DoS attacks in wireless sensor networks: a repeated game theory approach, International Journal of Network Security 2007; 5(2):145–53.8

[2] Aura, T., Nikander, P., Leiwo, J., DoS-resistant authentication with client puzzles, In: Proceedings of the Eighth International Workshop on Security Protocols 2001; LNCS 2133:170–7.10

[3] Bellare M. and Rogaway P., Entity authentication and key distribution, Advances in Cryptology - CRYPTO'93 1993; LNCS 773: 232–249.1

[4] Bocan, V., Threshold puzzles: the evolution of DoS-resistant authentication, Transactions on Automatic Control and Computer Science 2004; 49(63):171–6.11

[5] Burrows M., Abadi M. and Needham R., A logic of authentication, ACM Transactions on Computer Systems (TOCS) 1990; 8(1):18–36.21

[6] Hwang M.-S., Chong S.-K. and Chen T.-Y., DoS-resistant ID-based password authentication scheme using smart cards, The Journal of Systems and Software 2010; 83(1):163-72.14

[7] Juang W.-S., Efficient Multi-server Password Authenticated Key Agreement Using Smart Cards, IEEE Trans. on Consumer Electronics Feb. 2004; 50(1):251-5.2

[8] Juang W.-S., Efficient Password Authenticated Key Agreement Using Smart Cards, Computers & Security March 2004; 23(2):167-73.3

[9] Juang W.-S., Efficient Three-party Key Exchange Using Smart Cards, IEEE Trans. on Consumer Electronics May 2004; 50(2):619-24.4

[10] Juang W.-S., Efficient User Authentication and Key Agreement in Ubiquitous Computing, Proc. of the 2006 International Conference on Computational Science and its Applications (ICCSA'06), LNCS 3983:396-405.5

[11] Juang W.-S., Chen S.-T. and Liaw H.-T., Robust and Efficient Password Authenticated Key Agreement Using Smart Cards, IEEE Trans. on Industrial Electronics 2008; 55(6):2551-6.6

[12] Juels, A., Brainard, J., Client puzzles: a cryptographic defense against connection depletion attacks. In: Proceedings of the NDSS'99 (Networks and Distributed Security Systems), February 1999:151–65.12

[13] Laurens, V., Saddik, A.E., Nayak, A., Requirements for client puzzles to defeat the denial of service and the distributed denial of

service attacks. International Arab Journal of Information Technology 2006; 3(4):326–33.13

[14] Minier M., Phan R. C. and Pousse B. Distinguishers for ciphers and known key attack against Rijndael with large blocks, in AFRICACRYPT 2009; LNCS 5580:60-76.16

[15] Nordin, B., 2004. Match-on-card technology white paper. Technical Report, Precise Biometrics; 2004.20

[16] van Oorschot P. C. and Wiener M. J., A Known-Plaintext Attack on Two-Key Triple Encryption, Advances in Cryptology - EUROCRYPT'90 1991; LNCS 473:318-25.17

[17] Peng, T., Leckie, C., Ramamohanarao K., Survey of network-based defense mechanisms countering the DoS and DDoS problems. ACM Computing Surveys 2007; 39(1).9

[18] B. Schneier, *Applied cryptography, 2nd edition*. John Wiley & Sons Inc., 1996.15

[19] Wang R.-C., Juang W.-S. and Lei C.-L., User Authentication Scheme with Privacy-preservation for Multi-server Environment, IEEE Communications Letters 2009; 13(2): 157-9.

[20] Wang R.-C., Juang W.-S. and Lei C.-L., A Robust Authentication Scheme with User Anonymity for Wireless Environments, International Journal of Innovative Computing, Information and Control 2009; 5(4): 1069-80.

[21] Wen H.-A., Lee T.-F. and Hwang T., Provably secure three-party password-based authenticated key exchange protocol using weil pairing, IEE Proc.-Commun. 2005; 152(2):138–43.7

[22] Kocher P., Jaffe J. and Jun B., Differential power analysis, Advances in Cryptology – Crypto'99 1999: 388-97.18

[23] Messerges T. S., Dabbish E. A. and Sloan R. H., Examining smart card security under the threat of power analysis attacks, IEEE Transactions on Computers 2002; 51(2): 541-52.19

[24] Kim, H. S., Lee, S. W., Yoo, K. Y., ID-based password authentication scheme using smart cards and fingerprints, ACM SIGOPS Operating Systems Review 2003; 37(4): 32–41.22

Morphological and Biochemical Response of *Cicer arietinum* L. var. pusa-256 towards an Excess of Zinc Concentration

Sudarshana Sharma[1], *Parmanand Sharma[2], Shankari P. Datta[1], Varsha Gupta[1]

[1]Department of Biochemistry, Bundelkahnd University Jhansi 284128, India
[2] School of Environmental Sciences, Jawaharlal Nehru University, New Delhi 110067, India
pnsjnu@gmail.com

Abstract:

The toxic effect of zinc (Zn) at increasing concentration was studied with special attention being given to the morphogenic and biochemical response of *Pisum sativum* L. *Cicer arietinum* plants were grown in different concentration of $ZnSO_4$ (0, 10, 25, 50, 75 and 100 μM) for 15 days. In respective to their controls, low concentration (10 and 25 μM) of Zn greatly stimulated the seed germination, while it was inhibited by highest concentration of Zn (100μM). Radical, hypocotyls length and root length (TI) and plant height (TI) were also increased up to 25 μM of Zn addition and after that a significant reduction were noticed at 75 and 100μM. The effects of toxicity of Zn on chlorophyll content and antioxidant enzymes activity include CAT, APX and GPX were investigated. The data showed that the low concentration of Zn (25μM) addition induced in chlorophyll content and high levels of Zn reduced the chlorophyll synthesis in the leaves of this plant. Maximum and minimum chlorophyll content were observed at 25 and 100 μM of Zn addition respectively. Activities of antioxidant enzymes were indicated close relationship with increase in Zn concentration and shoots showed higher activity of antioxidant enzymes than roots. The activity of APX in shoot and root were higher than CAT and GPX. [Life Science Journal. 2010;7(1): 95 – 98] (ISSN: 1097 – 8135).

Key words: Seed Germination; Hypocotyls Length; *Cicer arietinum* Plant; Antioxidant enzymes.

1. INTRODUCTION

With the development of industries, mining activities, application of waste water and sewage sludge on land, phytotoxicity of the heavy metals pollution has serious implications in soil degradation and it may reduce both the quality and efficiency of plants (Ali et al., 1999). Although certain metals like Cu, Mn, Fe and Zn are crucial for plants and are used as micronutrients, however, at higher concentrations they may reveal strong toxicity. They obstruct plant growth as do the other heavy metals like Cd, Hg, or Pb, which have no function in plant metabolism (Ali et al., 2000).

Zn is a microelement with important physiological functions in plants, however, at higher concentrations it can become toxic, thus leading to physiological and morphological disturbances and, eventually to decreased yield. It triggers enzymes by incorporating themselves into metalloenzymes of the electron transport system. Zn plays a vital role in the cell division, cell expansion, proteins synthesis, and also in carbohydrate, nucleic acid and lipid metabolism (Collins, 1981). As Zn forms stable complexes with DNA and RNA it might also influence DNA and RNA stability. But on the other hand a higher concentration of Zn in the plant tissue seriously affects activity of several enzymes and other fundamental metabolic processes. An excess of Zn also reduced photosynthetic rate as a part of enzymes concerned in the photosynthesis. A toxic concentration of Zn in the plant tissue seriously affects activity of several enzymes and other fundamental metabolic processes. Ali et al., (2000) carried out a brought study and affirmed that an excess of

Zn also reduced photosynthetic rate as a part of enzymes concerned in the photosynthesis. Nitrogen metabolism is also affected by diverse ways by an excess of Zn. The protein content is found to be reduced; nitrogen-fixation and nitrate reductase activity was also concealed by Zn toxicity (Phalsson, 1989).

The protein content was found to be reduced; nitrogen-fixation and nitrate reductase activities were also concealed by Zn toxicity. An overindulgence of both essential and toxic heavy metals has been found to be allied with generation of free radicals. Free radicals or ROS are toxic by-products, generated at low levels in non-stressed plant cells in chloroplasts and mitochondria, and also by cytoplasmic, membrane-bound or exocellular enzymes concerned in redox reactions (especially photosynthetic electron transport processes and respiration). Extra amounts of ROS occur under stressful conditions and over production of these ROS such as superoxide, H_2O_2 and OH^* results in the plants exposed to stress conditions including metal stress (Galligo et al., 1999). ROSs are known to spoil cellular membranes by inducing lipid peroxidation or interruption of electron transport chain. The activation of lipoxygenase, an enzyme that arouse lipid peroxidation, has been reported after cadmium revelation (Smeets et al., 2005). As a consequence, tissues snubbed by oxidative stress generally contain elevated concentration of APX, GPX and CAT and demonstrate an increased assembly of ethylene (Schutzendubel et al., 2001).

Hence, the objective of this study was to evaluate the effect of additional supply of Zn in the form of

$ZnSO_4.2H_2O$ on the morphological and biochemical response of *Cicer arietinum* L. Disparity in some stress related parameters such as root, shoot length, plant height, photosynthetic pigments and antioxidant enzymes was also examined in relation to Zn concentrations.

2. MATERIAL AND METHODS:

2.1 Seeds Surface Sterilization and Treatment Process

Seeds of *Cicer arietinum* (Var.-Pusa-256) L. were collected from Seed Cooperative Committee, Jhansi, India and surface sterilized with 1% $HgCl_2$ for 30 min. They were rinsed with tap water followed by double distilled water and allowed to soak in de-ionized water and different concentrations of $ZnSO_4.7H_2O$ solutions for four hours (0, 10, 25, 50, 75 and 100mM solution). For morphological and biochemical studies 25 properly soaked seeds were transferred to plastic boxes, layered with sterilized germinating paper, and kept in incubator at 22 ± 2^0C in three replicates. Paper of boxes was already soaked with different $ZnSO_4.7H_2O$ solutions. Seedlings were harvested after 15 days of treatment, roots and shoots were separated and lengths were measured.

2.2 Seed Germination and Measurement of Hypocotyl and Radicle Length

For germination test ten properly soaked seeds were placed in petriplates lined with germinating paper in three replicates and germination test was performed after 72 hours in a separate set of experiments. A 2mm radicle emergence from seed was considered as germinated seed. Measurements of hypocotyl and radicle length were done with five seedlings from each treatment after 15 days.

2.3 Plant growth parameters and tolerance index

A number of plant growth parameters, viz. root-shoot lengths, root fresh and dry weights, plant height and chlorophyll content in leaves were determined. Chlorophyll a and b in leaves were measured by Machlachlan and Zalik, (1963).

Tolerance indices (TI) of root length and plant height against each concentration were calculated following Baker et al., 1994.

TI (%) = Mean length metal solution/ mean length for control solution X100

2.4 Enzyme assay

Different enzymes were assayed in crude extract of root and shoot. For preparation of crude extract, 1.0 gram of plant material was crushed in chilled mortar and pestle with 5 ml of 50 mM phosphate buffer (pH-7.5). Homogenate were centrifuges for 10 min at 10,000 rpm at 4^0C and supernatant were directly used for assay of CAT, APX, and GPX by Chance and Maehly (1959), Asada (2001) and Chang and Kao (1998) respectively.

2.5 Statistical analysis

All the results were expressed as mean value ±SD for three replications. For each replication we have taken plant material by weight from different boxes. For statistical analyses all the data were subjected to one way ANOVA test using GPIS software (1.13) (Graphpad, California, USA).

3. RESULTS:

3.1 Germination Assay and Morphological Analysis

Seeds were initially exposed to various concentrations of $ZnSO_4.2H_2O$ in order to review the adverse effects of Zn on seed germination and radicle emergence in *Cicer arietinum* L. seeds. Means of seed germination percentage after 72 hours are shown in table-1. Results indicated that seed germination rate had an upward trend up to 25mM Zn concentration, but at 50-100mM inhibitory effects were demonstrated compared to their relevant controls. It showed that low Zn concentrations (10 and 25mM) had significantly stimulatory effect ($p < 0.05$) whereas, the higher concentrations (75-100mM) become noxious and significantly suppressed the germination ($p < 0.001$). The mean radicle and hypocotyl lengths of *Cicer arietinum* seedlings at 15 days were also augmented significantly ($p < 0.01$) up to 25mM Zn addition and were the lowest at 100mM ($p < 0.001$) Zn (Table 1).

The consequence of different Zn concentrations on root fresh and dry weight, tolerance index and plant height index were shown in table 1. It was observed that Zn concentration up to 50mM showed a positive response to biomass production ($p < 0.001$). As Zn concentration increased (75 and 100mM) biomass was significantly reduced compared to the control ($p < 0.001$). Root length (TI) significantly increased ($p < 0.001$) up to 50mM and then a significantly declined ($p < 0.001$) compared to their respective control. An analogous pattern was observed for plant height (TI).

3.2 Chlorophyll

The effects of Zn addition on photosynthetic pigments (Chlorophyll a, b) are shown in Fig 1A. *Cicer arietinum* plants grown in 25mM of Zn supply, contained maximum chlorophyll content and a statistically significant ($p < 0.001$) reduction was observed at 75-100mM of Zn supply

3.3 Antioxidant Enzymes

The effect of Zn addition in various concentrations on antioxidant enzymes in *Cicer arietinum* shoots and roots are shown in Fig. 1A&B. All antioxidant enzymes were amplified linearly with Zn addition and found utmost at 100mM Zn concentration. Rate of APX was highest among three antioxidant enzymes, followed by CAT and GPX at all treatments. Shoots of *Cicer arietinum* plants contained more antioxidants enzymes activity than roots.

Table 1: The effect of Zn addition on seed germination (72 h) and morphology of *Cicer arietinum* seedlings (15 d)

Notation: [a] p<0.001; [b] p<0.01; [c] p<0.05 compared to control within a column. All the data are mean of three values ±SD.

| Zn treatment (mM)	Germination (%)	Radical and Hypocotyls length (cm/plant)		Root biomass (g/plant)		Tolerance Index (%)	
		Radical length	Hypocotyls length	Fresh weight	Dry weight	Root length	Plant height
0	88.9±0.78	7.4±0.90	9.3±.82	0.1±0.04	0.05±0.03	100±0.00	100±0.00
10	93.7±2.70	9.9±0.84[c]	11.6±0.79	0.15±0.01	0.07±0.01	134.8±2.72[a]	124.5±4.01[a]
25	96.5±2.69	10.5±0.94[b]	12.5±0.69[b]	0.2±0.02[b]	0.09±0.02	143.8±3.96[a]	134.3±5.08[a]
50	85.4±2.04[cb]	7.6±0.64[cb]	10.8±0.88[ab]	0.24±0.02[ab]	0.1±0.03	103.8±3.07[a]	115.8±4.58[a]
75	76.5±2.39[bac]	6.3±0.61[a]	8.5±1.10[ac]	0.22±0.02[ac]	0.08±0.04	86.1±4.01[ba]	90.8±2.31[a]
100	57.8±4.65[a]	4.6±0.28[bab]	5.6±0.39[c]	0.16±0.02[c]	0.06±0.03	63.0±4.06[a]	59.8±4.78[a]
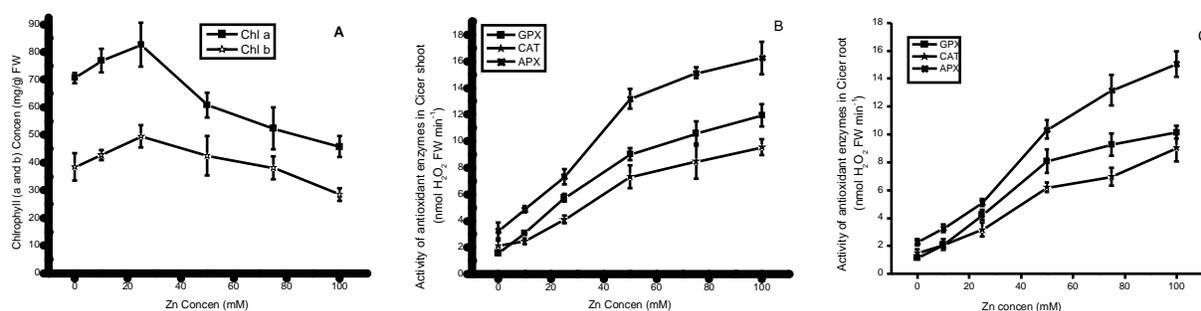
Figure 1: The effect of Zn toxicity on Chlorophyll contents (A) antioxidant enzymes of shoot (B) and root (C). All the data are mean of three values ±SD.

DISCUSSION:

Zn at lower concentrations enhanced *Cicer arietinum* seed germination. This is because Zn is a micronutrient and indispensable for plant growth (Wierzbicka and Obidzinska, 1998). But at higher quantity it abridged the germination percentage, which is consistent with other researcher's findings (Herrero et al., 2003; Ataci et al., 2005). The abridged germination of seeds under Zn stress could be a depressive effect of high concentration of metal on the activity of amylases and on succeeding transfer of sugars to the embryo axes. Zeid (2001). Thus, our results supported the conclusions of Ali et al., 2000, who pragmatic that at critical level Zn could behave as toxic metals such as Cd and Pb. Decline in growth can be due to the obstruction of heavy metals with metabolic processes allied with regular growth of plant (Wierzbicka and Obidzinska, 1998). In the best of our acquaintance it was the first study which deals the Zn toxicity on radicle and hypocotyls length. Declining pattern in growth of plants could be due to the obstruction of metabolic processes which allied with regular growth of plants

Lower Zn concentration increased the chlorophyll content while it explained a diminution at higher values. It was might be due to eagerly gathering of Zn in the leaf, that significantly affects metabolic processes in the chloroplast (Van Assche and Clijsters, 1986). Hampp et al.,

(1976) observed that Zn subdued photosynthetic CO_2 fixation and Hill activity of isolated spinach chloroplast.

In the present research work activity of antioxidant enzymes increased linearly with Zn supply. Excess of Zn can persuade oxidative stress in plants, which can escort formation of Reactive Oxygen Species. Antioxidant enzymes may alter the H_2O_2 to the H_2O in the plant cells and counteract the toxicity effect of H_2O_2 (Rezai and Farboodnia, 2008). Hence to shield cells against oxidative stress, antioxidant enzymes augmented proportionally, which is also consistent with our results.

APX is the most important peroxidase in H_2O_2 detoxification operating both in cytosol and chloroplasts (Mittova et al., 2000). Therefore, APX was the enzyme which illustrated maximum activity in *Cicer arietinum* shoots and roots. All the antioxidant enzymes studied in this effort explain maximum activity in shoots compared to roots. It might be due to translocation of Zn in aerial parts as a micronutrient and this augmented the concentration of antioxidant enzymes in shoots compared to roots.

This study showed that a 25mM of Zn concentration enhanced seed germination, augmented radicle and hypocotyls lengths, chlorophyll content, fresh weight, as well as tolerance indices. The activities of antioxidant enzymes were also significantly appropriate at this concentration. Below and above 25mM Zn concentration, chlorophyll contents and oxidative stress were augmented,

which led to diminution in development of *Cicer arietinum* plants. Hence we recommended that 25mM Zn may be favorable for plant growth and this concentration of Zn may be recommended for the cultivation of plants.

ACKNOWLEDGEMENT

Corresponding To:
Parmanand Sharma
School of Environmental Science,
Jawaharlal Nehru University,
New Delhi, India-110067
Phone No. - +91 9968897332
Fax No. +91 11 26741502
E-mail: pnsjnu@gmail.com

REFERENCES
1. Ali G, Srivastava PS, Iqbal M. Morphogenic and biochemical response of *Bacopa monniera* cultures to Zn toxicity. Plant Sc 1999; 143: 187-3.
2. Ali G, Srivastava PS, Iqbal M. Influence of cadmium and Zn on growth and photosynthesis of *Bacopa monniera* cultivated in vitro. Biol. Plant 2000; 43: 599-01.
3. Asada K. Ascorbate peroxidase: A hydroxide scavenging in plants. Physiol. Plant 2001; 85: 235-41.
4. Ataci O, Agar G, Battal P. Change in phytohormone contents in chickpea seeds germinating under lead or zinc stress. Biol. Plant 2005; 49: 215-22.
5. Baker AJM, Reeves RD, Hajar ASM. Heavy metals accumulation and tolerance in British population of metallophyte *Thalapsi caerulescens* J. and C. New Phytol 1994; 127: 61-8.
6. Chance B, Mahely A C. The assay of catalase and peroxidaseIn: Click, D. (Ed). *Method of biochemical analysis*, Interscience Publishers. New York, 1959 1: 357-25.
7. Chance CJ, Kao CH. H_2O_2 metabolizing enzymes during senescence of rice leaves: Change in enzyme activities in light and darkness. Plant Growth Regulation 1998; 25: 11-15.
8. Collins JC. In Lepp, N. W. (ed.), *Effect of Heavy Metal Pollution on Plants*, Vol. 1. Applied Science Publishers, London and New Jersey, 1981: p. 145.
9. Galligo SM, Benavides MP, Tomoro M L. Effect of Cd ions on antioxidant defense system in sunflower cotyledons. Biol. Plant 1999; 42: 49-5.
10. Hampp RK, Beulich, Ziegler H. Effect of zinc and cadmium on photosynthetic CO2-fixation and Hill activity of isolated spinach chloroplasts, Z. Plant Physiol 1976; 77: 336–44.
11. Herrero EM, Lopez-Gonzazalvez A, Ruiz MA, Lucas-Garcia JA, Barbas C. Uptake and distribution of Zn, Cd, Pb and Cu in *Brassica napus* and *Helianthus annus* grown in conta minated soils. Inter. J. Phytoremed 2003; 5: 153-67.
12. Machlachlan S, Zalik S. Plastid structure, chlorophyll concentration and free amino acid composition of a chlorophyll mutant on Barley. Can. J. Bot 1963; 41: 1053-62.
13. Mittova V, Volokita M, Guy M, Tal M. Activities of SOD and the ascorbate-glutathione cycle enzymes in subcellular compartments in leaves and roots of the cultivated tomato and its wild salt-tolerant relative *Lycopersicon pennellii*. Physiol. Plant 2000: 110: 45-1.
14. Phalsson A M B. Toxicity of heavy metals (zn, cu, cd, pb) to vascular plants. *Water*, Air, Soil Pollut 1989; 47: 287-19.
15. Rezai K, Farboodnia T, Manganese toxicity effects on chlorophyll content and antioxidant enzymes in pea plant (*Pisum sativum* L. *c.v. qazvin*). Agri. J 2008; 3: 454-8.
16. Schutzendubel A, Polle A. Plant responses to abiotic stresses: heavy metal-induced oxidative stress and protection by mycorrhization. J Exp. Bot 2002; 53: 1351-65.
17. Smeets K, Cuyoers A, Lambrechts A, Semane B, Hoet P, Van Laere A, Vangronsveld J. Induction of oxidative stress and antioxidant mechanism in *Phaseolus vulgaris* after Cd application. Plant Physiol 2005; 43: 437-43.
18. Van Assche F, Clijsters H, Inhibition of photosynthesis in *Phaseolus vulgaris* by treatment with toxic concentration of zinc; effect on ribulose-1, 5-bisphosphate carboxylase:oxygenase, J. Plant Physiol 1986; 125: 355–60.
19. Wierzbicka M, Obidzinska J. The effect of lead imbibitions and germination in different plant species. Plant Sc 1998; 137: 155-71.
20. Zeid IM. Responses of *Phaseolus vulgaris* to chromium and cobalt treatments. Biol Plant 2001; 44:111- 5.

An Efficient and Flexible Matching Strategy for Content-based Image Retrieval

Mann-Jung Hsiao [1,*], Yo-Ping Huang [2], Tienwei Tsai [3], Te-Wei Chiang [4]

[1]Department of Computer Science and Engineering, Tatung University, Taipei 104, Taiwan; [2]Department of Electrical Engineering, National Taipei University of Technology, Taipei 106, Taiwan; [3]Department of Information Management, Chihlee Institute of Technology, Taipei County 220, Taiwan; [4]Department of Accounting Information Systems, Chihlee Institute of Technology, Taipei County 220, Taiwan

hsiao@mis.knjc.edu.tw
Received February 2, 2008

Abstract

With the rapid growth of multimedia applications and digital archives, content-based image retrieval (CBIR) has emerged as an important area and received lots of attentions for the past decades. In practice, there are two major problems raised by a CBIR system: the feature descriptions of images and the expressions of users' search preferences. To tackle these problems, we present a DCT-based feature descriptor coupled with an efficient way of expression for users' preferences in this paper. Our approach partitions images into a number of regions with fixed absolute locations. Each region is represented by its low-frequency DCT coefficients in the YUV color space. Two policies are provided in the matching procedure: local match and global match. In the local match, the user formulates a query by selecting the interested region in the image. Candidate images are then analyzed, by inspecting each region in turn, to find the best matching region with the query region. For those query images without clear objects, the user can select the option "global match" instead. The experimental system shows that this approach is generally effective and particularly suited for images with interested regions having features which significantly differ from the global image features. With the help of friendly GUI, our system also allows users of any experience level to effortlessly get interested images from database. [Life Science Journal. 2010; 7(1): 99 – 106] (ISSN: 1097 – 8135).

Keywords: Content-based image retrieval; region of interest; region-based image retrieval; discrete cosine transform.

1. Introduction

With the explosive growth of commerce on the Internet, businesses are advancing digital imaging even more swiftly. As digital images quickly increase in number, researchers are continually developing improved access methods to retrieve images from a large database. Generally, image retrieval procedures can be roughly divided into two approaches: annotation-based image retrieval (ABIR) and content-based image retrieval (CBIR). In ABIR, images are often annotated by words, such as time, place, or photographer. To access the desired image data, the seeker can construct queries using homogeneous descriptions, such as keywords, to match these annotations. Although ABIR potentially offers the most accurate information when images are well-named or annotated, it still has the following drawbacks[1]. First, manual image annotation is time-consuming and therefore costly. Second, human annotation is subjective. Furthermore, some images could not be annotated because it is difficult to describe their content with words. Research in the area of image databases also shows that text, specifically provided to facilitate image retrieval, is inadequate for conducting searches[2]. Even an enormous amount of descriptive text cannot adequately substitute for the content of the image itself. Unlike ABIR, CBIR tends to index and retrieve images based on their visual content. CBIR avoids many problems associated with traditional ways of retrieving images by keywords. Thus, a growing interest in the area of CBIR has been established in recent years.

CBIR is a complex and challenging problem spanning diverse algorithms all over the retrieval processes including color space selection, feature extraction, similarity measurement, retrieval strategies, relevance feedback, etc. Some general reviews of CBIR techniques can be found in the literature [3-7]. Smeulder et al. reviewed more than 200 references in this field[3]. Datta et al. studied 120 of recent approaches[4]. Veltkamp et al. gave an overview of 43 content-based image retrieval systems[5]. Deselaers et al. presented an experimental comparison for a large number of different features[6]. Liu et al. provided a comprehensive survey of the recent technical achievements in high-level semantic-based image retrieval[7]. Although various CBIR techniques have been established and good performance results were demonstrated, there are still many problems not satisfactorily solved. In order to improve the retrieval performance of a CBIR system, we propose an efficient and flexible matching strategy that employs a DCT-based feature descriptor coupled with an efficient way of expression for users' preferences.

The feature extraction method is highly essential in CBIR. Being an elementary process, the feature extraction will be invoked very frequently; therefore, it should be time-efficient and accurate. Some transform type feature extraction techniques can be applied to reduce the dimension of the vector in representing an image, such as wavelet, Walsh, Fourier, 2-D moment, DCT, and Karhunen–Loeve. Among these methods, the DCT is used in many compression and transmission areas, such as JPEG, MPEG and others. Due to the superiority in energy compacting property, the DCT is often used to extract dominant features of images. Through the extraction of the low-frequency DCT coefficients, the goal of reduction of dimensionality in

feature space can be achieved. In our approach, an image is first converted to the YUV color space and then transformed into DCT coefficients for each image (or region)**.** Psycho-perceptual studies have shown that the human brain perceives images largely based on their luminance value (i.e., Y component), and only secondarily based on their color information (i.e., U and V components). Therefore, only the Y component is considered in our approach, so as to reduce the computation cost. That is, only a block size of 4x4 DCT coefficients in the upper-left corner constitutes the feature vector of an image (or a region).

Obtaining the semantics or the meaning of an image is another important issue in CBIR. Visual feature alone is not enough to distinguish between images. Two semantically different images can have very similar visual contents. For example, indoor images have often similar red color as sunset images. Partitioning or segmenting the image into regions may reveal the "true" objects within an image. To look at the objects (or regions) in the image, instead of looking at the image as a whole, is a way to obtain the semantic of an image, which is known as region-based image retrieval (RBIR)[8]. It contributes to more meaningful image retrieval, however, the segmentation algorithms are complex and computation intensive and the segmentation results are often not correct. To solve this, some approaches break images into a fixed number of regular rectangular regions. Rudinac et al. partitioned images into 4x4 non-overlapped regions and 3x3 overlapped regions[9]. It is expectable that using more regions better results may be produced but the execution speed becomes unsatisfactory slow for a large database. Amir et al. divided images at a coarser granularity level in the IBM TRECVID video retrieval system, using a fixed 5-region layout (4 equal corner regions and an overlapping center region of the same size)[10]. Instead of pursuing sophisticated segmentation methods, we extend the Amir's spatial layout of regions to solve the problem stated above. In our CBIR system, the images are first segmented into regular regions. The user can select the region of interest (ROI) in the query image to express his/her intentions. Candidate images are then analyzed, by inspecting each region in turn, to find the best matching region with the query region. In other words, the distance between the query image and a candidate image is the smallest distance between the query region and five regions within the candidate image. The experiment results will verify that the selection of ROI is very important in CBIR.

To further allow users to express their query specifications, the feature vector is categorized into four groups to represent its average grayness and three directional texture characteristics: vertical, horizontal and diagonal. It is suitable to find out an optimal set of weights; each weight emphasizes an individual feature. However, the weights are strongly depends on the query image and the user's personal perceptions or query intentions. Therefore, a friendly user interface is employed for users to express their personal view of perceptual texture properties for the ROI. The experimental system shows that with the help of weights the performance is further improved.

This paper is organized as follows. The next section introduces color space selection and feature vector construction. Section 3 discusses related issues about the region of interest and segmentation. The similarity measurement is presented in Sec. 4 and the performance evaluation method used is given in Sec. 5. Section 6 presents experimental results. Finally, conclusions are drawn in Sec. 7.
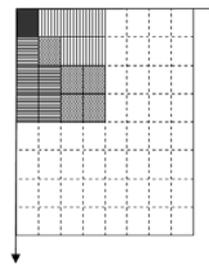
Figure 1. The upper left DCT coefficients used in our approach: (a) ▇ DC, (b) ▥ vertical texture feature, (c) ▤ horizontal texture feature, and (d) ▨ diagonal texture feature.

2. Feature Extraction

2.1 Color Space

A color space is a method by which we can specify, create and visualize color. Different color spaces are better for different applications [11], for example some equipment has limiting factors that dictate the size and type of color space that can be used. Some color spaces are perceptually linear, i.e. a one-unit change in stimulus will produce the same change in perception wherever it is applied. Many color spaces, particularly in computer graphics, are not linear in this way. Among these color spaces, the YUV color space is a bit unusual. The vast majority of DVDs already store information in the YUV color space. The Y component determines the brightness of the color (referred to as luminance or luma), while the U and V components determine the color itself (the chroma). Y ranges from 0 to 1 (or 0 to 255 in digital formats), while U and V range from -0.5 to 0.5 (or -128 to 127 in signed digital form, or 0 to 255 in unsigned form). Some standards further limit the ranges so the out-of-bounds values indicate special information like synchronization.

In our approach, the YUV color space is used for two reasons: 1) efficiency and 2) ease of extracting the features based on the color tones. One another neat aspect of YUV is that you can throw out the U and V components and get a grey-scale image. Since the human eye is more responsive to brightness than it is to color, many lossy image compression formats throw away half or more of the samples in the chroma channels to reduce the amount of data to deal with, without severely destroying the image quality. Therefore, only the Y

component is used in our preliminary study. There are many slightly different formulas to convert between YUV and RGB. The only major difference is a few decimal places. The following equations are used to convert from RGB to YUV spaces:

$$Y(x, y) = 0.299R(x, y) + 0.587G(x, y) + \\ 0.114B(x, y), \quad (1)$$

$$U(x, y) = 0.492(B(x, y) - Y(x, y)), \text{ and} \quad (2)$$

$$V(x, y) = 0.877(R(x, y) - Y(x, y)). \quad (3)$$

2.2 Feature vector

The fundamental problem for CBIR systems is to extract features for every image and to define a similarity measure for comparing images. The features serve as an image representation in the view of a CBIR system. Image contents can be defined at different levels of abstraction. At the first lowest level, an image is a collection of pixels. Pixel level content is rarely used in retrieval tasks. The raw data can be processed to produce numeric descriptors capturing specific visual characteristics called features. The most important features for image databases are color, texture and shape. In general, a feature-level representation of an image requires significantly less space than the image itself. Some transform type feature extraction methods can be applied to reduce the number of dimensions, such as Karhunen-Loeve (KLT), discrete Fourier transform (DFT), discrete cosine transform (DCT), and discrete wavelet transform (DWT), etc. Among these methods, DCT has been known for its excellent energy compacting property. It has received a great deal of attention and is widely used in image compression. For most images, most significant DCT coefficients are concentrated around the upper left corner; the significance of the coefficients decays with increased distance.

After an image is converted to the YUV color space, it is equally divided into four rectangular regions and one additional central region. Then the DCT is performed over the Y component for a whole image (global features) and five regions (regional features). Details on the segmentation will be explained in the next section. Eventually, an image is represented by one global feature and five regional features, each of which is constituted by a block of 4x4 DCT coefficients. As a result, only 96 DCT coefficients are needed for each image.

Note that the image is inherently a subjective medium and it might contain multiple concepts, that is, the perception of image content is very subjective, and the same content can be interpreted differently. For example, one user might be more interested in a different dominant feature of the image than the other, or two users might be interested in the same feature (e.g., texture), but the perception of a specific texture might be different for the two users. To solve this problem, the feature vector is categorized into four groups: the DC coefficient (V_1) represents the average energy of the image and all the remaining AC coefficients contain three directional feature vectors: vertical (V_2), horizontal

(V_3), and diagonal (V_4), as shown in Figure 1. The user can give different weight for each texture feature based on their perceptions for a query.
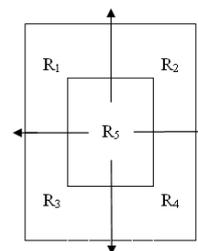
Figure 2. The five rectangular regions used in our approach.

3. Region of Interest and Segmentation

Another problem for CBIR systems is that users' intentions are diverse. For example, if an image with cloudy blue sky over green grass is used as a query, one might be seeking images with cloudy blue sky as the main theme whereas another might be seeking images largely containing green grass. This issue will be examined in our experiments later. Within this great diversity, it is suggested that a CBIR system should assist users in expressing their intentions behind the query. This leads to a number of solutions that do not treat the image as a whole, but rather deal with regions within an image[12,13]. Partitioning or segmenting the image into regions may reveal the "true" objects within an image, thus contributing to more meaningful image retrieval. The interested object/region in a query is commonly defined as region of interest (ROI). For the CBIR task that the user is only interested in a portion/region of an image, it is defined as localized content-based image retrieval[13] or region-based image retrieval (RBIR)[8].

A. Region of interest

In general, existing CBIR can be categorized into two major classes, namely, global methods and localized methods[12]. Global methods exploit features from the whole image and compute the similarity between images while local methods extract features from a region (portion) of an image and compute the similarity between regions. In RBIR, an image has to be segmented into regions before indexing and retrieval. However, it is hard to locate the ROI in the image when the interested object/region occupies only a small part of the image because the image background can have dominant impact on the feature extraction. The most direct way to solve the problems is to let the user select a ROI while conducting a query. As far as the target region is selected, the concept in the query image is expressed more accurately.

B. Segmentation

There have been many automatic segmentation algorithms proposed in RBIR. For example, SIMPLIcity[14] and WALRUS[15] are both wavelet-based and region-based CBIR systems. An obvious drawback of such systems is that the segmentation algorithms are

complex and computation intensive and the size of the search space is sharply increased due to exhaustive generation of subimages. In addition, the retrieval performance is affected significantly because the segmentation results are often incorrect. Therefore, the automatic detection of subimages remains an elusive task. In our work, we resort to a rectangular segmentation method, breaking images into a fixed number of regular rectangular regions. It seems that the use of more regions achieves a better result. However, it is not always the case and the execution speed becomes unsatisfactory slow for a large database.

The first step in our retrieval technique is to segment the image into regions that (ideally) would be easy for users to select their ROI. For this purpose, we need a segmentation method that is effective in rendering homogeneous regions in a short time. Figure 2 illustrates the five rectangular regions segmented in our approach. They are obtained by dividing the image into four non-overlapping regions and one central region with the same size as others, which is similar to the layout of the IBM TRECVID video retrieval system[10]. To avoid noise during the local match, our system allows users to select the ROI from the segmented five regions and only this region is then compared with regions in other images in the collection.

4. Similarity Measurement

In CBIR systems, image are in general represented and organized into n-dimensional feature vectors. Following to image representation, similarity measure is one of the key items in the process of image retrieval that affects the effectiveness and the efficiency of the retrieval technique. In practice, it is hard to define a distance between two sets of feature points such that the distance could be sufficiently consistent with a person's concept of semantic closeness of two images. Therefore, there are very few theoretical arguments supporting the selection of one distance over the others; computational cost is probably a more important consideration in the selection.

During the retrieval process, the query image and the database images are compared by evaluating the distance between their corresponding feature vectors. To exploit the energy preservation property of DCT, we use the sum of squared differences (SSD) as the distance function. Using a simpler distance on lower dimensional features means that computation can be saved both in the evaluation of distance and in the number of comparisons to be performed. For the local match, similarity measurement is performed based on region similarity. For the global match, the whole image is regarded as a "large" region. The distance function is defined as follows.

Overall region visual similarity relies on the combination of the four following discriptors: $DC(V_1)$, vertical texture (V_2), horizontal texture (V_3), and diagonal texture (V_4). Let Q and X denote the query image and a database image, respectively. V_k is the k-th feature vector of an image or a region (In our approach, $k = 1$ to 4). C_n

is a vector component in V_k. Assume the distance d_k is the distance between the k-th feature vector V_k^q of the ROI (e.g., the i-th region R_i^q) in Q and the k-th feature vector V_k^x of the j-th region R_j^x in X. Then,

$$d_k = d(R_i^q, R_j^x) = \sum_{C_n^q \in V_k^q, C_n^x \in V_k^x} (C_n^q - C_n^x)^2. \quad (4)$$

Similarity is evaluated as a weighted aggregation of image features. w_k is the weight assigned to the k-th feature vector in a query to express its importance. Thus the overall distance between two regions is:

$$D(R_i^q, R_j^x) = \sum_{k=1}^{4} w_k d_k. \quad (5)$$

When the user selects an interest region R_i^q in the query image Q and issues a query, candidate images are hence analyzed, by applying equations (4) and (5) for each region in turn, to find the best matching region in an image X, which having a smallest distance with the query region. The distance between Q and X can thus be defined as:

$$D(Q, X) = \underset{j=1 \, to \, 5}{Min}(D(R_i^q, R_j^x)). \quad (6)$$

In general, the conventional computer vision recognition-based task looks for the object to be searched with as small and as accurate a retrieved list as possible. But in CBIR, the goal is to extract as many "similar" objects as possible, the notion of similarity being very loose as compared to the notion of exact match.

5. Performance Evaluation

CBIR aims at searching image databases for specific images that are similar to a given query image. Many CBIR systems are available but it is difficult to assess which of these systems is the best as it is not possible to compare CBIR systems quantitatively and objectively. One reason for this is the absence of a standard database to determine a standard set of quantitative performance measures.

There are two commonly used performance measures in CBIR: the precision rate p and the recall rate r, which are adapted from textual information retrieval. They are defined as

$$p_M = \frac{n_r}{M}, \text{ and} \quad (7)$$

$$r_M = \frac{n_r}{N_r}, \quad (8)$$

where M is the total number of retrieved images, N_r is the total number of relevant images in the database, and n_r is the number of relevant images retrieved. It is assumed that the user inspects the m first images of the ranked list. So for every $m = 1, 2, …, M$, precision p_m and the recall r_m are calculated. Note that considering one additional image may raise the precision or lower it.

This process can be interpreted as looking only at the locally optimal answer sets for which recall and precision cannot be improved simultaneously by inspecting further images.

In practice, when the number of relevant images is greater than the size of the answer list, recall is meaningless as a measure of the retrieval quality. To overcome this problem, a measure called efficacy is introduced[16]:

$$\eta_M = \begin{cases} n_r / N_r \, , \; if \; N_r \leq M \\ n_r / M \, , \; if \; N_r > M \end{cases} \qquad (9)$$

where η_M is called the efficacy of retrieval for a given short-list of size M. If $N_r \leq M$, η_M becomes the traditional recall of information retrieval; if $N_r > M$, η_M is indeed the precision of information retrieval.
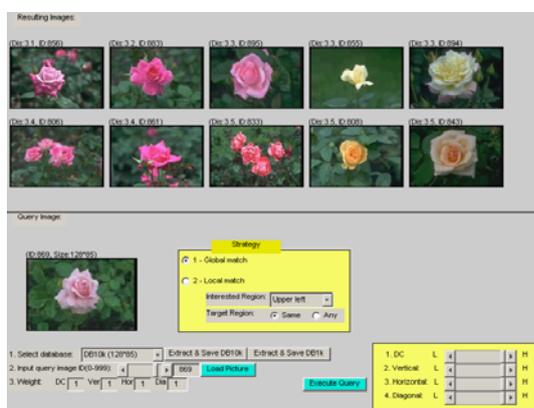
Figure 3. The system interface, browsing a query's result.

6. Experimental Results

In order to implement, test, and validate our approach, we develop a CBIR system with a general-purpose image database including 1,000 color images, which was downloaded from the WBIIS database[17]. Five categories of images, including eagles, brown animals, cloudy sky, mountain scene, and flowers were selected as benchmark images; each of these images was used in turn to query the image database. The returned images are considered relevant (or hit) once they appear in the same category to the query. Unlike recognition-based systems, CBIR systems require versatility and adaptation to the user, rather than the embedded intelligence desirable in recognition tasks. Therefore, design efforts in our CBIR system are devoted to combine light computation, great flexibility and friendly user interface such that the system is evaluative enough to let users conduct a query, modify parameters, and browse the results for benchmarking.

During the query process, it's hard to guess what object is the target of users. In our system, users can specify a whole image (global match) or a particular ROI (local match) as a query. Figure 3 is the interface of our system, where the user can specify the ROI, adjust the weight of each feature, and inspect the retrieved results.

The ROI capabilities in the system, allowing the expressions of interested region in the query image, are highly appealing to capture a certain level of semantics and can be used much in the same way as words. For example, the system will accept queries like "Find me all the images containing the contents in the upper left region of the query image." To accomplish this, the user can select any one of the regions (upper left, upper right, lower left, lower right, and center) for local match (or regional match). For those query images without clear objects, the user can select the option "global match" to conduct the query. For a single region query (i.e., regional match), there are two options" "same" and "any", which means the ROI of the query image is compared with the "same" or "any" region of the candidate images.

After the user loads a query image and selects the ROI, the system first initializes a set of uniformly distributed weights for features (i.e., the default weights). Then the user's specific information needs can be described by adjusting the weight of each feature. To achieve the best possible results, the feature vector of the ROI is compared with the feature vectors of all predefined regions of candidate images. Through exhaustive searches, the top ten in similarity are displayed to the user, ranked in the ascending order of the distance to the query image from the left to the right and then from the top to the bottom. Note that the similarity is computed on the basis of the default or adjusted weights, modeling what users see when they look at the query image.
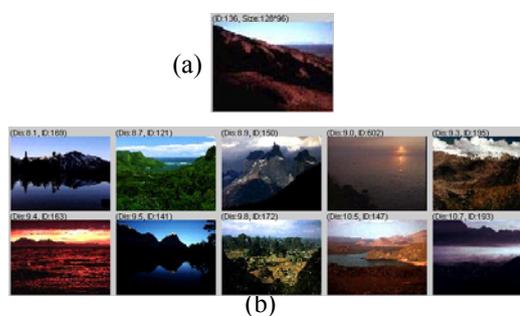
Figure 4. (a) The query image; (b) retrieval results using global match.

Several queries are first given for better illustrating the use of global match and local match. For the first query, an image of a mountain scene is given as the query image, shown as Figure 4(a). Since no obvious object/region appears in the image, the user can not pick the region which is perceptually meaningful as the ROI. Thus, the user selects the option "global match" to conduct the query. Figure 4(b) gives a very promising result. In the second query image, as shown in Figure 5(a), there is a round bright object in the center, surrounded by darkness and a faint glow. Figure 5(b) shows the results using the global match while Figure 5(c) shows the results using the local match with the option "any". It is observed that local match explores more interesting images than global match, which returns

images with shinning objects at other regions. Another example of local match often happens in the real world.

(a)

(b)

(c)
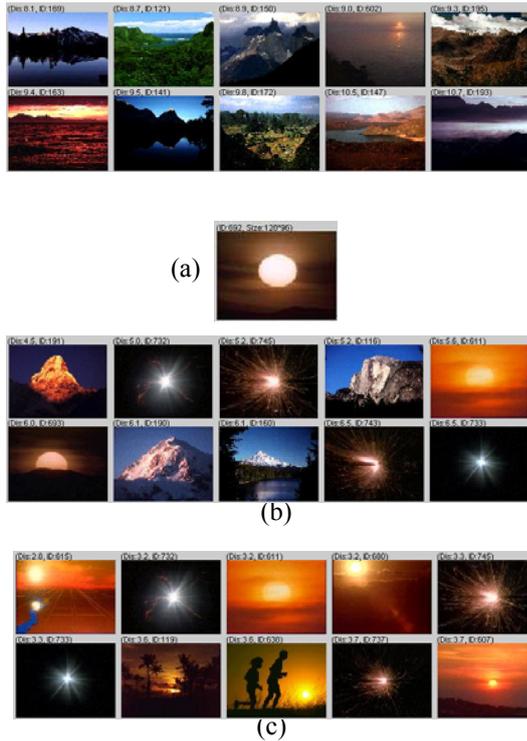
Figure 5. (a) The query image; (b) retrieval results using global match; (c) retrieval results using local match (options: "center" and "any").

(a)

(b)
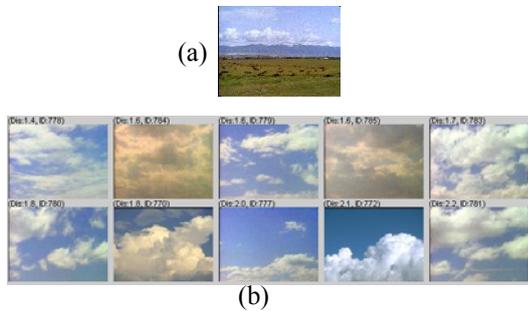
Figure 6. (a) The query image; (b) retrieval results using local match (options: "upper left" and "any")

If a user wants to find out images with cloudy blue sky, but only has an image like Figure 6(a) in hand, he/she can selects the ROI that contains his/her target object. It can be seen that the result in Figure 6(b) matches the user's needs, without containing grass "objects" as in the query image.

A series of experimental results are collected to show the feasibilities of our solution. The next experiment examines the appropriateness of the feature vector (i.e., Y-component) and weights adjustment. The benchmark query targets are manually picked from five commonly accepted categories. Tables 1 to 5 show all the query results; each for one individual category. Table 6 summarizes the search results for all of the categories. It

can be noticed that the average efficacy is improved from 72.38% to 79.05% if the proper weights are given. Some of the query examples even result in great improvements by giving different weights. For instance, while using ID 240 as the query image, the number of the retrieved relevant images increases from 5 to 9 if the weights adjusted from (1,1,1,1) to (0,1,1,1). Generally speaking, in the query process, users can adjust the weights through a set of experiments, with the goal of learning which features are most likely to contribute to the query.

The following experiment verified the necessity of ROI. We purposely choose ten queries with poor performance on the global match, compared with the same queries on the local match. Table 7(a) shows the retrieval results for global match, where the queries do not perform ROI selection and use the whole image for feature construction. In the local match, as shown in Table 7(b), users can select their ROI with the same weights (i.e., default weights) as those in the global match. It is obvious that ROI selection makes great improvement raising efficacy from 44% to 56%. Next, to further evaluate the effectiveness of the weight adjustment, we conduct queries with the same ROI selections but different weight settings. From Table 7(c), it can be seen that the weight adjustment can improve the discrimination ability as in the experiment 1, raising efficacy from 66% to 81%.

Table 1. The average efficacy of global match for category 1.

Category ID = 1 (# of related image)	Image ID	Default weights	Hit	Adjusted weights	Hit
Eagle (9)	275	1111	4	1011	5
	276	1111	7	1110	8
	277	1111	5	1111	5
	278	1111	5	1111	5
	281	1111	2	1011	6
	285	1111	6	1011	7
	286	1111	6	1111	6
	287	1111	6	1111	6
	289	1111	6	1111	6
Average Efficacy		58.02%		66.67%	

Table 2. The average efficacy of global match for category 2.

Category ID = 2 (# of related image)	Image ID	Default weights	Hit	Adjusted weights	Hit
Brown animals (18)	219	1111	7	1111	7
	220	1111	10	1111	10
	221	1111	9	1110	10
	222	1111	8	1111	8
	223	1111	6	1111	6
	224	1111	6	1111	6
	225	1111	8	1111	8
	235	1111	7	1110	8
	236	1111	6	1110	7
	237	1111	6	1110	8
	239	1111	6	1111	6
	240	1111	5	0111	9
	241	1111	9	1101	10
	242	1111	5	0111	6
	243	1111	3	1101	5
	244	1111	4	1111	4
	245	1111	2	1100	5
	246	1111	9	0111	10
Average Efficacy		64.44%		73.89%	

Table 3. The average efficacy of global match for category 3.

Category ID = 3 (# of related image)	Image ID	Default weights	Hit	Adjusted weights	Hit
Cloudy Sky (22)	275	1111	4	1011	5
	764	1111	7	1101	8
	766	1111	4	1111	4
	767	1111	4	0111	5
	768	1111	7	1110	8
	769	1111	5	1011	6
	770	1111	10	1111	10
	771	1111	9	1111	9
	772	1111	9	1111	9
	773	1111	5	1111	5
	774	1111	5	1011	7
	775	1111	5	1111	5
	776	1111	10	1111	10
	777	1111	10	1111	9
	778	1111	9	1101	10
	779	1111	9	1110	10
	780	1111	10	1111	10
	781	1111	9	1011	10
	782	1111	9	1011	10
	783	1111	9	1111	9
	784	1111	10	1111	10
	785	1111	10	1111	10
Average Efficacy		76.36%		80.45%	

Table 4. The average efficacy of global match for category 4.

Category ID = 4 (# of related image)	Image ID	Default weights	Hit	Adjusted weights	Hit
Mountain scene (13)	105	1111	8	1011	9
	106	1111	9	1110	9
	121	1111	9	1110	9
	124	1111	9	1110	10
	136	1111	10	1111	10
	143	1111	10	1111	10
	144	1111	10	1111	10
	147	1111	9	1011	10
	150	1111	9	1110	10
	165	1111	9	1011	10
	177	1111	6	1011	9
	178	1111	9	1111	9
	195	1111	10	1111	8
Average Efficacy		90.00%		94.62%	

Table 5. The average efficacy of global match for category 5.

Category ID = 5 (# of related image)	Image ID	Default weights	Hit	Adjusted weights	Hit
Flowers (26)	800	1111	7	1011	8
	801	1111	4	1011	5
	802	1111	4	1011	6
	805	1111	6	1110	7
	806	1111	8	1011	9
	808	1111	8	1111	8
	811	1111	7	1110	8
	812	1111	6	1111	6
	824	1111	9	1111	9
	827	1111	7	1011	8
	828	1111	9	1111	9
	830	1111	9	1111	9
	833	1111	8	1111	8
	837	1111	3	1011	7
	838	1111	9	1111	9
	840	1111	7	1110	8
	845	1111	8	1111	8
	853	1111	9	1111	9
	856	1111	9	1111	9
	857	1111	8	1111	8
	859	1111	8	1011	9
	861	1111	7	1111	7
	862	1111	8	1111	8
	866	1111	5	1011	8
	869	1111	10	1111	10
	892	1111	7	1111	7
Average Efficacy		73.08%		79.62%	

Table 6. The comparison of global match for five categories.

Category ID	Category (# of related image)	Default weights	Adjusted weights
1	Eagle (9)	58.02%	66.67%
2	Brown animals (18)	64.44%	73.89%
3	Cloudy Sky (22)	76.36%	80.45%
4	Mountain scene (13)	90.00%	94.62%
5	Flowers (26)	73.08%	79.62%
Average Efficacy		72.38%	79.05%

Table 7. The comparison of global match and local match (ROI).

Image ID	(a) Global		(b) ROI(1)			(c) ROI(2)		
	Default weights	# of relevant images	Selected region	Default weights	# of relevant images	Selected region	Adjusted weights	# of relevant images
603	1,1,1,1	3	upper left	1,1,1,1	6	upper left	1,1,0,1	7
608	1,1,1,1	3	lower left	1,1,1,1	5	lower left	1,0,1,1	7
609	1,1,1,1	5	center	1,1,1,1	7	center	1,1,1,1	9
633	1,1,1,1	5	upper right	1,1,1,1	6	upper right	1,1,0,1	8
637	1,1,1,1	4	lower right	1,1,1,1	5	lower right	1,1,1,0	7
638	1,1,1,1	4	lower right	1,1,1,1	8	lower right	1,1,1,0.5	8
645	1,1,1,1	3	lower left	1,1,1,1	4	lower left	0,1,1,1	7
604	1,1,1,1	6	lower left	1,1,1,1	10	lower left	1,1,1,1	10
653	1,1,1,1	6	lower left	1,1,1,1	7	lower left	1,0,1,1	9
680	1,1,1,1	5	upper left	1,1,1,1	8	upper left	1,1,0.5,0.5	9
Efficacy	44.00%			66.00%			81.00%	

7. Conclusions

In CBIR, the queries are often exploratory searches to decide which image is relevant for a certain purpose during the retrieval. For example, users usually search the web for images without assuming that the objects they are looking for are unique. Any objects described by the same information are good enough for a user's generic need. Therefore, CBIR systems require versatility and adaptation to the users, rather than the sophisticated intelligence for exact recognition tasks. Another problem in CBIR is that it is hard to guess what object is the target of users. In practice, the region of interest (ROI) is easy to observe but hard to isolate through automatic region analysis. Even though automatic segmentation can isolate multiple objects in an image, users still have to explicitly select which is their interested one. Thus, it is quite useful if a priori knowledge of the ROI is provided by users.

Under above considerations, this paper presents a general and effective feature descriptor and provides a simple way for users to express their ROI. The retrieval can be either global or local, focusing on the whole image or a particular region. During the retrieval procedures, users can adjust the weight of each individual feature through a series of experiments, with the goal of learning which features are most likely to contribute to the query. The experiment results show that the proposed DCT-based feature descriptor, coupled with a selection of ROI, can easily extend the capability of CBIR to RBIR. It is also observed that the introducing of weight adjustment explores more interesting images and improves the retrieval performance. Some promising properties of our approach are highlighted as follows:

1. It is very computationally efficient and provides good-enough performance.
2. It bridges the semantic gap by providing the

functionality of ROI.

3. It offers great flexibility for users to express their personal view on each individual feature.
4. It is simple and easily implementable.

Now the system is ready for retrieving the images through either global or local match, in which queries can be formulated at a simple semantic level. The experiments show that our approach provides a generic and efficient solution for image retrieval. However, we found that the color tones of the retrieved images are not always similar to that of the query image even though they are similar from the viewpoint of texture or shape. This is because only Y component is used in the feature vector for retrieval efficiency. In the future, we are going to consider the use of the U and V components and find out a balance point between efficiency and accuracy. In addition, from the computational point of view, CBIR systems are potentially expensive and have response times growing with the ever-increasing sizes of the databases associated to them. To address this challenge, our continuing study includes designing a multiple-stage CBIR system and developing a filter that eliminates those candidate images with widely distinct features at an earlier stage.

*Correspondence:

hsiao@mis.knjc.edu.tw;

M.-J. Hsiao is currently an instructor at Kang-Ning Junior College of Medical Care and Management.

References

1. Brahmi D, Ziou D. Improving CBIR systems by integrating semantic features. Proc. RIAO France 2004; 291-305.
2. Besser, Howard. Visual Access to Visual Images: The UC Berkely Image Database Project. Library Trends 1990; 38(4); 787-798.
3. Smeulders A W M, Worring M, Santina S, Gupta A, Jain R. Content-based image retrieval at the end of the early years. IEEE Trans. Patt. Anal. Mach. Intell. 2000; 22(12); 1349-1380.
4. Datta R, Li J, Wang Z. Content-based image retrieval - approaches and trends of the new age. Proc. Int. Workshop on Multimedia Information Retrieval, ACM 2005; 253-262.
5. Veltkamp R C, Tanase M. Content-based image retrieval systems: A survey. Tech. Rep. UU-CS-2000-34, Utrecht University, Available online from:
   http://give-lab.cs.uu.nl/cbirsurvey/cbir-survey.pdf.
6. Deselaers T, Keysers D, Ney H. Features for image retrieval: an experimental comparison. Information retrieval 2008; 11(2); 77-107.
7. Liu Y, Zhang D, Lu G, Ma W Y. A survey of content based image retrieval with high-level semantics. Pattern Recognition 2007; 40(1); 262–282.
8. Islam M M, Zhang D, Lu G. Comparison of retrieval effectiveness of different region based image representations. The 6th Int. Conf. on Information, Communications & Signal Processing 2007; 1-4.
9. Rudinac S, Uscumlic M, Rudinac M, Zajic G, Reljin B. Global Image Search vs. Regional Search in CBIR Systems. Proc. of the 8th Int. Workshop on Image Analysis for Multimedia Interactive Services 2007.
10. Amir A, Berg M, Chang S-F, Hsu W, Iyengar G, Lin C-Y, Naphade M, Natsev A, Neti C, Nock H, Smith J, Tseng B, Wu Y, Zhang D. IBM research Trecvid-2003 video retrieval system. Proc. of NIST TrecVid 2003.
11. Ford A, Roberts A. Colour Space Conversions. Available at http://www.poynton.com/PDFs/coloureq.pdf 1998.
12. Li W-J, Yeung D-Y. Localized Content-Based Image Retrieval Through Evidence Region Identification. IEEE Computer Society Conference on Computer Vision and Pattern Recognition 2009.
13. Rahmani R, Goldman S A, Zhang H, Cholleti S R, Fritts J E. Localized content-based image retrieval. IEEE Transactions on Pattern Analysis and Machine Intelligence 2008; 30(11);1902-1912.
14. Wang Z, Li J, Wiederhold G. SIMPLIcity: Semantic-Sensitive Integrated Matching for Picture Libraries. IEEE Trans. on Pattern Analysis and Machine Intelligence 2001; 23(9); 947-963.
15. Natsev A, Rastogi R, Shim K. WALRUS: A Similarity Retrieval Algorithm for Image Databases. IEEE Trans. on Knowledge and Data Engineering 2004; 16(3); 301-316.
16. Huang PW, Dai SK. Design of a Two-Stage Content-Based Image Retrieval System Using Texture Similarity. Information Processing and Management 2004; 40(1); 81-96.
17. Wang J Z. Content Based Image Search Demo Page. Available at http://bergman.stanford.edu/~zwang/ project /imsearch/WBIIS.html 1996.

Complete Assignment of 1H and 13C NMR Spectra of Tilmicosin Phosphate

Na Zhang[1] , Le Tao[2],   Qiang Wang[2] , Jun-biao Chang[1, 2 *]

[1] College of Pharmaceutical Science and Technology, Tianjin University, Tianjin 300072, China
[2] Department of Chemistry, Zhengzhou University, Zhengzhou, Henan 450000, China
Email: changjunbiao@zzu.edu.cn
Received: October 25, 2009

Abstract

The ^{1}H and ^{13}C NMR spectroscopic data of tilmicosin phosphate has been fully assigned by combination of one- and two-dimensional experiments (DEPT, HMBC, HMQC, ^{1}H-^{1}H COSY). The site of combination with phosphoric acid was assigned by comparing the ^{13}C NMR chemical shifts between tilmicosin and its phosphate. [Life Science Journal. 2010; 7(1): 107 – 110] (ISSN: 1097 – 8135).

1. Introduction

Tilmicosin, a semi-synthetic macrolide antibiotic derived from the macrolide antibiotic tylosin and 20-dihydro-20-deoxy-20-(*cis*-3, 5-dimethylpiperidin-1-yl) -desmycosin, is effective in the treatment of respiratory diseases in cattle against a broad range of bacteria. The free form is moderately soluble in aqueous solutions, while the chloride and phosphate salts are highly soluble[1]. Synthesis of tilmicosin was described by Debono et al[2,3].

The ^{1}H and ^{13}C NMR data of tilmicosin and its derivatives were discussed previously[4,5,6,7]. However, there is no literature precedent investigating the NMR data of tilmicosin phosphate.

The present study focused on the complete ^{1}H and ^{13}C NMR assignments of tilmicosin phosphate (Figure 1), and compared the ^{13}C NMR chemical shifts between tilmicosin and its phosphate, to assign the position which combined with phosphoric acid.
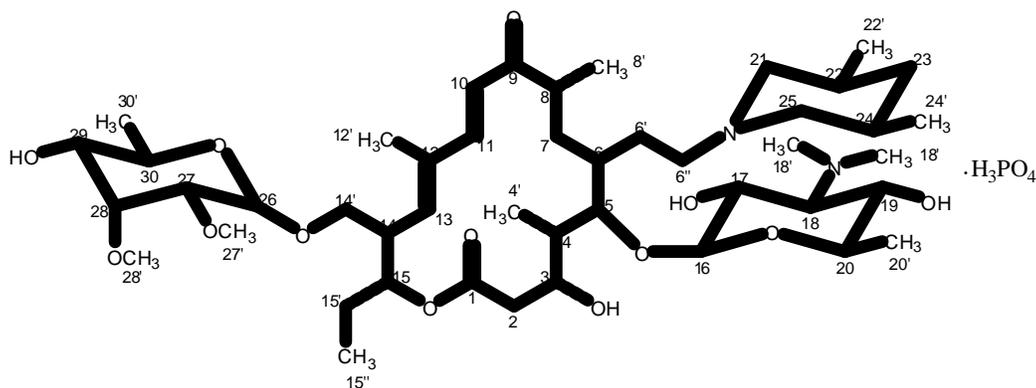

Figure 1. The structure of tilmicosin phosphate

2. Materials and Methods

Compound (Tilmicosin Phosphate) was provided by Xinxiang Ruite Fine Chemical Co. Ltd., Henan, China.

All NMR experiments were performed at 298K on a solution of the compound (40 mg) dissolved in 0.6 mL of D$_2$O on a Bruker Avance 300MHz instrument. ^{1}H NMR, ^{13}C NMR, quantitative ^{13}C NMR, DEPT-90, DEPT-135 NMR and ^{31}P NMR measurements were recorded with a 5 mm QNP probe. 2D NMR experiments were performed with a broadband inverse (BBI) probe equipped with a Z-gradient coil.

^{1}H NMR spectra were recorded at a frequency of 300.13 MHz with a spectral width of 6 kHz and a 7.20 μs (90°) pulse. The acquisition time was 2.7s and relaxation delay 2s; 16 scans with 32K data points were used. ^{13}C NMR, DEPT-90 and DEPT-135 spectra were

recorded at a frequency of 75.47 MHz with a spectral width of 22.7 kHz and a 7.30 μs (90°) pulse. The acquisition time was 0.72s and relaxation delay 2s; 9k scans with 32K data points were used. The quantitative ^{13}C NMR spectrum was obtained using the zgig pulse program and with relaxation delay 20s, other parameters were as above. The HMQC spectra were obtained using the hmqcgpqf pulse program. The spectra resulted from a 256 x 1024 data matrix with 8 scans per t_1 increment. Spectral widths of 2480Hz in f_2 and 16650 Hz in f_1 were used. The acquisition time was 0.21s, the d2 delay was 3.45 ms (corresponding to an average ^{1}J$_{(C,H)}$ of 145Hz) and the relaxation time was 2s. The HMBC spectra were obtained using the hmbcgplpndqf pulse program. The spectra resulted from a 256 x 1024 data matrix with 8 scans per t1 increment. Spectral widths of 2480Hz in f_2

and 16650 Hz in f_1 were used. The acquisition time was 0.21s, the d2 and d6 delays were set to 3.45 ms (1/2$J_{C,H}$) and 71.43 ms (corresponding to an average 1/$^{n}J_{C,H}$ of 7 Hz) and the relaxation time was 2s. The ^{1}H-^{1}H COSY spectra were obtained using the cosydfph pulse program. The spectra result from a 256 x 1024 matrix with 8 scan per t_1 increment. Spectral widths of 2856 Hz in both f_1 and f_2 dimensions were used. The acquisition time was 0.20s and the relaxation time was 2s. ^{31}P NMR spectra were recorded at a phosphorus frequency of 121.44 MHz with a spectral width of 6 kHz and a 7.20 μs (90°) pulse.

Chemical shifts are given on the δ scale and are referred to 1,4-dioxane (external standard, sealed in a 1mm capillary) at δ = 3.70 ppm for ^{1}H, δ = 67.8 ppm for ^{13}C[10], and 85% H_3PO_4 (external standard, sealed in a 1mm capillary) at δ = 0.0 ppm for ^{31}P. Coupling constants J are reported in Hz. The following abbreviations were used: s, d and m, for singlet, doublet and multiplet, respectively.

3. Result and Discussion

The molecular formula of tilmicosin phosphate was deduced as $C_{46}H_{81}N_2O_{13}$ through HRMS, which showed an [M+1] peak at m/z 869.5732 (calcd for $C_{46}H_{81}N_2O_{13}$, 868.5660).

The 3,5-dimethyl-piperidino moiety was comprised of *cis*-isomer (85%) and *trans*-isomer (15%), the latter of which was excluded based on quantitative ^{13}C NMR spectrum. The quantitative ^{13}C NMR and DEPT spectra showed 44 signals (including 46 carbon atoms) comprising of 12 methyl, 9 methylene, 22 methine and 3 quaternary carbons, which confirmed the molecular formula.

The down field signal at δ 210.22 and 175.15 could be assigned to the ketone (C-9) and lactone (C-1)

carbons. The presence of two olefinic bonds could be interred by signals at δ 150.36, 144.79, 136.73 and 119.29, respectively. Because the signal at δ 136.73 was a quaternary carbon, it could be assigned to C-12. The signals at δ 102.88 and 101.26 belong to the anomeric carbon atom. This indicated that there were two sugar molecules attached to tilimicosin. [8,9]

The ^{1}H NMR spectrum showed presence of the double bonds at δ 6.96 (1H, d, J=15.37Hz), 6.30 (1H, d, J=15.37Hz) and 5.61 (1H, d, J=10.25Hz), and the signal at δ 5.61 could be assigned to H-13. Two methoxy and two N-methyl protons were observed at δ 3.20 (3H, s), 3.10 (3H, s) and 2.63 (6H, s). Two signals at δ 4.25 (^{1}H, d, J=8.05Hz) and 4.17 (1H, d, J=7.32Hz) were assigned to the hydrogen atoms attached to the anomeric carbons by their chemical shifts and HMQC spectrum. [9]

The sginal at δ 2.81 (^{1}H, m) showed ^{1}H-^{1}H COSY correlations with H-13 was assigned to H-14. H-14 also showed ^{1}H-^{1}H COSY correlations with H-15 at δ 4.52. The proton at δ 4.25 showing ^{3}J correlations with two methane and one methylene was assigned to H-26. The other proton attached to anomeric carbon at δ 4.17 was assigned to H-16 and authenticated by HMBC. The coupling constants of H-16 and H-26 were 7.32Hz and 8.05Hz respectively, indicating β configuration to H-16 and H-26[9]. Other protons and carbons could be assigned by ^{1}H-^{1}H COSY, HMQC and HMBC.

H-4, H-6 and H-6' could not be identified in the ^{1}H NMR spectrum, because of the complexity of the coupling correlations and the large number of protons in the high field of the spectrum. Their chemical shifts were assigned by HMQC.

Table 1. ^{1}H and ^{13}C chemical shift and ^{1}H-^{1}H COSY, HMBC correlations of tilmicosin phosphate

position	δ (^{1}H), multiplicities and J (Hz)	δ (^{13}C)	^{1}H-^{1}H COSY	HMBC (H C)
1	/	175.15	/	/
2	2.28 (m)	40.15	H-2, H-3	C-1, 3, 4, 4'
	1.85 (d, 17.93)		H-2	
3	3.34 (m)	67.77	H-2	C-1
4	1.48 (m)	41.27	/	/
4'	0.65 (m)	9.12	/	C-3, 4, 5
5	3.23 (m)	80.14	/	C-3, 4, 6, 6', 7
6	1.13 (m)	36.52	/	/
6'	1.66 (m)	23.74	/	/
	1.46 (m)			
6''	3.00 (m)	59.12	/	C-8
7	1.53 (m)	32.90	H-7, H-8	C-5, 8'
	1.19 (m)		H-7	
8	2.72 (m)	45.89	H-7, H-8'	C-8', 9
8'	0.90 (m)	17.28	H-8	C-7, 9
9	/	210.22	/	/
10	6.30 (d, 15.37)	119.29	H-11	C-9, 12
11	6.96 (d, 15.37)	150.36	H-10	C-9, 10, 12, 12', 13
12	/	136.73	/	/
12'	1.51 (s)	12.92	H-13	C-11, 12, 13
13	5.61 (d, 10.25)	144.79	H-12', H-14	C-11, 12', 14, 14', 15
14	2.81 (m)	45.22	H-13, H-15	C-14', 15
14'	3.64 (m)	70.56	H-14'	C-13, 14, 15, 26

	3.39 (m)			
15	4.52 (m)	76.58	H-14, H-15'	C-1, 15"
15'	1.50, 1.28 (m)	25.19	H-15, H-15"	C-15, 15"
15"	0.56 (m)	9.50	H-15'	C-15, 15'
16	4.17 (d, 7.32)	102.88	H-17	C-5, 20
17	3.37 (m)	69.01	H-16, H-18	C-16
18	2.97 (m)	70.87	H-17, H-19	C-17, 18', 19
18'	2.63 (s)	42.03	/	C-18, 18'
19	3.18 (m)	69.49	H-18	C-20, 20'
20	3.17 (m)	73.01	H-20'	C-16, 19, 20'
20'	0.97 (m)	17.48	H-20	C-19, 20
21	2.98 (m)	50.00	H-21	C-22, 22', 23
	2.15 (m)		H-21, H-22	
22	1.56 (m)	29.64	H-21, H-22'	C-24
22'	0.60 (m)	18.32	H-22	C-21, 22, 23
23	1.55 (m)	39.19	H-23	C-21, 22, 24
	0.51 (m)			
24	1.54 (m)	29.03	H-24', H-25	/
24'	0.60 (m)	18.55	H-24	C-23, 24, 25
25	3.29 (m)	58.02	H-24, H-25	C-21, 23, 24, 24'
	2.10 (m)		H-25	
26	4.25 (d, 8.05)	101.26	H-27	C-14', 28, 30
27	2.82 (m)	80.83	H-26, H-28	C-26, 27'
27'	3.10 (s)	58.69	/	C-27
28	3.60 (m)	79.61	H-27, H-29	C-26, 27, 28', 29, 30
28'	3.20 (s)	62.25	/	C-28
29	3.01 (m)	73.23	H-28, H-30	C-28, 30, 30'
30	3.38 (m)	70.45	H-29, H-30'	C-26, 29, 30'
30'	0.87 (m)	17.48	H-30	C-29, 30

The signal of ^{31}P NMR at δ 2.077 showed the existence of phosphate.
The difference between tilmicosin[6,7] and its phosphate was shown in Table 2.

Table 2. The difference of ^{13}C NMR data between tilmicosin and its phosphate

position	δ (tilmicosin phosphate)	δ (tilmicosin[6], Acetone-d_6)	δ (tilmicosin[7], CDCl$_3$)
1	175.15	173.01	172.06
2	40.15	40.25	39.44
3	67.77	67.35	66.29
4	41.27	42.77	42.14
4'	9.12	9.30	9.195
5	80.14	80.03	79.20
6	36.52	32.86	31.55
6'	23.74	25.21	24.06
6"	59.12	55.38	54.34
7	32.90	34.53	33.97
8	45.89	45.89	45.17
8'	17.28	18.15	17.87
9	210.22	203.62	203.92
10	119.29	119.81	118.12
11	150.36	147.95	147.76
12	136.73	135.31	134.39
12'	12.92	13.16	12.92
13	144.79	143.07	143.16
14	45.22	45.77	45.17
14'	70.56	69.41	69.30
15	76.58	74.79	73.76
15'	25.19	25.65	25.40
15"	9.50	9.95	9.52
16	102.88	105.58	104.08
17	69.01	71.35	71.16
18	70.87	71.73	70.08
18'	42.03	42.03	41.69

19	69.49	71.91	70.85
20	73.01	73.94	73.16
20'	17.48	18.21	17.73
21	50.00	59.77	58.72
22	29.64	30.86	29.94
22'	18.32	19.88	19.48
23	39.19	43.47	42.35
24	29.03	30.65	29.80
24'	18.55	19.88	19.76
25	58.02	64.32	63.42
26	101.26	102.05	101.12
27	80.83	82.76	81.88
27'	58.69	59.41	59.72
28	79.61	81.41	79.82
28'	62.25	61.74	61.71
29	73.23	74.00	72.63
30	70.45	70.32	70.58
30'	17.48	17.92	17.73

4. Conclusion

The difference of chemical shifts of C-6'', C-21 and C-25 between tilmicosin and its phosphate was larger than that of C-18 and C-18', which indicated that the phosphoric acid was combined with the nitrogen atom of 3,5-dimethyl-piperdino group.

Correspondence author:

Junbiao Chang, Department of Chemistry, Zhengzhou University, Zhengzhou, Henan 450001, China. Tel: 86-371-67783017; e-mail: changjunbiao@zzu.edu.cn.

REFERENCES

1. Yerramilli V.S.N.M., Apex, NC USP 7282487.
2. Manuel D., Herbert A.K. USP 4820695.
3. Manuel Debono, Kevin E. Willard, Herbert A. Kirst, Julie A. Wind, Gary D. Crouse, Eddie V. Tao, Jeffery T. Vicenzi, Fred T. Counter, John L. Ott, Earl E. Ose, Satoshi Omura The Journal of Antibiotics, 1989, 42(8), 1253-1267.
4. H.A. Kirsi, K.E. Willard, M. Debono, J.E. Toth, B.A. Truedell, J.P. Leeds, J.L. Ott, A.M. Felty-Duckworth, F.T. Counter, E.E. Ose, G.D. Crouse, J.M. Tustin, Satoshi Omura. The Journal of Antibiotics, 1989, 42(11), 1673-1683.
5. Lawrence C.C., Herbert A.K., Thomas R.S., Jack B.C., Andrew G.W. The journal of antibiotics, 1995, 48, 671-675.
6. Herbert A. Kirst; Alvin L. Donoho; Lawrence C. Creemer; Julie A. Wind; Donnis M. Berry; John L. Occolowitz; Jonathan W. Paschal. J. Agric. Food Chem. 1994, 42, 1219-1222.
7. Shu-rong LV. Master Dissertation, Ocean University of China, Tsingtao, 2004, 18-20.
8. De-quan YU, Jun-shan YANG. The handbook of analytical chemistry (2nd end), Vol. 7, Chemistry Industry Press: Beijing, 1999, 495-497, 497-498 and 901-904.
9. Tian-zeng Zhao. Carbon-13 NMR spectroscopy, Henan Science and Technology Press: Zhengzhou, 1993.
10. Jian QI, Xiu-xiang GAO, Mei-xian Zhao, Jun-feng XIANG, Chong-xi LIN, Yi-zhuang XU, Jin-guang WU. Chemical Journal of Chinese Universities, 2007, 28(5), 913-917.

Life Science Journal

(Acta Zhengzhou University Overseas Edition)

Call for Papers

The academic journal "*Life Science Journal*" (ISSN: 1097-8135) is inviting you to publish your papers.

Life Science Journal, the Acta Zhengzhou University Oversea Version registered in the United States, is an international journal with the purpose to enhance our natural and scientific knowledge dissemination in the world under the free publication principle. The journal is calling for papers from all who are associated with Zhengzhou University-home and abroad. Any valuable papers or reports that are related to life science-in their broadest sense-are welcome. Other academic articles that are less relevant but are of high quality will also be considered and published. Papers submitted could be reviews, objective descriptions, research reports, opinions/debates, news, letters, and other types of writings. Let's work together to disseminate our research results and our opinions.

Please send your manuscript to editor@sciencepub.net.

Life Science Journal

ISSN 1097-8135

9 771097 813002